UNIVERSITAT POLITÈCNICA DE VALÈNCIA

Departamento de Máquinas y Motores Térmicos

DOCTORAL THESIS

"Development and validation of a virtual engine model for simulating standard testing cycles"

Presented by

D. Ángel Auñón García

Supervised by

Dr. D. Francisco José Arnau Martínez

València, April 2021

DOCTORAL THESIS

``Development and validation of a virtual engine model for simulating standard testing cycles''

Presented by: D. Ángel Auñón García
Supervised by: Dr. D. Francisco José Arnau Martínez

THESIS EXAMINERS

Dr. D. Óscar García Afonso (Universidad de La Laguna)
Dr. D. Miguel Ángel Reyes Belmonte (Universidad Rey Juan Carlos)
Dr. D. Francisco Vera García (Universidad Politécnica de Cartagena)

DEFENSE COMMITTEE

Chairman: Dr. D. José Manuel Luján Martínez (Universitat Politècnica de València)
Secretary: Dr. D. Francisco Vera García (Universidad Politécnica de Cartagena)
Member: Dr. D. José Vicente García Ortiz (Universidad Jaume I)

València, April 2021

Abstract

The new regulations regarding greenhouse emissions and air quality have led the technological progress of the internal combustion engines during the recent years. Improvements in the combustion process, turbocharging, thermal management, after-treatment systems and techniques such as the exhaust gases recirculation, have resulted in cleaner internal combustion engines. The adoption of the new type approval test in Europe, so-called WLTP, which represents a more realistic driving cycle than its forerunner the NEDC, as well as the need to evaluate pollutant emissions at different conditions of ambient temperature and altitude, represent a challenge for manufacturers when it comes to design and optimise their engines. In this context, one-dimensional engine models offer the possibility to develop and test different solutions with enough accuracy, while hastening the engine design process and reducing its costs.

The main objective of this thesis is to develop a complete virtual engine model able to simulate transient conditions of engine speed and load, as well as different ambient conditions of pressure and temperature. The engine model is used to predict the main thermo-and fluid dynamic variables at different engine locations and the tailpipe pollutant emissions.

Furthermore, engine cold start and its operation at low temperature is associated to a greater fuel consumption, hydrocarbon (HC) and carbon monoxide (CO) emissions; as well as more nitrogen oxide (NO_x) emissions due to the deactivation of the exhaust gases recirculation systems. A solution to mitigate these negative effects is to heat up the after-treatment system so as to achieve its activation temperature as soon as possible. In the work presented, this goal is addressed through two different standpoints. On the one hand, variable valve timing systems have been studied as a way to increase the exhaust gases temperature. With this option it is possible to reduce CO and HC emissions by 40-50 % and NO_x emissions by 15 % during the first stage of the WLTC cycle, at the expense of a penalty in the fuel consumption. On the other hand, the thermal insulation of the exhaust system has also been studied with the same objective. In this case, it is possible to

reduce CO and HC emissions by 30 %, while not improving NO_x ones.

Keywords: one-dimensional model; internal combustion engine; pollutant emissions; variable valve timing; thermal insulation

Resumen

Las nuevas regulaciones en materia de emisiones de efecto invernadero y calidad del aire han conducido la evolución tecnológica de los motores de combustión interna durante los últimos años. Las mejoras en el proceso de la combustión, la sobrealimentación, la gestión térmica, los sistemas de post tratamiento y técnicas como la recirculación de gases de escape, han permitido que los motores de combustión interna de hoy en día sean cada vez más limpios. La adopción en Europa del nuevo ciclo de homologación WLTP, que considera un ciclo de conducción más realista que su predecesor el NEDC, así como la necesidad de evaluar las emisiones contaminantes en diferentes escenarios de temperatura ambiente y de altitud, suponen un desafío para los fabricantes a la hora de diseñar y optimizar sus motores. En este contexto, el modelado unidimensional del motor ofrece la posibilidad de desarrollar y probar diferentes soluciones con la suficiente precisión, a la vez que permite agilizar el proceso de diseño del motor y reducir los costes de éste.

El objetivo de esta tesis es el de desarrollar un modelo completo de motor virtual que permita simular condiciones transitorias de régimen de giro y grado de carga, así como diferentes condiciones ambientales de presión y temperatura. Con este modelo de motor se pretende predecir las principales variables termo-fluidodinámicas en diferentes puntos del motor y las emisiones contaminantes liberadas en el escape.

Por otra parte, el arranque en frío y el funcionamiento a bajas temperaturas están asociados a un mayor consumo, mayores emisiones de hidrocarburos (HC) y monóxido de carbono (CO), así como mayores emisiones de óxidos de nitrógeno (NO_x) debido a la desactivación de los sistemas de recirculación de gases de escape. Para paliar estos efectos adversos, una opción es lograr que el sistema de post tratamiento alcance su temperatura de activación lo más pronto posible. En este trabajo se aborda este objetivo mediante dos soluciones. Por un lado, se ha explorado la posibilidad de elevar la temperatura de los gases en el escape mediante un sistema de distribución variable. Con este método se pueden reducir las emisiones de CO

y HC en torno a un 40-50 % y las emisiones de NO_x hasta un 15 % durante la primera fase del ciclo WLTC, a costa de una penalización en el consumo de combustible. Por otro lado, también se ha estudiado la posibilidad de aislar térmicamente el sistema de escape. En este caso, es posible reducir las emisiones de CO y HC en torno a un 30 % sin mejorar las de NO_x.

Palabras clave: modelado unidimensional; motor de combustión interna; emisiones contaminantes; distribución variable; aislamiento térmico

Resum

Les noves regulacions en matèria d'emissions d'efecte d'hivernacle i qualitat de l'aire han conduït la evolució tecnològica dels motors de combustió interna durant els darrers anys. Les millores en el procés de la combustió, la sobrealimentació, la gestió tèrmica, els sistemes de post tractament i tècniques com la recirculació de gasos d'escapament, han permès que els motors de combustió interna d'avui dia siguen cada vegada més nets. L'adopció a Europa del nou cicle d'homologació WLTP, que considera un cicle de conducció més realista que el seu predecessor el NEDC, així com la necessitat d'avaluar les emissions de gasos contaminants en diferents escenaris de temperatura ambient i humitat, suposen un repte per als fabricants a l'hora de dissenyar i optimitzar els seus motors. En aquest context, el modelatge unidimensional del motor ofereix la possibilitat de desenvolupar i provar diferents solucions amb la suficient precisió, al mateix temps que agilitza el procés de disseny del motor i reduïx els costos derivats d'aquest.

L'objectiu d'aquesta tesi és el de desenvolupar un model complete de motor virtual que permeta simular condiciones transitòries de règim de gir i grau de càrrega, així com diferents condicions ambientals de pressió i temperatura. Amb aquest model de motor es pretén predir les principals variables termo-fluidodinàmiques en diferents punts del motor i les emissions contaminants alliberades en l'escapament.

Per altra banda, l'arrancada en fred i el funcionament a baixes temperatures están associats a un major consum, majors emissions d'hidrocarburs (HC) i monòxid de carboni (CO), així com majors emissions d'òxids de nitrògen (NO_x) degudes a la desactivació dels sistemes de recirculació de gasos d'escapament. Per a pal·liar aquestos efectes indesitjats, una opció és aconseguir que el sistema de post tractament arribe a la seua temperatura d'activació el més prompte possible. En aquest treball, aquest objectiu s'aborda mitjançant dues solucions. Per una banda, s'ha investigat la possibilitat d'augmentar la temperatura dels gasos en l'escapament per mitjà d'un sistema de distribució variable. Amb aquest mètode s'ha aconseguit

reduïr les emissions de CO i HC al voltant d'un 40-50 % i les emissions de NO_x fins a un 15 % durant la primera fase del cicle WLTC, a costa d'una penalització en el consum de combustible. Per altra banda, també s'ha estudiat la possibilitat d'aïllar tèrmicament el sistema d'escapament. En aquest cas, és possible reduir les emissions de CO i HC vora un 30 % sense millorar les de NO_x.

Paraules clau: modelatge unidimensional; motor de combustió interna; emissions contaminants; distribució variable; aïllament tèrmic

List of publications

The work presented in this thesis is underpinned by the following papers:

[1] J. Martin, F. Arnau, P. Piqueras, and Á. Auñón. "Development of an Integrated Virtual Engine Model to Simulate New Standard Testing Cycles". *WCX World Congress Experience*. SAE International, 2018. doi: 10.4271/2018-01-1413

[2] F. J. Arnau, J. Martín, B. Pla, and Á. Auñón. "Diesel engine optimization and exhaust thermal management by means of variable valve train strategies". *International Journal of Engine Research*, Advance online publication, (2020). issn: 20413149. doi: 10.1177/14680874199894804

[3] F. J. Arnau, J. Martín, P. Piqueras, and Á. Auñón. "Effect of the exhaust thermal insulation on the engine efficiency and the exhaust temperature under transient conditions". *International Journal of Engine Research*, Advance online publication, (2020). doi: 10.1177/1468087420961206

[4] J. R. Serrano, F. J. Arnau, J. Martín, and Á. Auñón. "Development of a Variable Valve Actuation Control to Improve Diesel Oxidation Catalyst Efficiency and Emissions in a Light Duty Diesel Engine". *Energies*, 13 (17), (2020), p. 4561. doi: 10.3390/en13174561

Division of work between authors

This thesis is based on the papers mentioned above, whose author signatures are in order of seniority. The author of this thesis was responsible of preparing and running the simulations required for this work and post-processing of the simulation and test bench data. Debugging tasks and code implementation of the condensation model presented in chapter 2 and cam valve actuators in chapter 4 were carried out under supervision of Dr. Arnau. The methodologies, main research strategies and results discussion were performed in collaboration with Dr. Arnau, Dr. Martín and Prof. Serrano.

Funding acknowledgements

The author wishes to acknowledge the financial support received through the FPI S2 2018 1048 grant of *Programa de Apoyo para la Investigación y Desarrollo* (PAID) of Universitat Politècnica de València.

Acknowledgments

First of all, I wish to thanks my supervisor Dr. Francisco José Arnau Martínez for his mentoring and patience, specially during the last months. Special thanks also for the professors who were directly or indirectly involved in this research: Prof. José Ramon Serrano, Dr. Jaime Martín, Dr. Benjamín Plá, Dr. Pedro Piqueras, Dr. Luis Miguel García-Cuevas and Dr. Javier López. I want to extend my gratitude to Juan Antonio López for carrying on the experimental tests and all the members of CMT-Motores Térmicos, those including researchers I worked with, professors, technicians and administration staff —specially Amparo Cutillas for her dedication and patience.

I would like to also thank Dr. Héctor Climent, who not only was the first CMT professor I met during my studies, but the person who guide my final degree project and introduced me to the research environment.

Of course, I wish to thank my folks at the office in order of *seniority*: Artem Dombrovsky, Alberto Hernández, Manuel Hernández, Daniel Tarí, Ausiàs Moratal, Pablo Soler, Chaitanya Patil, Julián Miguel and Francisco Moya. Thank you for turning the office into a small family.

I would like to address a few words to the special friends I made during the period of the thesis outside my department. Thanks Raquel for becoming like a sister to me. Thanks Jéssica for your sweetness and your little words when I needed them most. Thanks Verónica for teaching me that our friendship continues even over the longest distance, as in an escape room that fortunately never ends. Thanks Aysha for your true friendship and for every Friday afternoon. And finally, thanks to the fabulous Silvia for letting me know you as you are and for all the time we have spent during the last two years. I hope we can enjoy more hiking and more experiences together.

And heartily, to my mother and family for their support, sacrifice and because I am who I am now because of you.

Valencia, December 2020

"[A]nd do the other things, not because they are easy, but because they are hard; because that goal will serve to organize and measure the best of our energies and skills."

— John F. Kennedy

Contents

1 Introduction 1

1.1 Motivation . . . 2

1.2 Objective . . . 6

1.3 Thesis layout . . . 6

Chapter 1 References . . . 9

2 Engine and experimental method 13

2.1 Introduction . . . 14

2.2 Reference engine . . . 14

2.3 Test cell description . . . 15

2.4 Driving cycle test procedure . . . 23

2.5 Data analysis procedure . . . 25

2.5.1 Pollutant emissions calculation . . . 25

2.5.2 Test repeatability and uncertainty . . . 27

2.6 Experimental campaign . . . 29

Chapter 2 References . . . 33

3 Development of a virtual engine model 37

3.1 Introduction . . . 39

3.2 Model description . . . 40

3.2.1 Gas dynamics model . . . 42

3.2.1.1 Boundary conditions . . . 46

3.2.1.2 Heat transfer at pipes . . . 48

3.2.1.3 Turbocharger sub-model . . . 49

3.2.1.4 In-cylinder conditions model 51
3.2.1.5 Blow-by model 53
3.2.1.6 Water condensation model 57
3.2.2 Injection rate model 59
3.2.3 Combustion model 65
3.2.3.1 Combustion model calibration 71
3.2.4 Emissions model 76
3.2.4.1 NO_x emissions model 76
3.2.4.2 Soot, CO and UHC emissions model 79
3.2.5 After-treatment systems model 82
3.2.5.1 After-treatment system lumped model 83
3.2.5.2 Pressure drop 85
3.2.5.3 Porous media properties 86
3.2.5.4 Filtration 86
3.2.5.5 Reaction mechanism 87
3.2.5.6 Heat transfer in the after-treatment systems . . . 88
3.2.5.7 After-treatment model calibration 89
3.2.6 Heat transfer model 94
3.2.6.1 In-cylinder heat transfer model calibration 98
3.2.7 Thermo-hydraulic model 100
3.2.8 Mechanical losses model 104
3.2.8.1 Mechanical losses model calibration 105
3.2.9 Control, vehicle and driver models 108
3.3 Validation of the virtual engine model 113
3.3.1 Validation of the turbocharger model 113

3.3.2 Validation of the after-treatment systems model . . 115
3.3.3 Validation of the complete virtual engine model . . . 117
3.4 Conclusions . . . 127
Chapter 3 References . . . 136

4 Exhaust thermal management by means of VVT strategies 139
4.1 Introduction . . . 141
4.1.1 Valve events of a four-stroke engine . . . 143
4.1.2 Variable valve timing strategies . . . 143
4.1.2.1 Modifying intake valve opening (IVO) . . . 144
4.1.2.2 Modifying intake valve closing (IVC) . . . 145
4.1.2.3 Modifying exhaust valve opening (EVO) . . . 147
4.1.2.4 Modifying exhaust valve closing (EVC) . . . 147
4.1.2.5 Valve lift actuation . . . 148
4.2 Model description . . . 149
4.3 Variable valve timing methodology . . . 150
4.4 Results and discussion . . . 154
4.4.1 Steady-state analysis . . . 154
4.4.2 Transient analysis . . . 168
4.5 Conclusions . . . 180
Chapter 4 References . . . 185

5 Development of a VVT control to improve DOC efficiency 189
5.1 Introduction . . . 190
5.2 Model preparation . . . 192
5.3 Control system methodology . . . 194

5.4 Results and discussion 206
5.4.1 Adding DOC light-off temperature in the VVT control. 222
5.5 Conclusions 227
Chapter 5 References 231

6 Exhaust thermal insulation under transient conditions 235
6.1 Introduction 236
6.2 Model preparation 238
6.3 Exhaust insulation methodology 240
6.4 Results and discussion 245
6.5 Conclusions 260
Chapter 6 References 264

7 Concluding remarks 267
7.1 Introduction 268
7.2 VVT and thermal insulation comparison 268
7.3 Future works 275

Bibliography 279

List of Tables

2.1 Reference engine specifications. 15
2.2 Test cell instrumentation. 22
2.3 Steady-state test for combustion model calibration. 30
2.4 Engine and test cell temperatures at transient operating conditions. 30
2.5 Engine and test cell temperatures at steady operating conditions. 30
3.1 Fitting constants values of the combustion model. 72
4.1 Variable valve actuation strategies. 153
4.2 Simulated steady-state operating points. 155
5.1 Transient cases. 201
6.1 Thermal insulation cases. 242
6.2 Simulation transient conditions. 245

List of Figures

1.1 Global anthropogenic greenhouse emissions by sector in 2016. Total is 49.4 CO_2 equivalent gigatonnes. Source: Climate Watch [8]. Chart: Our World in Data [9]. 2

1.2 World surface temperature anomaly [10, 11]. Annual average temperature from 2010 to 2020 relative to the base period from 1950 to 1980. Data sources: land surface: GHCN-v4, ocean surface: ERSST-v5. Robinson map projection. Gray areas signify missing data. 3

1.3 Global car sales by powertrain type, projection up to 2030. Source: Boston Consulting Group [19]. 5

2.1 Engine layout indicating the pressure, temperature and exhaust gases measurement points. 17

2.2 Flame ionisation detection (FID) system sketch. 20

2.3 Chemiluminiscent detector sketch. 21

2.4 NEDC and WLTC European driving cycles comparison [25]. . . 23

2.5 Experimentally tested points and the operating points along the WLTC. 31

3.1 Flow-chart of the virtual engine model (VEMOD) modules. . . 41

3.2 Representation of the real engine and the sub-models in VEMOD. 42

3.3 Discretisation of a 1D duct according to the Finite Volume Method. 44

3.4 Gases circuit diagram in VEMOD. 47

3.5 Multiple 1D-1D connection boundary. 48

3.6 Scheme of the turbocharger lumped heat transfer model. . . . 51
3.7 Scheme of the blow-by model. 54
3.8 Blow-by mass flow. 56
3.9 Pressure in the ring grooves. 56
3.10 Scheme of the variables involved in the water liquid condensation model. 57
3.11 Boundary conditions of the water condensation model test. . . 58
3.12 Liquid water condensed depending on the LP-EGR cooler outlet temperature and the fuel-air equivalence ratio. 58
3.13 Simulated injection rate. 60
3.14 Injector opening time (A) 61
3.15 Maximum injection rate (B) 62
3.16 Injector closing time (C) 63
3.17 Hydraulic lag (D) 63
3.18 Injection rates for an ET swept at p_{inj} = 1600 bar 64
3.19 Injection rates for a p_{inj} swept (400 to 1600 bar) at ET = 2 ms. 64
3.20 Effect of the fuel-air equivalence ratio (left) and EGR (right) on the ignition delay. 68
3.21 Accumulated injected and burned fuel masses (quasi-steady conditions assumption). 70
3.22 Mixing time at the start of the injection for quasi-steady and transient conditions. 70
3.23 Mixing time at the end of the injection for quasi-steady and transient conditions. 71
3.24 Accumulated injected and burned fuel masses (quasi-steady + transient conditions assumption). 71

3.25 Cylinder heat release (J) and pressure (bar) at 1250 rpm for different loads (13%, 26%, 50%, 76% and 100%). 73

3.26 Cylinder heat release (J) and pressure (bar) at 3500 rpm for different loads (25%, 50%, 75% and 100%). 74

3.27 Experimental and simulated IMEP comparison. 75

3.28 NO model constant as a function of the excess of oxygen and temperature. 77

3.29 NO mass fraction in equilibrium as a function of the excess of oxygen and temperature. 77

3.30 Experimental and simulated NO_x mass flow at turbine outlet. 78

3.31 Evolution of the mean squared error for each epoch. 80

3.32 Prediction vs experimental CO emissions. 81

3.33 Prediction vs experimental UHC emissions. 81

3.34 Prediction vs experimental soot emissions. 82

3.35 Flow-chart of the flow-through lumped model. 84

3.36 Flow-chart of the wall-flow lumped model. 85

3.37 Scheme of the regions of soot regeneration in the wall-flow particulate filter. 88

3.38 Methodology for the flow-through model calibration. 89

3.39 Methodology for the DPF model calibration. 90

3.40 Mass flow prediction (a) and pressure drop coefficient determination (b) in motoring tests. 90

3.41 DOC outlet gas temperature (a) and canning surface temperature (b) at 2500 rpm and engine load steps from 5 % to 40 %. 91

3.42 HC and CO conversion efficiency during thermal stabilisation in different steady-state operating conditions. 92

3.43 DPF response during the soot loading test under steady-state conditions. 93

3.44 DPF response during the active regeneration test under steady-state conditions. 94

3.45 Fitting constant C_{w1}. 98

3.46 Flow-chart to determine the uncertainties in motoring conditions. 99

3.47 Flow-chart of the thermo-hydraulic circuit model. 101

3.48 Mesh, path and branch sketch in the hydraulic circuits. 102

3.49 Coolant circuit diagram in VEMOD. 103

3.50 Oil circuit diagram in VEMOD. 103

3.51 Friction and auxiliaries mechanical losses distribution. 107

3.52 Experimental and simulated brake power comparison. 108

3.53 Flow-chart of the main output variables of the control model imposing test bench data. Rounded boxes correspond to the final actuator values. 110

3.54 Flow-chart of the main output variables of the control model imposing only engine speed and torque or fuel mass. Rounded boxes correspond to the final actuator values. 111

3.55 Turbine inlet and outlet temperatures during a load transient at 1250 and 2000 rpm. 114

3.56 HC and CO cumulative emissions over the WLTC. 115

3.57 DPF outlet gas temperature (a) and cumulative soot collected (b) over the WLTC cycle. 116

3.58 Air mass flow during the WLTC at 20 °C room temperature. . . 118

3.59 Modelled vs experimental air mass flow during the WLTC at 20 °C room temperature. 118

3.60 Compressor outlet (boost) pressure during the WLTC at 20 °C room temperature. 119

3.61 Modelled vs experimental compressor outlet (boost) pressure during the WLTC at 20 °C room temperature. 119

3.62 Brake torque during the WLTC at 20 °C room temperature. . . 120

3.63 Brake torque during the WLTC at −7 °C room temperature. . . 120

3.64 Turbine outlet temperature during the WLTC at 20 °C room temperature. 121

3.65 Turbine outlet temperature during the WLTC at −7 °C room temperature. 121

3.66 CO_2 mass flow during the WLTC at 20 °C room temperature. . 122

3.67 Accumulated CO_2 mass during the WLTC at 20 °C room temperature. 122

3.68 CO_2 mass flow during the WLTC at −7 °C room temperature. . 123

3.69 Accumulated CO_2 mass during the WLTC at −7 °C room temperature. 123

3.70 NO_x mass flow during the WLTC at 20 °C room temperature. . 124

3.71 Accumulated NO_x mass during the WLTC at 20 °C room temperature. 124

3.72 NO_x mass flow during the WLTC at −7 °C room temperature. . 125

3.73 Accumulated NO_x mass during the WLTC at −7 °C room temperature. 125

3.74 Oil temperature at engine outlet during the WLTC at 20 °C room temperature. 126

3.75 Oil temperature at engine outlet during the WLTC at −7 °C room temperature. 126

3.76 Coolant temperature at engine outlet during the WLTC at 20 °C room temperature. 127

3.77 Coolant temperature at engine outlet during the WLTC at −7 °C room temperature. 127

4.1 Four stroke diesel engine P-V diagram (top) and engine timing diagram (bottom). 144

4.2 Exhaust and intake valve lift profiles for each configuration. . 151

4.3 Steady-state results: BSFC variation vs temperature variation at DOC inlet. The variation is referred to the baseline camshaft. 158

4.4 Pressure vs volume diagram, 2 bar BMEP at 1500 rpm. 160

4.5 Steady-state results: CO_2 mass fraction at IVC variation vs specific NO_x emissions variation. The variation is referred to the baseline camshaft. 163

4.6 EGR and IGR relative difference respect to the baseline, 4 bar BMEP at 1250 rpm. 164

4.7 Steady-state results: Air−fuel equivalence ratio (λ) variation vs specific CO emissions variation. The variation is referred to the baseline camshaft. 166

4.8 Time to reach DOC light-off temperature. 168

4.9 Mass averaged temperature at DOC inlet during the low speed stage of the WLTC. 169

4.10 Time to reach coolant thermostat threshold (80 °C) 170

4.11 Accumulated fuel consumption over the low speed stage of the WLTC. 172

4.12 Accumulated combustion NO_x emissions over the low speed stage of the WLTC, difference with respect to the baseline case. 173

4.13 Accumulated combustion CO emissions over the low speed stage of the WLTC, difference with respect to the baseline case. 174

4.14 Accumulated unburned HC emissions over the low speed stage of the WLTC, difference with respect to the baseline case. . . . 174

4.15 Accumulated combustion PM (soot) emissions over the low speed stage of the WLTC, difference with respect to the baseline case. . . . 175

4.16 Mass averaged temperature at DOC inlet variation (°C) vs fuel consumption variation (%) respect to the baseline during the low speed stage of the WLTC. . . . 176

4.17 NO_x accumulated mass variation (°C) vs fuel consumption variation (%) respect to the baseline during the low speed stage of the WLTC. . . . 177

4.18 NO_x accumulated mass variation (%) vs mass averaged temperature at DOC inlet variation (°C) respect to the baseline during the low speed stage of the WLTC. . . . 177

4.19 CO accumulated mass variation (°C) vs fuel consumption variation (%) respect to the baseline during the low speed stage of the WLTC. . . . 178

4.20 CO accumulated mass variation (%) vs mass averaged temperature at DOC inlet variation (°C) respect to the baseline during the low speed stage of the WLTC. . . . 179

5.1 VVT control patented by Madison Finlay, 1968. . . . 190

5.2 Valve profile parameters that can be modified in runtime. . . . 192

5.3 *EP+IP* and *EVrO* control blocks. . . . 193

5.4 Exhaust and intake valve lift profiles for each case. . . . 196

5.5 Methodology flow-chart. . . . 197

5.6 Discarded and stored steady-state simulations applying EP + IP with an intake delay/exhaust advance of 20 and 60 CAD in 2 and 4 valves. . . . 199

5.7 Discarded and stored steady-state simulations applying EVrO with different exhaust opening, duration and lift. 200

5.8 EP+IP angular shift and turbine outlet temperature for Case 1. 201

5.9 EP+IP angular shift and turbine outlet temperature for Case 2. 202

5.10 EP+IP angular shift and turbine outlet temperature for Case 3. 202

5.11 EVrO parameters maps and turbine outlet temperature for Case 4. 204

5.12 EVrO parameters maps and turbine outlet temperature for Case 5. 205

5.13 WLTC temperature at turbine outlet. 207

5.14 Time above a certain temperature at turbine outlet. 208

5.15 WLTC DOC outlet temperature. 209

5.16 WLTC exhaust advance and intake delay. 210

5.17 WLTC EVrO opening, duration and lift. 210

5.18 WLTC HC accumulated conversion efficiency. 212

5.19 WLTC CO accumulated conversion efficiency. 212

5.20 WLTC NO_x accumulated mass. 213

5.21 Time to reach DOC light-off temperature, engine start at 20 °C ambient temperature. Percentage variation compared to the baseline case. 215

5.22 Time to reach coolant thermostat threshold, engine start at 20 °C ambient temperature. Percentage variation compared to the baseline case. 215

5.23 Accumulated fuel consumption, engine start at 20 °C ambient temperature. Percentage variation compared to the baseline case. 216

5.24 Accumulated tailpipe NO_x emissions, engine start at 20 °C ambient temperature. Percentage variation compared to the baseline case. 216

5.25 Accumulated CO emissions at DOC outlet, engine start at 20 °C ambient temperature. Percentage variation compared to the baseline case. 217

5.26 Accumulated HC emissions at DOC outlet, engine start at 20 °C ambient temperature. Percentage variation compared to the baseline case. 218

5.27 Fuel consumption variation (%) versus CO accumulated mass variation (%) trade-offs during the low speed stage of the WLTC, variations with respect to the baseline. 220

5.28 Fuel consumption variation (%) versus HC accumulated mass variation (%) trade-offs during the low speed stage of the WLTC, variations with respect to the baseline. 221

5.29 WLTC DOC outlet temperature. 223

5.30 WLTC exhaust advance and intake delay. 224

5.31 Accumulated fuel consumption, engine start at 20 °C ambient temperature. Percentage variation compared to the baseline case. 225

5.32 Accumulated tailpipe NO_x emissions, engine start at 20 °C ambient temperature. Percentage variation compared to the baseline case. 225

5.33 Accumulated CO emissions at DOC outlet, engine start at 20 °C ambient temperature. Percentage variation compared to the baseline case. 226

5.34 Accumulated HC emissions at DOC outlet, engine start at 20 °C ambient temperature. Percentage variation compared to the baseline case. 227

6.1 Engine layout with the exhaust components which have been thermally insulated. 241

6.2 Accumulated turbocharger heat to ambient and heat to oil over the WLTC at 20°C room temperature. 243

6.3 Turbocharger temperatures of the baseline engine exhaust and the EM + TE case over the WLTC at 20°C room temperature. . 244

6.4 WLTC accumulated gas enthalpy at turbine outlet, difference respect to the baseline case. 247

6.5 Coolant temperature at engine outlet over the WLTC transient cycle. 248

6.6 LP-EGR and HP-EGR activation at ambient and cold conditions, respectively. 249

6.7 WLTC CO accumulated emissions variation downstream the after-treatment system. 250

6.8 WLTC CO accumulated conversion efficiency. 251

6.9 WLTC HC accumulated emissions variation downstream the after-treatment system. 253

6.10 WLTC HC accumulated conversion efficiency. 254

6.11 Time to reach light-off temperature and warm-up time when simulating the WLTC transient cycle. 256

6.12 Accumulated fuel consumption, CO and HC emissions versus accumulated exhaust enthalpy. Variations compared to the baseline case. 258

6.13 Accumulated pumping losses variation compared to the baseline case. 259

7.1 Turbine outlet temperature, WLTC at a room temperature of 20 °C. 270

7.2 Time above a certain temperature at turbine outlet considering the low speed stage of the WLTC, room temperature of 20 °C. . 271

7.3 Time to reach DOC light-off temperature, engine start at 20 °C ambient temperature. Percentage variation compared to the baseline case. 272

7.4 Accumulated fuel consumption, engine start at 20 °C ambient temperature. Percentage variation compared to the baseline case. 272

7.5 Accumulated tailpipe NO_x emissions, engine start at 20 °C ambient temperature. Percentage variation compared to the baseline case. 273

7.6 Accumulated CO emissions at DOC outlet, engine start at 20 °C ambient temperature. Percentage variation compared to the baseline case. 274

7.7 Accumulated HC emissions at DOC outlet, engine start at 20 °C ambient temperature. Percentage variation compared to the baseline case. 274

List of symbols

Latin characters

A	Area
a	Speed of sound
C	Courant number
D	Diameter
d	Distance
e	Specific internal energy
e_t	Specific total internal energy
f	Pipe wall friction factor
h	Heat transfer coefficient, specific enthalpy, head loss, Plank constant
h_0	Specific stagnation enthalpy
I	Moment of inertia
k	Thermal conductivity
L	Characteristic length
M	Torque
m	Mass, test repetition, median of a population
$\dot{m}$	Mass flow
N	Engine speed
n	Test measurement points
Nu	Nusselt number
P	Power
p	Pressure
Pr	Prandt number
q	Specific heat
Q	Heat

R Ideal gas constant

R^2 Coefficient of determination

r Radius

Re Reynolds number

S Surface

T Temperature

t Time

Y Mass fraction

U Internal energy

u Flow speed

V Cell volume

$\dot{V}$ Volumetric flow

v Specific volume, vehicle speed

W Work

Z Gearbox ratio

Greek characters

α Angular acceleration

γ Specific heat capacities ratio or adiabatic index

Δ Interval, difference

ϵ Error

η Efficiency

λ Air–fuel equivalence ratio

μ Dynamic viscosity, friction coefficient, mean of a population

ν Wave frequency

ρ Density

σ Standard deviation of a population

ϕ Fuel-air equivalence ratio

ω Rotational speed

Sub- and Superscripts

a	Auxiliaries
accum	Accumulated
avg	Average
b	Brake
base	Baseline
bb	Blow-by
conf	Configuration
cyl	Cylinder
eff	Effective
exp	Experiment
fr	Friction
g	Gas
gb	Gearbox
i	Cell number, parcel, indicated
in	Inlet
inj	Injection
int	Internal
max	Maximum
min	Minimum
mod	Model
n	Chemical specie
out	Outlet
p	Pumping
t	Total
w	Cell wall

Acronyms

0D	Zero-dimensional
1D	One-dimensional
AAN	Artificial neural network
ACT	Apparent combustion time
BDC	Bottom dead centre
BMEP	Break mean effective pressure
BSFC	Break specific fuel consumption
CA	Crank angle
CFD	Computational fluid dynamics
CFL	Courant-Friedrichs-Lewy
CI	Compression ignited
CLD	Chemiluminiscence detection
CO	Carbon monoxide
CO_2	Carbon dioxide
CR	Compression ratio
DI	Direct injection
DOC	Diesel oxidation catalyst
DOHC	Double overhead camshaft
DPF	Diesel particle filter
EATS	Exhaust after-treatment system
ECU	Engine control unit
EGR	Exhaust gas recirculation
ET	Energization time
EVC	Exhaust valve closing
EVO	Exhaust valve opening

EVrO	Exhaust valve re-opening
FAR	Fuel-air ratio
FID	Flame ionization detection
FVM	Finite volume method
HC	Hydrocarbons
HCCI	Homogeneous charge compression ignition
HRR	Heat release rate
HSDI	High speed direct injection
HP-EGR	High pressure exhaust gas recirculation
ID	Ignition delay
IGR	Internal gas recirculation
IMEP	Indicated mean effective pressure
LNT	Lean NO_x trap
LP-EGR	Low pressure exhaust gas recirculation
MPD	Magneto-pneumatic detector
MUSCL	Monotone upstream-centred scheme for conservation laws
NDIR	Non-dispersive infrared
NEDC	New European driving cycle
NIST	National Institute of Standards and Technology
NO	Nitrogen monoxide
NO_x	Nitrogen oxides
PLC	Programmable logic computer
PM	Particle matter
RCCI	Reactivity controlled compression ignition
RDE	Real driving emissions
RTD	Resistance temperature detector
SCR	Selective catalytic reduction

SI	Spark ignited
SMAPE	Symmetric mean average percent error
SOC	Start of combustion
SOE	Start of energization
SOI	Start of injection
PM	Particle matter
TBC	Thermal barrier coating
TDC	Top dead centre
UHC	Unburned hydrocarbons
VEMOD	Virtual Engine Model
VGT	Variable geometry turbine
VVA	Variable valve actuation
VVT	Variable valve timing
WCAC	Water charge air cooler
WHO	World Health Organisation
WLTC	Worldwide harmonized light-duty vehicles test cycle
YSZ	Yttria-stabilised zirconia

Chapter 1

Introduction

Contents

1.1 Motivation 2
1.2 Objective 6
1.3 Thesis layout 6
Chapter 1 References 9

1.1 Motivation

During the last years, the economic growth of China and India has increased the global car sales up to a maximum record of 92 million units in 2018 [5]. This continuous rise in energy and transport demand has turned into a major threat to the environment and biosphere, leading even to an aggravation of the climate change [6, 7]. Transportation activities were responsible of 16.2 % of the global anthropogenic greenhouse emissions [8], as it is shown in Figure 1.1, and 11.9 % were due to road transport; which in fact were originated by internal combustion engines.

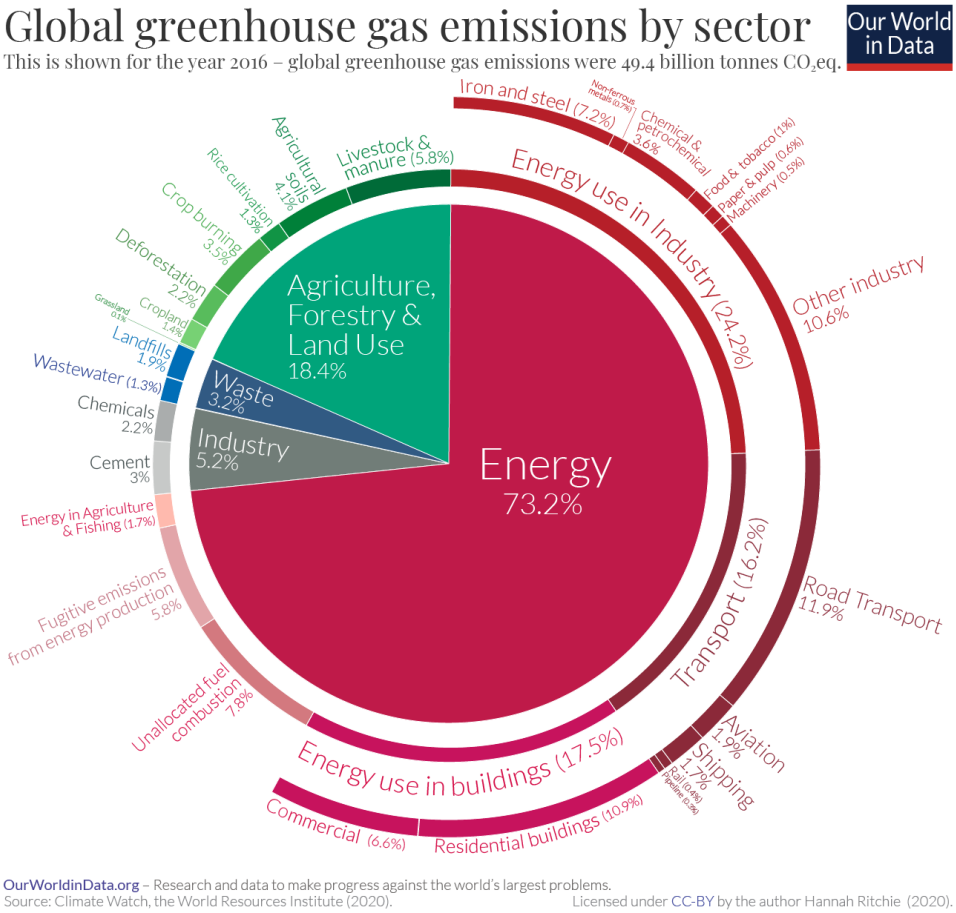

Figure 1.1: *Global anthropogenic greenhouse emissions by sector in 2016. Total is 49.4 CO_2 equivalent gigatonnes. Source: Climate Watch [8]. Chart: Our World in Data [9].*

The increase of greenhouse gases concentration, such as CO_2, CH_4 and N_2O, is leading to a temperature rise process known as global warming. The effect of this temperature rise in illustrated in Figure 1.2. The average temperature variation of the Earth surface during the last 10 years (2010-2020) is compared to a reference period (1951-1980). The comparison of the average temperatures results in an increment of 0.82 °C. As it can be seen in the map, the temperature increment is widespread throughout the planet. The hottest areas are located in land regions of the north hemisphere. The higher temperature increase in the north hemisphere compared to the south is because of the larger areas of land. Since water heat capacity is higher than ground, water temperature increase is lower.

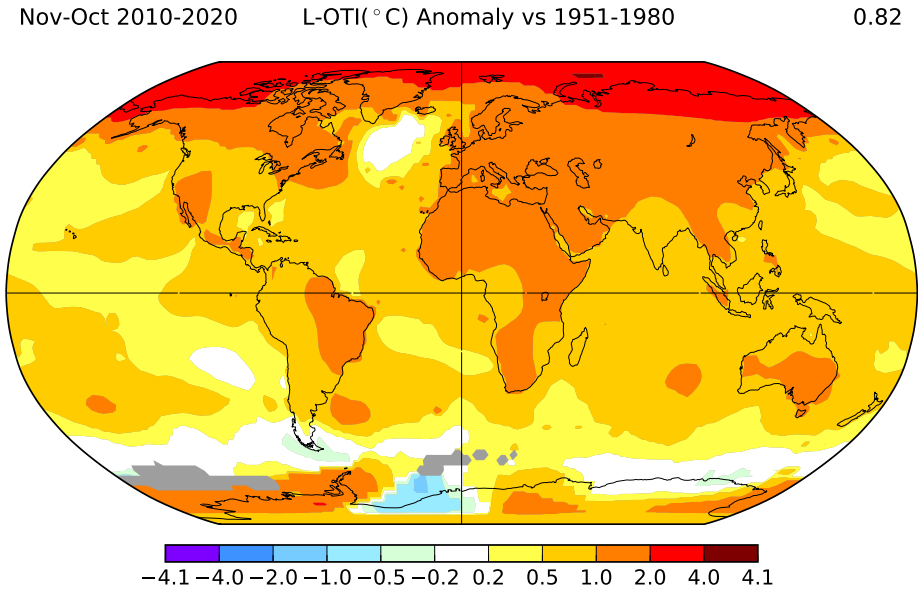

Figure 1.2: *World surface temperature anomaly [10, 11]. Annual average temperature from 2010 to 2020 relative to the base period from 1950 to 1980. Data sources: land surface: GHCN-v4, ocean surface: ERSST-v5. Robinson map projection. Gray areas signify missing data.*

With the aim of reducing greenhouse emissions of the automotive sector, all major economic areas of the world have been adopting strict emissions targets. With regard to European Union, regulation policies establish

a CO_2 target of 95 g/km and 147 g/km for passenger cars and light duty vehicles respectively before 2021. From 2021 these emissions targets will be based on the new type approval cycle, the worldwide harmonised light duty vehicle test procedure (WLTP), in substitution of the previous new European driving cycle (NEDC). For 2025, Regulation (EU) 2019/631 [12] states that new vehicles must meet a target 15 % lower than in 2021, and for 2030 passenger cars must face a target 37.5 % lower than in 2021; while light duty commercial vehicles will face a limit of 31 %.

However, not only the increase in CO_2 emissions is a global concern. Local pollution originated from industrial and transportation activities is another issue in dense populated areas. According to the last Eurobarometer, prior to the COVID outbreak, air quality and climate change was the second major concern of Europeans, right after immigration [13]. Moreover, 80 % of Europeans would like every new trade agreement concluded by the EU to include the highest environmental and social standards [14]. According to the World Health Organisation (WHO) [15], exposure to air pollutants may affect human health in several ways, leading to increased mortality and morbidity. Currently, air pollution is the largest environmental risk factor in the world. High number of air pollutants are associated with significant excess mortality or morbidity, including nitrogen oxides, ozone, carbon monoxide, sulphur dioxides and fine particle matter.

In this regard, governments around the world are taking measures to restrict urban traffic in dense populated cities. In EU, the in force Directive 2008/50/EC [16] urges member states to monitor the concentration of these mentioned pollutants and take measures to not exceed the limits established by law. Accordingly, some cities are applying restrictions to the traffic in urban areas, such as Paris [17], where at least Euro 4 diesel and Euro 2 petrol light duty vehicles are allowed to access urban area. Furthermore, a diesel ban for all vehicles is scheduled to come into force by 2024 in this city [18].

In order to reduce the fleet average CO_2 emissions during the following years, the powertrain electrification of the future vehicles is a must. As indicated in Figure 1.3, according to a study by Boston Consulting Group [19], in the next years there will be a vehicle fleet decrease in purely powered by

petrol and diesel, in favour of hybrid (HEV), plug-in hybrid (PHEV) and mild hybrid (MHEV) vehicles. As the total cost of ownership (TCO) of the battery electric vehicles (BEV) is predicted to go down over the next years, due to the development of new batteries and the commitment of the largest car manufacturers in this type of propulsion technology [20, 21], an increase in the adoption of battery electric vehicles is forecasted from the second half of this decade. So the expected future in the next few years is a mixed transportation system, where engine technology will be spread depending on the autonomy requirements of transport.

EXHIBIT 1 | Global Car Sales Through 2030 by Powertrain Type

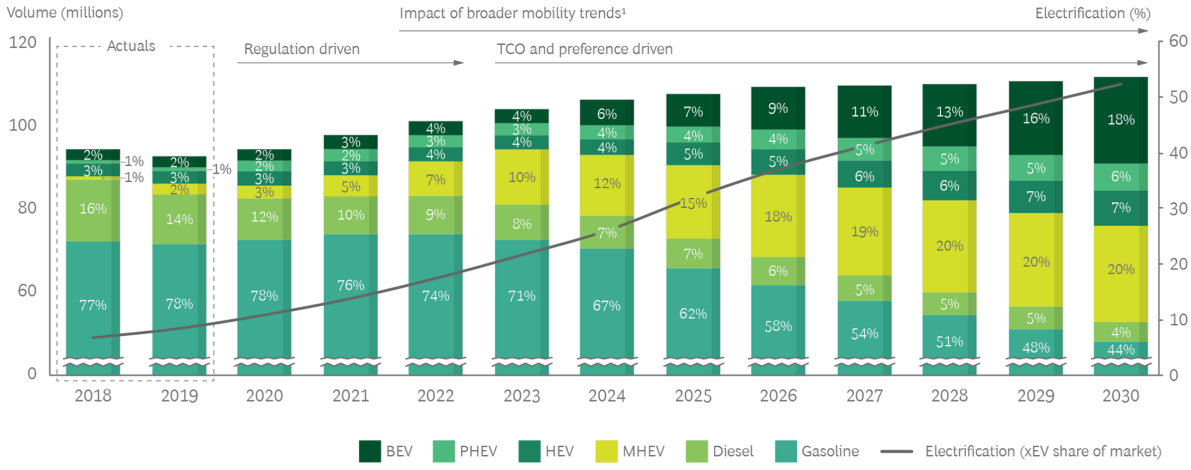

Source: BCG analysis.
Note: BEV = battery electric; PHEV = plug-in hybrid electric; HEV = full hybrid electric; MHEV = mild hybrid electric. Because of rounding, the percentage total for a particular year may not equal 100%.
¹Including such changes in consumer mobility behavior as car and ride sharing.

Figure 1.3: *Global car sales by powertrain type, projection up to 2030. Source: Boston Consulting Group [19].*

Regarding engine modelling, it has become an essential part in the design of internal combustion vehicles, allowing a significant reduction in terms of development time and cost. Computational simulation has replaced previous design methodologies such as prototype manufacturing and trial-and-error tests. One-dimensional gas dynamics models are used widely in engine design since they offer results with good precision at a reduced computational cost, thereby hastening the process of developing and optimising solutions. Currently and in the coming years, with the widely

electrification of the internal combustion engines, modelling engine energy management will be of great importance in the design of new powertrains.

1.2 Objective

The main objective of this thesis is to develop a virtual engine model able to simulate transient operating conditions at different ambient pressure and temperature conditions. To achieve the major aim of this thesis, some goals needed to be accomplished:

- The individual calibration of the different engine sub-models.
- The integration of these models into the complete engine model and the validation of it at different operating conditions.

The second objective of this thesis is to employ the engine model to reduce the pollutant emissions formed during the combustion process. To this extent, two methods have been studied to achieve a quicker warm-up of the after-treatment system, thereby reducing tailpipe pollutant emissions during the engine warm-up:

- One first study analysing the effect of different variable valve timing technologies with the aim of increasing the exhaust temperature.
- A second study considering the thermal insulation of the exhaust system, from the cylinder exhaust ports to the turbine volute, with the aim of reducing heat losses across these elements and preserve the enthalpy of the exhaust gases.

1.3 Thesis layout

After this introductory chapter, this thesis is organised in the following manner:

Chapter 2 presents the reference internal combustion engine on which the virtual model is based. A description of the test cell and the different systems available to measure pollutant emissions are included in this chapter. The methodology to perform steady-state tests and the type approval cycle used to test the engine at transient operating conditions is explained as well in chapter 2.

The virtual engine model is detailed in chapter 3. Its description has been divided into different sections concerning each of the sub-models. The main processes, assumptions and results of each sub-model is described in its respective section. The calibration procedure of some sub-models is also detailed, as well as the validation results of the complete engine model under transient conditions of speed and load.

Chapter 4 introduces a study employing the engine model detailed in the previous chapter. The study is centred on analysing the effect of different variable valve timing approaches in the engine performance, the diesel catalyst efficiency and the pollutant emissions formation.

With the results and conclusions presented in chapter 4, chapter 5 presents an optimisation study of different variable valve timing strategies to increase the catalyst efficient, and thereby reduce HC and CO emission. A control system is developed and simulated to maximise the turbine outlet temperature at any operating point. Chapter 4 also presents the results of these controlled variable valve timing strategies in transient operating conditions.

In chapter 6, a study of the effect of the thermal insulation of the exhaust system is carried out. The same engine model is used to analyze the effect on the engine and catalyst performance by thermally insulating the engine exhaust ports, the exhaust manifold and the turbine volute.

Finally, chapter 7 presents a concluding study combining the most advantageous variable valve timing solutions described in chapter 5 with the exhaust thermal insulation proposed in chapter 6. The resulting solution achieves a 40 % reduction in HC and CO emissions. Chapter 7 finishes with some remarks about future studies.

Chapter 1 References

[5] International Energy Agency (IEA). *Global car sales by key markets, 2005-2020*. Accessed 2020-12-10 at https://www.iea.org/data-and-statistics/charts/global-car-sales-by-key-markets-2005-2020. 2020 (cit. on p. 2).

[6] J. S. Gaffney and N. A. Marley. "The impacts of combustion emissions on air quality and climate – From coal to biofuels and beyond". *Atmospheric Environment*, 43 (1), (2009), pp. 23 –36. issn: 1352-2310. doi: https://doi.org/10.1016/j.atmosenv.2008.09.016 (cit. on p. 2).

[7] J. Cook et al. "Consensus on consensus: a synthesis of consensus estimates on human-caused global warming". *Environmental Research Letters*, 11 (4), (2016), p. 048002. doi: 10.1088/1748-9326/11/4/048002 (cit. on p. 2).

[8] CAIT data: Climate Watch. *GHG Emissions*. Accessed 2020-12-05 at https://www.climatewatchdata.org/ghg-emissions. World Resources Institute. 2020 (cit. on p. 2).

[9] H. Ritchie and M. Roser. *Emissions by sector*. Accessed 2020-12-04 at https://ourworldindata.org/emissions-by-sector. Our World in Data. September, 2020 (cit. on p. 2).

[10] N. Lenssen, G. Schmidt, J. Hansen, M. Menne, A. Persin, R. Ruedy, and D. Zyss. "Improvements in the GISTEMP uncertainty model". *J. Geophys. Res. Atmos.*, 124 (12), (2019), pp. 6307–6326. doi: 10.1029/2018JD029522 (cit. on p. 3).

[11] GISTEMP Team. NASA Goddard Institute for Space Studies. *GISS Surface Temperature Analysis (GISTEMP), version 4*. Dataset accessed 2020-12-5 at https://data.giss.nasa.gov/gistemp/. 2020 (cit. on p. 3).

[12] Council of European Union. "Regulation (EU) 2019/631 of the European Parliament and of the Council of 17 April 2019 setting CO2 emission performance standards for new passenger cars and for new light commercial vehicles, and repealing Regulations (EC) No 443/2009 and (EU) No 510/2011". *Official Journal of the European Union*, L 111, (2019), pp. 13–53. url: http://data.europa.eu/eli/reg/2019/631/oj (cit. on p. 4).

[13] European Comission. *Standard Eurobarometer 92. Public opinion in the European Union*. Accessed 2020-12-7 at https://ec.europa.eu/commfrontoffice/publicopinion/index.cfm/ResultDoc/download/DocumentKy/88848. November, 2019 (cit. on p. 4).

[14] European Comission. *Standard Eurobarometer 92. Europeans' opinions about the European Union's priorities*. Accessed 2020-12-7 at https://ec.europa.eu/commfrontoffice/publicopinion/index.cfm/ResultDoc/download/DocumentKy/90252. November, 2019 (cit. on p. 4).

[15] M. Krzyzanowski, B. Kuna-Dibbert, and J. Schneider. *Engine Emissions Measurement Handbook*. WHO Regional Office for Europe, 2005. isbn: 92-890-1373-7 (cit. on p. 4).

[16] Council of European Union. "Directive 2008/50/EC of the European Parliament and of the Council of 21 May 2008 on ambient air quality and cleaner air for Europe". *Official Journal of the European Union*, L 152, (2008). url: https://eur-lex.europa.eu/eli/dir/2008/50/2015-09-18 (cit. on p. 4).

[17] Ministère de l'Environnement, de l'Énergie et de la Mer. "Décret n° 2016-847 du 28 juin 2016 relatif aux zones à circulation restreinte." *Journal Officiel de la République Française*, 150 (3), (2016). url: https://www.legifrance.gouv.fr/jorf/id/JORFTEXT000032790919 (cit. on p. 4).

[18] The CLARS Platform. *Urban Access Regulations in Europe*. Accessed 2020-12-8 at https://urbanaccessregulations.eu/countries-mainmenu-147/france/paris. Sadler Consultants Ltd. 2017 (cit. on p. 4).

[19] X. Mosquet, A. Arora, A. Xie, and M. Renner. *Who Will Drive Electric Cars to the Tipping Point?* Accessed 2020-12-05 at https://www.bcg.com/publications/2020/drive-electric-cars-to-the-tipping-point. Boston Consulting Group. 2020 (cit. on pp. 4, 5).

[20] G. Crabtree. "The coming electric vehicle transformation". *Science*, 366 (6464), (2019), pp. 422–424. issn: 0036-8075. doi: 10.1126/science.aax0704 (cit. on p. 5).

[21] International Energy Agency (IEA). *Global EV Outlook 2020*. Accessed 2020-12-10 at https://www.iea.org/reports/global-ev-outlook-2020. 2020 (cit. on p. 5).

“A central lesson of science is that to understand complex issues (or even simple ones), we must try to free our minds of dogma and to guarantee the freedom to publish, to contradict, and to experiment. Arguments from authority are unacceptable.”

— Carl Sagan

Chapter 2

Engine and experimental method

Contents

2.1 Introduction 14
2.2 Reference engine 14
2.3 Test cell description 15
2.4 Driving cycle test procedure 23
2.5 Data analysis procedure 25
2.5.1 Pollutant emissions calculation 25
2.5.2 Test repeatability and uncertainty 27
2.6 Experimental campaign 29
Chapter 2 References 33

2.1 Introduction

Prior to introducing the gas dynamics model, this chapter introduces the reference engine in which the virtual engine model is based. Details regarding the instruments and procedures for the experimental data acquisition are described in this chapter, so as to detail later the calibration and validation processes of the sub-models presented in the next Chapter 3.

2.2 Reference engine

The reference engine mentioned in the previous sections and using in the calibration of some of the VEMOD sub-models is a high speed direct injection (HSDI) diesel engine. This is a 4-cylinder in-line engine with a total displacement of 1.6 litres and compliant with EURO-5 emissions regulation.

From the point of view of thermal management, the low pressure EGR is cooled by a gas-coolant heat exchanger and another cooler, also known as water charge air cooler (WCAC), cools the intake air to the cylinders. In order to reduce the warm-up time, the thermostat electrovalve blocks the coolant flow through the engine block during engine warming. The turbocharger system consists of a radial compressor and a variable geometry turbine (VGT). This turbocharger is not cooled by water, but all the heat coming from the turbine and mechanical losses are dissipated by the lubricating oil and the surrounding ambient. Finally, the after-treatment system consists of a close-coupled DOC and DPF brick.

The main specifications of the reference engine are summarised in Table 2.1.

Type	EURO 5 HSDI Diesel engine
Displacement	1598 cm^3
Stroke	79.5 mm
Bore	80 mm
Compression ratio	14.5:1
Max. power @ speed	96 kW @ 4000 rpm
Max. torque @ speed	320 Nm @ 1750 rpm
Number of valves	4 per cylinder (2 int., 2 exh.)
Number of cylinders	4 in-line
Valvetrain	Double overhead camshaft (DOHC)
Fuel delivery	Common rail, direct injection
Boosting system	Turbocharger with VGT
EGR system	HP and cooled LP-EGR
Intake cooling system	Water charge air cooler (WCAC)
EAT System	Closed-coupled DOC + DPF

Table 2.1: Reference engine specifications.

2.3 Test cell description

In order to perform tests in the reference engine at room temperatures below 0 °C, a climate test cell is required. The climate test cell in which the reference engine was installed is able to cool the environment down to −15 °C. Temperature sensitive devices (gas analysers, fuel measurement system, etc.) where placed outside the climate chamber at constant temperature of 20 °C.

Engine speed and torque are controlled by an electrical dynamometer to run tests at steady and transient speed and load conditions. The Schenck dynamometer installed in the test bench is regulated based on the eddy current principle and is suitable to test light-duty engines, allowing a torque up to 400 Nm with a linear accuracy of 0.1 %. The engine speed is measured with a Kistler crank-angle encoder type 2613A, able to measure crank angle within an engine speed range from 0 to 20000 rpm with a precision of +0.02°. The engine operating point is controlled by using a program inter-

face developed by Horiba called STARS that communicates the engine dynamometer control with the engine pedal sensor and actuator. Electrical dynamometer torque and speed and pedal position are set by a PID controller working in closed loop. Vehicle speed is converted into an engine speed target knowing the gear ratio of the simulated vehicle. Then, engine torque is set by means of the electrical dynamometer load that takes into account the tire-road friction, powertrain transmission losses, aerodynamic drag and vehicle mass. The pedal position actuator allows reaching target engine speed as a response to torque variations.

The fuel measurement system used in the test cell consists of an AVL 733S fuel balance. This device measures the fuel mass flow based on the gravimetric measurement principle. Thus, the fuel consumed is calculated directly by measuring the rate at which the fuel measuring vessel weigh decreases. This vessel is linked to a bending beam, so the deformation (required to obtain the vessel weigh) is measured by means of a capacitive displacement sensor. Since the measuring vessel has to be refilled for each measurement, the fuel rate measurement can be considered as a discontinuous measurement procedure. The operation of the system is automatically performed by the STARS software, controlling the filling of the volume used to measure the fuel mass required by the engine. All in all, the fuel mass flow can be measured in a range from 0 to 150 kg/h with an uncertainty of 0.12 % and for fuel temperatures from –10 °C to 70 °C.

The air mass flow admitted by the engine is measured with an ABB Sensy flow meter FMT700-P. This device relies on the hot-film anemometry principle, which calculates the air mass flow by means of the required electric current for heating a platinum film resistor. This resistor is maintained at a constant overtemperature in relation to another platinum film within the gas flow. With an already known and constant gas composition, the mass flow can be determined by evaluating the heating current vs mass flow curve. The flow meter is able to measure a rate up to 900 kg of air per hour with a minimum accuracy of 0.8 % and a response time of 12 ms; thus, it suits the requirements derived from transient tests.

Gas, wall and coolant temperatures across the engine have been measure by using K-type thermocouples. This kind of thermocouples are used

widely and suitable thermometry devices in engine research since they cover a wide range of temperature conditions (3 to 1533 K) with a good precision: 0.75 % for positive temperatures and 2.2 % for temperatures below zero. In Figure 2.1, the engine layout and the main pressure and temperature measurement points are sketched. Like in the case of the temperature measurement, the average pressure in these locations is determined by PME P40 transmitters, which are able to measure gas pressures up to 400 bar with a linear uncertainty of 0.3 %.

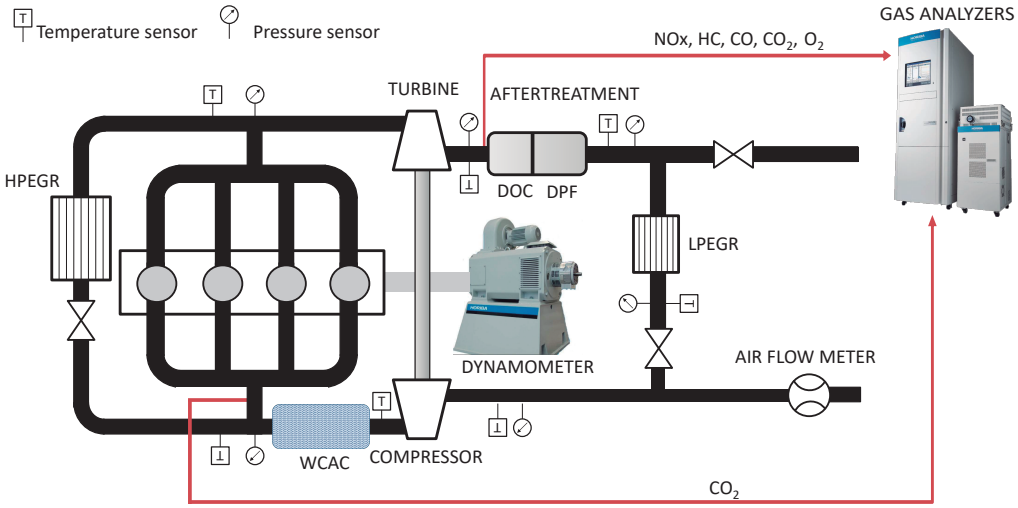

Figure 2.1: Engine layout indicating the pressure, temperature and exhaust gases measurement points.

In addition to on board engine measurement devices, several measurements were connected to the engine. All laboratory measurements devices were sampled at 10 Hz and handled by a programmable logic controller (PLC).

As far as pollutant emissions are concerned, Horiba MEXA-One gas analyser system was used to determine the concentration of the major exhaust pollutant gases. All measurements were obtained in volumetric concentration, so emission rates have to be calculated by means of the total gas mass flow. Moreover, a humidity correction has to be applied to the gas analyser results since the measurement is done in dry conditions (NO_x,

CO and CO_2). Gas sampling devices comprise several optical techniques for chemical analysis. In the following lines the main features and physical principles of the gas sampling techniques are described. More details about gas analysers operation can be found in the handbook by Adachi and Nakamura [22]. CO and CO_2 concentrations are obtained by means of non-dispersive infrared (NDIR) spectroscopy. This principle relies on the absorption spectroscopy: an infrared source emits beams direct to a sampling gas. According to the Beer-Lambert's law, the ratio between the transmitted and the incident radiation intensity, known as transmittance, depends on the concentrations of the attenuating species in the sample. Gas radiation absorbance is governed by a frequency depending absorbance coefficient specific for each chemical compound. Spectra features intensity, obtained by the Beer-Lambert's law, at constant pressure, temperature and absorption length are proportional to the concentration compound. Knowing this relation, molar concentration by chemical specie can be determined by comparing the measured features with previous calibrated conditions of the same species where molar concentration is known.

With the measurement of CO_2 concentration in both intake and exhaust manifolds, it is possible to obtain the amount of recirculated exhaust gases (EGR). EGR is a popular technique widely used in thermal engines to reduce NO_x emissions. It dilutes the cylinder oxygen concentration by trapping a portion of exhaust gases, thus reducing the combustion rate leading to lower peak combustion temperature that eventually reduces NO_x formation [23]. The amount of EGR can be quantified by the ratio between the recirculated exhaust gas mass flow and the total intake mass flow rate. However, by applying the species continuity conservation equation between the intake and the exhaust manifold EGR can be determined in terms of CO_2 concentration as shown in Equation 2.1. CO_2 is used since is the main product of the combustion (no matters the type of fuel burned) and its measurement is more reliable than other species whose concentration may be hundred times lower. The definition of EGR considers the same molecular mass for both fresh and exhaust gasses, which is a wrong assumption. A study of the influence on considering different molecular masses was carried out by Vera [24], who found that the error derived from this assumption is below

0.3 %.

$$EGR = \frac{\dot{m}_{\text{recirculated}}}{\dot{m}_{\text{air}} + \dot{m}_{\text{recirculated}}} = \frac{[CO_{2_{\text{intake}}}] - [CO_{2_{\text{ambient}}}]}{[CO_{2_{\text{exhaust}}}] - [CO_{2_{\text{ambient}}}]} \tag{2.1}$$

Regarding hydrocarbons (HC) emissions, the technique used to compute these emissions is known as flame ionisation detection (FID). FID is based on the fact that the combustion of HC in a hydrogen flame generates HC ions. The FID response is proportional to the number of carbon atoms contained in the sample and is a commonly used technique to account for total hydrocarbons (THC) contained in the exhaust gas in ppmC units. A sketch of the FID system is shown in Figure 2.2. The hydrogen flame is created in a burner nozzle be supplying a fuel gas (H_2 or a mixture of this with He or N_2) and combustion air. The sample gas is then introduced in the flame where HCs in the sample are ionised. An electric potential is applied across the nozzle to the collector that surrounds the nozzle. Consequently, an electric current is generated between the nozzle and the collector due to HC ions within the flame. As commented above, this current is proportional to the amount of carbon that passes through the flame as HCs, so the THC concentration can be determined. Usually in engine exhaust gas measurements and due to the fact that the FID sensitivity depends on each HC component, this sensitivity for each HC is represented by a response factor that indicates the relative sensitivity compared to propane used as calibration gas. The FID sensitivity depends not only on the concentration and type of HC in the sample gas but also on the flow rates of the combustion air and fuel gas. Fortunately, FID shows negligible interference form inorganic components such as CO, CO_2, H_2O and NO.

Nitrogen oxides (NO_x) are usually measured using the chemiluminiscence detection (CLD) technique. This technique address any reaction that involved light emissions and allows determining NO and NO_2 concentrations. In Figure 2.3, a simplified scheme of a NO detector using CLD is presented. In the reactor, the NO sampling gas is oxidised to NO_2 by means of an ozone (O_3) injection. This oxidation reaction produces a small fraction of excited NO_2^*. As this excited NO_2^* decays to its ground state, excitation energy is emitted as photons. This reaction is presented in Equation 2.2,

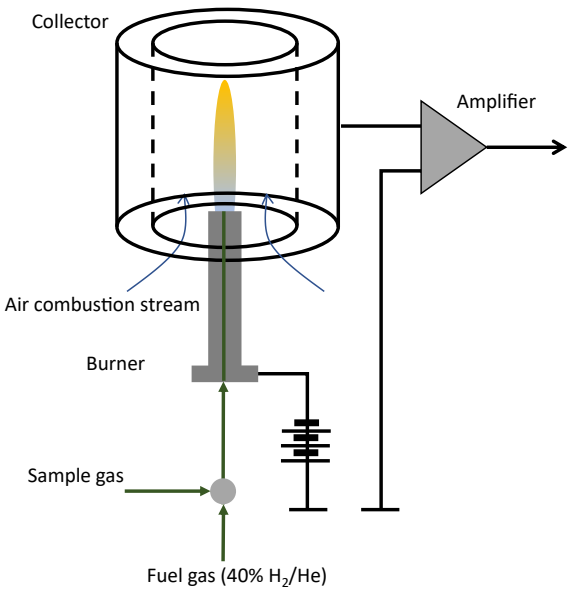

Figure 2.2: Flame ionisation detection (FID) system sketch.

where h is the Plank constant and ν is the wave frequency.

$$\begin{aligned} NO + O_3 &\longrightarrow NO_2^* + O_2 \\ NO_2^* &\longrightarrow NO_2 + h\nu \end{aligned} \tag{2.2}$$

The luminescence intensity is proportional to the NO amount that reacts with O_3, therefore, by detecting the intensity with a photodiode it is possible to determine the NO concentration in the gas sample. In order to measure NO_2 concentration, a converting unit (NO_x converter) packed with a carbon-based material is located before the photodiode detector to convert NO_2 into NO. NO_2 in the sample gas is reduced by reacting with carbon in the NO_x converter as explained in Equation 2.3.

$$\begin{aligned} NO_2 + C &\longrightarrow NO + CO \\ 2\,NO_2 + C &\longrightarrow 2\,NO + CO_2 \end{aligned} \tag{2.3}$$

The output of a CLD with a NO_x converter provides total concentration of NO and NO_2 which account for NO_x emissions concentration. If two CLD analysers are used it is possible to obtain NO and NO_2 concentrations separately.

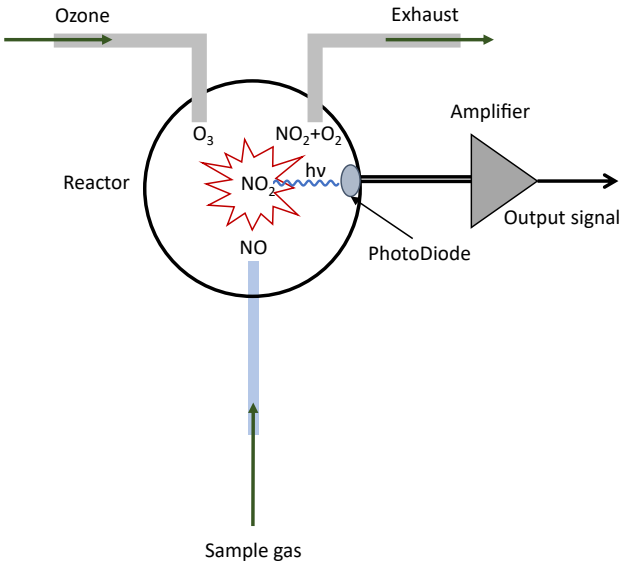

Figure 2.3: Chemiluminiscent detector sketch.

Oxygen (O_2) concentration in the exhaust line is measured by a magneto-pneumatic detector (MPD) with works based on the oxygen paramagnetic detection. When a gas sample is introduced in a magnetic field, chemical components with a high magnetic susceptibility, such as O_2, are drawn towards the magnet pole. Hence, the pressure near the magnetic pole rises in relation to the concentration of drawn components, mainly O_2 in the case of a diesel engine. The non-uniform oxygen concentration results in a pressure difference that leads to the mechanical displacement of a pressure sensor.

Finally, particle matter (PM) also mentioned as soot in this thesis is measured by means of an opacimeter. This device allows a continuous measurement of exhaust gas opacity. Basically, an exhaust gas sample is passed through a paper sheet of known thickness and density. The more particle matter mass in the gas sample, the darker the paper becomes. The opacity (in percentage) and the light absorption coefficient can be measured there-

fore by quantifying the loss of light intensity through the paper between a light source and a receiver. In addition, the system response time of 0.1 seconds and the possibility to make measurements upstream and downstream of the DPF makes it suitable for transient load tests measurements. The particle matter concentration is indirectly obtained empirically based on the opacity.

Gas analyser sensor locations are detailed in Figure 2.1. It should be pointed out that, even though exhaust gas concentrations are measured upstream the after-treatment system (according to the results presented in subsection 3.3.3), both upstream and downstream measurements were done for the calibration and results of the after-treatment model (subsection 3.3.2). All gas sampling lines are heated by electrical resistors to avoid in-line condensation that may alter the measurements. Pressure and temperature probes are placed so as the measure is taken in the centre of the gas flow stream, except those that measure wall temperatures. The intake air mass flow meter is previously filter to avoid the inclusion of any dust or dirt particle. Finally, Table 2.2 summarises all the test cell equipment described in this section.

Variable	Instrument	Range	Accuracy
Crank angle	Kistler encoder type 2613A	0.1-6°, speed: 1-20 krpm	+0.02°
Torque	Schenck dynamometer	0-400 Nm	±0.1%
Gas/wall temp.	k-type thermocouple	3-1533 K	±2.2%, 0.75%
Duct pressure	PMA Transmitter P40	0-400 bar	Linearity 0.3%
Air mass flow	ABB flow meter FMT700-P	0-900 kg/h	±0.8%
Fuel mass flow	AVL 733S fuel balance	0-150 kg/h	±0.12%
Coolant flow	Krohne 400 Optiflux	4.5-90 L/min	±0.5%
Oil pressure	Piezoresistive transducer	0-10 bar	±25 mbar
In-cylinder pres.	AVL GH13P	0-200 bar	Linearity 0.3%
Opacity	AVL439 Opacimeter	0-100%	0.01%
CO	Horiba MEXA-One (NDIR)	0-5000 ppm, 0-12 vol%	1% Full scale
CO_2	Horiba MEXA-One (NDIR)	0-20 vol%	1% Full scale
O_2	Horiba MEXA-One (MPD)	0-22 vol%	1% Full scale
THC	Horiba MEXA-One (FID)	0-20000 ppmC	1% Full scale
NO/NO_2	Horiba MEXA-One (CLD)	0-10000 ppm	1% Full scale

Table 2.2: Test cell instrumentation.

2.4 Driving cycle test procedure

In the European Union, type approval emission tests are required by law for all new light-duty vehicle models and for the engines used in heavy-duty vehicles. Since 2017, the new type approval worldwide harmonised light duty vehicle test cycle (WLTC) substitutes the previous new European driving cycle (NEDC). A comparison of the dynamic conditions of both cycles is presented in Figure 2.4. The new type approval differs from the NEDC in the higher intensity of transient conditions, the longer cycle duration and the impact of vehicle optional features on the CO_2 emissions. Furthermore, WLTC intends to be a more realistic driving cycle in order to provide real emissions and consumption data.

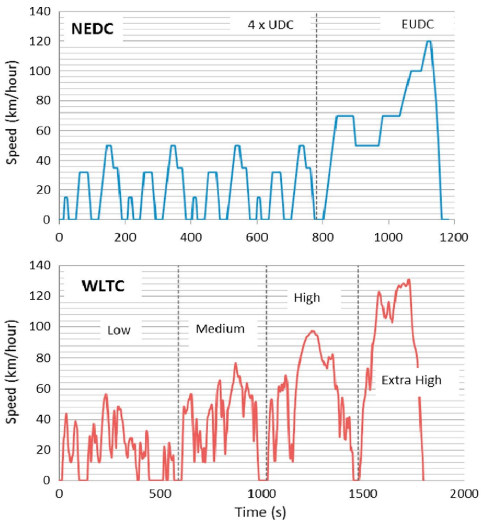

Parameters	NEDC	WLTC
Duration (s)	1180	1800
Distance (km)	11.03	23.27
Average speed (km/h)	33.6	46.5
Maximum speed (km/h)	120.0	131.3
Stop duration (%)	23.7	12.6
Constant driving (%)	40.3	3.7
Acceleration (%)	20.9	43.8
Deceleration (%)	15.1	39.9
Average positive acceleration (m/s^2)	0.59	0.41
Maximum positive acceleration (m/s^2)	1.04	1.67
Average positive "speed*acceleration" (m^2/s^3)	1.04	1.99
Maximum positive "speed*acceleration" (m^2/s^3)	9.22	21.01
Average deceleration (m/s^2)	-0.82	-0.45
Minimum deceleration (m/s^2)	-1.39	-1.50

Figure 2.4: *NEDC and WLTC European driving cycles comparison [25].*

Along this thesis, all the engine transient tests and transient simulations are performed according to the WLTC class 3 cycle. Driving cycles are one of the main tools that engineers have to analyse engine performance, mainly from the point of view of engine efficiency and pollutant emissions.

Driving cycles are performed by means of the electric dynamometer. Engine speed and torque are the engine target variables required to run driving cycles. This two variables are calculated based on the vehicle speed and gear ratio defined by the WLTC and the specific features of the vehi-

cle. The vehicle model used for testing was a typical mid-size car from the European market. Thus, engine speed (N) is calculated according to Equation 2.4, where v is the vehicle speed, D is the car wheel diameter and Z is the gearbox ratio.

$$N = \frac{v}{\pi \cdot D \cdot Z} \tag{2.4}$$

The engine power (P) is calculated in Equation 2.5 from the increase of vehicle kinetic energy, the road friction power losses (P_{road}), the inertia of the powertrain transmission and car wheel (I), the road aerodynamic power losses ($P_{\text{aerodynamic}}$) and the mechanical efficiency of the gearbox (η_{gb}).

$$P = \left(\frac{\frac{m}{2} \cdot (v_{t+1}^2 - v_t^2)}{t} + I \cdot \alpha + P_{\text{road}} + P_{\text{aerodynamic}} \right) \cdot \frac{1}{\eta_{\text{gb}}} \tag{2.5}$$

The first term of the sum ($m/2 \cdot (v_{t+1}^2 - v_t^2)$) represents the variation of kinetic energy of the vehicle. In case of no variation in the vehicle velocity, the required power is only owing to the road, transmission and aerodynamic frictional losses since they are vehicle speed dependent. At this point, engine torque (M) can be calculated according to Equation 2.6.

$$M = \frac{P}{2 \cdot \pi \cdot N} \tag{2.6}$$

As briefly mentioned in section 2.3, the output signal of a PID controller handles the engine pedal position to reach the target engine speed. For an specific gear ratio, when the load torque is increased by the dynamometer, engine speed falls down. So as to avoid the speed down, the position of the pedal actuator varies to increase the injected fuel rate and reach the speed target.

After a driving cycle test, a common procedure is to regenerate the DPF by applying high engine loads during half an hour. This operating condition increases the exhaust temperature and burns the particle matters deposits

in the particle filter. The pressure drop across the DPF is monitored, so the regeneration process is ensured.

2.5 Data analysis procedure

This section describes the procedure carried out for data analysis. On one hand, the calculation of the pollutant emissions rates from their raw concentrations has to be explained. On the other hand, the experimental test repeatability is analysed in terms of sampling standard deviation. Process variabilities are caused by inherent and random instabilities of a process. In order to detect biased test outcomes, an outlier detection procedure designed for relatively low amount of available samples is proposed.

2.5.1 Pollutant emissions calculation

The measurement of the exhaust gas concentrations involves a delay between these measurements and other engine variables such as engine speed or air and fuel mass flows [26]. This particular delay is due to two reasons. On one hand, the delay necessary to analyse the gas sample and this delay depends on each chemical specie and the technique used to measure its concentration. On the other hand, the distance between the point where the sample is collected and the gas analyser device results in a delay defined this length and the gas velocity. The gas velocity through the sample pipes is produced by the vacuum pressure generated by the gas analyser pump, which remains constant during the whole cycle. Some authors have implemented physical behaviour models to account for this delay [26] while other authors analyse the delay by correlation methods comparing the pollutant measurement with other related variables like engine speed and air mass flow rate [27]. In the work presented in this thesis a correlation method is used based on the convolution between pollutants and air mass flow signals [28]. Convolution is a mathematical operation (Equation 2.7) on two functions (p and m) that produces a third function ($p * m$) that expresses

how the shape of one is modified by the other.

$$(p * m)(t) \triangleq \int_{-\infty}^{+\infty} p(\tau) \cdot m(t-\tau)\mathrm{d}\tau \tag{2.7}$$

Where $p(t)$ and $m(t)$ are the pollutant and air mass flow signals in the time domain and τ is a dummy variable. Equation 2.8 presents the convolution of two functions in case they are finite discrete signals (which is the case of a measured signal in the test cell), where n is any point of the discrete signal and n is a shift coefficient.

$$(p * m)[n] = \sum_{i=-\infty}^{+\infty} p[i] \cdot m[n-i] \tag{2.8}$$

The point where the convolution function is maximum indicates the mismatch delay between signals that must be corrected to synchronise both measurements. Emissions mass flow rate are calculated using the pollutant concentrations and the air and fuel mass flow rates according to Equation 2.9, where $M_{\text{pollutant}}$ and M_{air} are the molecular masses of the pollutant and the air respectively and $C^*_{\text{pollutant}}$ is the corrected pollutant concentration.

$$\dot{m}_{\text{pollutant}} = \frac{M_{\text{pollutant}}}{M_{\text{air}}} \cdot (\dot{m}_{\text{air}} + \dot{m}_{\text{fuel}}) \cdot C^*_{\text{pollutant}} \tag{2.9}$$

Species concentrations that are measured in dry basis —NO_x, CO and CO_2 in this case due to the gas analyser used and described in section 2.3— have to be corrected in order to take into account the exhaust gas water vapour content. Pollutant emissions have been corrected according to European Commission Directive 2005/55/EC [29] and included in the in force regulation (EC) No 595/2009.

2.5.2 Test repeatability and uncertainty

Part of the error that affects the results obtained in the test cell are due to the uncertainties of the measurement devices indicated in Table 2.2. In addition to this error, engine performance and boundary test conditions variability also affect the measurements. Beyond the accuracy of the engine actuators and sensors, a variability is presented when the same test is performed several times. Repeatability is defined by the U.S. National Institute of Standards and Technology (NIST) as the ability to repeat an assessment in the future, in a manner that is consistent with, and hence comparable to, prior assessments. Repeatability condition include:

- The same measurement procedure.
- The same observer.
- The same measuring instrument and used under the same conditions.
- The same location.
- Repetition over a short period of time.

According to such conditions, a procedure for anomalous results detection was defined to quantify the natural variability of the process [30]. This procedure is divided in two parts. The first part calculates the weighted average of the relative error of test variables. This relative error is weighted accounting for the instantaneous variable measurement magnitude. Equation 2.10 defines this weighted relative error and a discrete approximation according to Riemann sum in the right side where $\bar{x}$ is the instantaneous measured average variable, $\bar{\beta}$ is the instantaneous average relative error of each variable (both obtained from the average of several repetitions of the same test) and n is the number of test measurements points.

$$\epsilon = \frac{\int_0^t \bar{\beta}(t) \cdot \bar{x}(t) \mathrm{d}t}{\int_0^t \bar{x}(t) \mathrm{d}t} \approx \frac{\sum_{i=0}^{i=n} \bar{\beta}(t) \cdot \bar{x}_i}{\sum_{i=0}^{i=n} \bar{x}_i} \tag{2.10}$$

The instantaneous average relative error ($\bar{\beta}$) is calculated as indicated in Equation 2.11, where m is the number of test repetitions by case and α is the instantaneous relative error of each test repetition defined in Equation 2.12, where x is the variable under study during the j test repetition.

$$\bar{\beta} = \frac{1}{m} \cdot \int_{j=0}^{j=m} \alpha_j \tag{2.11}$$

$$\alpha_j = \frac{|x_j - \bar{x}|}{\bar{x}} \tag{2.12}$$

The error definition in Equation 2.10 expressed how high is the dispersion of the entire tests set related to the averaged variable value. Measured variables, such as pipe/manifold pressures and temperatures, fuel and air mass flows, engine speed and torque show a relative error (ϵ) lower than 5%. The second part of the outlier detection method concerns the pollutant emissions variability. Since pollutants emissions variation between test repetitions can be high compared to the rest of the test variables [31], an additional analysis based on cumulative emissions instead of instantaneous measurements is applied. A threshold value is considered to discriminate atypical measurements when the distance between the pollutant mass and the closest quartile is higher than 1.5 times the interquartile range. Moreover, the existence of extreme values is studied though the comparison of the mean and median of the data set. In case of adding an anomalous test in a sample, the median remains with low variations while the mean is strongly modified. The comparison between median and mean is characterised by the ratio of the absolute difference between the median and mean divided by the median of the data set as shown in Equation 2.13, where SK is the median-mean skewness coefficient, m and μ are the pollutant median and mean between the test respectively.

$$SK\ (\%) = \frac{|m - \mu|}{m} \cdot 100 \tag{2.13}$$

This skewness coefficient measures the central tendency of the data set distribution. Considering the experimental variability as a symmetric dis-

tribution, the higher this coefficient, the skewed the data set because of the presence of an outlier. A threshold value of 4 % for this coefficient has been used to consider a measurement as an atypical one.

Once the absence of outliers is ensured, mean results are obtained by averaging the dataset of each test type. For small dataset size, lower than 10, the standard deviation (σ) can be inferred from the population range as indicated in Equation 2.14.

$$\sigma = \frac{R}{d_{2,n} \cdot \sqrt{n}} \tag{2.14}$$

Where R is the population range, $d_{2,n}$ is the control limit factor and n is the population size. In the experimental tests performed for this thesis, three repetitions of each test were carried out, both for the steady-state and transient operating conditions tests.

2.6 Experimental campaign

In previous sections, the calibration results of the main sub-models integrated in VEMOD were discussed. The complete engine model has been validated in steady and transient operating conditions. The engine operating points considered for the calibration of the virtual engine are those enumerated in Table 2.3 and vary from low to high engine speed and from low to high load with the aim of covering a wide range of the engine map and testing points belonging the WLTP cycle. These points are presented as well in Figure 2.5 for the sake of clarity. The mentioned figure shows the operating points of the entire WLTC as blue dots and the measured points in steady-state conditions, where those measured with the engine under hot operating conditions are depicted with a red dot • and those carried out at −7 °C are depicted with a green ring ◦. As indicated in Table 2.4, hot operating conditions refers to a test cell temperature of 20 °C and an engine coolant temperature around 80 °C (standard operating temperature), while cold conditions means that the test cell temperature is −7 °C. As it can be observed by Figure 2.5, the experimentally measured points intend to cover

Engine speed [rpm]	load [%]
850	idle
1000	21, 44, 66, 88
1250	13, 26, 50, 76, 100
1500	11, 25*, 50, 75*, 100
2500	25, 50, 75, 100
3500	25*, 50, 75, 100

* both hot and cold tests were performed.

Table 2.3: Steady-state test for combustion model calibration.

Conditions	Engine temp.	Test cell temp.
Warm	already warm (≈ 80°C)	20°C
Cold	already warm (≈ 80°C)	−7°C

Table 2.4: Engine and test cell temperatures at transient operating conditions.

the complete operating map of the engine, emphasising the range covered by the WLTC cycle.

To validate the engine in transient conditions of speed and load, experimental tests were performed in three different environment temperatures: cold engine start and a test cell temperature of 20 °C, cold engine start and a test cell temperature of −7 °C, and a third environment in which the engine is already warm and the test cell temperature is 20 °C. Table 2.5 summarises this three temperature conditions that are hereafter used in this thesis.

The transient test reproduced in the test bench is the WLTC class 3 cycle. This type approval cycle is divided in four stages according to the average

Conditions	Engine temp.	Test cell temp.
Warm	already warm (≈ 80°C)	20°C
Ambient	cold start at 20°C	20°C
Cold	cold start at 80°C	−7°C

Table 2.5: Engine and test cell temperatures at steady operating conditions.

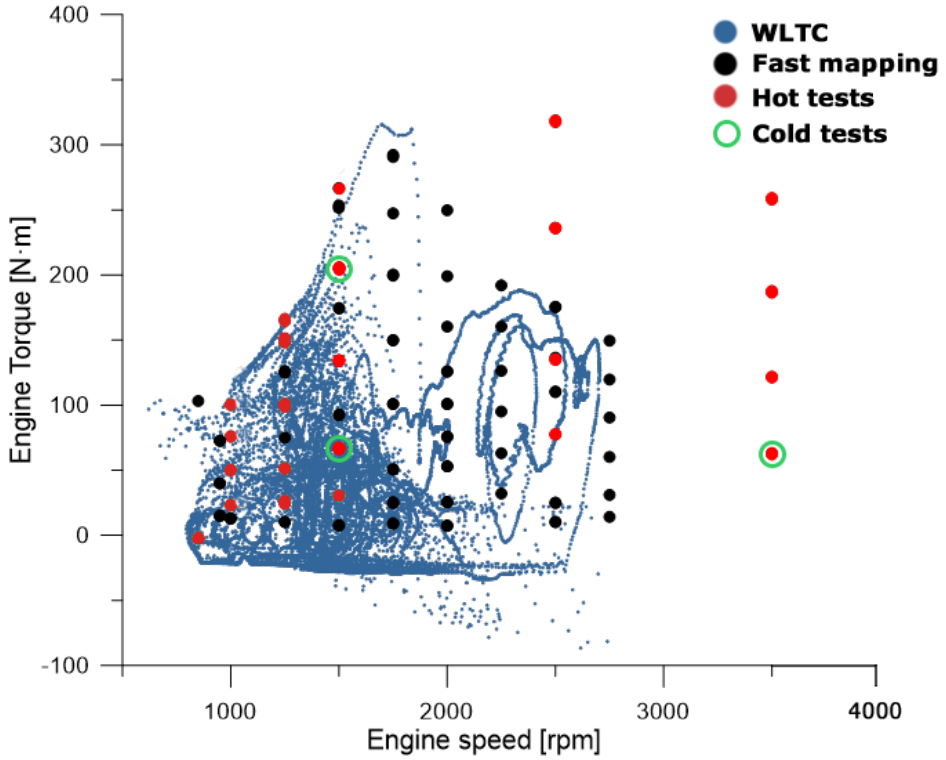

Figure 2.5: Experimentally tested points and the operating points along the WLTC.

vehicle speed during these stages (low, medium, high and extra high). The procedure of how the transient test is carried out is explained in section 2.4. The data analysis presented in section 2.5 is applicable to both steady and transient tests. In this way, three repetitions of each test were performed in the same test cell and keeping all the test repeatability precepts.

Chapter 2 References

[22] M. Adachi and H. Nakamura. *Engine Emissions Measurement Handbook*. Horiba Ltd., 2013. doi: 10.4271/jpf-hor-002 (cit. on p. 18).

[23] A. Maiboom, X. Tauzia, and J. F. Hétet. "Infuence of high rates of supplemental cooled EGR on NOx and PM emissions of an automotive HSDI diesel engine using an LP EGR loop". *International Journal of Energy Research*, 32 (15), (2008), pp. 1383–1398. issn: 0363907X. doi: 10.1002/er.1455. url: https://onlinelibrary.wiley.com/doi/abs/10.1002/er.1455 (cit. on p. 18).

[24] F. Vera. "Efecto de la recirculación del gas de escape en el proceso de la renovación de la carga en motores turbo-sobrealimentados". PhD thesis. Universitat Politècnica de València, 2004 (cit. on p. 18).

[25] J. Pavlovic, B. Ciuffo, G. Fontaras, V. Valverde, and A. Marotta. "How much difference in type-approval CO2 emissions from passenger cars in Europe can be expected from changing to the new test procedure (NEDC vs. WLTP)?" *Transportation Research Part A: Policy and Practice*, 111, (2018), pp. 136–147. issn: 09658564. doi: 10.1016/j.tra.2018.02.002 (cit. on p. 23).

[26] J. T. Messer, N. N. Clark, and D. W. Lyons. "Measurement delays and modal analysis for a heavy duty transportable emissions testing laboratory". *International Congress and Exposition*. SAE International, 1995. doi: 10.4271/950218 (cit. on p. 25).

[27] G. Konstantas and A. Stamatelos. "Quality assurance of exhaust emissions test data". *Proceedings of the Institution of Mechanical Engineers, Part D: Journal of Automobile Engineering*, 218 (8), (2004), pp. 901–914. issn: 09544070. doi: 10.1243/0954407041581075 (cit. on p. 25).

[28] J. D. Pakko. "Reconstruction of time-resolved vehicle emissions measurements by deconvolution". *SAE International Journal of Fuels and Lubricants*, 2 (1), (2009), pp. 697–707. issn: 19463952. doi: 10.4271/2009-01-1513 (cit. on p. 25).

[29] Council of European Union. "Directive 2005/55/EC of the European Parliament and of the Council of 28 September 2005 on the approximation of the laws of the Member States relating to the measures to be taken against the emission of gaseous and particulate pollutants from compression-ignition engines for use in vehicles, and the emission of gaseous pollutants from positive-ignition engines fuelled with natural gas or liquefied petroleum gas for use in vehicles".

Official Journal of the European Union, L 275, (2005). url: http://data.europa.eu/eli/dir/2005/55/oj (cit. on p. 26).

[30] A. Moratal. "Experimental Analysis of Thermal Management Influence on Performance and Emissions in Diesel Engines at low ambient Temperature". PhD thesis. Universitat Politècnica de València, 2018 (cit. on p. 27).

[31] K. Robinson, S. Ye, Y. Yap, and S. T. Kolaczkowski. "Application of a methodology to assess the performance of a full-scale diesel oxidation catalyst during cold and hot start NEDC drive cycles". *Chemical Engineering Research and Design*, 91 (7), (2013), pp. 1292–1306. issn: 02638762. doi: 10.1016/j.cherd.2013.02.022 (cit. on p. 28).

“All things are hidden, obscure and debatable if the cause of the phenomena is unknown, but everything is clear if its cause be known.”

— Louis Pasteur

Chapter 3

Development of a virtual engine model

Contents

3.1 Introduction 39
3.2 Model description 40
3.2.1 Gas dynamics model 42
3.2.1.1 Boundary conditions 46
3.2.1.2 Heat transfer at pipes 48
3.2.1.3 Turbocharger sub-model 49
3.2.1.4 In-cylinder conditions model 51
3.2.1.5 Blow-by model 53
3.2.1.6 Water condensation model 57
3.2.2 Injection rate model 59
3.2.3 Combustion model 65
3.2.3.1 Combustion model calibration 71
3.2.4 Emissions model 76

3.2.4.1 NO_x emissions model 76
3.2.4.2 Soot, CO and UHC emissions model 79
3.2.5 After-treatment systems model 82
3.2.5.1 After-treatment system lumped model . . . 83
3.2.5.2 Pressure drop 85
3.2.5.3 Porous media properties 86
3.2.5.4 Filtration 86
3.2.5.5 Reaction mechanism 87
3.2.5.6 Heat transfer in the after-treatment systems 88
3.2.5.7 After-treatment model calibration 89
3.2.6 Heat transfer model 94
3.2.6.1 In-cylinder heat transfer model calibration 98
3.2.7 Thermo-hydraulic model 100
3.2.8 Mechanical losses model 104
3.2.8.1 Mechanical losses model calibration 105
3.2.9 Control, vehicle and driver models 108
3.3 Validation of the virtual engine model 113
3.3.1 Validation of the turbocharger model 113
3.3.2 Validation of the after-treatment systems model 115
3.3.3 Validation of the complete virtual engine model 117
3.4 Conclusions 127
Chapter 3 References 136

3.1 Introduction

The virtual engine model presented in this thesis is part of a series of continuous improvements of a complete one-dimensional (1D) wave action model [32] developed in the research institute CMT-Motores Térmicos (hereafter CMT) of the Universitat Politècnica de València (UPV).

The program was conceived by Corberán in 1984 [33] by using the method of characteristics to solve hyperbolic partial differential equations systems and based on the formulation and postulates exposed by Benson [34]. In successive improvements, the method of characteristics was substituted by a faster and less diffusive finite difference scheme. Desantes, Chust and Llorens [35] carried out a comparative study in 1993, where different schemes were tested. The conclusion was that the most suitable schemes to solve the compressible flow through the engine pipes were two step Lax-Wendroff and the predictor-corrector MacCormak. Few years ago, another comparative study was carried out by Payri, Galindo, Serrano and Arnau [36], where modern high resolution schemes like total variation diminishing (TVD) schemes were tested to be used in the code for solving the flow through the pipes. The evolution of the program presented in this thesis has replaced the finite difference scheme by a finite volume method (FVM) explained in subsection 3.2.1.

In addition to the evolution of the 1D fluid-dynamic methods, some other sub-models have been included and improved within the program. To remark some of these sub-models, cylinder and plenums make use of zero-dimensional (0D) filling and emptying models [33, 37], the turbine boundary conditions model by Payri et al. [38, 39] or the heat transfer in ducts model by Reyes [40], with later improvements by Serrano [41] and Galindo et al. [42]. Since the thesis of Galindo [43] and a set of theoretical and experimental researches [44, 41, 45, 46], the model began to be able to calculate transient load simulations. Currently, the modularity of the code allows the user to easily incorporate new sub-models that solve complex problems and they can interact with each other.

3.2 Model description

The models presented in this chapter have been integrated into VEMOD, a 0D-1D gas dynamics tool that has been developed at CMT-Motores Térmicos. This computational tool arises as a response to highly limiting requirements of emission standards imposed by new homologation procedures, closer to real-world driving conditions in terms of engine dynamic operation, ambient temperature and altitude concerns. The current context demands the support of new computational tools able to accurately predict engine performance and emissions while reducing the cost of expensive tests campaigns. VEMOD, which has been developed as a standalone tool to simulate new standard testing cycles, fulfils these objectives by means of an engine model covering the calculation of the different processes that take place in an internal combustion engine. Its global flowchart is shown in Figure 3.1. Here, blue boxes represent the engine model modules. Firstly, the air management is computed by means of a 1D gas dynamics model (subsection 3.2.1) which performs the calculations of the flow properties along the intake and exhaust systems as well as the high and low pressure EGR paths. Thus, specific sub-models are considered for the boosting system (subsubsection 3.2.1.3), air-charge and EGR coolers, throttle valves, heat transfer including gas-to-wall heat exchange and wall temperature prediction (subsubsection 3.2.1.2). The gas dynamics model is coupled to a cylinder model that predicts the in-cylinder conditions based on the combustion process (subsubsection 3.2.1.4). Detailed heat transfer model is used to obtain the heat rejection to the chamber walls (subsection 3.2.6) while mechanical losses model allows obtaining the brake power (subsection 3.2.8). An emission sub-model is coupled to the combustion process to predict raw NO_x, CO, HC, and soot emissions. As explained physical approach is used for NO_x while neural network approach have been used to predict CO, HC and soot (subsubsection 3.2.4.2). Different exhaust after-treatment systems, such as DOC, DPF and deNO_x systems (i.e. LNT or SCR) can be considered. The after-treatment sub-models combine thermo-and fluid-dynamic with chemical modelling in order to assess the tailpipe emissions (subsection 3.2.5). In addition, it is possible to link the heat transfer models with the hydraulic sub-model (subsection 3.2.7),

so a complete coolant and lubricant oil circuits can be modelled.

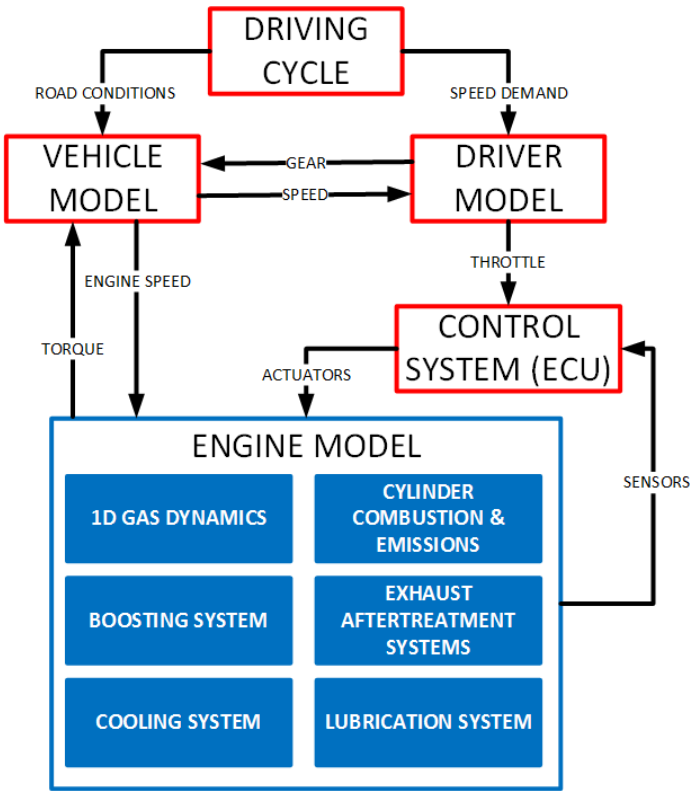

Figure 3.1: *Flow-chart of the virtual engine model (VEMOD) modules.*

Besides, in Figure 3.1 the red boxes concern the different control sub-models (subsection 3.2.9), which have been developed in Matlab/Simulink. They operate the engine model by actuating over the different actuators defined in the engine model. One is the control system model which emulates the electronic control unit (ECU) of the engine. And another one is the vehicle model, which manages the vehicle response and determines the engine speed as main input for the engine model. However, it is possible to operate the engine model without requiring the vehicle and driver sub-model, just using the virtual ECU sub-model to manage the operating point of the engine. Furthermore, it is even possible to leave aside any control system to run the engine model at a steady operating point. Different control elements have been developed and included in VEMOD, such as PIDs, triggers, switches, look-up tables, etc., so it will be possible to use VEMOD without the need of Matlab/Simulink.

VEMOD uses four different time scales to simulate the different engine processes. Gas dynamics and in-cylinder thermodynamics are calculated with a time-step which varies to ensure numerical stability and depending on the presence of an engine. For reference purposes, a time-step of 0.01 ms can be given. Injection, combustion and emissions formation may require even smaller time steps. In such case, the current time step of the gas-dynamics model is divided into smaller parts. Thermal evolution of the engine block and the liquids is solved once per cycle (and hence time-step depends on the engine speed). Control system and vehicle model are executed with a fixed time step of 20 ms.

3.2.1 Gas dynamics model

The thermo-and fluid dynamic model is the core of VEMOD and responsible of simulating the evolution of the gas in the different engine components such as, cylinders and engine pipes, reservoirs, turbocharger, heat exchangers or after-treatment systems, by means of specific sub-models that are linked with it. Figure 3.2 shows a brief summary of the sub-models that make up the engine model, their functions and how they interact with the different fluid circuits.

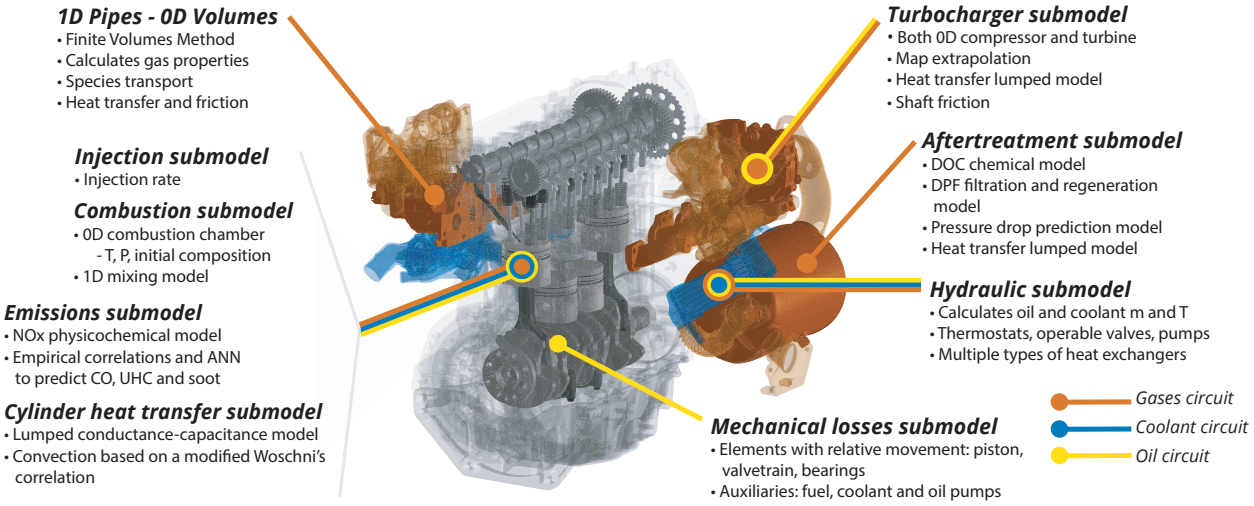

Figure 3.2: Representation of the real engine and the sub-models in VEMOD.

The engine is based on 1D ducts and 0D elements such as the cylinders or the gas coolers. The older two-step Lax-Wendroff scheme in finite differences [47] was replaced by a finite volume method (FVM) [48], leading to a better result in terms of mass, momentum and energy conservation. Thus, the 1D ducts gas dynamics can now by solved using a first order accurate Godunov-derived scheme reconstruction [49], using a second order accurate finite volume method based on the Lax-Wendroff method, or using a second order monotone upstream-centred scheme for conservation laws (MUSCL) [50] to improve the spatial accuracy during the integration. According to the flow characteristics in each duct it is possible to use one of these methods as a trade-off between precision and computational time. The linear extrapolation of the state vector —represented as **W** in Equation 3.2— to the cell boundaries is limited using a monotonised central slope limiter by van Leer, and the fluxes are computed using the Harten-Lax-van Leer-Contact approximate Riemann solver [51]. The numerical technique is extremely conservative so big mesh size can be used to reduce computation time.

All the relevant phenomena taking place along the duct are considered, this includes the wave interactions, which has an important effect on volumetric efficiency —especially in the intake/exhaust manifolds—, the species transport —since the thermodynamic properties of the gas depend on the composition and the temperature—, the heat transfer between the gas and the duct walls, so it is possible to obtain the wall temperatures or impose them, and the friction between gas and walls. Since the ducts are discretised in small cells, the conservation equations for mass, momentum and energy are solved at each cell at every time step. Figure 3.3 shows the discretisation of a 1D duct into these cells. The scalar properties are calculated in the center of each cell and the flux variables are computed at each cell interface. The Equation 3.1 shows the conservation equations system in its vector form for a given cell.

$$\frac{\delta \mathbf{W}_i}{\delta t} \cdot V_i + \left(- \mathbf{F}(\mathbf{W})_{i-1,i} \cdot A_{i-1,1} + \mathbf{F}(\mathbf{W})_{i,i+1} \cdot A_{i,i+1} \right) + \mathbf{C}_i \cdot V_i = 0 \qquad (3.1)$$

Where **W** is the state vector defined in Equation 3.2, **F(W)** is the flux vec-

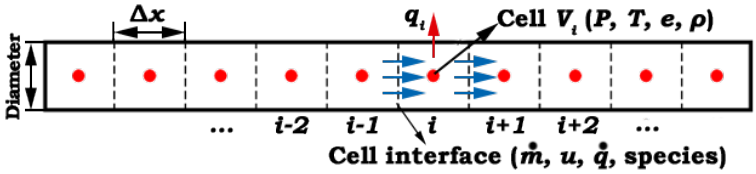

Figure 3.3: Discretisation of a 1D duct according to the Finite Volume Method.

tor defined in Equation 3.3, **C** is the source term defined in Equation 3.4 taking into account the fluid friction and heat transfer in the cell, $A_{i-1,1}$ refers to the boundary surface between cells i - 1 and i, $A_{i,i+1}$ refers to the boundary surface between cells i and i + 1 and V_i is the cell volume.

$$\mathbf{W} = \begin{pmatrix} \rho \\ \rho \cdot u \\ \rho \cdot e_t \end{pmatrix} \tag{3.2}$$

$$\mathbf{F(W)} = \begin{pmatrix} \rho \cdot u \\ (\rho \cdot u^2 + p) \\ \rho \cdot u \cdot h_0 \end{pmatrix} \tag{3.3}$$

$$\mathbf{C} = \begin{pmatrix} 0 \\ p \cdot (A_{i,i+1} - A_{i-1,1}) \\ 0 \end{pmatrix} + \begin{pmatrix} 0 \\ \rho \cdot G \\ -\rho q \end{pmatrix} \tag{3.4}$$

In the state vector expression (Equation 3.2), ρ is the fluid density, u is the flow speed and e_t is the specific total internal energy. In the flux vector Equation 3.3, p refers to the fluid pressure in the cell. And, finally, G and q in Equation 3.4 are the fluid friction in the cell —defined in Equation 3.5, where f is the wall friction factor and D is the duct diameter— and the heat transfer per unit mass, respectively. The specific heat transfer is defined in Equation 3.6, where A_i is the surface area of cell i and h_i is the heat transfer

coefficient between fluid and the pipe wall.

$$G = \frac{1}{2} \cdot u \cdot |u| \cdot f \cdot \frac{4}{D} \tag{3.5}$$

$$q = A_{\mathrm{i}} \cdot h_{\mathrm{i}} \cdot (T_{\mathrm{g}} - T_{\mathrm{w,\,int}})_{\mathrm{i}} \cdot \Delta t \tag{3.6}$$

It is known that the stability requirement for the calculation method limits the time step depending on the mesh size. Thus, the use of small ducts in some parts of the engine reduces the speed of the calculation. For a defined mesh size, the time step is restricted by the Courant-Friedrichs-Lewy (CFL) condition [52], whose mathematical expression is given by Equation 3.7:

$$\frac{\Delta t}{\Delta x} \cdot |u - a| < C \tag{3.7}$$

Where Δt is the timestep, Δx is the mesh size, u is the gas velocity, a is the in-pipe speed of sound and C is the Courant number (a value lower than 1 is required, so 0.8 has been used). It defines a stability condition of numerical methods for hyperbolic equations such as the Euler equations governing the 1D flow in pipes.

In 0D elements, where a predominant flow direction does not exists (like in the cylinders or heat exchangers), the thermodynamic properties are considered homogeneous, and only the mass and energy balances are performed every time step as indicated in Equation 3.8 and Equation 3.9, respectively, where the subscript n refers to the current timestep and $n - 1$ refers to the previous timestep. U refers to the internal energy in the 0D element, $\dot{m}_{\mathrm{i}}$ is the mass flow per each inlet and outlet boundary of the 0D element, W is the work involving the fluid, Q is the heat transferred and released and h_{i} is the fluid enthalpy per each inlet and outlet boundary of the 0D element. Work, heat transferred and heat released depend on the 0D element and a specific model is required for each case, for example, a

cylinder model or a cooler model.

$$m_{n} = m_{n-1} + \sum_{i=1}^{inputs} \dot{m}_{i} \cdot \Delta t \tag{3.8}$$

$$U_{n} = U_{n-1} - W - Q_{transferred} - Q_{released} + \sum_{i=1}^{inputs} \dot{m}_{i} \cdot h_{i} \cdot \Delta t \tag{3.9}$$

The air path of the tested engine has been implemented by means of pipes and volumes. The diagram of this engine in VEMOD is indicated in Figure 3.4, where the main engine systems have been labelled. A brief summary of the 1D and 0D element that make up the gas dynamics model is featured below:

- Pipes length and diameter are set according to the real values of the engine pipes. In order to reduce computational time, mesh sizes along the engine are generally 30 mm, as fine meshes in specific elements increase the calculation time. In pipes longer than 1 m, mesh size is 200 mm to avoid further discretisation when it is not required.
- The model contains 19 volumes: 4 represent the cylinders. The turbocharger is defined by two 0D volumes (compressor and turbine). The different gas heat exchangers are presented by 3 different volumes: intercooler, low pressure EGR (LP-EGR) cooler and high pressure EGR (HP-EGR) cooler. One volume represents the intake manifold, and another one volume represents the exhaust manifold. The after-treatment system is comprised by 2 volumes representing the diesel oxidation catalyst (DOC) inlet and outlet boundaries and 2 other volumes for the diesel particulate filter (DPF) boundaries. The four volumes left have been implemented for pipe joints.

3.2.1.1 Boundary conditions

The different possible connections between elements have been implemented according to different boundary conditions to compute the energy,

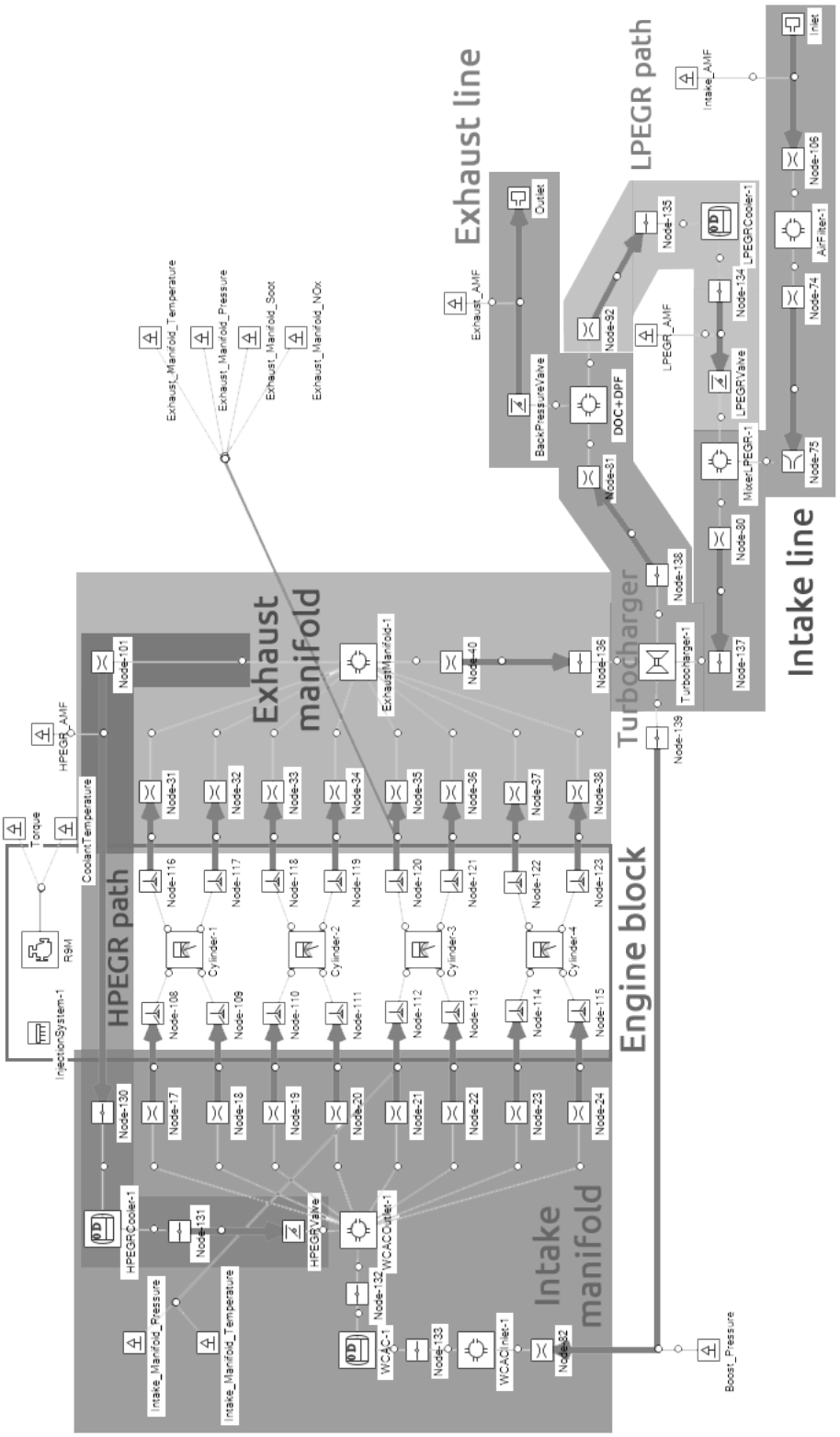

Figure 3.4: Gases circuit diagram in VEMOD.

mass and momentum fluxes (flux henceforth) between cells. Thus, for example, a valve is represented as a discharge coefficient between two elements. In 1D-0D connections, to calculate the flux at the last cell interface, a virtual pipe is considered. It consist of the last cell connected from the pipe and another one with the properties of the 0D element (pressure, temperature and chemical composition). 1D-1D connections are also computed by means of virtual pipes consisting of the cells that are directly connected. This connection can be used to join ducts with different diameters and different external cooling properties or flow restrictions. Multiple 1D-1D connections, like the one shown in Figure 3.5, require an auxiliary 0D element connected in the intersection of the multiple ducts in order to obtain the flux at their outmost cells interfaces.

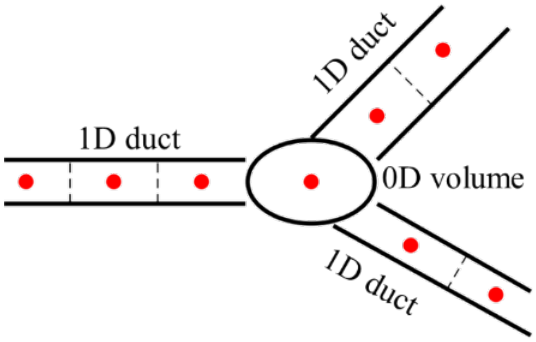

Figure 3.5: Multiple 1D-1D connection boundary.

3.2.1.2 Heat transfer at pipes

Heat transfer is a key issue during the simulation of the cold engine start conditions. The gas dynamics model calculates the internal heat transfer from the gas to the wall in each cell of the pipe at every time step according to Equation 3.6. The gas temperature is calculated every timestep, while the internal wall temperature $T_{w,in}$ is updated by means of a simple conductance-capacitance model every engine cycle, taking into account the external heat transfer and the wall thermal inertia.

The internal heat transfer coefficients (h) at each cell are calculated using different correlations depending on the pipe type. Thus, under this ap-

proach, pipes are divided into intake or exhaust pipes, and intake or exhaust ports. In these cases, the correlations used are based on the studies by Depcik et al. [53], Santos [54] and Reyes [40]. In a similar way, the external heat transfer coefficient is calculated depending on the pipe type and whether it is cooled by air or by water using the correlations presented by Churchill et al [55] and Dolz [56]. The velocity of the vehicle can also be considered for calculating the external heat transfer.

3.2.1.3 Turbocharger sub-model

The turbocharger presented in this engine model is based on zero-dimensional compressor and turbine sub-models. They use data provided by the supplier maps for both turbine and and compressor to compute the flow and the turbomachine efficiencies at any operating point within the maps [57, 58, 59]. Besides, the model is able to extrapolate outside these maps so it is possible to simulate off-design conditions [57, 60].

The extrapolation of the compressor includes two procedures, one for the compression ratio and another one for the compressor efficiency. The procedure for the compression ratio [58] uses different mathematical approaches depending on the zone of the map (low pressure ratio zone, low speed zone and high speed zone). This compression ratio extrapolation model uses a generalised ellipse fitting approach developed by Leufvén [61] for the low pressure ratio and high speed extrapolation. Additionally, for the low speed region, a model proposed by Martin et al. [62] is used, which is in turn a modification of the method of Jensen et al. [63]. It consists in keeping the coefficients of the Jensen's equation, tuned for the lowest measured speed line, for lower extrapolated speeds lines. For the compressor adiabatic efficiency [59], a zonal approach was considered in order to adapt to different phenomena found beyond the usual compressor working conditions. Special attention was taken in the low speed extrapolation conditions, since it is the most critical zone because the compressor usually operates in this region at low engine loads.

The extrapolation of the turbine considers a procedure to obtain the reduced mass flow and the adiabatic efficiency [57]. The method uses thirteen

calibration coefficients which are fitted using a limited set of available turbine map data. Seven coefficients are fitted independently for the reduced mass flow and six for the efficiency. The reduced mass flow calibration coefficients must be fitted in the first place since one of them, the quotient between the rotor and the stator discharge coefficients, is used in the efficiency model equation. The reduced mass flow and the efficiency variables are interrelated since the reduced mass flow appears in the efficiency equation and the efficiency appears in the mass flow equation. As both variables appear implicitly, after fitting the calibration coefficients, a system with the reduced mass flow and the efficiency equations must be solved, using an iterative procedure, for extrapolation purposes.

The extrapolation procedure used in compressor and turbine requires the adiabatic efficiency. If the supplier maps were measured in non-adiabatic conditions, the model is able to remove the effect of heat on the efficiency by means of the heat transfer model. However, if this conditions are unknown, the model is also able to remove this effect by assuming typical values for this calculation. The heat transfer model is not only used for the adiabatisation process, but to predict heat fluxes in the turbocharger and thereby their effect on engine performance when simulating different operating points in a complete forced induction engine. The heat transfer between the gas and the turbocharger, the heat transfer between the turbocharger housing and oil —or coolant if it exists— and with the ambient are calculated by a 1D lumped model [64] whose diagram is shown in Figure 3.6. The 1D lumped model comprehends 5 internal nodes, representing the turbine housing (T), the compressor housing (C) and 3 different metal nodes for the central components (H_1, H_2 and H_3). The model is completed with two external nodes representing the exhaust gas and the air. The 3 metal nodes are set between the turbine and the compressor to obtain a more precise temperature field in this high temperature gradient section. All this metal nodes are connected by means of conductive conductances. The convective heat between the walls and the different fluids are calculated by empirical correlations based in dimensionless numbers and fitted for several turbochargers. External heat transfer considers both convection and radiation [65].

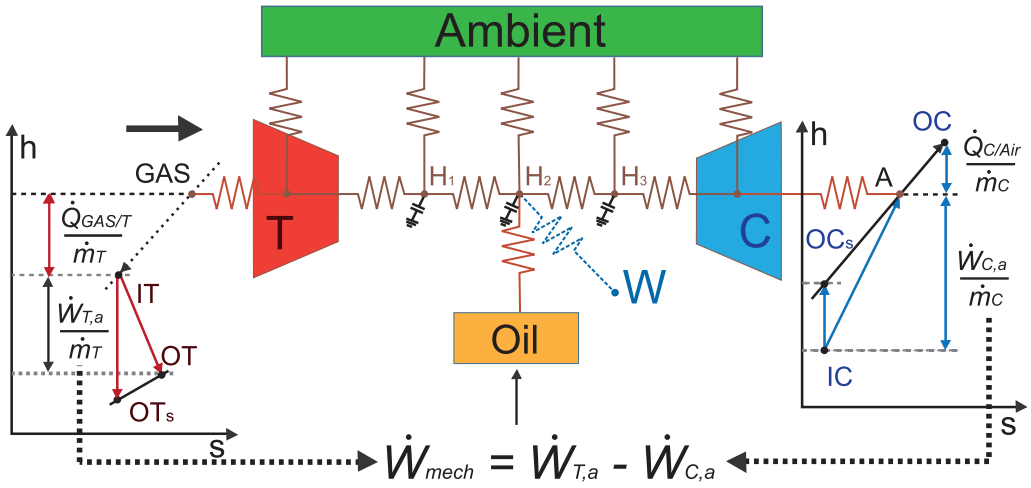

Figure 3.6: Scheme of the turbocharger lumped heat transfer model.

The mechanical losses in the turbocharger shaft are also considered by modelling the shaft bearings friction, since it is linked to the heat transfer model and the friction losses in the shaft are turned into heat transferred to the lubricating oil. The turbocharger mechanical losses model [66] is based on the Navier-Stokes equations applied to the two kinds of bearings (journal and thrust) normally used on this type of element. Making some assumptions, a simplified model for the two bearings has been obtained. The model takes into account the working point (turbocharger speed, oil temperature and axial force) and the geometrical characteristics of the bearings.

3.2.1.4 In-cylinder conditions model

The thermodynamic calculation of in-cylinder conditions is carried out by means of a 0D model whose main hypotheses are the following:

1. Chamber pressure is assumed to be uniform. This is normally assumed in diesel combustion because both fluid and flame velocities are smaller than the speed of sound [67].
2. Five chemical species are considered: N_2, O_2, H_2O, CO_2 and fuel

vapour. Pollutant species are taken into account for emission purposes but in order to accelerate the calculation they are neglected for the calculation of the thermodynamic properties of the mixture.

3. Perfect gas behaviour is assumed. As Lapuerta et al. [68] showed, the error committed with this assumption is negligible.

4. Specific heats depend on the temperature and gas composition. This hypothesis is consistent with the two previous ones.

5. Internal energy is calculated assuming mean uniform temperature in the chamber. This is the hardest hypothesis. It may be an important issue at the beginning of the combustion. However, the error diminishes as the combustion progresses because dilution and heat transfer tend to uniform the temperature.

6. Heat transfer to the chamber walls is considered as later described. The fraction of the fuel energy lost by heat transfer to the chamber walls depends on the engine size (the larger the engine, the more adiabatic it is) and the operating conditions (the higher the load and the engine speed, the more adiabatic it is). For a high speed direct injection (DI) diesel engine typical values range from 10 % at full load and 4000 rpm to 30 % at low load and 1000 rpm. Therefore, consideration of heat transfer — depending on operating conditions — is necessary in order to obtain accurate predictions of indicated parameters or the thermodynamic state of the charge [69]. During cold engine start, glow plug heat power is accounted for the in-cylinder energy balance.

7. Blow-by leakage is considered by means of the model described in the next subsection. The blow-by mass flow is a good indicator of the integrity of the piston rings and lubricant. In normal operating conditions, the blow-by mass flow is not critical (see subsubsection 3.2.1.5), however, in small DI diesel engines at low engine speeds, blow-by mass rates can achieve 4-5 % of the trapped air; moreover, during the cold start, it is usual to have more than 20 % [70, 71]. Thus, it is necessary to consider it in the mass and the energy balances.

8. Fuel injection is considered since it is an important issue for both the mass and the energy balances. It has been checked at CMT that the

error in the energy balance can reach 7 % in the case of rich fuel–air equivalence ratio.

9. Engine deformation is considered. Usually, in-cylinder 0D models do not consider engine deformations in the instantaneous volume calculation. However, deformations in diesel engines —where pressure can easily reach 150 bar at the top dead centre— can be higher than 2 % at this point. Thus, a simple deformation model will be used to estimate the real in-cylinder volume [72].

3.2.1.5 Blow-by model

The accurate determination of the instantaneous blow-by presents several challenges regarding the rings assembly dynamics, the rings deformation, the gas thermal and fluid dynamic when the flow passes through the crevices, etc. In this section, the blow-by model implemented in VEMOD is briefly described. The model allows the calculation of the instantaneous flow through each ring gap and so it provides the gas leakage from the chamber and the boundary condition for the friction model. Detailed description of the model can be found in [73].

Firstly, some simplifications and hypotheses have to be made regarding the piston-rings assembly and blow-by phenomena:

1. No rings relative motion nor deformation is taken into account. The rings are assumed to be rigid bodies always in contact with the bottom face of the groove. Accordingly, the volumes between rings and grooves, and between adjacent rings are constant.
2. It is assumed that all the gas leakage occurs only through the rings gaps, which are modelled as nozzles. This is consistent with the previous hypothesis, since the bottom ring face is always in contact with the groove and hence no gas leakage through them can occur.
3. The flow through the gaps is modelled as an adiabatic (due to the low time for heat exchange assumed) and reversible flow (isentropic nozzle).

4. Volumes between rings are assumed to be isothermal systems and the gas temperature is assumed to be the mean temperature between the piston and liner walls. This can be justified by the high heat transfer rate due to the high area/volume ratio. This assumption is supported by the work of Furuhama and Tada [74], who experimentally determined the gas and wall temperatures, observing very similar values between them.

In Figure 3.7 the simplified scheme of the piston pack geometry is presented. The model is composed of 4 volumes and 3 nozzles: the first volume (V_1) corresponds to the combustion chamber and the crevice between the chamber and the compression ring, the second volume (V_2) is the clearance between the compression and wiper rings, the third volume (V_3) is the clearance between the wiper and the oil rings and the fourth volume (V_4) is the clearance between the oil ring, the piston skirt and the crank case. As explained, each gap between rings is represented by a nozzle ($A_{\text{gap},1}$, $A_{\text{gap},2}$ and $A_{\text{gap},3}$).

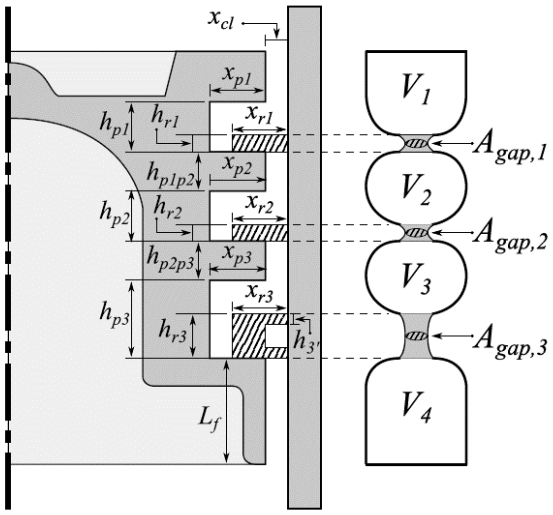

Figure 3.7: *Scheme of the blow-by model.*

As stated above, the gas in the volumes is assumed to be isothermal, thus the continuity equation for each volume can be expressed as in Equa-

tion 3.10.

$$\frac{\mathrm{d}p_{\mathrm{i}}}{\mathrm{d}t} = \frac{R \cdot T_{\mathrm{i}}}{V_{\mathrm{i}}} \cdot (\dot{m}_{\mathrm{i,in}} - \dot{m}_{\mathrm{i,out}}) \tag{3.10}$$

where for each i volume, R is the gas constant, T_{i} is the gas temperature, V_{i} is the volume and $\dot{m}_{\mathrm{i,in}}$ and $\dot{m}_{\mathrm{i,out}}$ are the instantaneous mass flow rates entering and exiting the volume, respectively. The mass flow through the ring gap is calculated by means of the isentropic nozzle model according to Equation 3.12.

$$\dot{m}_{\mathrm{i,j}} = C_{\mathrm{bb}} \cdot A_{\mathrm{gap,i}} \cdot p_{\mathrm{in}} \cdot \sqrt{\frac{x_{\mathrm{i}}}{R \cdot T_{\mathrm{in}}}} \tag{3.11}$$

where j corresponds to the downstream volume, C_{bb} is the apparent discharge coefficient to be experimentally adjusted by means of mean flow measurements, $A_{\mathrm{gap,i}}$ is the gap area of the ring, p_{in} is the inlet pressure, T_{in} is the inlet (upstream) temperature and x_{i} is calculated according to:

$$x_{\mathrm{i}} = \frac{2 \cdot \gamma}{\gamma - 1} \cdot \left[\left(\frac{p_{\mathrm{out}}}{p_{\mathrm{in}}} \right)^{\frac{2}{\gamma}} - \left(\frac{p_{\mathrm{out}}}{p_{\mathrm{in}}} \right)^{\frac{\gamma+1}{\gamma}} \right] \tag{3.12}$$

being p_{out} the outlet (downstream) pressure and γ the adiabatic index. Figure 3.8 and Figure 3.9 show the blow-by mass flow and the pressure in the ring grooves obtained with the model in a couple of operating conditions in a 1.6 litres diesel engine. As shown in the detail (upper corner of Figure 3.8), the model is able to detect the blow-back phenomena, which corresponds to the zones with negative blow-by mass flow between 90° and 300° CA.

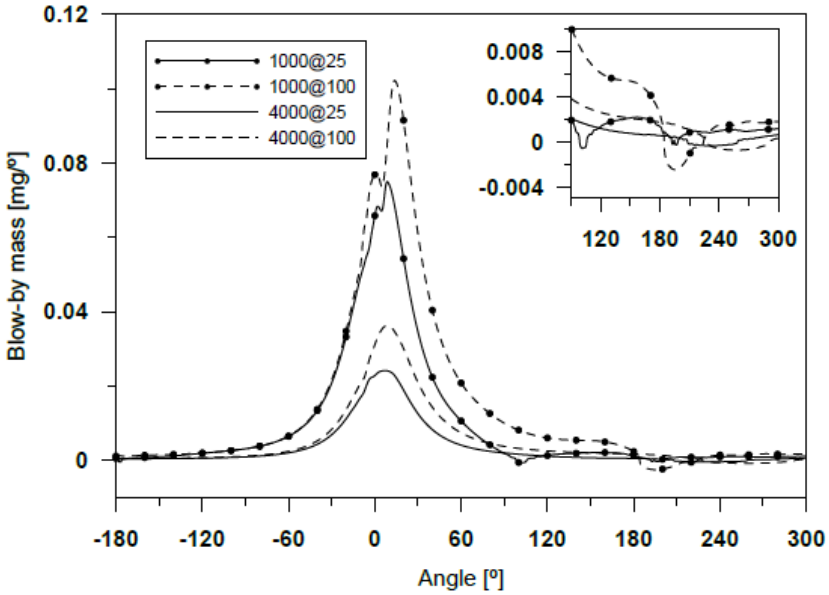

Figure 3.8: Blow-by mass flow.

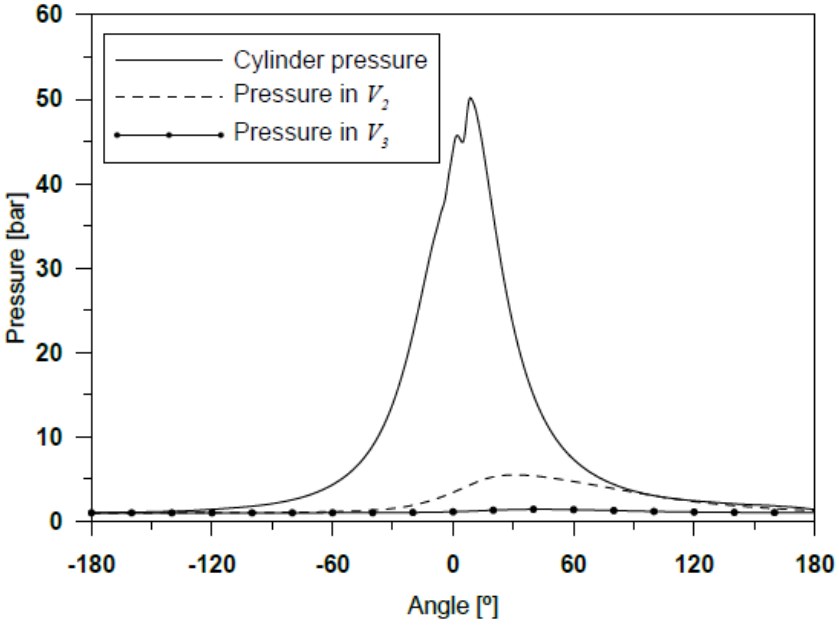

Figure 3.9: Pressure in the ring grooves.

3.2.1.6 Water condensation model

During the engine operation in cold conditions at −7 °C, condensation of the water vapour produced in the combustion process may occur at different points, especially at the EGR cooler outlet and downstream of the joint where the EGR (hot and with high water vapour content) and the fresh air (colder and with low water content) are mixed. In order to consider this phenomenon, a condensation model has been included in VEMOD to determine the locations where gas condensation may occur and to estimate the maximum quantity of water liquid condensed due to the psychrometric conditions in the gas, since no wall condensation is modelled. As a first approach, neither liquid transport nor re-evaporation is considered and the condensation is assumed to take place instantaneously, so no progressive mixing effect is considered. In order to reduce computation time the condensation is only tracked in the elements selected by the user; thus, condensation sensors can be connected to a pipe, downstream a heat exchanger (e.g., the EGR cooler) or downstream a pipe junction, like the joint of the low pressure EGR (LP-EGR) path and the intake pipe upstream the compressor. Figure 3.10 shows a scheme of the variables involved in the model.

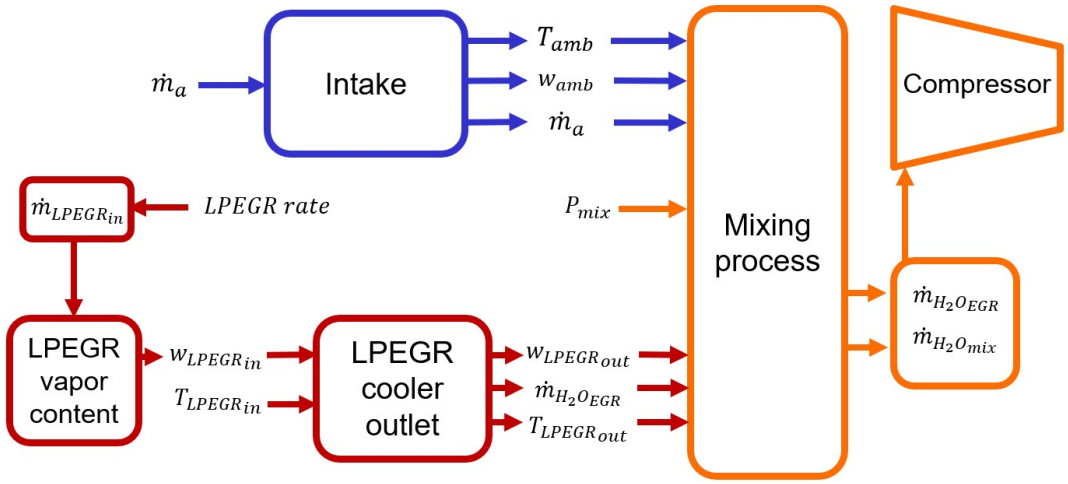

Figure 3.10: *Scheme of the variables involved in the water liquid condensation model.*

As shown in Figure 3.10, the simple model tracks the mass flows of air and LP-EGR, their local temperatures and water vapour mass fraction to

determine where and how much water is condensed. As an example of the sub-model performance, a simple application has been carried out estimating the condensed liquid water at the LP-EGR cooler outlet for different cases in which the engine fuel-air equivalence ratio (ϕ) and the LP-EGR cooler outlet temperature have been modified progressively as shown in Figure 3.11.

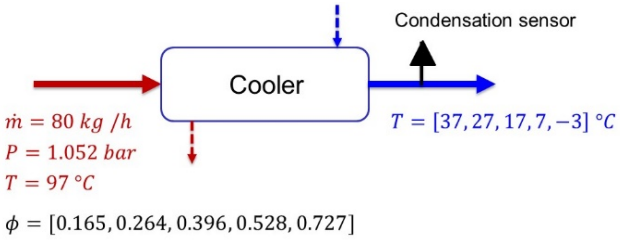

Figure 3.11: *Boundary conditions of the water condensation model test.*

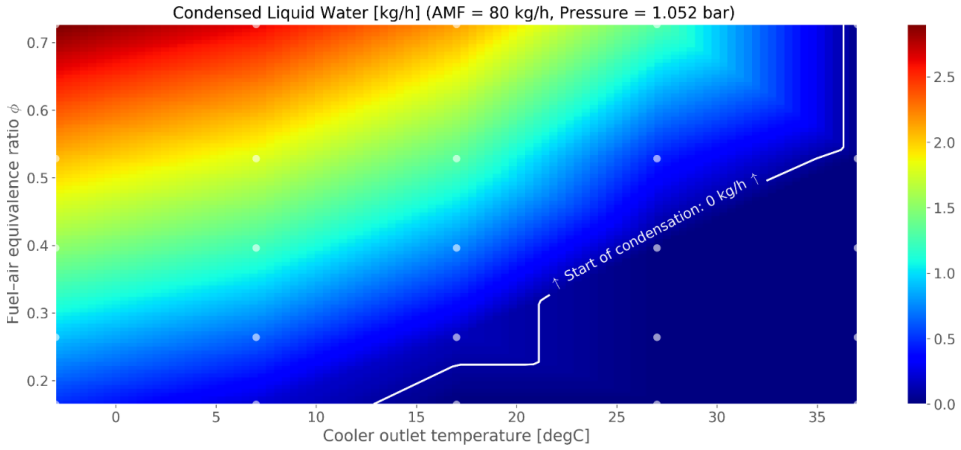

Figure 3.12: *Liquid water condensed depending on the LP-EGR cooler outlet temperature and the fuel-air equivalence ratio.*

During the simulation, LP-EGR inlet pressure, temperature and air mass flow remained constant. Figure 3.12 shows the resulting liquid water condensed for the fuel-air equivalence ratio and the cooler outlet temperature considered. As it can be seen, the simple model is able to determine that the higher the fuel-air ratio is, the higher the condensed water produced at saturation conditions and, the lower the outlet temperature, the greater the amount of water vapour that condenses into liquid water.

3.2.2 Injection rate model

The main input for the combustion sub-model described in subsection 3.2.3 is the injection rate. It is simulated by means of a semi-empirical model in which, starting from the injection settings —start of energisation time (SOE) and injected mass in each injection event— provided by the virtual ECU (later described), the injection rate is obtained. For each injection event the instantaneous injection rate is calculated assuming a simple shape composed of two or three straight lines (depending on whether the maximum needle lift is reached or not) representing the initial and final opening and closing transient processes, respectively, and a horizontal part representing the stationary maximum rate (if the complete needle opening is reached).

As shown in Figure 3.13, the model is based in four injector characteristics that are empirically obtained: the injector opening (A) and closing (C) times at maximum injection pressure (to reach maximum needle lift during the transient processes at the beginning and end of the injection event), the maximum injection rate (B) when the maximum needle lift is achieved, and finally, the hydraulic lag between the SOE and the start of the injection process (D). The values of these four parameters are calculated according to the expressions in Equations 3.13, 3.14, 3.15 and 3.16:

$$A = t_A \cdot \left[1 + A_0 \cdot \exp\left(-\frac{p_{inj}}{A_1}\right)\right] \tag{3.13}$$

$$B = B_0 + B_1 \cdot \sqrt{p_{inj} - p_{back}} \tag{3.14}$$

$$C = t_C \cdot \left[1 + C_0 \cdot \exp\left(-\frac{p_{inj}}{C_1}\right)\right] \tag{3.15}$$

$$D = D_0 + D_1 \cdot p_{inj} \tag{3.16}$$

Where p_{inj} is the injection pressure, p_{back} is the back pressure and t_A, A_0,

A_1, B_0, B_1, t_C, C_0, C_1, D_0 and D_1 are fitting constants to be fitted through an experimental injector characterisation campaign, as detailed below. It is worth to remark that the maximum injection rate, experimentally characterised as described, allows taking into account implicitly the dependency of the nozzle discharge coefficient with the injection pressure.

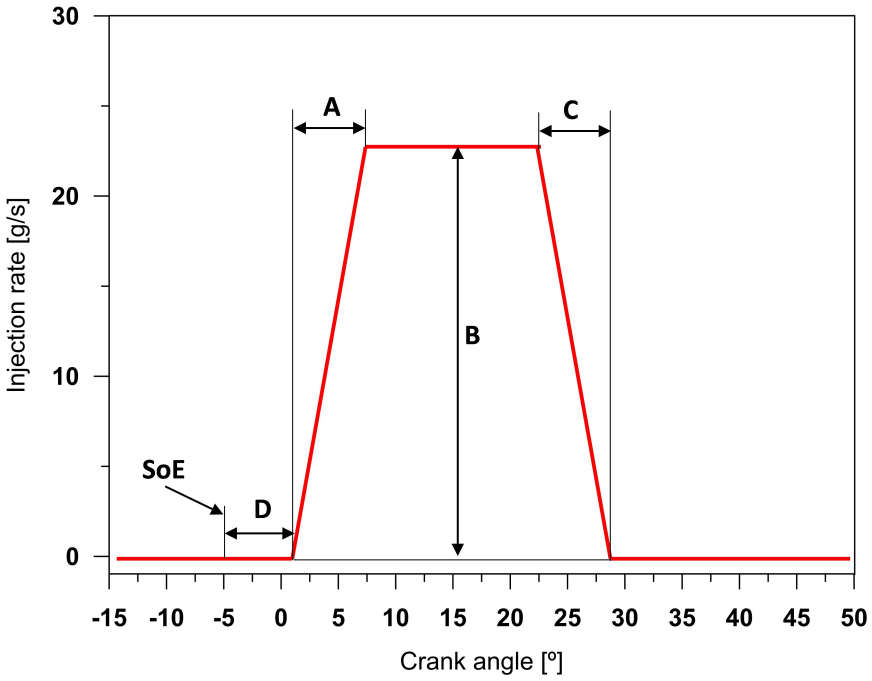

Figure 3.13: *Simulated injection rate.*

The injection rate model takes into account that for small injections (pilot and post injections) the stationary horizontal part of the injection will not be reached if the time for the complete needle opening is larger than the requirement for the injected mass of the event.

Calibration of the injection rate model

The calibration of the injection rate model was carried following the methodology detailed in [75]. For that, the injector (with 7 holes of 125 microns) was tested in the injector test rig under an experimental campaign where different rail pressures (from 400 to 1600 bar) and energisation times (ET) from 0.5 to 4 ms where tested. t_A, A_0, A_1, B_0, B_1, t_C, C_0, C_1, D_0 and D_1 where fitted in order to minimise the differences between the

simulated injection rates and the experimental injection rate. In the case of the injector opening time (Equation 3.13), the values obtained are:

- $t_A = 0.3\ ms$
- $A_0 = 2.5299$
- $A_1 = 453.3938\ bar$

And the result after the fitting process is shown in Figure 3.14.

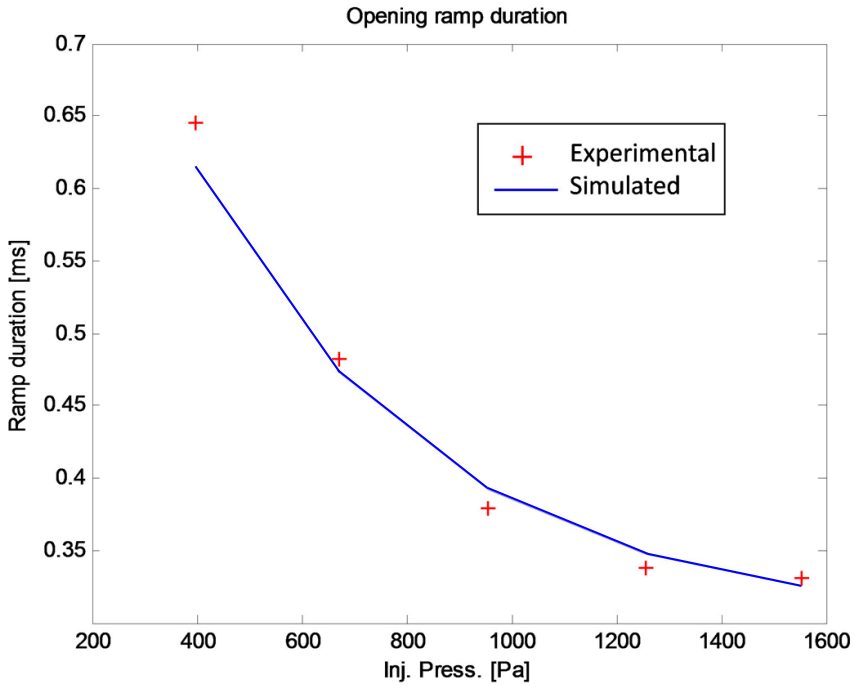

Figure 3.14: Injector opening time (A)

For the maximum injection rate (Equation 3.14) when the maximum needle lift is achieved, the values obtained (for $p_{back} = 50\ bar$) are:

- $B_0 = -1.8508e{-}3$
- $B_1 = 3.1851e{-}6$

And the result after the fitting process is shown in Figure 3.15.

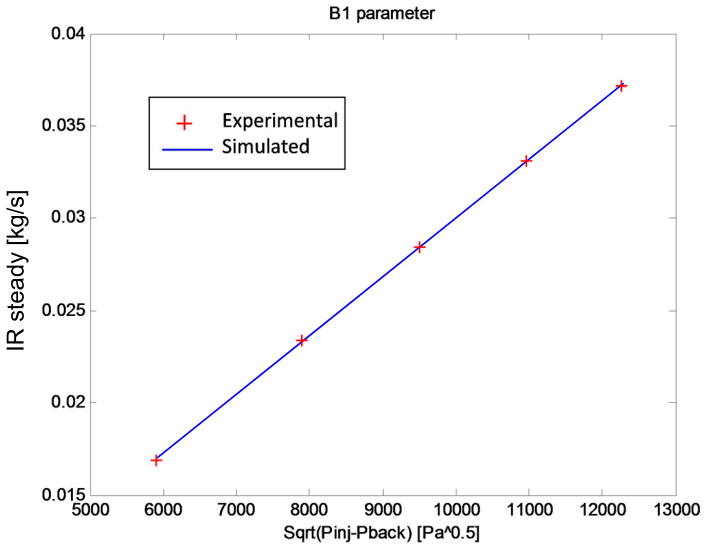

Figure 3.15: *Maximum injection rate (B)*

In the case of the injector closing time (Equation 3.15) the values obtained are:

- $t_C = 0.2\ ms$
- $C_0 = 2.0306$
- $C_1 = 538.2405\ bar$

Which results in the closing ramp fitting shown in Figure 3.16.

Finally, the values of the hydraulic lag between the SOE and the start of the injection (SOI) process (Equation 3.16) are:

- $D_0 = 0.2653\ ms$
- $D_1 = 5.7379\text{e}{-5}\ ms/bar$

The fitting results can be observed in Figure 3.17.

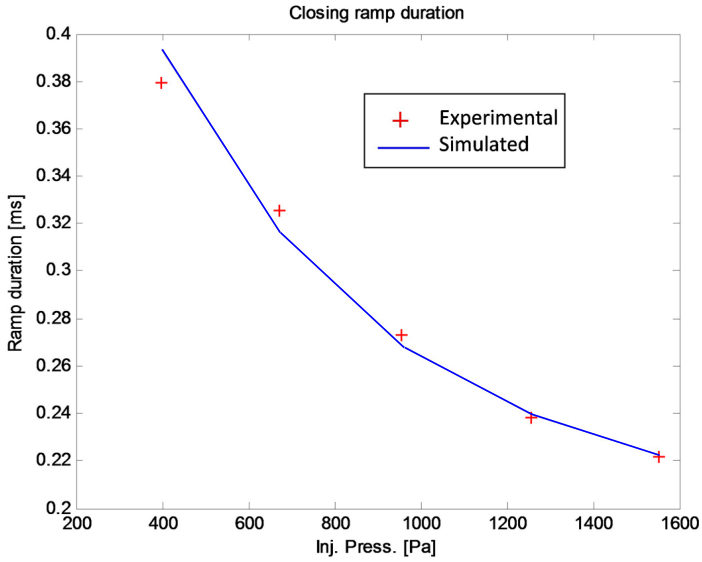

Figure 3.16: Injector closing time (C)

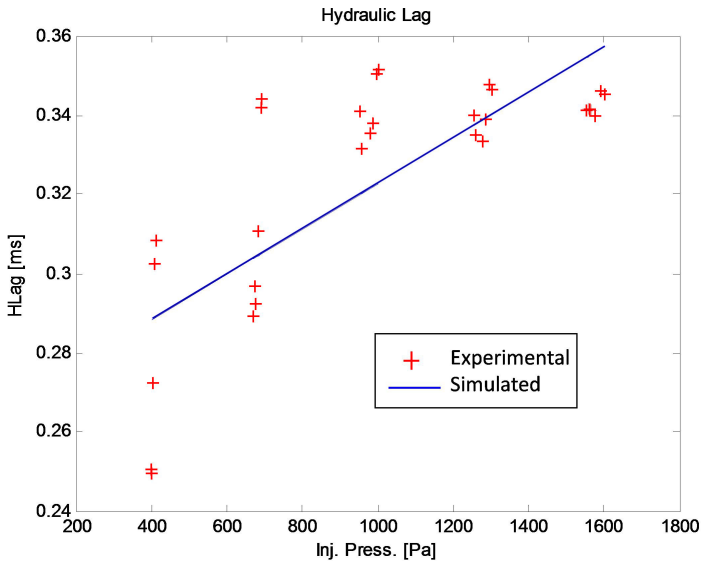

Figure 3.17: Hydraulic lag (D)

In this case, the fitting is not as good as in the case of A, B and C parameters, but also its variation is much smaller, so it was assumed that the fitting was suitable. This is also confirmed by the simulation shown below.

Once the model constant were calibrated, the following results are ob-

tained for an ET swept (0.35 to 2 ms) at 1600 bar of rail pressure (Figure 3.18) and a rail pressure swept (400 to 1600 bar) at ET=2 ms (Figure 3.19). As can be seen, the agreement between modelled and simulated injection rates is very good.

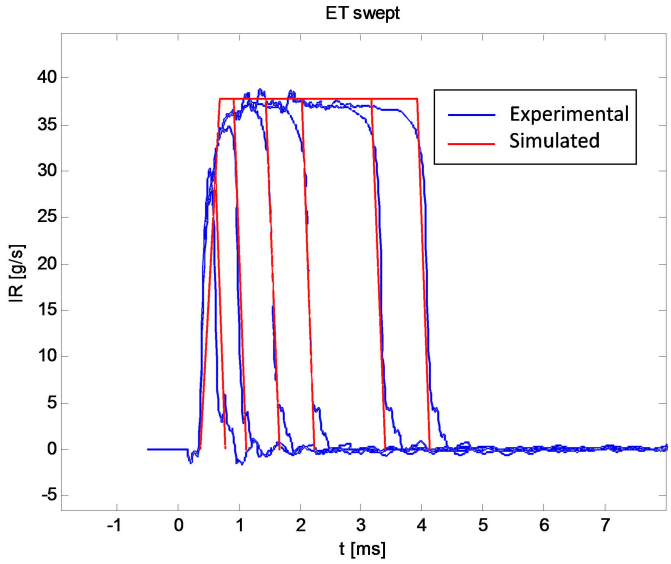

Figure 3.18: *Injection rates for an ET swept at p_{inj} = 1600 bar*

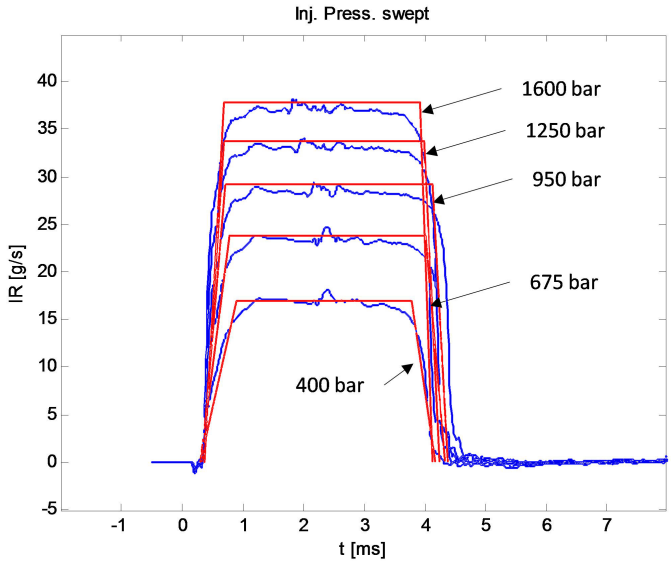

Figure 3.19: *Injection rates for a p_{inj} swept (400 to 1600 bar) at ET = 2 ms.*

3.2.3 Combustion model

Diesel combustion simulation can be classified in three categories: zero-dimensional single-zone models, quasi-dimensional or multi-zone models and multidimensional models.

Zero-dimensional single-zone models assume that the cylinder charge is uniform in both composition and temperature, at any time during the engine cycle. A key point of these calculation methods is the prediction of the effect of the different engine set-up parameters on the rate of heat release (ROHR). Some work about the analysis and prediction of the combustion laws is based on the description of the ROHR shape with a mathematical function without any relationship with the physics of the injection-combustion process [76]. Other zero-dimensional models used in the analysis and prediction of combustion laws are based on a simplified description of the physical phenomena that control the combustion process. In this last group appears the approach of Chmela et al. [77], describing the mixing-control combustion as a function of the kinetic energy of the injection. In the same way, Arrègle et al. [78, 79] developed the original version of the model in which is based the current model implemented in VEMOD: based on the parameter called as *apparent combustion time* (ACT), it identifies and quantifies the main physical variables that directly affect the air/fuel mixing process. It has been shown that suitably calibrated and validated zero-dimensional models are capable of predicting engine performance and fuel economy accurately and with a high computational efficiency. However, in general, the zero-dimensional models cannot be used to account for fuel spray evolution and spatial variation of mixture composition and temperature, which are essential to predict exhaust emissions.

On the other hand, multidimensional CFD models, like KIVA [80, 81], divide the space of the cylinder into a fine grid thus providing a high amount of spatial information. To this group belongs the model of Reitz et al. [82, 83, 84]. They propose an integrated numerical model based on KIVA code with improvements of turbulence, spray, ignition and combustion models. However in general, phenomenological sub-models of CFD code, describing fuel spray processes included in these models, present results that

may vary according to the assumed initial or boundary conditions. Consequently, the accuracy of the results cannot be always guaranteed. Furthermore, computational time and storage constrains still limit the use of such codes for design purposes.

As an intermediate step quasi-dimensional or 1D multi-zone models can be effectively used. They solve mass, energy and species equations. These models can provide the spatial information required to predict emission products and require significantly less computing resources compared to multi-dimensional models. This is the case of the 1D combustion model in VEMOD, based on the concept of ACT. Its aim is provide VEMOD with the capacity of predicting the heat release rate (HRR) and emissions through the calculation of local conditions in the combustion chamber.

As indicated above, the model implemented in VEMOD is an upgraded version of a combustion model developed at CMT [85] that has been improving progressively. In its actual state, the combustion model is composed of three main sub-models: ignition delay, premix combustion and diffusion combustion models; along with a 1D model describing the mixing process.

The approach for the mixing process, key issue for both the heat release and emissions predictions, is a physical model [85] based on the turbulent gas jet theory [86]. Even though it is not able to predict in detail the 3D spray behaviour, the model allows evaluating the local conditions through the mixing model. It uses a double discretisation:

1. First, the combustion chamber is divided into two volumes corresponding to bowl and dead volume. On the one hand, the bowl and dead volume have the same thermodynamic conditions (in fact their pressure and temperature are obtained by means of single zone 0D thermodynamic assumptions), but their composition is different once the combustion process has started. It is assumed that only the oxygen content of the bowl is available for the combustion process, and that the combustion products modify only the composition in the bowl. Later on, the composition of both regions is updated taking into account the mass exchange between them, which is governed by the evo-

lution of the % of volume useful for combustion (this % of volume is the k-factor of the combustion chamber at TDC, and varies with the piston position).

2. Furthermore, the spray is divided into a certain number of fuel elements. The composition and temperature of each fuel parcel is updated through the mass and energy balances taking into account the instantaneous entrained mass conditions and composition. Thus, each injected fuel parcel mixes with the entrained gases (whose composition and temperature correspond to the instantaneous chamber conditions) and, due to the combustion and the pollutant formation processes, the fuel parcel species suffer chemical transformations and its composition changes. The temperature of each parcel is calculated by means of its energy balance, considering the enthalpy flow of the entrained gas and assuming that products formed at each parcel reach the adiabatic temperature (it is calculated assuming n-heptane combustion starting from the temperature of the unburned mixture at the calculation step). Finally, the combustion products and pollutants formed during each calculation step in all the parcels change the mean bowl composition, thus affecting the gas properties, and the total heat release will be an input for the energy balance of the 0D chamber model.

The ignition delay (ID) model is based on a simplification and parameterisation of a complete n-heptane chemical kinetics description [87]. From this information, the ID_i (i stands for the parcel) can be calculated as a function of the local instantaneous conditions of each element. For that, the shell model, which tracks the Livengood-Wu integral [88] is used, hence the ignition of the parcel occurs when the condition of Equation 3.17 is met:

$$\int_{t=\mathrm{POI}}^{t} K_{ID1} \cdot p^{K_{ID2}} \cdot \frac{1}{ID_i} = 1 \tag{3.17}$$

where p is the in-cylinder pressure, POI is the point of injection of the parcel i and K_{ID1} and K_{ID2} are constants of the ignition model that have to

be adjusted. The model assumes that the active radicals leading to autoignition are cumulated up to reaching a critical concentration. Once this critical concentration is reached, autoignition takes place. The model takes into account the effects of the thermodynamic conditions (pressure and temperature) and the local composition (exhaust gas recirculation (EGR) and fuel-air ratio) of the parcel i, as shown in Figure 3.20. The start of combustion (SOC) is determined for the first element that reaches the autoignition conditions.

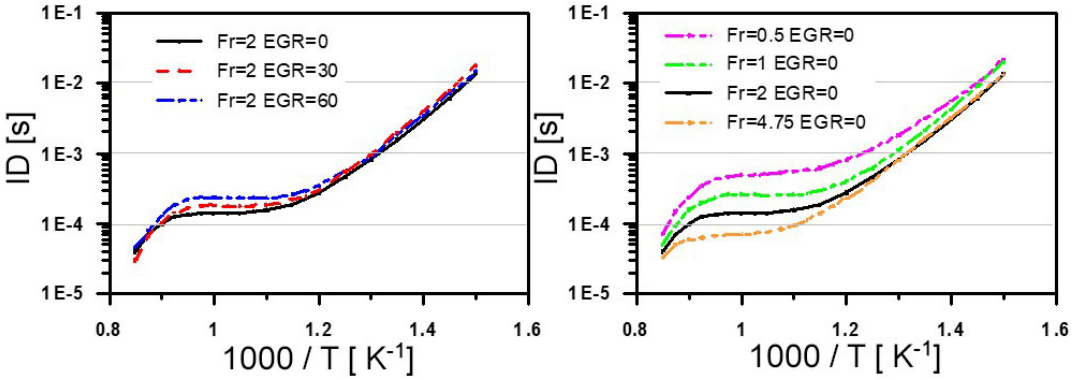

Figure 3.20: Effect of the fuel-air equivalence ratio (left) and EGR (right) on the ignition delay.

Due to the complexity of the local phenomena occurring close to the glow plug during cold start —which happens at the beginning of the WLTP cycle starting at cold conditions—, glow plug effect have been taken into account limiting the ignition delay time.

The premixed combustion model is an empirical model that determines that the premix combustion of an element i occurs when the condition in Equation 3.18 is met:

$$\int_{SOC}^{t_{burn}} K_{pmx1} \cdot Y_{O_{2,cyl}}^{0.955} \cdot \frac{Fr_i}{\exp(Fr_i - 1)} \cdot \exp\left(\frac{-K_{pmx2}}{T_{cyl}}\right) \cdot n^{K_{pmx3}} \cdot p_{inj}^{K_{pmx4}} \cdot \rho_{cyl}^{K_{pmx5}} \cdot dt = 1 \quad (3.18)$$

Where $Y_{O_{2,cyl}}$ is the bowl oxygen mass fraction, ρ_{cyl} is the air density in the bowl, Fr is the element relative fuel-air equivalence ratio, T_{cyl} is the bowl temperature, n is the engine speed, p_{inj} is the injection pressure and

K_{pmx1}, K_{pmx2}, K_{pmx3}, K_{pmx4} and K_{pmx5} are the premix burned mass model constants. This empirical expression is related to the propagation velocity of the premixed flame around the auto ignition point.

If the oxygen/fuel ratio is higher than the stoichiometric value it results in a poor premix situation and the entire fuel element mass is burned. In this situation, the bowl composition is updated with the combustion products resulting from this combustion. If the oxygen/fuel ratio is lower than the stoichiometric value, then it results in a rich premix situation. The fuel mass element gets burned in two stages: a rich premix combustion where the oxygen mass in the element determines the fuel mass that is burned (and the rest of the fuel mass remains unburned) and the diffusion combustion where the fuel mass remaining after rich premix combustion phase is burned in the diffusion combustion phase.

Finally, the diffusion combustion phase is assumed to be mixing controlled: the fuel mass in each element is burned when it reaches stoichiometric conditions, and the fulfilment of these conditions is determined by the mixing model. It should be pointed out that in order to reach an accurate prediction of the diffusion combustion, quasi-steady conditions and transient processes at the start and end of the injection are considered separately. In quasi-steady conditions a physical approach based on the turbulent gas jet theory is assumed [86]. Thus, the air entrainment is tracked according to Equation 3.19.

$$\frac{\mathrm{d}m_{\mathrm{i}}}{\mathrm{d}t} = K_{\text{mix}} \cdot m_{\text{f,i}} \cdot Y_{\text{f,i}} \cdot u_0 \cdot \rho_{\text{cyl}}^{0.5} \cdot d_0^{-1} \cdot Y_{O_{2,\text{cyl}}}^{0.955} \tag{3.19}$$

where K_{mix} is the constant of the model to be calibrated using experimental HRR, $m_{\text{f,i}}$ is the fuel mass of the parcel, $Y_{\text{f,i}}$ is the fuel mass fraction of the parcel, u_0 is the injection velocity and d_0 is the nozzle diameter. If this approach is taken during the complete diffusion combustion process, the transient processes at the start and end of the injection are not well simulated, as show in Figure 3.21. However, the quasi-steady evolution is well followed.

In order to correct the transient evolution, a parameterised correction

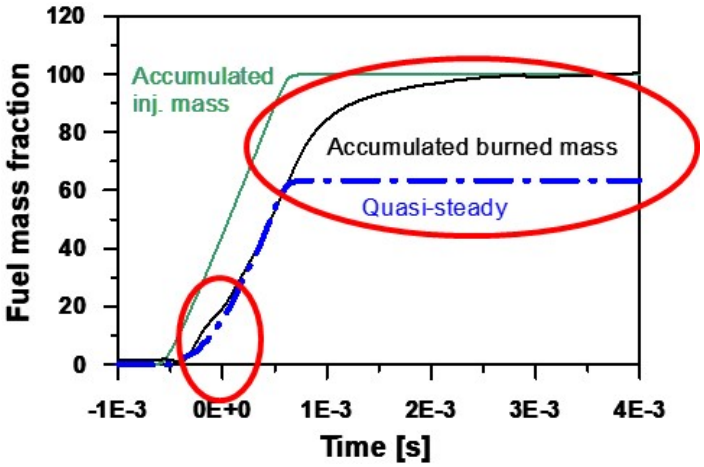

Figure 3.21: Accumulated injected and burned fuel masses (quasi-steady conditions assumption).

was applied based on CFD simulation of the initial and final parts of the combustion process. Thus, Figure 3.22 shows the mixing time calculated with the quasi-steady hypothesis and obtained with CFD. This initial enhancement of the mixing process allows correcting the initial slower combustion. Similar approach is applied for the end of the injection, as shown in Figure 3.23.

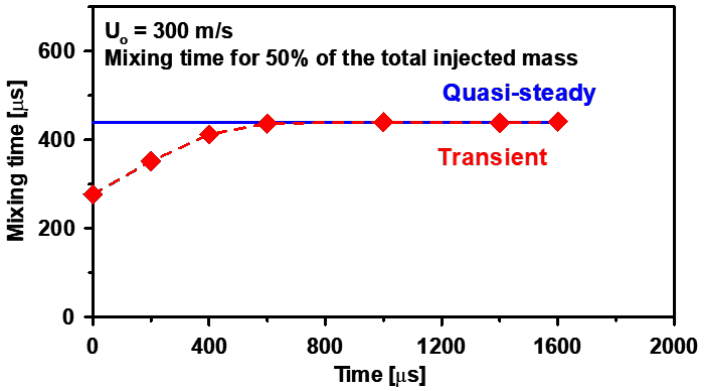

Figure 3.22: Mixing time at the start of the injection for quasi-steady and transient conditions.

After these corrections, the combustion process is correctly reproduced as shown in Figure 3.24.

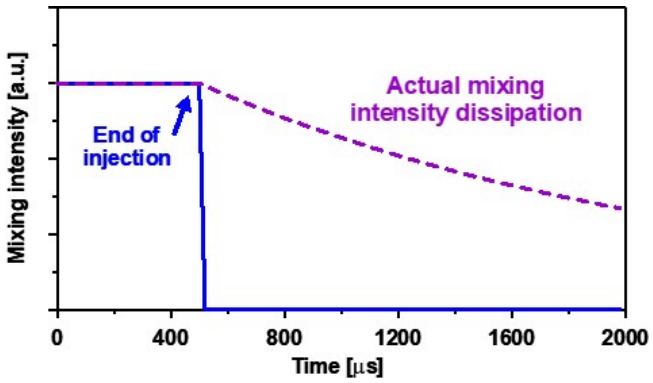

Figure 3.23: Mixing time at the end of the injection for quasi-steady and transient conditions.

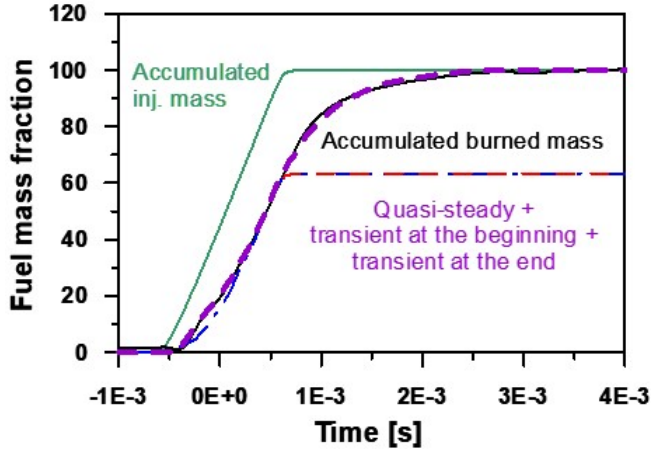

Figure 3.24: Accumulated injected and burned fuel masses (quasi-steady + transient conditions assumption).

3.2.3.1 Combustion model calibration

The calibration of the combustion model includes the determination of the different constants of the three sub-models described at subsection 3.2.3:

1. Ignition delay model: K_{ID1} and K_{ID2}
2. Premixed model: K_{pmx1}, K_{pmx2}, K_{pmx3}, K_{pmx4} and K_{pmx5}
3. Diffusion model: K_{mix}

The calibration was performed based on 26 steady-state points specified

before in Table 2.3, some of them at cold engine start conditions (−7 °C). Besides, as stated in subsection 2.5.2, three repetitions of every operating point were measured. Engine operating parameters were set according to the calibration included in the engine control unit (ECU). The number of injection pulses is different depending on the operating point (engine speed and load), thus, performing from one pilot, one pre-injection and one main injection at low engine speed; one pilot and main injections at medium engine speed and high load; and only one main injection at high engine speed and load. The calibration maps used in the virtual ECU described in subsection 3.2.9 reproduce the same injection strategy.

The criterion for the determination of the models constants was to minimise the difference between the experimental HRR and the simulated one. The values of the constants obtained are shown in Table 3.1.

Fitting constants	Value
K_{ID1}	3.22
K_{ID2}	3.5
K_{pmx1}	50000
K_{pmx2}	3
K_{pmx3}	0
K_{pmx4}	0
K_{pmx5}	0.5
K_{mix}	0.43961

Table 3.1: *Fitting constants values of the combustion model.*

Regarding the performance of the combustion model, Figure 3.25 and Figure 3.25 show the modelled and the experimental heat release and in-cylinder pressure obtained with VEMOD and CALMEC [89] (the combustion diagnosis tool used for the combustion analysis). In both figures, dashed lines correspond to the model prediction (blue is the heat released and green the in-cylinder pressure) while the solid lines correspond to the experimental values. The four solid lines (red is heat release and green the in-cylinder pressure) represent the four cylinders and give an idea about the real dispersion among them. Two different engine speeds have been plotted as an example, one at low engine speed (1250 rpm) in Figure 3.25 and

one at high engine speed (3500 rpm) in Figure 3.25.

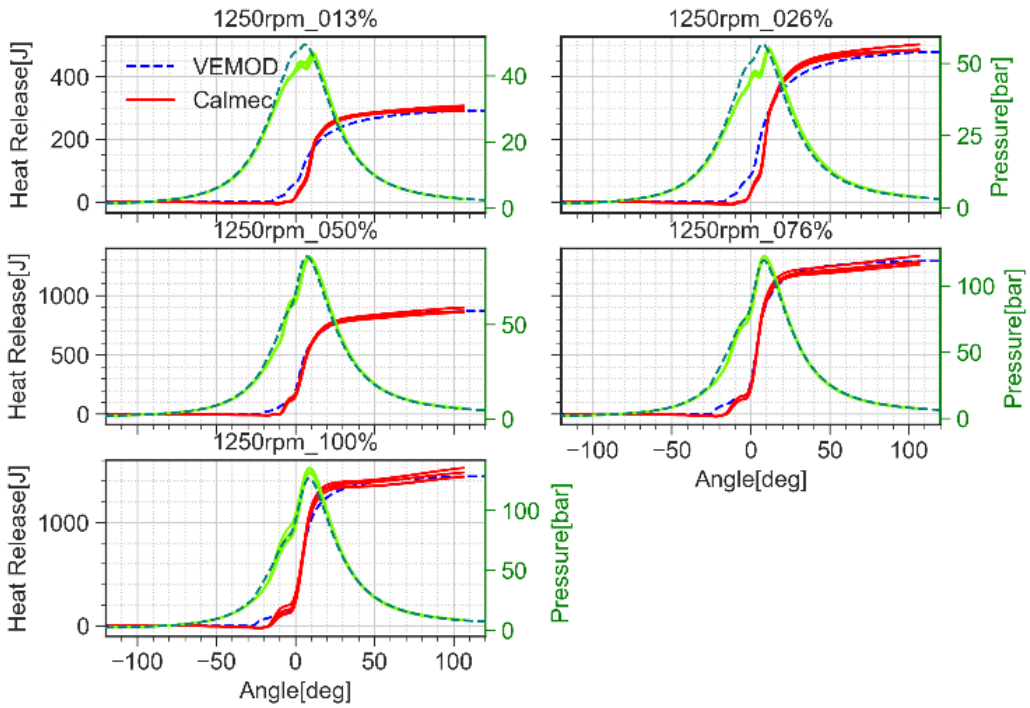

Figure 3.25: Cylinder heat release (J) and pressure (bar) at 1250 rpm for different loads (13%, 26%, 50%, 76% and 100%).

Both figures show a good global performance with a slightly slower combustion. At low load the prediction is not so accurate than at high load due to uncertainties such as the fuel repartition in each cylinder. Regarding the cylinder pressure, it can be observed that the pressure is well predicted, although simulated peak values are slightly lower at high speed and load. This is explained because of a slight overestimation of the incomplete combustion —the peak pressure difference is higher when the modelled cumulated heat release is lower in comparison with the average experimental value— and the blow-by. Besides, figures show that the combustion is well centred in all the cases.

It should be pointed out that the combustion model has no specific calibration parameter to consider the operating conditions, but a constant in the diffusion sub-model and other five in the premixed model which

are globally calibrated. As observed, except at low engine speed and load, the simulated heat release is in the experimental dispersion range among cylinders.

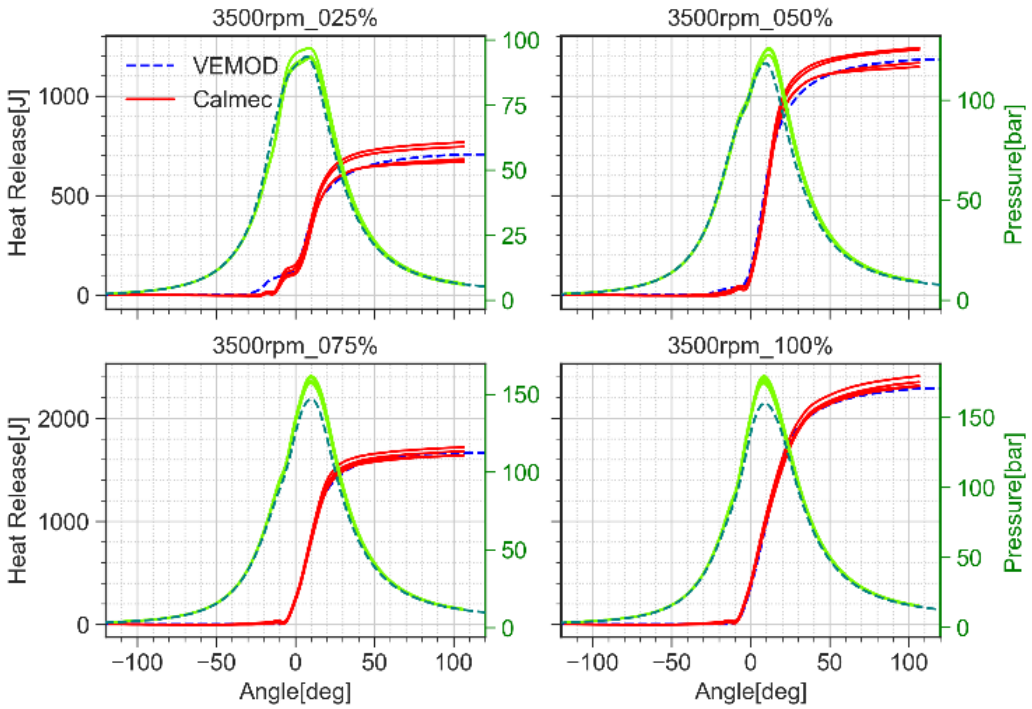

Figure 3.26: *Cylinder heat release (J) and pressure (bar) at 3500 rpm for different loads (25%, 50%, 75% and 100%).*

Regarding the performance of the in-cylinder model fed with the HRR calculated from the combustion model, Figure 3.27 shows the indicated mean effective pressure (IMEP) in different points covering the complete engine map. As it can be seen, there is a good agreement between experimental and modelled values, with a trend to slightly underestimate IMEP, specially at low load. When hot (20 °C) and cold (−7 °C) ambient conditions are compared, no difference in the performance is observed.

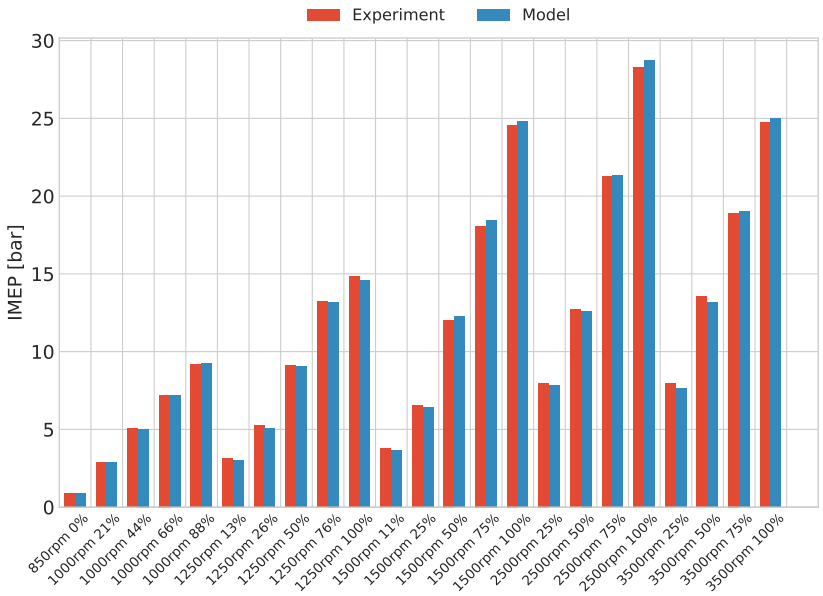

(a) Experimental and simulated IMEP (bar).

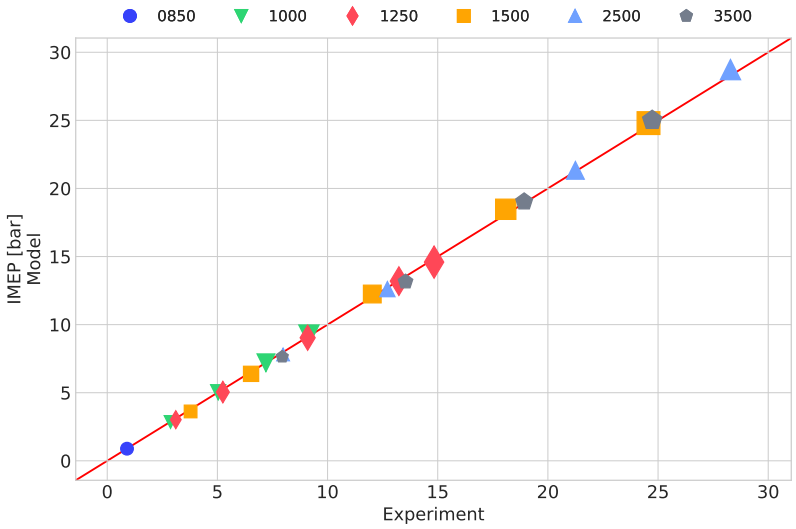

(b) IMEP model vs experiment.

Figure 3.27: *Experimental and simulated IMEP comparison.*

3.2.4 Emissions model

Regarding the emissions calculation, different approaches have been adopted to predict the pollutants formation. On the one hand, a physico-chemical approach has been used to predict NO_x [90], considering all the relevant mechanisms for NO_x formation and reduction. For the rest of pollutants —soot, carbon monoxide (CO) and unburned hydrocarbons (UHC) emissions—, which fundamentals are unclear and/or affected by many local phenomena, a neural network approach has been used to determine them.

3.2.4.1 NO_x emissions model

For the NO_x emissions model, all the relevant mechanisms for NO_x formation and reduction are considered, including thermal or Zeldovich [91], prompt and via N_2O and the re-burning effect, relevant at high EGR rates and fuel-air ratios. The model is implemented in a computational efficient way by tabulated chemistry where the instantaneous nitrogen monoxide (NO) production is computed in the following way according to Equation 3.20.

$$\frac{dY_{NO,i}}{dt} = K_{dY_{NO,i}} \cdot \frac{Y_{NO_{eq,i}} - Y_{NO_i}}{Y_{NO_{eq,i}}} \tag{3.20}$$

Where $Y_{NO,i}$ and $Y_{NO_{eq,i}}$ are the instantaneous NO concentration in the parcel i, and the corresponding concentration in equilibrium, respectively; and $K_{dY_{NO,i}}$ is a tabulated model constant. Both $K_{dY_{NO,i}}$ and $Y_{NO_{eq,i}}$ are tabulated as a function of pressure, temperature and oxygen excess, as shown in Figure 3.28 and Figure 3.29. In these figures the pressure effect is not shown.

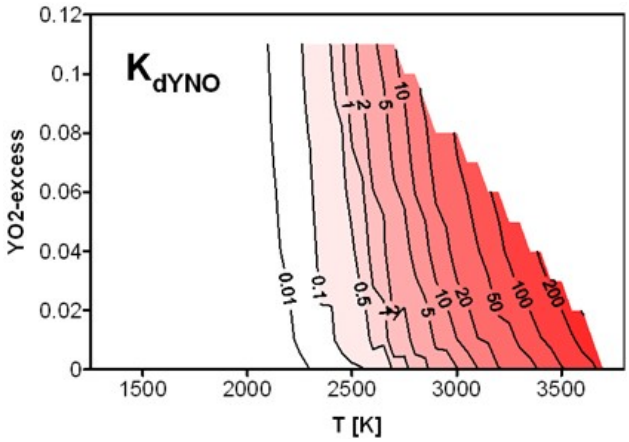

Figure 3.28: NO model constant as a function of the excess of oxygen and temperature.

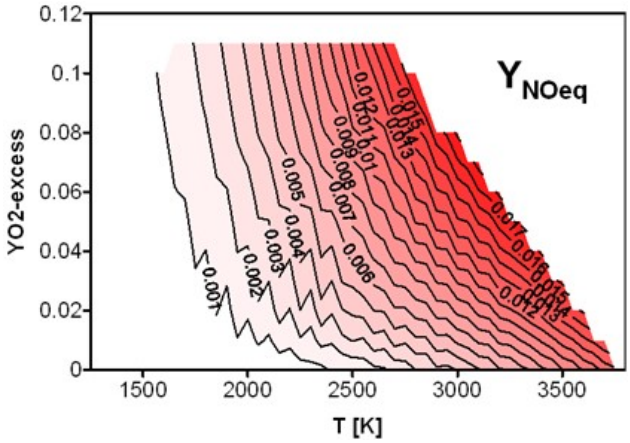

Figure 3.29: NO mass fraction in equilibrium as a function of the excess of oxygen and temperature.

Regarding the NO_x model calibration, the model includes 3 possible fitting constants:

- $K_{T\text{ad}}$ is a global calibration constant to correct the temperature at which the parameters included in Equation 3.20 are calculated. This constant slightly reduces the adiabatic temperature to be more realistic.
- The other two constants are scaling factors of the source term of NO and the re-burning efficiency. However, the values of these two constant have been set to 1 for the calibration process, so only the previous

$K_{T\,\mathrm{ad}}$ parameter has been fitted.

Even though the model approach is focused on nitrogen oxide, the most important part of NO_x, the calibration is carried out with the total experimental NO_x, thus applying an empirical correction to consider all the species. The same test matrix used for the combustion model calibration in Table 2.3 has been used for the NO_x model calibration. The value of the constant fitted is $K_{T\,\mathrm{ad}} = 0.9$ and Figure 3.30 shows the results obtained.

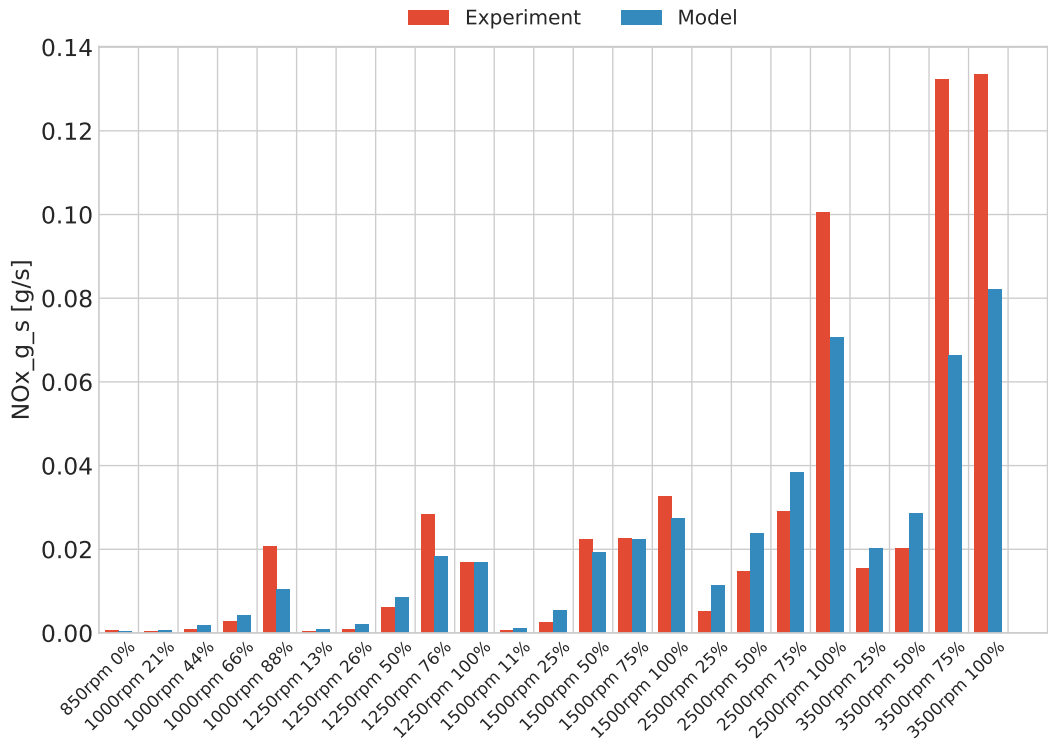

Figure 3.30: *Experimental and simulated NO_x mass flow at turbine outlet.*

As it can be seen, the global model performance is good, excepting at very high load where the model tends to underestimate NO_x formation. However, taking into account that the performance at lower load is much better (the mean percent error in the engine map is 11 %) and these points are more important for the transient validation (WLTC), it is concluded that the model performance is suitable.

3.2.4.2 Soot, CO and UHC emissions model

For the rest of the considered pollutants, the physical approach is not suitable due to complexity of their formation mechanisms and the important effect of the local phenomena, which cannot be considered with the 1D spray model and the 0D model of the thermodynamic conditions in the combustion chamber. However, it is necessary to have a certainty of the amount of these emissions released during the combustion process to estimate other physicochemical process such as the diesel particle filter (DPF) soot loading, the heat released at the diesel oxidation catalyst (DOC), etc. Consequently, an artificial neural network (ANN) approach has been used to determine them.

The methodology followed consisted on training an ANN in Matlab using as inputs the following variables:

- O_2 mass fraction, temperature, and density at the intake valve closing (IVC).
- The injection pressure.
- The ignition delay (ID) and the end of combustion (EOC).
- The engine speed.
- The coolant temperature.
- The fuel-air ratio in the combustion chamber, considering the amount of air in the EGR and residual gases.

The experimental database used to train the neural network is obtained from stationary operating conditions including the same points used for the combustion model calibration (see Table 3.1) and additional points including:

- Injection pressure swept at 2000 rpm and mid load.
- Fuel-air equivalence ratio swept at 2000 rpm.

- Main and main plus post-injection study at 1500 rpm and mid load.
- SOI swept at 1500 rpm and 3000 rpm and mid load points.

The training process consisted in selecting randomly a 70 % of the database data, plus new points (15 %). In order to reduce the prediction error and overfitting, the ANN is trained 100 times and both the error and the stability (according to the introduction of a perturbation in any input) are analysed every iteration. Figure 3.31 shows how the mean square error decreases with each epoch (evolution of the neural network). As the neural network is refined it is able to offer a better prediction. However, a limit must be imposed to avoid overfitting, which means that the ANN offers greater accuracy when the input data is within the training data, but the prediction error when the input data is new becomes higher. This limit can be seen in Figure 3.31 from epoch 26, where the error using training data (blue line) gets lower, but the errors using validation (green line) and new data (red line) start to increase. The final ANN consists of 14 inputs, one hidden layer made up to 10 neurons and one output. This process is repeated for each pollutant (soot, CO and UHC), so there is a neural network per each pollutant prediction.

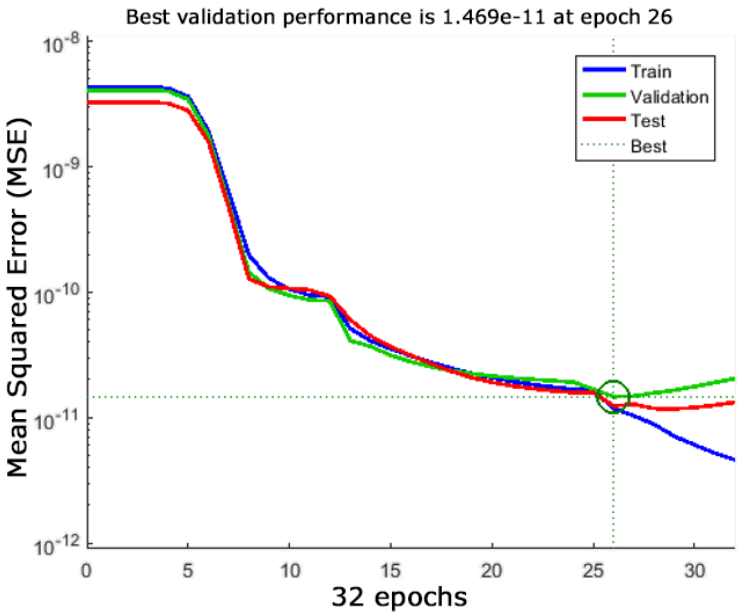

Figure 3.31: *Evolution of the mean squared error for each epoch.*

The final results of prediction vs measurements are shown in Figure 3.32, Figure 3.33 and Figure 3.34. It is observed that the neural network approach is running accurately and the mean percent error in all the cases is even lower than those obtained with the NO_x and its physicochemical approach.

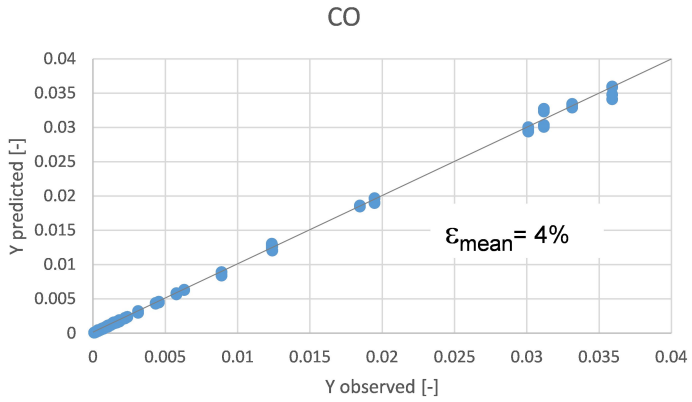

Figure 3.32: Prediction vs experimental CO emissions.

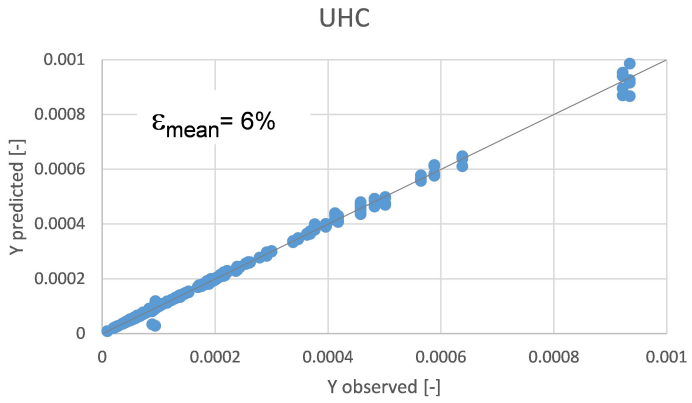

Figure 3.33: Prediction vs experimental UHC emissions.

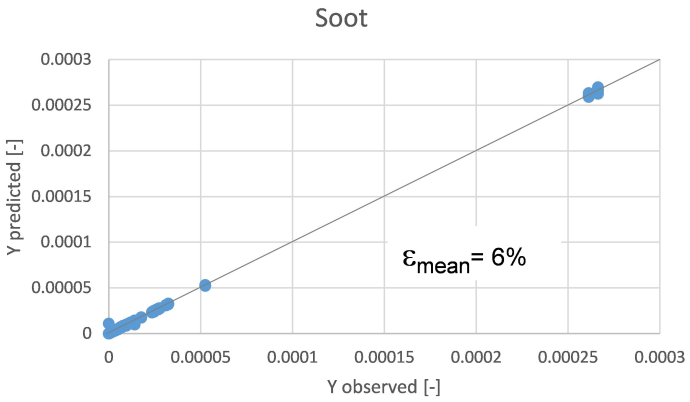

Figure 3.34: Prediction vs experimental soot emissions.

3.2.5 After-treatment systems model

Compression ignition (CI) engines require the combination of a wall-flow particulate filter, which collects the particulate matter (PM), with a series of flow-through monolithic reactors in charge for CO, HC and NO_x abatement due to the lean-burn combustion requirements of these engines. As a consequence, a great variety of architectures combining several devices is expected in the next years being the particular components conditioned by the specific NO_x abatement solution [92, 93]. As a particular response to the need of flexible computational tools for exhaust after-treatment systems, a classical lumped model is used in VEMOD, which is able to consider DOC, DPF and deNO_x systems, i.e. lean NO_x trap (LNT) or selective catalyst reduction (SCR), thus covering all the possible after-treatment systems in Diesel engines. The model formulation for wall-flow and flow-through monoliths is described in detail in [94]. Thus, a brief description of the model implemented is provided here.

The model conception is based on a modular approach covering pressure drop, heat transfer and chemical mechanism sub-models. The heat transfer modelling is based on a nodal approach adapted from 1D modelling to account for gas to wall heat exchange, heat losses to the environment and thermal inertia of the monolith substrate and the external canning.

The abatement of gaseous pollutants is modelled solving the chemical

species transport in the bulk gas and washcoat regions assuming quasi-steady flow. UHC accumulation has also been included in the DOC model.

In the case of wall-flow monoliths, the filtration efficiency computation is included as basic performance according to the proposal of Serrano et al. [95, 96]. In these devices, the geometrical properties of the porous medium and the inlet channel geometry are described as a function of the particulate matter load, which varies due to filtration and regeneration and impacts on chemical, thermo-and fluid-dynamic processes. Partial soot penetration into the porous wall is assumed [97]. The soot oxidation mechanism includes the modelling of the adsorption reactant phase on soot particles. Particulate size distribution variation due to filtration is taken into account in the DPF model.

3.2.5.1 After-treatment system lumped model

The implementation of the exhaust after-treatment system (EATS) model in VEMOD implies that the after-treatment devices are considered as boundary conditions between two 0D elements (inlet and outlet volumes). In this case, the thermodynamic properties are imposed at the inlet (pressure, temperature and composition) and outlet (pressure) of the flow-through or wall-flow device, as presented in Figure 3.35 and Figure 3.36. The lumped model solution provides the fluxes between these adjacent cells at time t, which are necessary to solve the flow properties at the end of the time step ($t + \Delta t$).

The **flow-through monolith model** deals with the main physical and chemical processes to determine the performance of the system in fluid-dynamic and emissions terms. It is comprised by three sub-models solving pressure drop, heat transfer and chemical reactions. As a lumped model, constant flow properties are assumed along the monolith length. The model provides a lumped description of the monolith substrate properties and the prediction of the flow properties at the monolith outlet. According to the flow-chart shown in Figure 3.35, the model is able to predict mass flow across the monolith. It is calculated by the pressure drop sub-model. The outlet gas composition, i.e. pollutants conversion efficiency, is com-

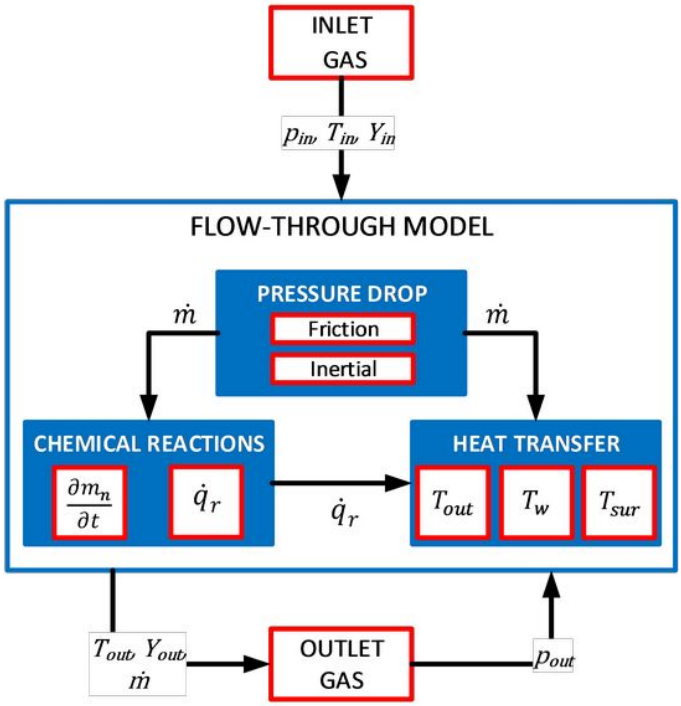

Figure 3.35: Flow-chart of the flow-through lumped model.

puted by the chemical reactions modelling. Finally, the outlet gas temperature as well as the substrate and external canning wall temperature are determined by the heat transfer and the heat released in the chemical reactions. To do that, the main input data are the inlet gas temperature and the composition. As stated, the inlet and outlet pressure are provided by the gas dynamics model.

The **wall-flow monolith model** is structured in the same way. The pressure drop, the inlet gas temperature and the composition are the input flow properties for the model solution in the gas dynamics software environment. Figure 3.36 shows the main interactions between the different sub-models. Due to the operation principle concerning particulate matter collection, this model includes filtration and soot oxidation sub-models. In turn, these processes, as well as a correct mass flow prediction from pressure drop, demand a porous medium sub-model to consider the variation in micro- and meso-geometry of the substrate and the inlet channels re-

spectively.

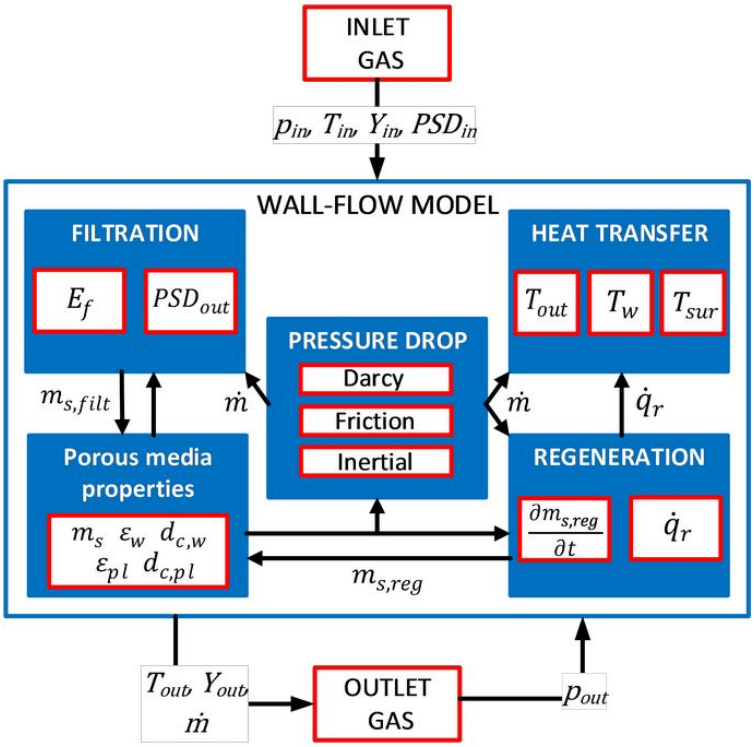

Figure 3.36: Flow-chart of the wall-flow lumped model.

3.2.5.2 Pressure drop

The placement of the after-treatment systems into the exhaust line involves a flow restriction directly related to the characteristics of their particular geometry and the flow properties. In flow-through monolithic reactors the resulting pressure drop can be expressed as reflected in Equation 3.21, where K_{DOC} is the pressure drop coefficient of the device, and ρ_{in} and u_{in} are inlet gas density and velocity, respectively.

$$\Delta p_{\mathrm{DOC}} = \frac{1}{2} \cdot K_{\mathrm{DOC}} \cdot \rho_{\mathrm{in}} \cdot u_{\mathrm{in}}^2 \tag{3.21}$$

In wall-flow monoliths, the importance of the inertial contribution is

higher due to the minor open area, with alternatively plugged channels and progressively reduced as soot is collected into the inlet channels. In addition to inertial and friction pressure drop, additional contributions appear due to the fact that the flow is forced to pass across the porous wall and the particulate layer, if this last exists because of soot or ash accumulation. Therefore, assuming incompressible flow, the particulate filter pressure drop can be expressed as in Equation 3.22, where subscripts Darcy, inertial and fr refer to pressure drop across the porous media (described mainly by the Darcy's law), inertial and friction contributions.

$$\Delta p_{\mathrm{DPF}} = \Delta p_{\mathrm{Darcy}} + \Delta p_{\mathrm{inertial}} + \Delta p_{\mathrm{fr}} \tag{3.22}$$

3.2.5.3 Porous media properties

The calculation of the pressure drop and the filtration efficiency in porous media is dependent on micro-geometry properties. The main parameters are the porosity and the mean pore diameter. Their definition in the porous wall, particulate layer and ash layer is based on the packed-bed of spherical particles theory, which considers the porous structure as a set of spherical unit cells. These unit cells fulfil that their porosity is the same as that of the porous medium being a unit collector placed in the core of the unit cell. A detailed description of the equations used for the calculation can be found at [94].

3.2.5.4 Filtration

The filtration sub-model computes the mass-based filtration efficiency and thus the amount of soot collected per unit cell. The model provides both the overall filtration efficiency, which is represented by that corresponding to the mode diameter of the particle emissions, and as a function of the particle size distribution (PSD) [95]. It is done according to Brownian and interception collection mechanisms around a single sphere. The inertial contribution is not included due to its negligible impact [95]. A detailed

description of the equations used for the calculation can be found at [94].

3.2.5.5 Reaction mechanism

The chemical conversion within the monolith is tackled integrating the one-dimensional chemical transport equations. It is considered in the axial channel direction for gaseous emissions in flow-through monoliths and across the porous wall to model the soot oxidation in wall-flow monoliths.

The chemical reaction sub-model for gaseous pollutant emissions computes their conversion efficiency integrating the one-dimensional chemical species transport equation into the gas stream and the washcoat along the monolith length [98]. Assuming quasi-steady flow, these governing equations are given by Equation 3.23 and Equation 3.24.

$$u_{\mathrm{in}} \cdot \frac{\mathrm{d}X_{\mathrm{n}}}{\mathrm{d}x} = -S_{\mathrm{p,\,cat}} \cdot k_{\mathrm{m,n}} \cdot \left(X_{\mathrm{n}} - X_{\mathrm{n,S}} \right) \tag{3.23}$$

$$\nu_{\mathrm{n}} R_{\mathrm{n}} + S_{\mathrm{p,\,wc}} \cdot k_{\mathrm{m,n}} \cdot \left(X_{\mathrm{n}} - X_{\mathrm{n,S}} \right) = 0 \tag{3.24}$$

Equation 3.23 regards the bulk gas equation. The left-hand side accounts for the convection transport of the species along the channel and the right-hand side represents the diffusion of species from the bulk to the channel surface. In a complementary fashion, Equation 3.24 represents the chemical species transport over the catalyst surface. It comprises the diffusion of the species from/to the surface and to/from the washcoat and the corresponding reaction rates. X_{n} and $X_{\mathrm{n,S}}$ are the molar fraction of species n into the gas and in the washcoat respectively, $S_{\mathrm{p,\,cat}}$ represents the geometric surface area related to the mass transfer from the gas to the catalyst surface and $S_{\mathrm{p,\,wc}}$ is the geometric surface area related to the mass transfer from the catalyst surface into the washcoat volume.

For the soot oxidation modelling, the regeneration sub-model in wall-flow particulate filters solves the conservation equation of the soot oxidis-

ing species accounting for a three-layer step. As sketched in Figure 3.37 particulate layer, coated porous wall and uncoated porous wall region are distinguished. The model considers that the soot oxidation in every region takes place in presence of O2, which becomes predominant at high temperatures and in catalysed filters, and NO_2, which is the main oxidant at low temperature.

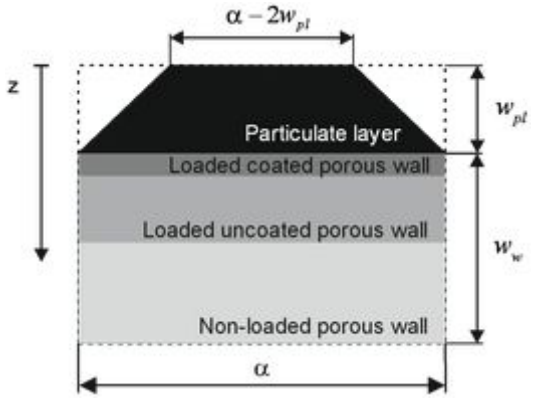

Figure 3.37: *Scheme of the regions of soot regeneration in the wall-flow particulate filter.*

As mentioned above, further details of the calculation of the reaction mechanism can be found in [94].

3.2.5.6 Heat transfer in the after-treatment systems

The prediction of the outlet gas temperature is dependent on the heat exchange between inlet gas and substrate wall, whose temperature is in turn conditioned by the heat released by the chemical species conversion and the heat transfer towards the environment. The proposed lumped model accounts for these phenomena from a nodal-based scheme where the heat transfer from gas to wall, the radial conduction, the convection and radiation to ambient, the axial conduction in the canning, the heat released and the monolith and canning thermal inertia are taken into account. By applying the energy balance and the continuity equation between monolith inlet and outlet, and considering the change in mass flow due to regeneration and filtration, it is possible to obtain the outlet gas properties of the EATS.

3.2.5.7 After-treatment model calibration

The methodology followed for the calibration —and validation— of the EATS is summarised in the Figure 3.38 for flow-through model (DOC, SCR, LNT) and Figure 3.39 (for DPF). Each figure describes the tests that are used for the calibration. Even though the SCR and LNT models have been built and included in VEMOD, the calibration has been carried out only with the DOC and DPF included in the reference engine described in section 2.2.

The detailed description of the complete process, the experimental condition used for the calibration and the fitting constants values determined can be found at [94]. A short summary of the results achieved after the calibration is provided here.

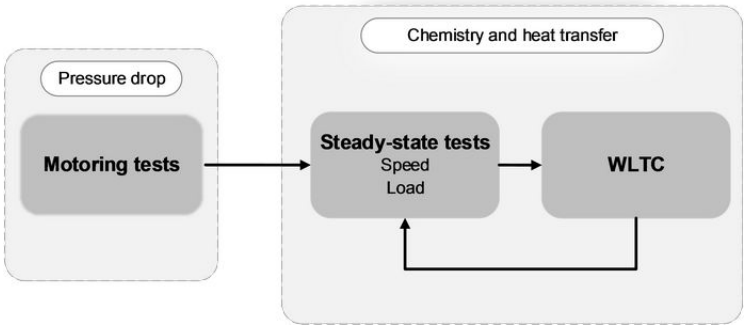

Figure 3.38: Methodology for the flow-through model calibration.

First of all, Figure 3.40 shows the prediction of mass flow across the DOC when the experimental pressure drop is imposed. The steps in Figure 3.40 (a) correspond to different engine speeds under motoring operation. The experimental instantaneous pressure drop coefficient is calculated according to Equation 3.21 for every operating point. The average value of every point (black empty circles in Figure 3.40 (b)), is used to obtain a fitting function covering a wider Reynolds number range to be applied to predict the mass flow under different operating conditions.

The steady-state tests were run at 1500 rpm, 2000 rpm and 2500 rpm varying the engine load from 5 % to 40 % in order to cover the low to

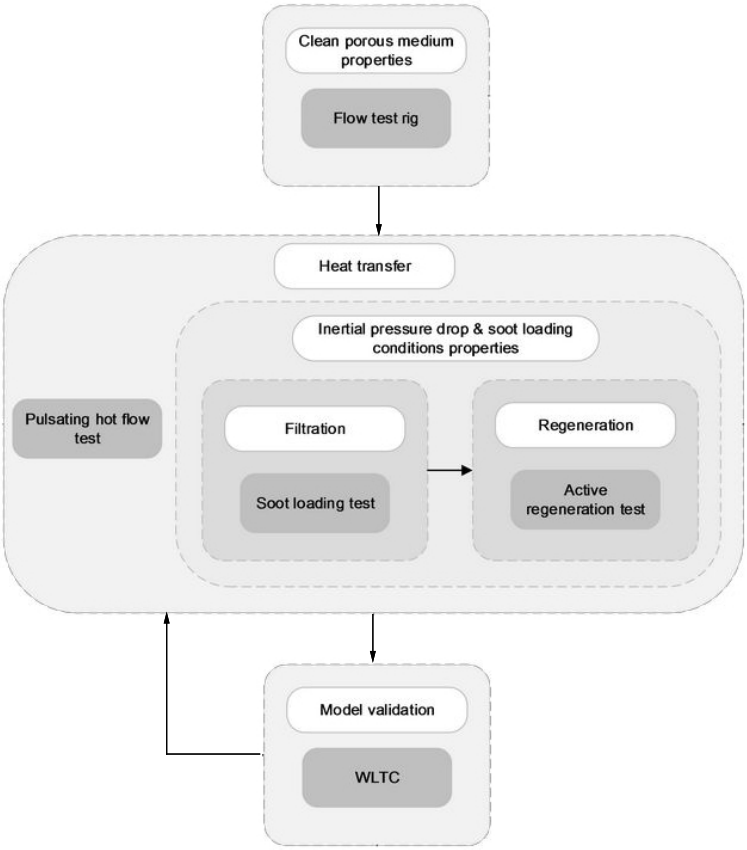

Figure 3.39: *Methodology for the DPF model calibration.*

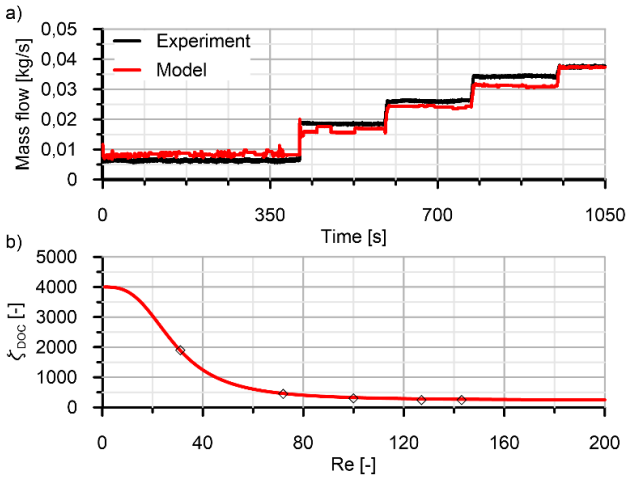

Figure 3.40: *Mass flow prediction (a) and pressure drop coefficient determination (b) in motoring tests.*

medium exhaust temperature range. Figure 3.41 compares experimental and modelling results concerning outlet gas and canning surface temperature in steady-state tests at 2500 rpm. Every step in temperature identifies a change in engine load. The inlet DOC gas temperature is represented by the dashed black series in plot (a). Being the surface temperature measured at the middle of the DOC monolith, the model shows good ability to predict the thermal response of the device, both in monolith and canning. The outlet gas temperature prediction is appreciably higher than the inlet gas temperature at low engine load because of the heat released by the CO and HC oxidation.

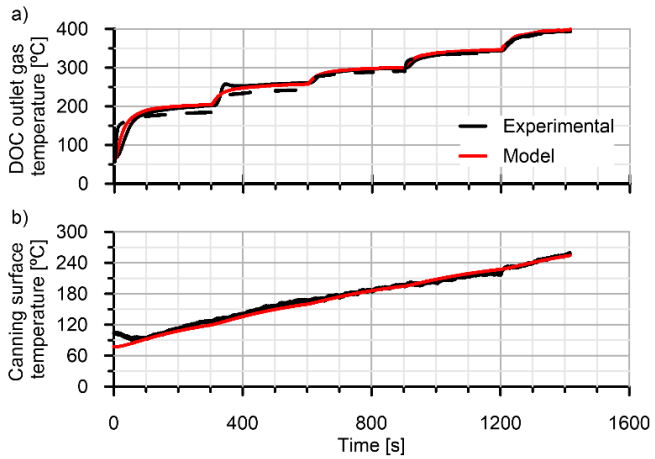

Figure 3.41: DOC outlet gas temperature (a) and canning surface temperature (b) at 2500 rpm and engine load steps from 5 % to 40 %.

Figure 3.42 represents the conversion efficiency of CO and HC corresponding to steady-state points at different engine speeds. Figure 3.42 (a) shows the DOC conversion efficiency when the engine is moved from motoring to 5 % engine load at 1500 rpm. It is shown how the CO conversion efficiency increases during the first seconds due to the progressively raise of the inlet temperature. However, HC conversion efficiency is high from the very beginning due to HC adsorption at low temperature. The model captures properly both the oxidation and adsorption processes providing a good prediction of the conversion efficiency for both pollutants. Plots (b) and (c) confirm the capability of the model to determine the conversion efficiency as the temperature raises, what progressively limits the conversion efficiency by mass transfer and pore diffusion processes. Although

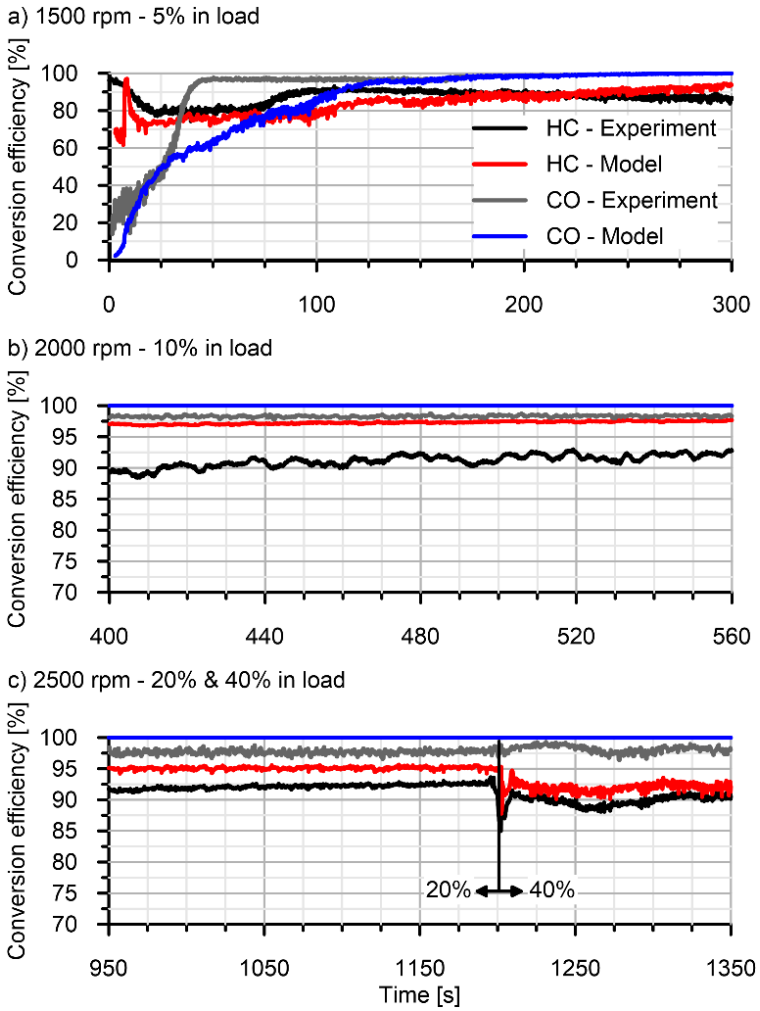

Figure 3.42: *HC and CO conversion efficiency during thermal stabilisation in different steady-state operating conditions.*

both CO and HC conversion efficiencies are slightly overestimated, the fitted model provide reliable results in transient operation, as it is shown in subsection 3.3.2.

Figure 3.43 (a) shows the mass flow prediction as a function of the soot load when the experimental pressure drop is imposed. The mass flow, which is almost constant, is properly predicted throughout the test as well as the soot load (Figure 3.43 (b)). Indeed, the soot load is a function of the mass flow but also depends on the computation of the filtration efficiency, whose evolution until the maximum value is zoomed in Figure 3.43 (c). Fi-

nally, Figure 3.43 (d) demonstrates that the model also accounts properly for heat transfer. An accurate prediction of the DPF outlet gas temperature is provided both during the thermal transient period and once steady-state conditions are reached.

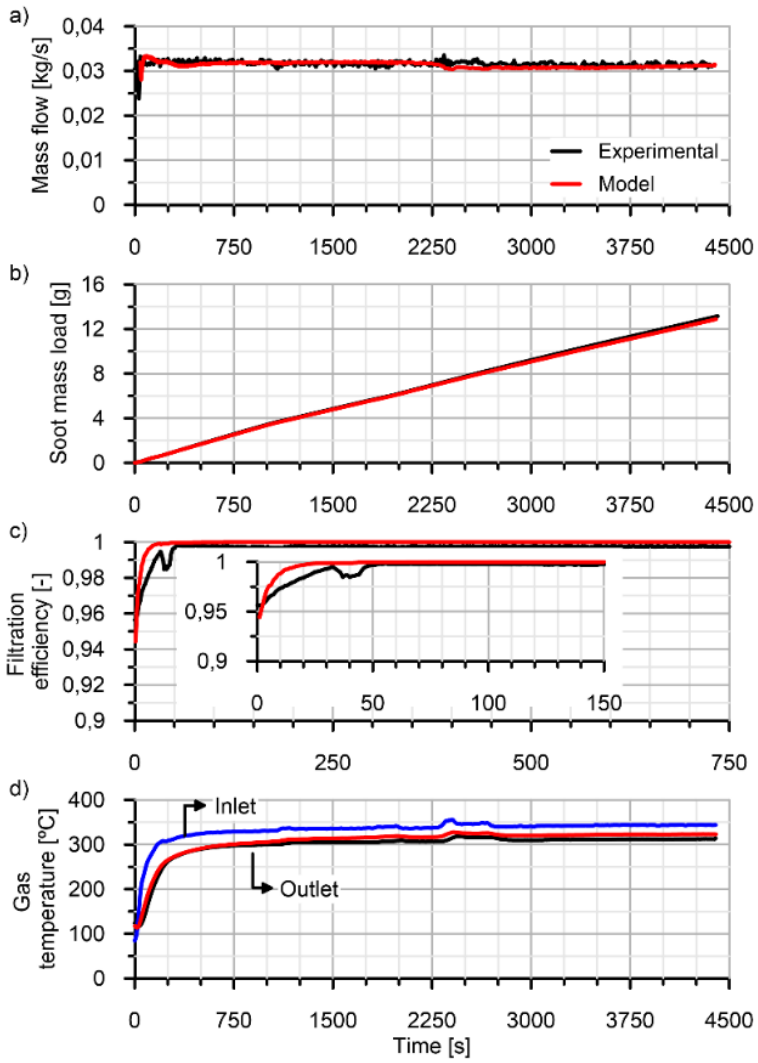

Figure 3.43: DPF response during the soot loading test under steady-state conditions.

Finally, the performance of the soot oxidation calibration during the regeneration process is summarised in Figure 3.44. It is performed after the soot loading test so that the initial substrate conditions are known from the end modelling shown in Figure 3.43. Again, the DPF pressure drop (a) is imposed as a boundary condition so that the fluid-dynamic model calcu-

lates the mass flow (b) across the DPF. Plot (c) represents the soot mass load prediction into the DPF distinguishing between porous wall and particulate layer throughout the regeneration process. The corresponding soot depletion rate governs the heat release rate determining the outlet gas temperature, which is plotted in Figure 3.44 (d).

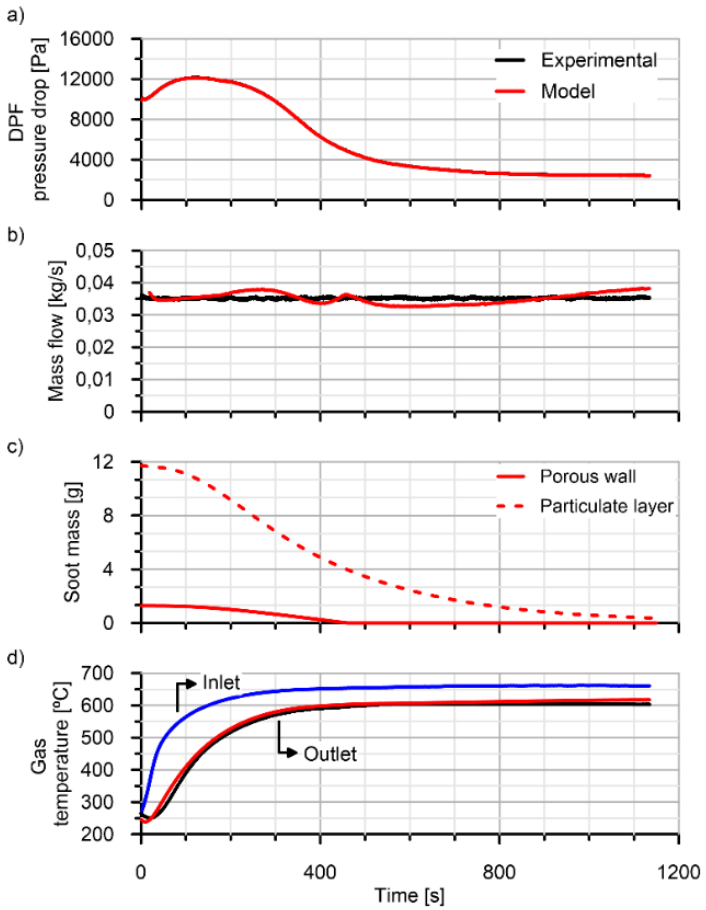

Figure 3.44: *DPF response during the active regeneration test under steady-state conditions.*

3.2.6 Heat transfer model

Heat transfer model in VEMOD is based on lumped conductance models (engine block, ducts and turbocharger) to take into account the heat transferred between the different fluids of the engine (gas and liquids: coolant and oil). Thus, the lumped conductance model allows linking in-cylinder,

port and turbocompressor processes with hydraulic circuits through the heat rejection calculation: 0D in-cylinder model, 1D ports model and 0D turbine and compressor models provides boundary conditions of gas temperature and heat transfer coefficient to calculate heat flux, whereas the nodal model provides detailed wall temperature and heat transfer repartition to coolant and oil circuit.

The lumped conductance model is composed of a number of small metallic elements as a result of dividing the cylinder head, the piston, and the liner into small metallic nodes. A characteristic mass and thermal capacitance of each node have been included in order to consider the transient simulation to be performed; they depend on its geometrical and material properties. These nodes can be in contact with other metallic node so the conductive conductances are computed (e.g. piston-piston nodes) or in contact with fluid nodes, like the chamber, a coolant node or an oil node, obtaining the convective conductances instead. Also the piston nodes have a source term due to the friction in this element.

The lumped model is initialised with geometrical information of the engine block (bore diameter, stroke, and ports diameters), the piston, the liner and the cylinder head materials, and the initial temperatures of the metallic nodes, oil and coolant. The nodes temperatures are then updated each cycle by applying a transient energy balance to each node, according to Equation 3.25.

$$\sum_j \frac{k_s \cdot A_{i,j}}{d_{i,j}} \cdot (T_{t_j} - T_{t_i}) + \sum_f h_f \cdot A_{i,f} \cdot (T_{t_{fluid}} - T_{t_i}) + \sum Q_{t_{gen,i}} = \frac{\rho_s \cdot V_i \cdot C_p}{\Delta t} \cdot (T_{t_i} - T_{t-\Delta t_i}) \tag{3.25}$$

where k_s is the conductivity between two nodes in contact, $A_{i,j}$ and $d_{i,j}$ are the contact area and the distance between nodes i and j in contact, respectively, T_{t_j}, T_{t_i}, $T_{t_{fluid}}$ are the nodes temperature at an specific instant t, h_f is the heat transfer coefficient of the fluid (gas or liquid), $Q_{t_{gen,i}}$ account for source terms (such as friction) and the terms at the right of the

equation represent the heating of the metallic node with a heat capacity $\rho_s \cdot V_i \cdot C_p$. The model has been improved to include the oil-coolant heat exchange through the block and the thermal inertia of liquids (coolant and oil), all of them key issues during transient operation starting from cold conditions. Finally, the model has been adapted to evaluate different thermal management strategies with split cooling system (independent coolant circuit in the cylinder-head and block).

The convective heat transfer in the chamber is calculated in VEMOD by means of a modified Woschni's correlation in which the original velocity terms due to the swirl motion, c_u, is improved in previous works by means of CFD calculations [99] to obtain the heat transfer coefficient shown in Equation 3.26, where C_{w1}, C_{w2} and C_2 are tuned with empirical data from motoring and firing tests [100], c_m is the mean piston speed, c_u is the instantaneous tangential velocity of the gas in the chamber, p_0 is the pressure in motoring conditions assuming a polytropic evolution, p and T_g are in-cylinder pressure and temperature, and p_{IVC}, T_{IVC} and V_{IVC} are pressure, temperature and volume at IVC, respectively.

$$h_w = C_1 \cdot D^{-0.2} \cdot p^{0.8} \cdot T_g^{-0.53} \cdot \left(C_{w1} \cdot c_m + C_{w2} \cdot c_u + C_2 \cdot \frac{V \cdot T_{IVC}}{p_{IVC} \cdot V_{IVC}} \cdot (p - p_0) \right)^{0.8} \tag{3.26}$$

This upgraded Woschni-based model has been extensively applied at CMT to calculate the heat transfer in different engines and operating conditions. Being the heat transfer in the chamber the main source of heat rejection, it is a critical issue during the operation in cold conditions such as that in the WLTC after the engine start at −7 °C. Thus, with the aim of assessing the validity of the VEMOD heat transfer model, a critical review of convective heat transfer models has been carried out. The first step was to carry out a survey of gas-wall heat transfer models validated at low temperature [101, 102, 103, 104]. The main conclusions obtained can be summarised as: on the one hand there are few works published on this topic, on the one hand no alternative models have been proposed in the literature. Thus, Jarrier et al. [101] used Woschni's correlation with the engine at 2.5 °C, Samhaber et al. [102] corrected heat flux at 0 °C by multiplying

heat flux value in warmed-up conditions by a factor equal to 1.15 (increase of 15 %), Uppuluri et al. [104], at −20 °C, used a correction map for heat flux: heat flux value in warmed-up conditions was multiplied by a correction factor depending on engine speed, SOC and air-fuel ratio. Finally Roberts et al. [103] performed a review of the internal combustion engine cold-start efficiency issue and potential solutions, highlighting the importance of heat produced by friction at low temperature, however no original approach for heat transfer is discussed.

Having in mind the previous comments, the assessment of the validity of Woschni's correlation under cold environment conditions is assumed as an important objective. For this purpose, the methodology followed is based on the analysis of the variation of the Woschni's fitting constant in cold and hot conditions.

As later described in subsubsection 3.2.6.1, C_{w2} is assumed to be proportional to C_{w1}, and thus in motoring conditions C_{w1} is the only constant to be tuned (C_2 is the scaling constant of the combustion term). For each motoring test, C_{w1} can be adjusted to comply with the first Law of Thermodynamics. If the heat transfer model took into account all the physic of the heat transfer phenomenon, the constant should be the same for each test, however at CMT it is known that a certain level of dispersion is usually found at different motoring conditions (for example at different engine speed or intake pressure). It was assumed as hypothesis to be checked in cold conditions that: if C_{w1} varies less when room temperature changes than when engine speed changes, the influence of temperature on heat transfer coefficient is smaller than the engine speed influence, and thus Woschni's heat transfer model and C_{w1} fitting are valid for hot and cold environment conditions. The analysis was performed in the reference engine detailed in section 2.2 and the test bench measured points in Table 2.3 was used for the analysis.

Figure 3.45 shows the values of the C_{w1} fitting constant in the reference engine. In this figure, the mean value and the variation range due to the repetition of the test is shown for different engine speeds. Purple arrow indicates the maximum difference found in the engine speed swept at the same ambient temperature, while green arrow represents the maximum

difference for tests at the same engine speed and different ambient temperature. The comparison between the arrows length allows the estimation of the relative effect of ambient temperature versus engine speed.

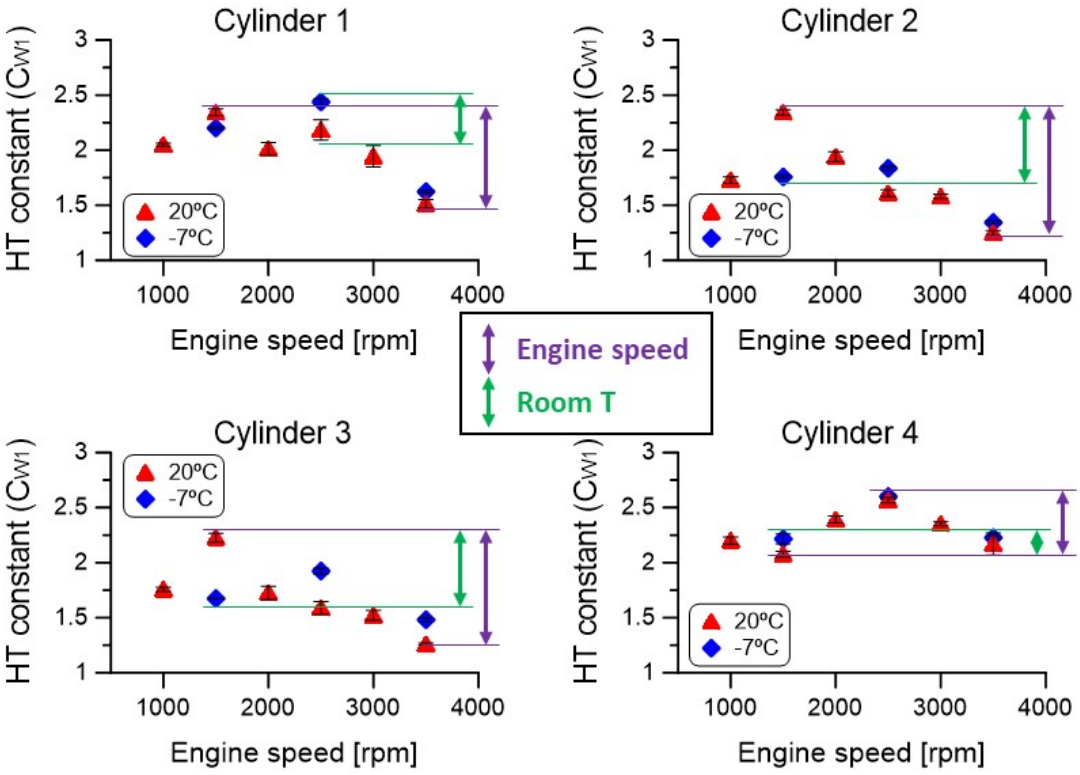

Figure 3.45: Fitting constant C_{w1}.

As it can be observed, in all cylinders, the influence of room temperature on the heat transfer fitting coefficient is smaller than engine speed influence, and hence it was concluded that there is no evidence that the Woschni-based heat transfer model of VEMOD is not valid for both hot and cold environment conditions. Thus, after the calibration, it is suitable for the simulations to be performed in the next studies carried out in this thesis.

3.2.6.1 In-cylinder heat transfer model calibration

The calibration of the heat transfer model is based on a combination of motoring and combustion tests. As shown in Equation 3.26, the in-cylinder heat transfer model used in VEMOD has three fitting constants: C_{w1} that is

a scaling factor of the piston mean velocity, C_{w2} that scales the tangential velocity due to the swirl, and finally C_2 which affects the combustion term. The methodology consists of two main steps:

1. In motoring conditions the constants C_{w1} and C_{w2} are fitted according to the methodology described in [100]. If experimental data at different swirl conditions is available, C_{w1} and C_{w2} can be both fitted independently. However when swirl swept are not available (like in the reference engine), it is assumed a constant ratio $C_{w1}/C_{w2} = 1.7$ and only C_{w1} is independently adjusted. Along with the heat transfer coefficient, there are other engines uncertainties such as:

   - Top dead centre position ($\Delta\alpha$).
   - Real compression ratio (CR) of each cylinder.
   - Calibration factor of the engine deformation model K_{def}.

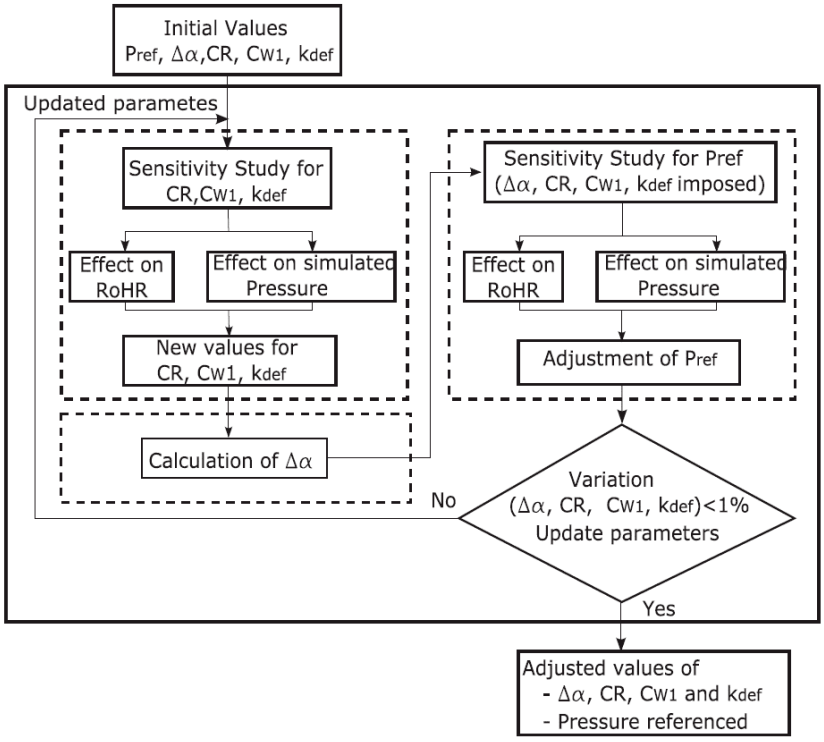

Figure 3.46: Flow-chart to determine the uncertainties in motoring conditions.

These parameters are obtained by the methodology shown in Figure 3.46. The fitting process is based on the sensitivity effect of such uncertainties on heat release and simulated pressure. The methodology is able to identify the separated influence of each parameter and to provide a set of values thanks to the multi-variable linear regression in motoring conditions. The method is flexible enough to deal with different number of uncertainties and can be applied to different engines and thermodynamic cycles. The results obtained by applying the analysis to the motoring measurements of the reference engine are:

- $C_{w1} = 1.6304$; $C_{w2} = 0.9590$
- $RC = 16.06$
- $K_{def} = 2.1723$

2. Once the motoring constants of the model have been obtained, the value of C_2 is fitted with the objective of getting a cumulated heat release in the combustion that matches the value of the total injected energy in each test. In this case the combustion matrix described in Table 2.3 was used and a final value of $C_2 = 0.001$ was adjusted.

3.2.7 Thermo-hydraulic model

Thermal management plays an important role in engine operation and it is a key issue during the transient operation, in particular in the transient operation after cold start. In this context, modelling the hydraulic circuits of the engine (coolant and lubricant oil) becomes necessary to assess potential improvements in thermal management. Thus, VEMOD includes a sub-model to simulate thermo-hydraulic circuits. The model is capable of analysing the hydraulic network to obtain flow rates and head losses distribution of the liquid. In addition, spatial distribution and temporal evolution of fluid temperature are simulated.

The thermo-hydraulic model in VEMOD includes sub-models for different types of heat exchangers to consider whichever type of gas-liquid,

liquid-liquid or gas-gas heat exchanger. The effect of the vehicle velocity on the radiator has also been included and the hydraulic circuit model has been evolved in order to consider split cooling in combination with the lumped conductance model.

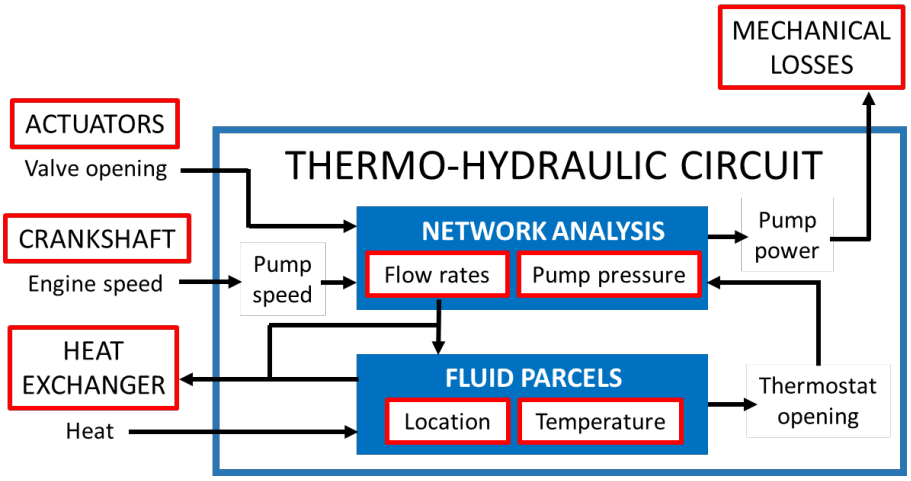

Figure 3.47: Flow-chart of the thermo-hydraulic circuit model.

The scheme of the model in its current state is sketched in Figure 3.47, where the interaction with other VEMOD sub-models is shown. The thermo-hydraulic model consists of two sub-models:

1. **Hydraulic circuits**. At the beginning of the simulation, VEMOD main execution creates a separate hydraulic model for each hydraulic circuit in the engine. Circuit configuration and components can be defined in detail (pipes, thermostats, operable valves, pumps and heat exchangers). Each circuit model is then evaluated at the end of every engine cycle. The hydraulic sub-model calculates mass flows of oil and coolant at different engine components like the engine block galleries, the EGR coolers, the turbocharger and the oil and coolant pumps. Some sub-models provide inputs to the circuits. In particular, engine speed or a reference rotational speed is multiplied by a fixed user-defined ratio to obtain pump speed. Moreover, control actuators can set the opening degree of valves. The process of creating the hydraulic circuit is flexible, since it is made up of generic components connected to each other. Then the user defines the specific properties (geometry, effi-

ciency, pumps characteristic curves, etc.) for each component, just in the same way as the gas circuit. The calculation method is summarised in the following way and illustrated in Figure 3.48:

(a) Firstly, starting from an arbitrary junction, all possible paths (open or closed) are determined.

(b) Paths are split at the junctions to create branches, which are a portion of a path between two consecutive junctions.

(c) Closed paths are recognised as meshes.

(d) For every branch, the head loss is calculated as a function of the flow in the branch according to Equation 3.27, where R_1 and R_2 are hydraulic resistances and $\dot{V}$ is the volumetric flow. In the case of pipes, the hydraulic resistances are calculated with Darcy-Weisbach equation every engine cycle.

$$H = h + R_1 \cdot \dot{V} + R_2 \cdot \dot{V}^2 \tag{3.27}$$

(e) Finally, the network is solved by applying the Kirchhoff laws (mass balance for the junctions and energy balance for meshes). Thus, the flow through each branch and the pumps power are obtained.

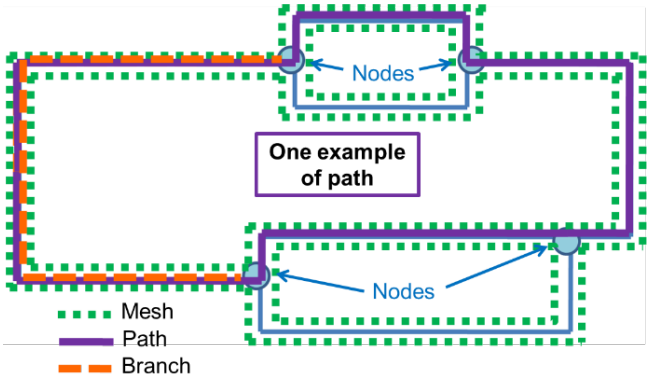

Figure 3.48: Mesh, path and branch sketch in the hydraulic circuits.

Figure 3.49 and Figure 3.50 show the coolant and oil circuits respectively in VEMOD. Main elements of both circuits are labelled in the diagrams. It can be observed that both circuits are driven by a respective pump and the oil temperature is dissipated by the oil cooler, connected to the coolant circuit as well.

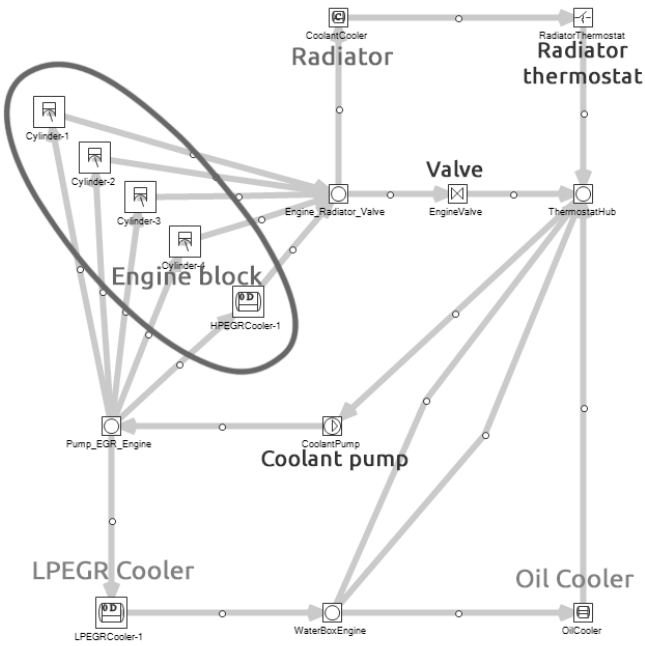

Figure 3.49: Coolant circuit diagram in VEMOD.

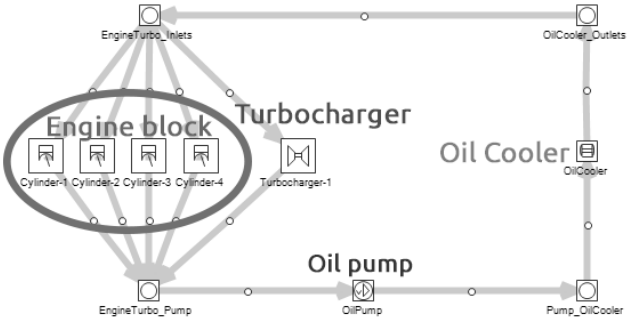

Figure 3.50: Oil circuit diagram in VEMOD.

2. The second part of the thermo-hydraulic model deals with the **calculation of the local temperature of the fluid**. In order to model the temperature distribution throughout the circuit, the fluid of each circuit (in the case of split cooling two independent circuits are considered) is divided into parcels. Each fluid parcel has a different temperature. Parcels are displaced and distributed among branches according to the flow rates calculated in the previous step. Temperature of the parcels is updated according to the heat provided by the heat exchanger mod-

els. In VEMOD, the heat exchangers model works independently of the hydraulic circuit model, even though they use results from each other. Thus, the heat exchangers model requires the flow and the inlet fluid temperature from the hydraulic circuit, and it provides the heat rejection to calculate the fluid heating or cooling in the exchanger. The efficiency of each heat exchanger is calculated considering the type of heat exchanger (shell and tubes, crossflow, etc.) and the flow characteristics Besides, it is possible to provide a tabulated exchanger efficiency. Finally, the heat transferred is obtained by applying the ε-NTU method [105]. In complex elements such as the engine block or the turbocharger, heat rejection is obtained with detailed lumped thermal networks. All heat transfer is assumed to take place in heat exchangers and so pipes and junctions are considered adiabatic.

3.2.8 Mechanical losses model

An existent dedicated friction and auxiliaries model [73] has been included in VEMOD to obtain the brake power from the indicated power. The calculation of the mechanical losses is required for the prediction of engine power as indicated in Equation 3.28.

$$\begin{aligned} N_{\mathrm{b}} &= N_{\mathrm{i}} - N_{\mathrm{p}} - N_{\mathrm{fr}} - N_{\mathrm{a}} \\ N_{\mathrm{fr}} &= N_{\mathrm{fr,\,piston}} + N_{\mathrm{fr,\,bearings}} + N_{\mathrm{fr,\,valvetrain}} \\ N_{\mathrm{a}} &= N_{\mathrm{fuel}} + N_{\mathrm{coolant}} + N_{\mathrm{oil}} \end{aligned} \tag{3.28}$$

In Equation 3.28, N represents the power and the subscripts b, i, p, fr and a stand for brake, indicated, pumping, friction and auxiliaries, respectively. Indicated and pumping power are computed from the instantaneous in-cylinder pressure and volume calculated by means of the 0D in-cylinder sub-model included in the gas dynamic model. Thus, friction and auxiliaries losses have to be determined.

The model considers two terms, on the one hand, the calculation of the friction due to engine elements with relative movement, N_{fr} in the piston

pack, bearings and valvetrain. Semi-empirical sub-models are used to calculate friction between piston pack and liner, bearings and valvetrains considering the kinematics, dynamics and tribological processes of each element. Detailed description of the model implemented can be found in the work done by Tormos et al. [73].

On the other hand, the calculation of the power required to drive the auxiliaries (N_a). Simple sub-models are used to determine the coolant, oil and fuel pumps power, taking into account information (flow and temperature) from the hydraulic circuits and fuel pump characteristics.

Other improvements have been implemented for the simulation of transient cycles at low ambient temperature. In this case the oil viscosity correlation, derived from the Vogel equation, has been modified to cover low temperatures (down to −35 °C). The new correlation implemented in VEMOD can be found in Equation 3.29, where μ_{oil} is the oil dynamic viscosity, T is the oil temperature, $K_1 = 2.2727e{-}4$, $K_2 = 894.0514$ and $K_3 = 153.7313$. This correlation has been fitted using available experiment data at CMT.

$$\mu_{oil} = K_1 \cdot \exp^{\frac{K_2}{T-K_3}} \tag{3.29}$$

3.2.8.1 Mechanical losses model calibration

To adjust the mechanical losses model, the total modelled losses are compared with the experimental ones as shown in Equation 3.30, where n is the engine speed and the subscripts exp and mod stand for experiment and model, respectively; and $k_{piston1}$, $k_{piston2}$, $k_{bearings}$ and $k_{valvetrain}$ are fitting constants.

$$\begin{aligned}(N_{fr} + N_a)_{exp} &= (N_{fr} + N_a)_{mod} \\ &= (k_{piston1} + k_{piston2} \cdot n) \cdot N_{fr,piston} + k_{bearings} \cdot N_{fr,bearings} \\ &\quad + k_{valvetrain} \cdot N_{fr,valvetrain} + N_a\end{aligned} \tag{3.30}$$

Since an experimental split of friction terms was not available, the calibration of the constants was performed simultaneously. No empirical correction of auxiliaries losses was done because their influence in the global losses is scarce, and the power required to run the fuel pump (the most important of all the auxiliaries terms) was independently calibrated with available data.

The calibration includes a complete swept of engine speed and load, resulting in the following values for the four fitting constants:

- $k_{\text{piston1}} = 2.8782$
- $k_{\text{piston2}} = 1.07\text{e}{-4}$
- $k_{\text{bearings}} = 3.0868$
- $k_{\text{valvetrain}} = 23.3821$

Figure 3.51 presents the results of the mechanical losses calibration. It can be concluded that there is a good agreement between the total modelled and experimental mechanical losses (represented by the black diamonds series). Also the detailed mechanical losses repartition in the reference engine is shown. As observed, friction losses increase with both the engine speed and load, where the piston assembly is the most important term. The effect of the speed is justified taking into account the higher relative velocity of all the elements. The effect of the load is mainly observed in the piston pack friction due to the higher in-cylinder pressure that affects the rings friction. Bearings and valvetrain friction losses are, in this order, less significant.

Regarding auxiliaries mechanical losses, coolant pump losses increase significantly with the engine speed. Even though the fuel pump losses also increases with the engine speed, in this case the effect of the load is clear: the higher the load is, the higher the losses are due to the rail pressure.

Once the mechanical losses model has been calibrated, the brake power can be obtained by adding their values to the net indicated power. As shown

in Figure 3.52, the global performance is good, but there are some discrepancies at low load and high engine speed where the maximum percentage error raises to 6 %.

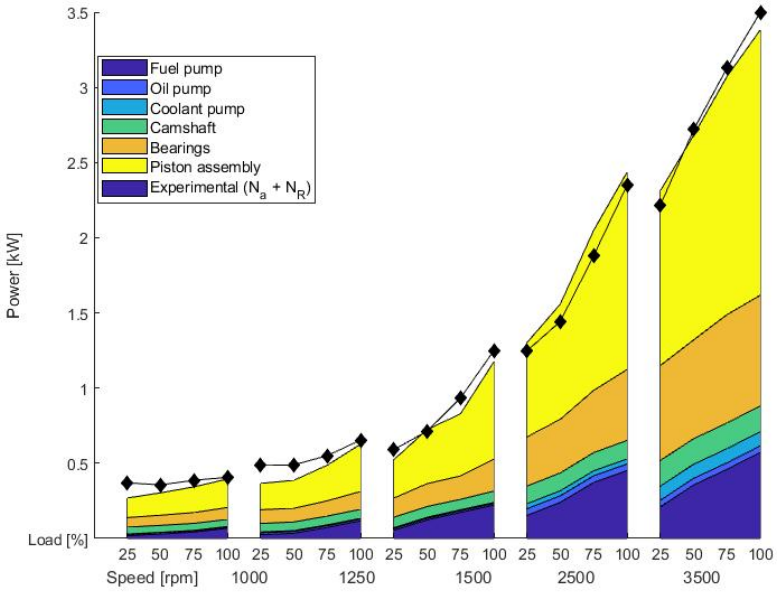

Figure 3.51: Friction and auxiliaries mechanical losses distribution.

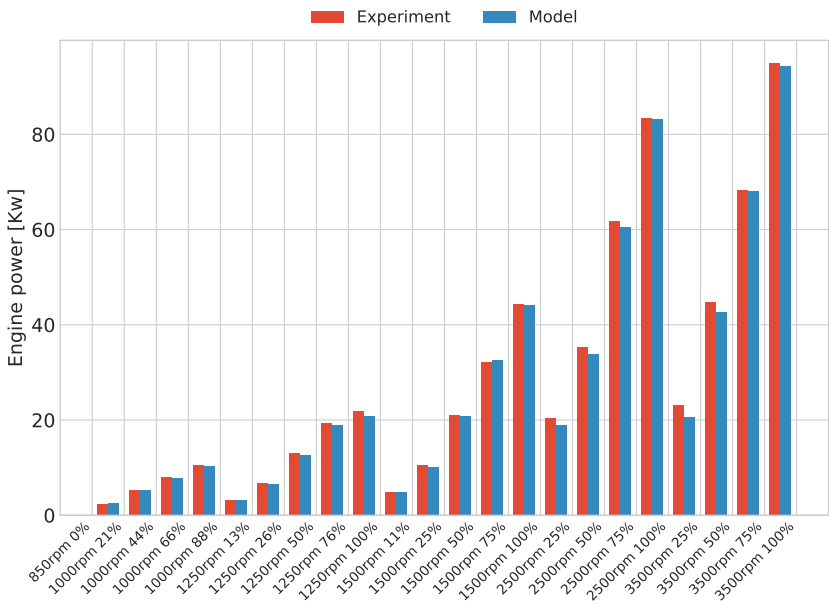

(a) Experimental and simulated brake power (kW).

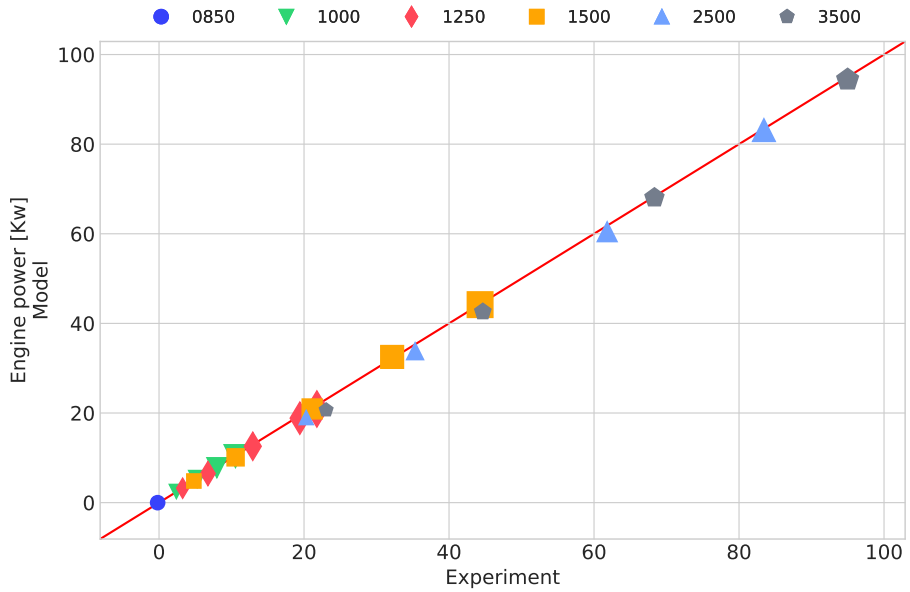

(b) Brake power model vs experiment.

Figure 3.52: *Experimental and simulated brake power comparison.*

3.2.9 Control, vehicle and driver models

The control sub-model allows controlling the operating point of the engine model, actuating as an engine control unit (ECU), operating the engine both in steady-state points and during transient evolutions. The flowchart of the vehicle, driver and control sub-model implemented in VEMOD was shown in Figure 3.1. This model is based on control algorithms built in Simulink that gather data from virtual sensors at certain parts of the virtual engine. These sensors measure all the required variables such as torque, coolant temperature, mass flow, pressure and temperature at different pipe locations or plenums, etc. The algorithms of control sub-model send the resulting values back to the the gas dynamics model by means of virtual actuators: engine speed, turbine rack position, valves position, injection pressure, and SOE and fuel mass of each injection pulse, etc. in order to simulate both stationary and transient tests.

The control sub-model is able to run simulations in three different

modes:

- **Imposing test bench data**. This mode corresponds to the simplest way to operate the engine model. Its purpose is to impose the same conditions as in the test bench engine to the virtual engine, so it is possible to validate the model performance. In this case, all injection settings (SOE, fuel mass split, injection pressure) are read from the experimental data and imposed to the injection model by means of the virtual actuators. Engine speed, intake manifold air mass flow (MAF) and pressure (MAP) are also set according to the experiment data. Low and high pressure EGR valves, back-pressure valve and turbine rack positions are set by the air loop control (MAF and MAP) as described in Figure 3.53. The experimental rack position of the variable geometry turbine (VGT) is used as the initial rack position and the control model actuates over it to achieve the intake pressure setpoint. Similarly, the model tweaks the different valve positions to keep the fresh air mass flow and the EGR. In the case of these valves, the position value is obtained from a map depending on the current engine speed and total fuelling rate, and later corrected by a PID controller. The P and I constants of the controllers are also obtained from similar maps included in the engine calibration. This calibration was created from the simulation of the 27 cases in the steady-state test matrix in Table 2.3 imposing the test bench settings.

- **Imposing engine speed and torque**. This mode requires the user defined engine speed and torque —both as a constant value for steady operation or a transient evolution. The torque control calculates the required fuel mass rate to achieve the torque target based on a calibration map. However, this fuel mass is limited by two filters: one ensures that the fuel mass does not exceed the one at full load for that engine speed, the other one limits the fuel mass to not surpass a certain fuel-air ratio to avoid an excessive soot formation. The flow-chart to obtain the fuel mass is indicated in the top part of Figure 3.54 by dashed border boxes. The other variables mentioned above concerning the injection settings are obtained by means of the calibration maps according to the current engine speed and the total fuel mass calculated in the

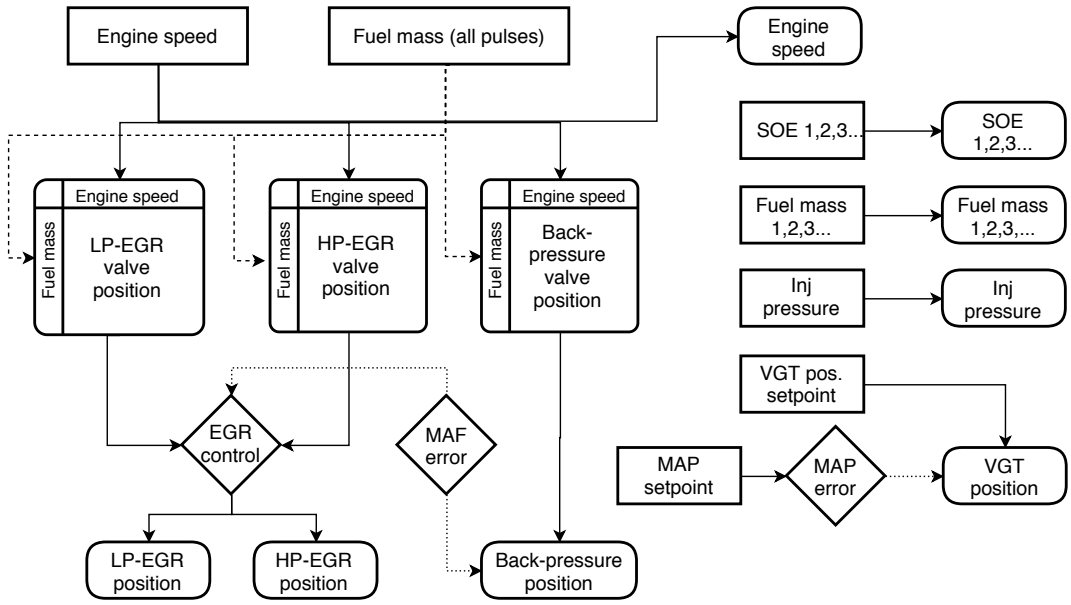

Figure 3.53: Flow-chart of the main output variables of the control model imposing test bench data. Rounded boxes correspond to the final actuator values.

step before. The air flow is controlled by a closed loop controller as in the previous mode. However, intake manifold pressure and mass flow (MAP and MAF), and VGT rack position initial setpoints are obtained from calibration maps, rather than from test bench data as before. The flow-chart of this control mode is sketched in Figure 3.54.

- **Imposing engine speed and fuel mass**. This mode is pretty similar as the previous one imposing torque. In this case, total fuel mass is a user input; so the calculation of the total fuel mass is omitted since torque is an output and not an input as in the previous mode. Figure 3.54 still represents the flow-chart of this control mode skipping the fuel filters sketched by dashed border boxes.

Other parameters and controllers are included in the model and the calibration, such as the ambient and coolant temperature sensor readings to switch from LP-EGR to HP-EGR and vice versa. The control flow-charts shown represent a summarised view of this control sub-model.

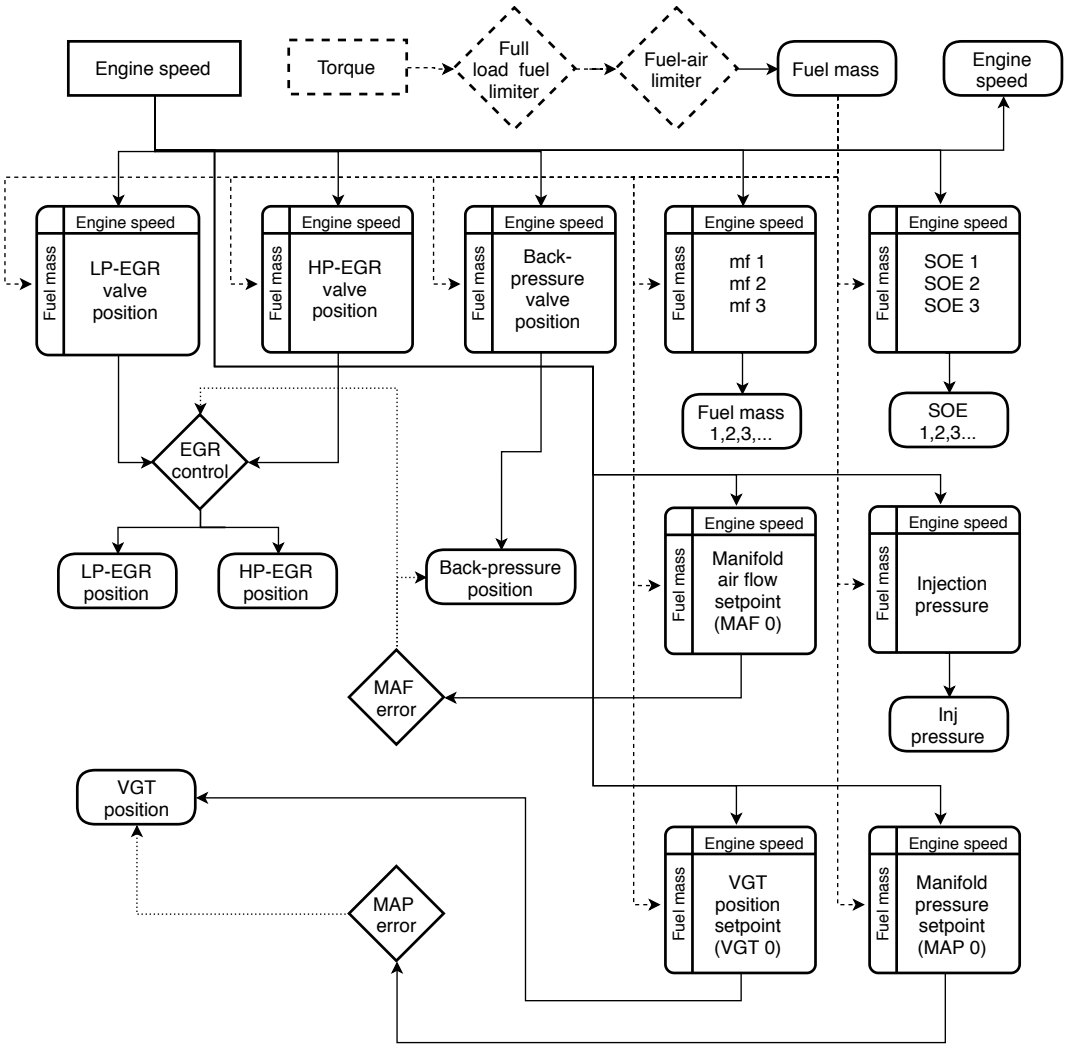

Figure 3.54: *Flow-chart of the main output variables of the control model imposing only engine speed and torque or fuel mass. Rounded boxes correspond to the final actuator values.*

The vehicle control includes a clutch model represented by the expressions in Equation 3.31, where M stands for torque $k(t)$ is coupling ratio from 0 to 1 imposed by the driver model, p_{max} is the maximum coupling pressure and S, μ_{clutch} and μ_{clutch} are the contact area between friction discs, the disc friction coefficient and the average radius of the clutch disc, respectively. The clutch model distinguishes between clutch slip and no clutch slip situations.

$$\begin{cases} M_{clutch}(t) = M_{engine}(t) \quad if \ M_{max}(t) \geq |M_{engine}(t)| \\ M_{clutch}(t) = M_{max}(t) \quad if \ M_{max}(t) < |M_{engine}(t)| \end{cases} \tag{3.31}$$
$$M_{max}(t) = k(t) \cdot p_{max} \cdot S \cdot \mu_{clutch} \cdot r_{clutch}$$

Another system that has been modelled is the gearbox, whose torque transferred to the gearbox M_{gb} is defined in Equation 3.32, where r_{gb} is the transmission ratio and k_{gb} is a factor depending on the gearbox efficiency (η_{gb}), the operation temperature (T), the inlet shaft speed ($\omega_{gb,in}$) and the torque (M_{clutch}).

$$M_{gb} = k_{gb} \cdot r_{gb} \cdot M_{clutch}(t)$$
$$\begin{cases} k_{gb} = \eta_{gb} \cdot (T, gear, \omega_{gb,in}, |M_{clutch}|) \quad if \ M_{clutch}(t) \geq 0 \\ k_{gb} = \frac{1}{\eta_{gb} \cdot (T, gear, \omega_{gb,in}, |M_{clutch}|)} \quad if \ M_{clutch}(t) < 0 \end{cases} \tag{3.32}$$

The vehicle dynamics model, which computes the instantaneous vehicle velocity, is fed with the gear box torque output and vehicle —data such as vehicle mass and front area, wheel effective radius, gearbox shafts inertia, etc.— and track information. The last one is important to account for the track grade (vertical angle of the road to apply the force balance in the vehicle), the track radius (curvature radius of the track that affects the rolling resistance), and the wind speed and direction to calculate the aerodynamic resistance. Vehicle control and dynamic properties have been set according to the available information from the engine supplier.

Finally, the driver model and logic consists of two parallel PID depending on active drive and logic. It is important to note that VEMOD can simulate any steady-state operating point without employing the control system sub-model, just by setting the target value of each actuator within the engine model. If a transient evolution is simulated, then the control system sub-model has to be used, but the system can be run without making use of the vehicle model by setting the speed and torque. This way the model becomes a highly flexible tool.

3.3 Validation of the virtual engine model

This section presents the validation process of the virtual engine model and the results at transient operating conditions. Recalling section 3.2, VEMOD is composed of different sub-models which were already developed in CMT and have been refined and adapted to model transient operating conditions. So first of all, the transient validation of some sub-models is presented, followed by the results of the complete virtual engine model.

3.3.1 Validation of the turbocharger model

The turbocharger model has been validated using engine load transients. In these tests the engine is stabilised at very low load and suddenly moves to full load. From the point of view of the turbocharger, the different parameters undergoes a lag due to its mechanical and thermal inertia. The results are also compared to those obtained using a turbocharger model based on maps. The main benefits of the turbocharger model included in the virtual engine are observed in turbine inlet and outlet temperatures, in particular in the predicted turbine temperature drop.

Figure 3.55 shows two load transients at different engine speeds (1250 and 2000 rpm). The experimental temperature was measured using a very low inertia transducer (an RTD with a measurement range from −75 °C to 850 °C) able to register transient evolution. The evolution of the turbine inlet and turbine outlet temperatures during the test has been compared

to the experimental data, the results obtained using a typical map-based model and the results provided by the turbocharger model proposed in VEMOD. T3 corresponds to the turbine inlet temperature and, in the case of the model one, is obtained by the engine model, so the turbocharger sub-model has been simulated along with the engine (injection, combustion and heat rejection) model. As it can be observed, the use of a map-based model (red line) underestimates the temperature drop in the turbine. Contrarily, the use of a heat transfer model (green line), as the one included in the model proposed, improves the prediction of the turbine outlet temperature, which is essential for the operation of the after-treatment system placed downstream the turbine.

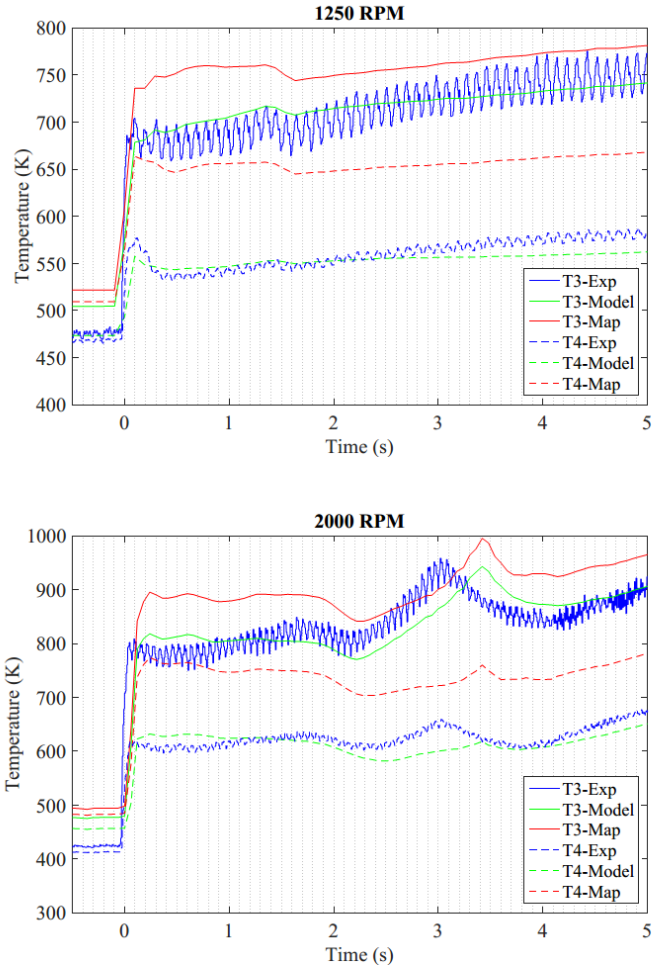

Figure 3.55: Turbine inlet and outlet temperatures during a load transient at 1250 and 2000 rpm.

3.3.2 Validation of the after-treatment systems model

In order to validate the performance of the after-treatment models, the calibrated DOC and DPF models were applied to the simulation of a WLTC run at ambient temperature. In this case the models were run without the rest of the VEMOD, using pressure upstream and downstream, temperature at the inlet and emissions at the inlet as boundary conditions. The discrepancy in the experimental and modelled inlet composition is due to the numerical uncertainty related with the gas diffusion in the intake pipe considered in the model (this phenomena concerns only at transient operating conditions). Figure 3.56 shows the experimental and modelled cumulative HC and CO emissions at both inlet and outlet boundaries of the DOC. The series are normalised with respect to the experimental accumulated emissions of every chemical specie at the DOC inlet side and at the end of the WLTC. As it can be observed, high accuracy is obtained during the whole WLTC, which requires good sensitivity to temperature, in terms of oxidation but also adsorption and desorption of HC, pore diffusion and mass transfer effects.

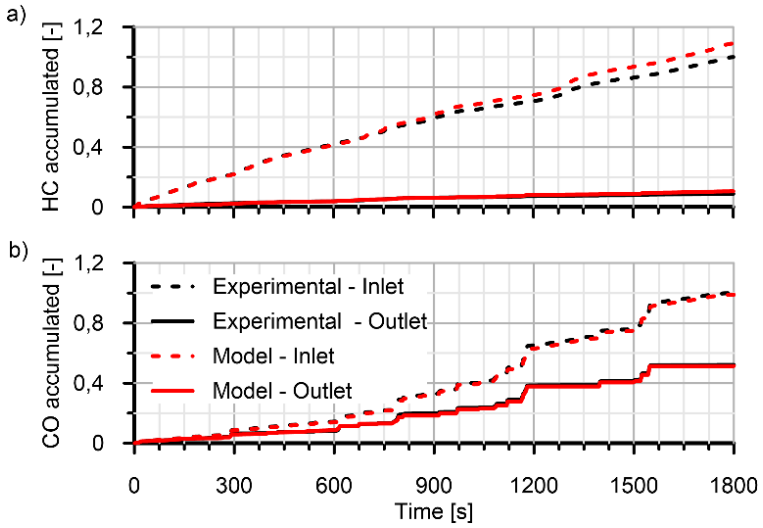

Figure 3.56: HC and CO cumulative emissions over the WLTC.

To complete the analysis, the DPF model response during WLTC driving conditions is evaluated. The DOC model, whose performance has been discussed above, determines the DPF inlet flow conditions. As shown in Figure 3.57 (a), the tailpipe gas temperature is predicted showing very good

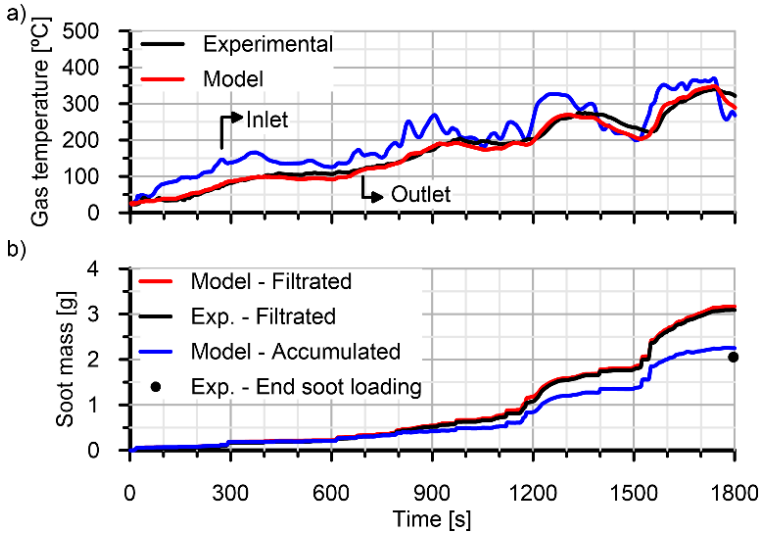

Figure 3.57: *DPF outlet gas temperature (a) and cumulative soot collected (b) over the WLTC cycle.*

agreement with experimental data (blue line represents tne DPF inlet temperature). In addition, Figure 3.57 (b) shows the soot accumulation into the DPF, which began the test free of soot deposits. In Figure 3.57 (b), the model filtrated soot mass shows very good agreement with the experimental results, which is obtained from the inlet to outlet difference in soot mass flow measurements. The experimental data are completed with the end soot load remaining into the DPF, which is based on DPF weighing data. The model provides the instantaneous amount of soot accumulated into the DPF, which is quantified as the difference between filtrated and regenerated soot mass. Since only the NO_x concentration was measured, 80 % of the NO_2 to NO_x ratio in equilibrium conditions was assumed in this test in order to define the NO_2 concentration at the DPF inlet. It is shown that the predicted final amount of soot mass into the DPF is 2.25 g, which is very close to the experimental value of 2.05 g. This good agreement provides high confidence on the potential of the presented tool to explore thermal management and DPF design strategies to enhance the passive regeneration performance.

3.3.3 Validation of the complete virtual engine model

The final validation at transient operating conditions has been carried out by means of the simulation of the WLTC cycle. In order to focus the analysis on the engine model performance, the WLTC simulations were performed by imposing some experimental values (engine speed and injection settings) while air mass flow and boost pressure are set as target to be follow at every instant by the control system, as indicated in subsection 3.2.9 (imposing test bench data).

Regarding the simulation of the WLTC, it is not only interesting to evaluate the model output prediction, but also the model response to engine speed and load variations. Thus, the first evaluation deals with the evolution of two main variables, the air mass flow and the boost pressure, when trying to follow the setpoints measured at the test bench, thus assessing the accuracy of the control model. The air mass flow variations shown in Figure 3.58 over time are well followed by the model, even though there are slightly higher model values at idle and low load over the low speed stage of the cycle. During this time, the engine is regulating the high pressure EGR valve and this mismatch constitutes a compromise between an accurate air flow response at idle and an accurate response during the peak demands when operating with this EGR valve opened. Nonetheless, the symmetric mean average percent error (SMAPE) —expressed in Equation 3.33 as a version of the one proposed by Flores [106] and where F is the forecast and A the actual value— is 5.2 % for the total WLTC.

$$SMAPE\,(\%) = \frac{\sum_{t=1}^{n} |F_t - A_t|}{\sum_{t=1}^{n} (F_t + A_t)} \cdot 100 \tag{3.33}$$

The agreement between modelled and experimental air mass flow can be better observed in Figure 3.59 where the blue dots, corresponding to the air mass flow during the low speed stage, fall to the model side of the bisector. Anyway, the coefficient of determination (R^2) is 0.947, which represents a good prediction, and 90 % of the points present an absolute error below 5.2 g/s.

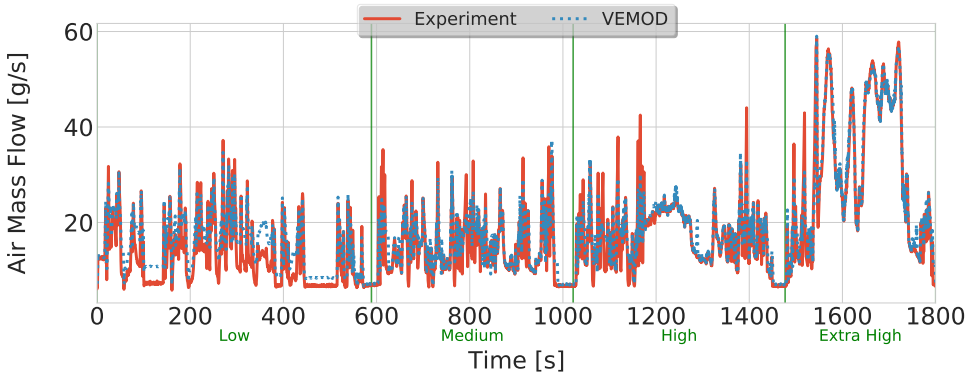

Figure 3.58: Air mass flow during the WLTC at 20 °C room temperature.

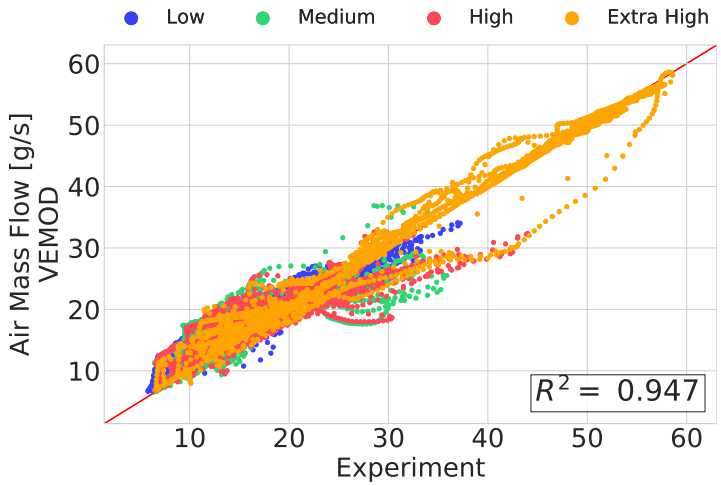

Figure 3.59: Modelled vs experimental air mass flow during the WLTC at 20 °C room temperature.

A similar behaviour is observed in the compressor outlet pressure evolution shown in Figure 3.60. In this case the model peak values are higher at low load and the agreement between model and experiment is accurate in the extra high speed stage. The SMAPE for the whole WLTC cycle is 1.35 % and the R^2 is 0.947 (Figure 3.61). If both speed stages are analysed independently, the R^2 during the low speed stage is 0.757, while coefficient of determination in the extra high speed stage is 0.983. During 90 % of the time, the SMAPE is below 3.39 %.

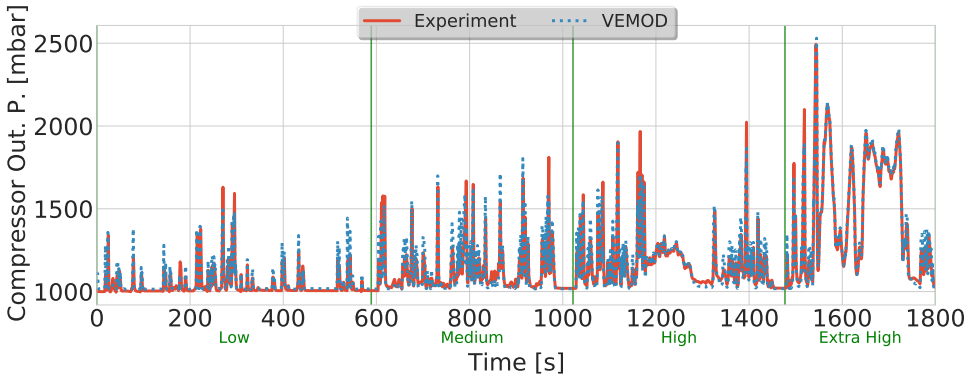

Figure 3.60: Compressor outlet (boost) pressure during the WLTC at 20 °C room temperature.

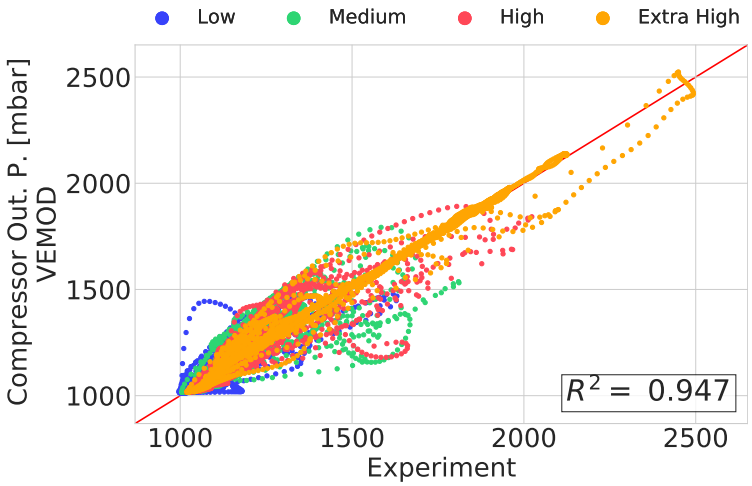

Figure 3.61: Modelled vs experimental compressor outlet (boost) pressure during the WLTC at 20 °C room temperature.

Figure 3.62 and Figure 3.63 show the torque evolution over time at 20 °C and at −7 °C test cell temperature. It can be observed that the prediction is quite accurate, with coefficients of determination of 0.937 and and 0.936 respectively, and the model response to the dynamic variations are well followed. As stated in subsection 3.2.3, in cold starting the glow plug effect is considered in terms of the heat contribution and reduction of ignition delay, thus ensuring the suitable engine combustion. However, in the cold WLTC (starting at −7 °C), some issues due to misfiring cycles after the end of glow plug energising were detected, resulting in a torque abatement. The combustion model was refined to fix this problem. In terms of error evaluation,

the SMAPE error is 9.8 % for the whole WLTC at 20 °C, whilst the error at cold conditions (−7 °C) is 11.2 %.

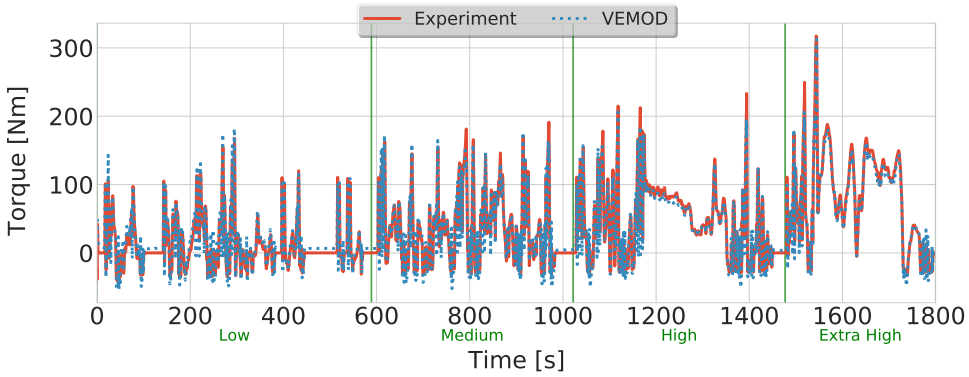

Figure 3.62: Brake torque during the WLTC at 20 °C room temperature.

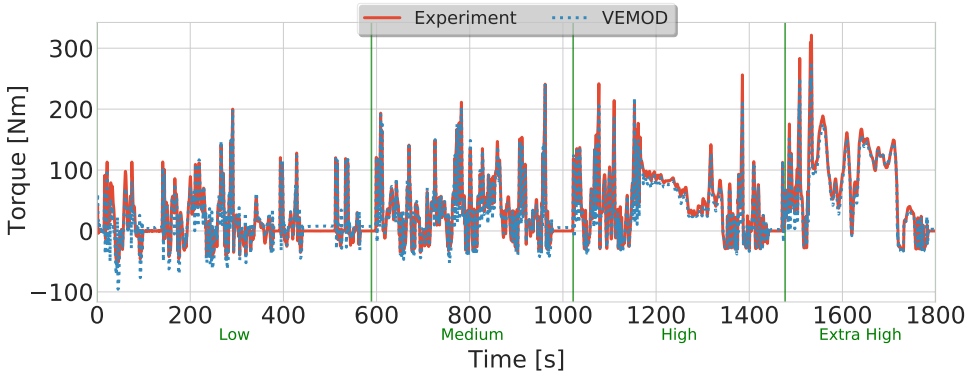

Figure 3.63: Brake torque during the WLTC at −7 °C room temperature.

Turbine outlet temperature, shown in Figure 3.64 and Figure 3.65 presents a good model response to variations. However, the model is more sensitive to these changes and responses with higher maximum and lower minimum values. The coefficient of determination at a room temperature of 20 °C is 0.904 and the one at −7 °C is 0.910. It is observed that the initial predicted turbine outlet temperature differs from the initial experimental value (more evident in Figure 3.65). This is mainly due to fact that the initial predicted temperature corresponds to the exhaust hot gases at the first simulated cycle, while the initial experimental temperature is the ambient one. Moreover, since the thermocouple has a specific thermal inertia, the instantaneous predicted temperature evolution (which is more responsive

than the graphed one) has been filtered by applying a moving average, trying to reproduce the sensor behaviour. At a room temperature of 20 °C, 80 % of the points are predicted with a SMAPE error below 8.9 %. The SMAPE for 80 % of the points at a room temperature of −7 °C is below 10.9 %.

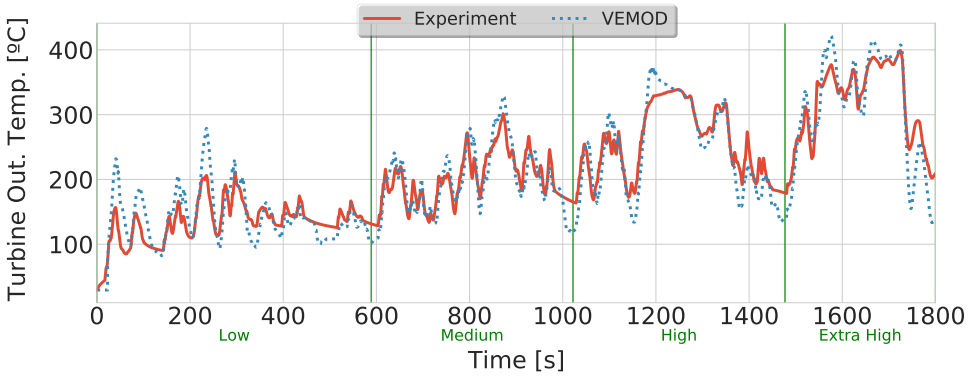

Figure 3.64: Turbine outlet temperature during the WLTC at 20 °C room temperature.

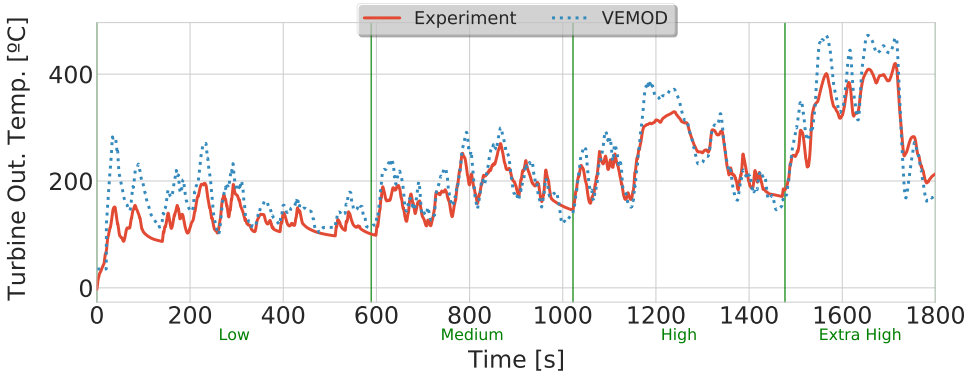

Figure 3.65: Turbine outlet temperature during the WLTC at −7 °C room temperature.

Regarding pollutant emissions, CO_2 variations are well followed and its prediction is accurate as shown in Figure 3.66 and Figure 3.68, where the CO_2 mass flow is plotted along the whole WLTC. In this case, the coefficient of determination of the model prediction is 0.981 at 20 °C and 0.966 at −7 °C.

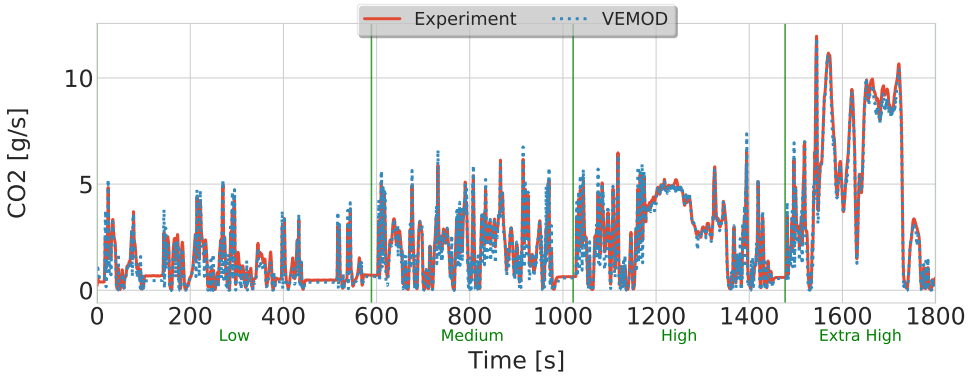

Figure 3.66: CO_2 mass flow during the WLTC at 20 °C room temperature.

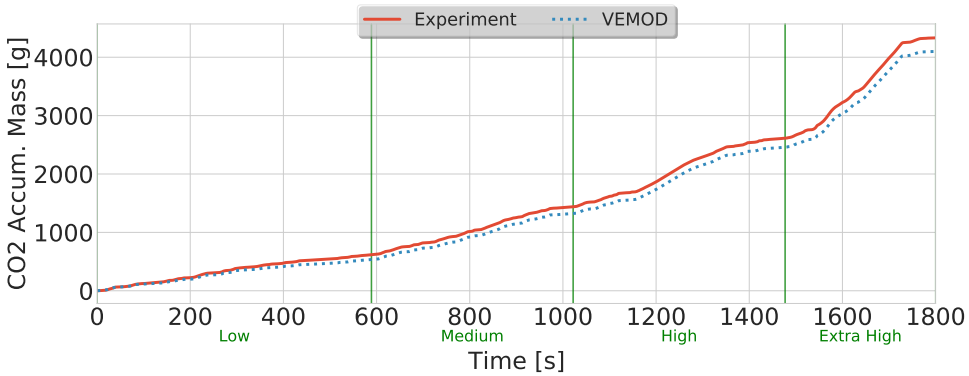

Figure 3.67: Accumulated CO_2 mass during the WLTC at 20 °C room temperature.

As observed in Figure 3.67 and Figure 3.69, the predicted CO_2 accumulated mass fits well the real behaviour, although the model slightly underestimates the CO_2 formation (which is directly related to the fuel consumption) at 20 °C and overestimates it at −7 °C. Nevertheless, SMAPE error for the total cycle is 3.6 % when starting the engine at 20 °C and 5.4 % at −7 °C.

By contrast, NO_x prediction shown in Figure 3.70 (at 20 °C) and in Figure 3.72 (at −7 °C) is not so accurate, specially in cold ambient conditions where it is clearly overestimated until the extra high speed stage. At ambient temperatures below zero, the activation of the intake glow plugs are modelled by modifying the ignition delay during 150 seconds. After this time, the accumulated error is rather constant until the extra high speed stage. At 20 °C, the prediction is slightly overestimated, specially at the end of the extra high speed stretch where more NO_x emissions are produced.

The coefficient of determination are 0.479 at 20 °C and 0.756 at −7 °C. Regarding the error, the SMAPE is 8.9 % for the whole test cycle at room ambient conditions (Figure 3.71) and 15.2 % at cold conditions (Figure 3.73).

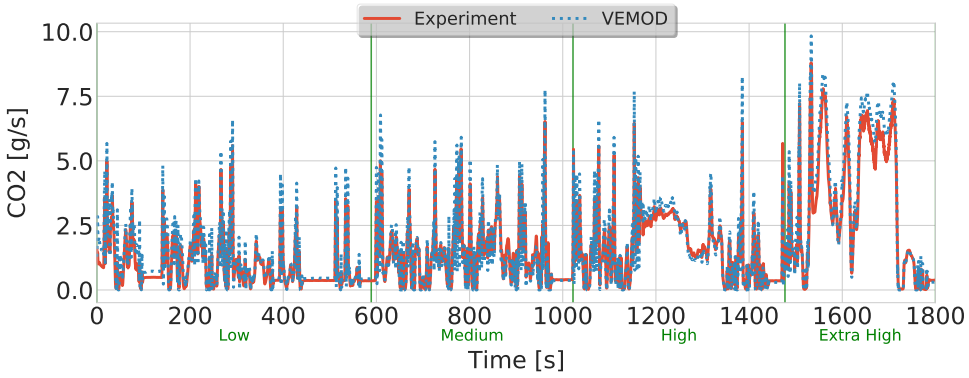

Figure 3.68: *CO_2 mass flow during the WLTC at −7 °C room temperature.*

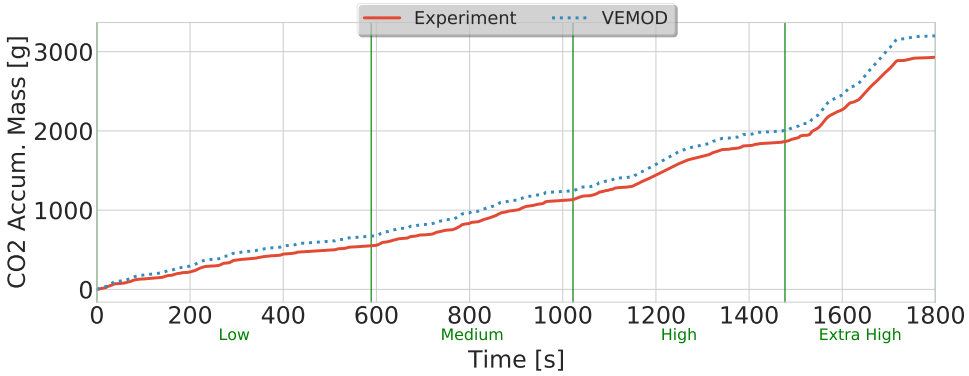

Figure 3.69: *Accumulated CO_2 mass during the WLTC at −7 °C room temperature.*

Although the prediction is acceptable at 20 °C —both with the engine already warm and cold— the prediction at a room temperature of −7 °C should be improved and there is room to find a better solution with the current physicochemical model proposed in subsubsection 3.2.4.1, by re-adjusting the three calibration constants presented in that model.

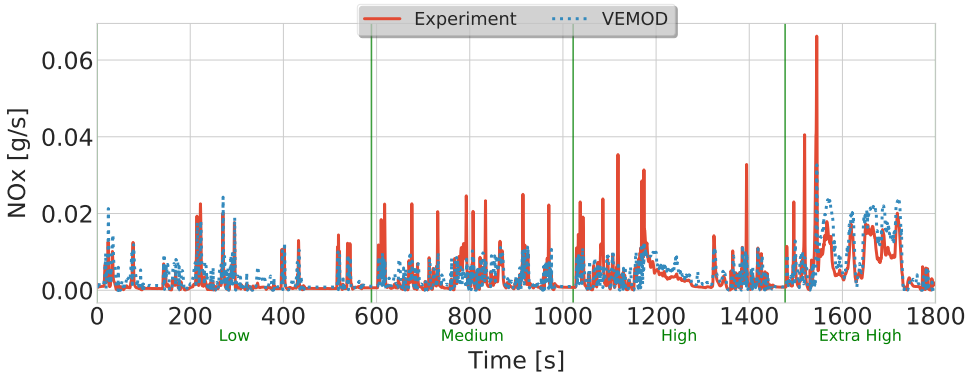

Figure 3.70: NO_x mass flow during the WLTC at 20 °C room temperature.

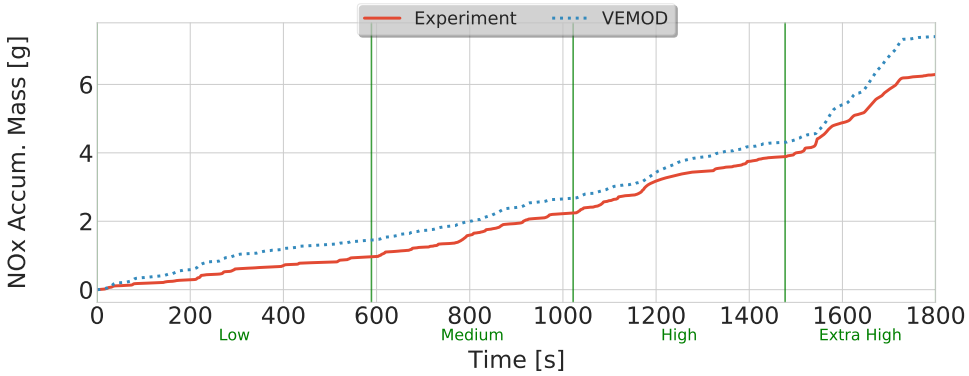

Figure 3.71: Accumulated NO_x mass during the WLTC at 20 °C room temperature.

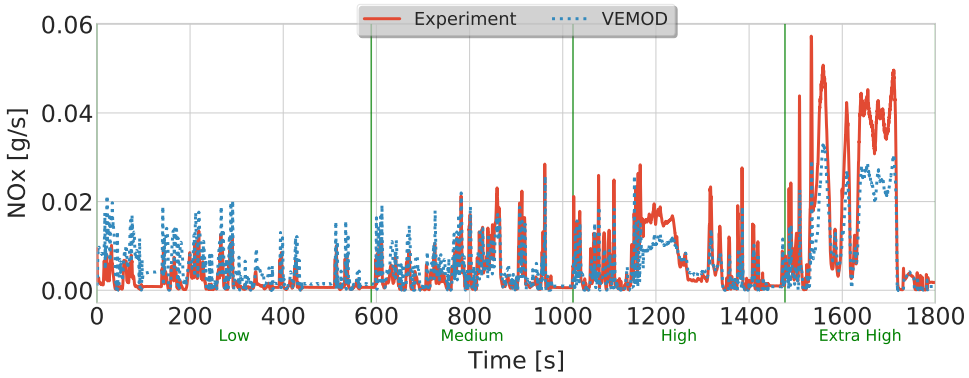

Figure 3.72: NO_x mass flow during the WLTC at −7 °C room temperature.

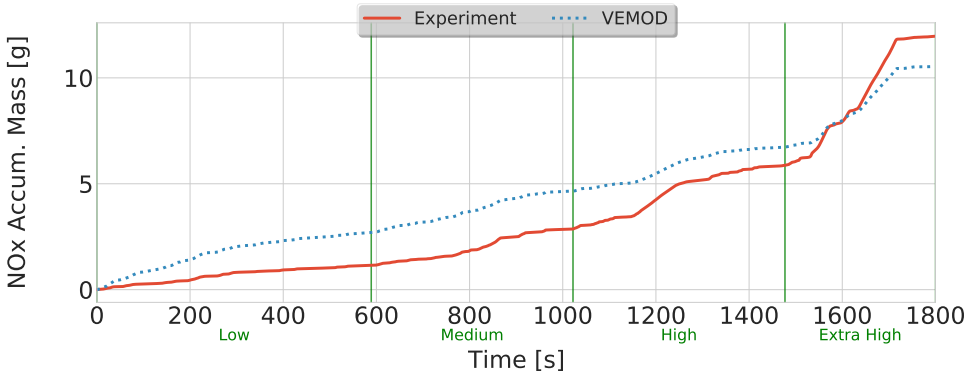

Figure 3.73: Accumulated NO_x mass during the WLTC at −7 °C room temperature.

Regarding the thermal analysis of the engine, a comparison between measured and simulated oil temperature is presented in Figure 3.74 and Figure 3.75 at both room temperature conditions in the test cell. At 20 °C, the model matches the experimental temperature evolution quite good with an R^2 of 0.998. However, at cold conditions (−7 °C), the model starts to increase the oil temperature faster than the experimental one, although later both slopes are similar. This is caused by the heat repartition in the engine block. At these cold conditions, the model is underestimating the heat transferred from the block to the ambient and, consequently, overestimating the heat amount dissipated by the oil. The coefficient of determination at a room temperature of −7 °C is 0.981. In terms of error evaluation, the SMAPE is 0.6 % for the test at 20 °C and 7.8 % at −7 °C.

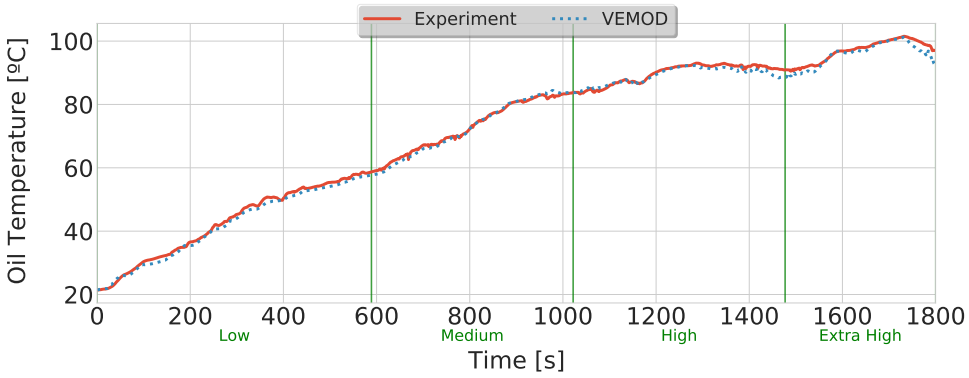

Figure 3.74: Oil temperature at engine outlet during the WLTC at 20 °C room temperature.

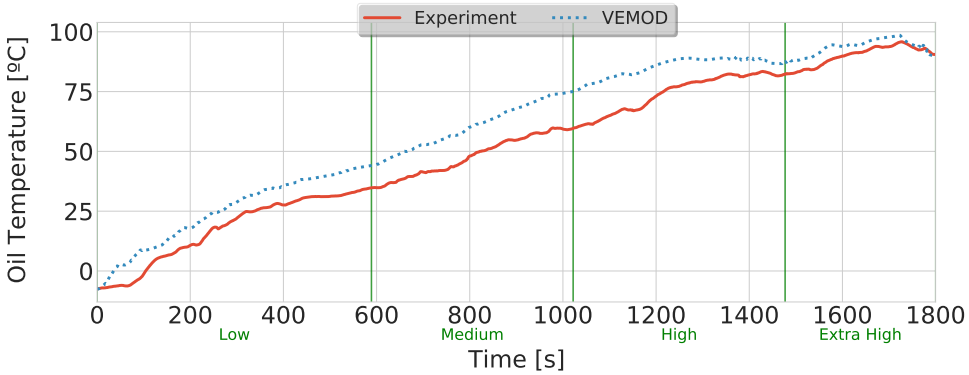

Figure 3.75: Oil temperature at engine outlet during the WLTC at −7 °C room temperature.

Finally, the prediction of coolant temperature during the WLTC is assessed in Figure 3.76 and Figure 3.77. Similarly as happened to the oil temperature, during the engine warm-up (until 80-85 °C) the model is underestimating the heat transferred from the block to the ambient and, thus the coolant temperature is higher during this stage in cold conditions. The prediction is assessed with a coefficient of determination of 0.997 —at a room temperature of 20 °C— and 0.966 in cold conditions (−7 °C). In the case of the coolant prediction, the error (indicated by the SMAPE) is 1.9 % at 20 °C and 6.1 % for the test at −7 °C.

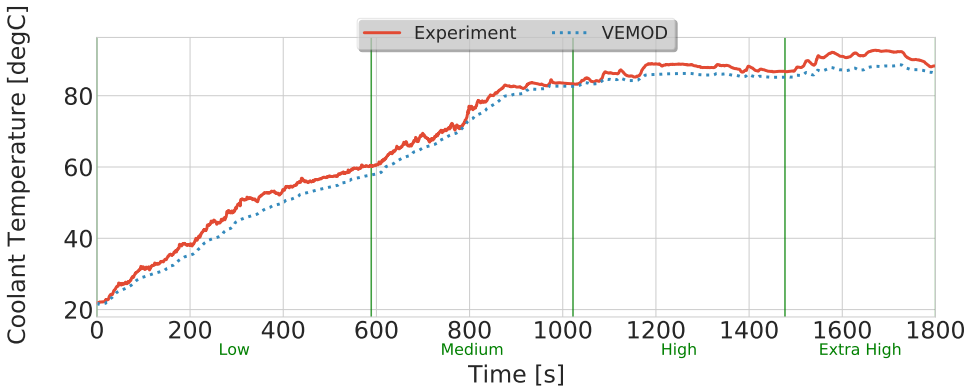

Figure 3.76: Coolant temperature at engine outlet during the WLTC at 20 °C room temperature.

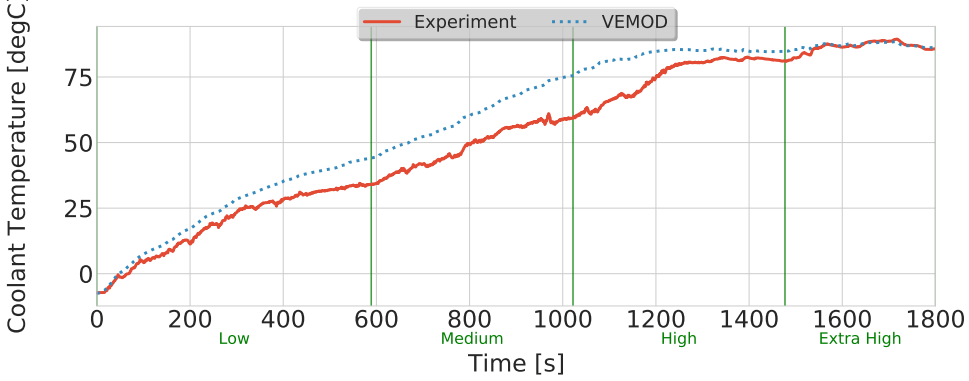

Figure 3.77: Coolant temperature at engine outlet during the WLTC at −7 °C room temperature.

3.4 Conclusions

In this chapter, a complete engine model developed in CMT-Motores Térmicos has been described. The model allows the possibility to perform multiple studies and imposing different boundary conditions like simulating high altitude and low temperature operating conditions like those presented in the RDE type approval test.

All the sub-models presented in VEMOD have been developed and calibrated individually as described in their respective sections in this chapter. After this process, the complete engine model has been validated with ex-

perimental tests under steady and transient conditions. The model is able to predict key engine variables like torque, intake pressure, turbine outlet temperature, coolant temperature and also CO_2 and NO_x emissions.

The result of the work carried out is a standalone tool, that can be coupled with Matlab/Simulink, able to reproduce experimental conditions or a completely predictive evolution including the vehicle and using engine settings from the virtual ECU, providing reliable results with acceptable precision.

With the aim of developing solutions for reducing tailpipe emissions, specially during the cold engine start, the virtual engine model tool is exploited in the following chapters. Thus, in chapter 4 and chapter 5, variable valve timing is proposed as a way to increase exhaust temperature for a faster warm-up of the oxidation catalyst. In chapter 6 the thermal insulation of different sections of the exhaust line is explored for the same purpose.

Chapter 3 References

[32] CMT – Motores Térmicos, Universitat Politècnica de València. *OpenWAM*. Accessed 2020-10-26 at http://openwam.webs.upv.es/docs/. 2016 (cit. on p. 39).

[33] J. M. Corberán. "Contribución al modelado del proceso de renovación de la carga en motores de combustión interna alternativos." PhD thesis. Universitat Politècnica de València, 1984 (cit. on p. 39).

[34] R. S. Benson and N. D. Whitehouse. *Internal Combustion Engines: A Detailed Introduction to the Thermodynamics of Spark and Compression Ignition Engines, Their Design and Development, Volume 1*. 1979. isbn: 1483140024 (cit. on p. 39).

[35] J. M. Desantes, M. D. Chust, and J. Llorens. "Análisis comparativo de métodos numéricos para la resolución del flujo no estacionario en colectores de motores de combustión interna alternativos". *II Congreso de Métodos Numéricos en Ingeniería*. 1993 (cit. on p. 39).

[36] F. Payri, J. Galindo, J. R. Serrano, and F. J. Arnau. "Analysis of numerical methods to solve one-dimensional fluid-dynamic governing equations under impulsive flow in tapered ducts". *International Journal of Mechanical Sciences*, 46 (7), (2004), pp. 981 –1004. issn: 0020-7403. doi: https://doi.org/10.1016/j.ijmecsci.2004.07.014 (cit. on p. 39).

[37] F. Payri, J. M. Desantes, and J. M. Corberán. "A quasi-steady model on gas exchange process, some results". *Motor Sympo'88*. 1988 (cit. on p. 39).

[38] F. Payri, J. Benajes, and M. Reyes. "Modelling of supercharger turbines in internal-combustion engines". *International Journal of Mechanical Sciences*, 38 (8-9), (1996), pp. 853–869. issn: 00207403. doi: 10.1016/0020-7403(95)00105-0 (cit. on p. 39).

[39] F. Payri, J. Galindo, and J. R. Serrano. "Variable geometry turbine modelling and control for turbocharged diesel engines transient operation". *THIESEL 2000*. Thermo- and Fluid-dynamic Processes in Diesel Engines, 2000. doi: 10.1243/09544070260137507 (cit. on p. 39).

[40] M. Á. Reyes. "Contribución al modelado del proceso de transferencia de calor en colectores de escape de motores alternativos". PhD thesis. Universitat Politècnica de València, 1994 (cit. on pp. 39, 49).

[41] J. R. Serrano. "Análisis y modelado del transitorio de carga en motores turboalimentados de encendido por compresión". PhD thesis. Universitat Politècnica de València, 1999 (cit. on p. 39).

[42] J Galindo, J. R. Serrano, H Climent, and F. J. Arnau. "New one-dimensional fluid-dynamic model for automotive intercoolers". *Conference A proceeding of 8th European Automotive Congress (EAEC)*. 2001 (cit. on p. 39).

[43] J. Galindo. "Diseño de uniones de colectores de escape de motores alternativos". PhD thesis. Universitat Politècnica de València, 1998 (cit. on p. 39).

[44] F. Payri, E. Reyes, and J. R. Serrano. "A model for load transients of turbocharged diesel engines". *International Congress & Exhibition*. SAE International, 1999. doi: 10.4271/1999-01-0225 (cit. on p. 39).

[45] J. Benajes, J. M. Luján, V. Bermúdez, and J. R. Serrano. "Modelling of turbocharged diesel engines in transient operation. Part 1: Insight into the relevant physical phenomena". *Proceedings of the Institution of Mechanical Engineers, Part D: Journal of Automobile Engineering*, 216 (5), (2002), pp. 431–441. issn: 09544070. doi: 10.1243/0954407021529237 (cit. on p. 39).

[46] F. Payri, J. Benajes, J. Galindo, and J. R. Serrano. "Modelling of turbocharged diesel engines in transient operation. Part 2: Wave action models for calculating the transient operation in a high speed direct injection engine". *Proceedings of the Institution of Mechanical Engineers, Part D: Journal of Automobile Engineering*, 216 (6), (2002), pp. 479–493. doi: 10.1243/09544070260137507 (cit. on p. 39).

[47] J. Galindo, J. R. Serrano, F. J. Arnau, and P. Piqueras. "Description of a semi-independent time discretization methodology for a one-dimensional gas dynamics model". *Journal of Engineering for Gas Turbines and Power*, 131 (3), (2009). 034504. issn: 07424795. doi: 10.1115/1.2983015 (cit. on p. 43).

[48] R. J. LeVeque. *Finite Volume Methods for Hyperbolic Problems*. Cambridge University Press, 2002. doi: 10.1017/cbo9780511791253 (cit. on p. 43).

[49] S. K. Godunov. "A difference method for numerical calculation of discontinuous solutions of the equations of hydrodynamics [English title page]". *Matematicheskii Sbornik*, (1959) (cit. on p. 43).

[50] B. van Leer. "Towards the ultimate conservative difference scheme. V. A second-order sequel to Godunov's method". *Journal of Computational Physics*, 32 (1), (1979), pp. 101–136. issn: 10902716. doi: 10.1016/0021-9991(79)90145-1 (cit. on p. 43).

[51] E. F. Toro, M. Spruce, and W. Speares. "Restoration of the contact surface in the HLL-Riemann solver". *Shock Waves*, 4 (1), (1994), pp. 25–34. issn: 1432-2153. doi: 10.1007/BF01414629 (cit. on p. 43).

[52] R. Courant, K. Friedrichs, and H. Lewy. "Über die partiellen Differenzengleichungen der mathematischen Physik". *Mathematische Annalen*, 100 (1), (1928), pp. 32–74. issn: 1432-1807. doi: 10.1007/BF01448839 (cit. on p. 45).

[53] C. Depcik and D. Assanis. "A universal heat transfer correlation for intake and exhaust flows in an spark-ignition internal combustion engine". *SAE 2002 World Congress & Exhibition*. SAE International, 2002. doi: 10.4271/2002-01-0372 (cit. on p. 49).

[54] R. Santos. "Estudio del aprovechamiento de la energía de los gases de escape en motores diésel". PhD thesis. Universitat Politècnica de València, 1999 (cit. on p. 49).

[55] S. W. Churchill and M. Bernstein. "A correlating equation for forced convection from gases and liquids to a circular cylinder in crossflow". *Journal of Heat Transfer*, 99 (2), (1977), pp. 300–306. issn: 15288943. doi: 10.1115/1.3450685 (cit. on p. 49).

[56] V. Dolz. "Contribución al Modelado de la transmisión de calor en los MCIA y su aplicación en el aprovechamiento energético de los gases de escape durante los transitorios de carga". PhD thesis. Universitat Politècnica de València, 2006 (cit. on p. 49).

[57] J. R. Serrano, F. J. Arnau, L. M. García-Cuevas, A. Dombrovsky, and H. Tartoussi. "Development and validation of a radial turbine efficiency and mass flow model at design and off-design conditions". *Energy Conversion and Management*, (2016). issn: 01968904. doi: 10.1016/j.enconman.2016.09.032 (cit. on p. 49).

[58] J. Galindo, R. Navarro, L. M. García-Cuevas, D. Tarí, H. Tartoussi, and S. Guilain. "A zonal approach for estimating pressure ratio at compressor extreme off-design conditions". *International Journal of Engine Research*, 20 (4), (2019), pp. 393–404. doi: 10.1177/1468087418754899 (cit. on p. 49).

[59] J. Galindo, A. Tiseira, R. Navarro, D. Tarí, H. Tartoussi, and S. Guilain. "Compressor Efficiency Extrapolation for 0D-1D Engine Simulations". SAE International, 2016. doi: 10.4271/2016-01-0554 (cit. on p. 49).

[60] J. R. Serrano, P. Olmeda, F. J. Arnau, and V. Samala. "A holistic methodology to correct heat transfer and bearing friction losses from hot turbocharger maps in order to obtain adiabatic efficiency of the turbomachinery". *International Journal of Engine Research*, 21 (8), (2020), pp. 1314–1335. issn: 20413149. doi: 10.1177/1468087419834194 (cit. on p. 49).

[61] O. Leufvén. "Modeling for control of centrifugal compressors". PhD thesis. Linköpings universitet, 2013. url: https://citeseerx.ist.psu.edu/viewdoc/download?doi=10.1.1.393.817&rep=rep1&type=pdf (cit. on p. 49).

[62] G. Martin, V. Talon, P. Higelin, A. Charlet, and C. Caillol. "Implementing turbomachinery physics into data map-based turbocharger models". *SAE World Congress & Exhibition*. SAE International, 2009. doi: 10.4271/2009-01-0310 (cit. on p. 49).

[63] J. P. Jensen, A. F. Kristensen, S. C. Sorenson, N. Houbak, and E. Hendricks. "Mean value modeling of a small turbocharged diesel engine". SAE International, 1991. doi: 10.4271/910070 (cit. on p. 49).

[64] P. Olmeda, V. Dolz, F. J. Arnau, and M. A. Reyes-Belmonte. "Determination of heat flows inside turbochargers by means of a one dimensional lumped model". *Mathematical and Computer Modelling*, 57 (7-8), (2013), pp. 1847–1852. issn: 08957177. doi: 10.1016/j.mcm.2011.11.078 (cit. on p. 50).

[65] F. Payri, P. Olmeda, F. J. Arnau, A. Dombrovsky, and L. Smith. "External heat losses in small turbochargers: Model and experiments". *Energy*, 71, (2014), pp. 534–546. issn: 03605442. doi: 10.1016/j.energy.2014.04.096 (cit. on p. 50).

[66] J. R. Serrano, P. Olmeda, A. Tiseira, L. M. García-Cuevas, and A. Lefebvre. "Theoretical and experimental study of mechanical losses inautomotive turbochargers". *Energy*, 55, (2013), pp. 888–898. issn: 03605442. doi: 10.1016/j.energy.2013.04.042 (cit. on p. 51).

[67] F. A. Williams. *Combustion Theory (2nd Ed.)* Benjamin-Cummings Publishing Co., 1985. isbn: 0805398015 (cit. on p. 51).

[68] M. Lapuerta, R. Ballesteros, and J. R. Agudelo. "Effect of the gas state equation on the thermodynamic diagnostic of diesel combustion". *Applied Thermal Engineering*, 26 (14-15), (2006), pp. 1492–1499. issn: 13594311. doi: 10.1016/j.applthermaleng.2006.01.001 (cit. on p. 52).

[69] C. D. Rakopoulos, G. M. Kosmadakis, and E. G. Pariotis. "Critical evaluation of current heat transfer models used in CFD in-cylinder engine simulations and establishment of a comprehensive wall-function formulation". *Applied Energy*, 85 (5), (2010), pp. 1612–1630. issn: 03062619. doi: 10.1016/j.apenergy.2009.09.029 (cit. on p. 52).

[70] F. Payri, A. Broatch, J. R. Serrano, L. F. Rodríguez, and A. Esmorís. "Study of the potential of intake air heating in automotive DI Diesel engines". *SAE 2006 World Congress & Exhibition*. SAE International, 2006. doi: 10.4271/2006-01-1233 (cit. on p. 52).

[71] C. D. Rakopoulos, G. M. Kosmadakis, A. M. Dimaratos, and E. G. Pariotis. "Investigating the effect of crevice flow on internal combustion engines using a new simple crevice model implemented in a CFD code". *Applied Energy*, 88 (1), (2011), pp. 111–126. issn: 03062619. doi: 10.1016/j.apenergy.2010.07.012 (cit. on p. 52).

[72] F. Payri, P. Olmeda, J. Martín, and A. García. "A complete 0D thermodynamic predictive model for direct injection diesel engines". *Applied Energy*, 88 (12), (2011), pp. 4632–4641. issn: 03062619. doi: 10.1016/j.apenergy.2011.06.005 (cit. on p. 53).

[73] B. Tormos, J. Martín, R. Carreño, and L. Ramírez. "A general model to evaluate mechanical losses and auxiliary energy consumption in reciprocating internal combustion engines". *Tribology International*, 123, (2018), pp. 161–179. issn: 0301679X. doi: 10.1016/j.triboint.2018.03.007 (cit. on pp. 53, 104, 105).

[74] S. Furuhama and T. Tada. "On the Flow of Gas Through the Piston-Rings : 1st Report, The Discharge Coefficient and Temperature of Leakage Gas". *Bulletin of JSME*, 4 (16), (1961), pp. 684–690. doi: 10.1299/jsme1958.4.684 (cit. on p. 54).

[75] R. Payri, F. J. Salvador, J. Gimeno, and G. Bracho. "A new methodology for correcting the signal cumulative phenomenon on injection rate measurements". *Experimental Techniques*, 32, (2008), pp. 46–49. issn: 07328818. doi: 10.1111/j.1747-1567.2007.00188.x (cit. on p. 60).

[76] I. I. Vibe. "Brennverlauf und Kreisprozess von Verbrennungsmotoren". *VEB Verlag Technik*, (1970) (cit. on p. 65).

[77] F. G. Chmela and G. C. Orthaber. "Rate of heat release prediction for direct injection diesel engines based on purely mixing controlled combustion". *International Congress & Exposition*. SAE International, 1999. doi: 10.4271/1999-01-0186 (cit. on p. 65).

[78] J. Arrègle, J. J. López, J. M. García, and C. Fenollosa. "Development of a zero-dimensional Diesel combustion model. Part 1: Analysis of the quasi-steady diffusion combustion phase". *Applied Thermal Engineering*, 23 (11), (2003), pp. 1301–1317. issn: 13594311. doi: 10.1016/S1359-4311(03)00079-6 (cit. on p. 65).

[79] J. Arrègle, J. J. López, J. M. García, and C. Fenollosa. "Development of a zero-dimensional Diesel combustion model: Part 2: Analysis of the transient initial and final diffusion combustion phases". *Applied Thermal Engineering*, 23 (11), (2003), pp. 1319–1331. issn: 13594311. doi: 10.1016/S1359-4311(03)00080-2 (cit. on p. 65).

[80] A. A. Amsden, T. D. Butler, P. J. O'Rourke, and J. D. Ramshaw. "KIVA-A comprehensive model for 2-D and 3-D engine simulations". *SAE International Congress and Exposition*. SAE International, 1985. doi: 10.4271/850554 (cit. on p. 65).

[81] A. A. Amsden. "KIVA-3V: A Block-Structured KIVA Program for Engines with Vertical or Canted Valves". *LA Report*. Los Alamos National Laboratory, 1997 (cit. on p. 65).

[82] M. A. Gonzalez D., Z. W. Lian, and R. D. Reitz. "Modeling diesel engine spray vaporization and combustion". *International Congress and Exposition*. SAE International, 1992. doi: 10.4271/920579 (cit. on p. 65).

[83] S. C. Kong, Z. Han, and R. D. Reitz. "The development and application of a diesel ignition and combustion model for multidimensional engine simulation". *International Congress and Exposition*. SAE International, 1995. doi: 10.4271/950278 (cit. on p. 65).

[84] Y. Yi and R. D. Reitz. "Modeling the effect of primary atomization on diesel engine emissions". *SAE 2003 World Congress & Exhibition*. SAE International, 2003. doi: 10.4271/2003-01-1041 (cit. on p. 65).

[85] J. Arrègle, J. J. López, J. Martín, and E. M. Mocholí. "Development of a mixing and combustion zero-dimensional model for diesel engines". *SAE 2006 World Congress & Exhibition*. SAE International, 2006. doi: 10.4271/2006-01-1382 (cit. on p. 66).

[86] J. M. Desantes, J. Arrègle, J. J. López, and A. Cronhjort. "Scaling laws for free turbulent gas jets and diesel-like sprays". *Atomization and Sprays*, 16 (4), (2006), pp. 443–474. issn: 10445110. doi: 10.1615/AtomizSpr.v16.i4.60 (cit. on pp. 66, 69).

[87] V. Hamosfakidis and R. D. Reitz. "Optimization of a hydrocarbon fuel ignition model for two single component surrogates of diesel fuel". *Combustion and Flame*, 132 (3), (2003), pp. 433–450. issn: 00102180. doi: 10.1016/S0010-2180(02)00489-3 (cit. on p. 67).

[88] J. C. Livengood and P. C. Wu. "Correlation of autoignition phenomena in internal combustion engines and rapid compression machines". *Symposium (International) on Combustion*, 5 (1), (1955), pp. 347–356. issn: 00820784. doi: 10.1016/S0082-0784(55)80047-1 (cit. on p. 67).

[89] F. Payri, P. Olmeda, J. Martin, and R. Carreño. "A New Tool to Perform Global Energy Balances in DI Diesel Engines". *SAE International Journal of Engines*, 7 (1), (2014), pp. 43–59. issn: 19463944. doi: 10.4271/2014-01-0665 (cit. on p. 72).

[90] F. Payri, J. Arrègle, J. Javier López, and E. Mocholí. "Diesel NOx modeling with a reduction mechanism for the initial NOx coming from EGR or re-entrained burned gases". *SAE World Congress & Exhibition*. SAE International, 2008. doi: 10.4271/2008-01-1188 (cit. on p. 76).

[91] Y. B. Zeldovich. "25. The Oxidation of Nitrogen in Combustion and Explosions". *Selected Works of Yakov Borisovich Zeldovich, Volume I*. Princeton University Press, 2015. doi: 10.1515/9781400862979.364 (cit. on p. 76).

[92] F. Posada, A. Isenstadt, and H. Badshah. *Estimated cost of diesel emissions-control technology to meet future california low NOx standards in 2024 and 2027*. Tech. rep. International Council on Clean Transportation, 2020. url: https://theicct.org/sites/default/files/publications/HDV-emissions-compliance-cost-may2020.pdf (cit. on p. 82).

[93] *Future Light and Heavy Duty ICE Powertrain Technologies*. Tech. rep. ERTRAC Working Group, 2016. url: https://www.ertrac.org/uploads/documentsearch/id11/Future%20Light-duty%20Powertrain%20Technologies%20and%20Fuels.pdf (cit. on p. 82).

[94] F. Payri, F. J. Arnau, P. Piqueras, and M. J. Ruiz. "Lumped Approach for Flow-Through and Wall-Flow Monolithic Reactors Modelling for Real-Time Automotive Applications". *WCX World Congress Experience*. SAE International, 2018. doi: 10.4271/2018-01-0954 (cit. on pp. 82, 86–89).

[95] J. Galindo, J. R. Serrano, P. Piqueras, and Ó. García-Afonso. "Heat transfer modelling in honeycomb wall-flow diesel particulate filters". *Energy*, 43 (1), (2012), pp. 201–213. issn: 03605442. doi: 10.1016/j.energy.2012.04.044 (cit. on pp. 83, 86).

[96] J. R. Serrano, H. Climent, P. Piqueras, and E. Angiolini. "Filtration modelling in wall-flow particulate filters of low soot penetration thickness". *Energy*, 112, (2016), pp. 883–898. issn: 03605442. doi: 10.1016/j.energy.2016.06.121 (cit. on p. 83).

[97] J. R. Serrano, F. J. Arnau, P. Piqueras, and Ó. García-Afonso. "Packed bed of spherical particles approach for pressure drop prediction in wall-flow DPFs (diesel particulate filters) under soot loading conditions". *Energy*, 58, (2013), pp. 644–654. issn: 03605442. doi: 10.1016/j.energy.2013.05.051 (cit. on p. 83).

[98] D. Kryl, P. Kočí, M. Kubíček, M. Marek, T. Maunula, and M. Härkönen. "Catalytic converters for automobile diesel engines with adsorption of hydrocarbons on zeolites". *Industrial and Engineering Chemistry Research*, 44 (25), (2005), pp. 9524–9534. issn: 08885885. doi: 10.1021/ie050249v (cit. on p. 87).

[99] F. Payri, X. Margot, A. Gil, and J. Martin. "Computational study of heat transfer to the walls of a di diesel engine". *SAE 2005 World Congress & Exhibition*. SAE International, 2005. doi: 10.4271/2005-01-0210 (cit. on p. 96).

[100] J. Benajes, P. Olmeda, J. Martín, and R. Carreño. "A new methodology for uncertainties characterization in combustion diagnosis and thermodynamic modelling". *Applied Thermal Engineering*, 71 (1), (2014), pp. 389–399. issn: 13594311. doi: 10.1016/j.applthermaleng.2014.07.010 (cit. on pp. 96, 99).

[101] L. Jarrier, J. C. Champoussin, R. Yu, and D. Gentile. "Warm-up of a D.I. diesel engine: Experiment and modeling". *SAE 2000 World Congress*. SAE International, 2000. doi: 10.4271/2000-01-0299 (cit. on p. 96).

[102] C. Samhaber, A. Wimmer, and E. Loibner. "Modeling of engine warm-up with integration of vehicle and engine cycle simulation". *Vehicle Thermal Management Systems Conference & Exposition*. SAE International, 2001. doi: 10.4271/2001-01-1697 (cit. on p. 96).

[103] A. Roberts, R. Brooks, and P. Shipway. "Internal combustion engine cold-start efficiency: A review of the problem, causes and potential solutions". *Energy Conversion and Management*, 82, (2014), pp. 327–350. issn: 01968904. doi: 10.1016/j.enconman.2014.03.002 (cit. on pp. 96, 97).

[104] S. Uppuluri, H. R Khalane, Y. Umbarkar, and A. Naiknaware. "Cold-Ambient Warm-Up Predictions: A Novel Approach Using 1D Computational Models". *SAE 2016 World Congress & Exhibition*. SAE International, 2016. doi: 10.4271/2016-01-0198 (cit. on pp. 96, 97).

[105] A. Broatch, P. Olmeda, J. Martin, and J. Salvador-Iborra. "Development and Validation of a Submodel for Thermal Exchanges in the Hydraulic Circuits of a Global Engine Model". *WCX World Congress Experience*. SAE International, 2018. doi: 10.4271/2018-01-0160 (cit. on p. 104).

[106] B. E. Flores. "A pragmatic view of accuracy measurement in forecasting". *Omega*, 14 (2), (1986), pp. 93–98. issn: 03050483. doi: 10.1016/0305-0483(86)90013-7 (cit. on p. 117).

“When we do perceive a ‘before’ and an ‘after’, then we say that there is time. For time is just this number of motion in respect of ‘before’ and ‘after’.”

— Aristotle in Physics

Chapter 4

Exhaust thermal management by means of VVT strategies

Contents

4.1 Introduction 141
4.1.1 Valve events of a four-stroke engine 143
4.1.2 Variable valve timing strategies 143
4.1.2.1 Modifying intake valve opening (IVO) 144
4.1.2.2 Modifying intake valve closing (IVC) 145
4.1.2.3 Modifying exhaust valve opening (EVO) . . 147
4.1.2.4 Modifying exhaust valve closing (EVC) . . . 147
4.1.2.5 Valve lift actuation 148
4.2 Model description 149
4.3 Variable valve timing methodology 150
4.4 Results and discussion 154

4.4.1 Steady-state analysis 154
4.4.2 Transient analysis 168
4.5 Conclusions 180
Chapter 4 References 185

4.1 Introduction

One of the major goals of engine developers and manufacturers is to minimise fuel consumption and emissions. Specially in diesel engines, a great challenge is the cold engine start and heating phase, since heating techniques are a compromise between a fast heat-up of the after-treatment system and a low penalty in fuel consumption.In this context, the variable valve timing (VVT) of the exhaust valves can be a key technology for increasing after-treatment system temperatures after cold start and during the engine warm-up.

VVT technology was introduced in the automotive industry by the middle of the last century with the aim of improving the engine performance. With traditional camshafts, the valve timing is the same for all engine speeds and conditions. However, an engine requires large amounts of air when operating at high speeds —a typical requirement for racing applications. On the contrary, if the camshaft keeps the valves open for longer periods of time at lower engine speeds, unburned fuel may exit the engine, leading to lower engine performance and increased emissions in petrol engines. In diesel engines, this modification of the valve timings results into backflows into the intake manifold that worsens volumetric efficiency. So in this way, VVT meant a solution for controlling the air flow depending on the engine speed.

In the late 1960s, Fiat became the first automotive manufacturer to patent a functional variable valve timing system including variable lift. The system, which was developed by Giovanni Torazza, used hydraulic pressure to vary the fulcrum of the cam followers [107]. The hydraulic pressure changed according to engine speed and intake pressure. Nonetheless, Alfa Romeo was the first manufacturer to use a variable valve timing system in production cars [108]. The 1980 Alfa Romeo Spider 2000 had a mechanical VVT system in SPICA fuel injected cars sold in the United States. Some years later, the same system was also used in the 1983 Alfetta 2.0 Quadrifoglio Oro models as well as other cars.

Anyhow, when it comes to VVT in the automobile world, Honda springs to mind. In 1989, Honda released the VTEC system [109]. Honda launched the production of a system that allow an engine the ability to operate on two completely different cam profiles, eliminating a major compromise in engine design. One profile is designed to operate the valves at low engine speeds, which provides good road performance, low fuel consumption and low emissions output. The second is a high lift, long duration profile and comes into operation at high engine speeds to provide an increase in power output. The first VTEC engine Honda produced was the B16A which was installed in the Integra, CRX, and Civic hatchback available in Japan and Europe. In this way, Honda was the first manufacturer extending VVT to a whole range of vehicles. Other manufacturers have developed VVT systems during the last years, such as the VarioCam system by Porsche, VANOS by BMW or VTi by the PSA group.

Concerning the introduction of variable valve timing in diesel engines, it took some decades to see VVT in commercial engines. Caterpillar developed the C13 and C15 Acert engines [110] in 2007. Both engines used VVT technology to reduce NO_x emissions, so as to meet the 2002 EPA requirements. In the same way, Mitsubishi developed and started mass production of its 4N13 1.8 L engine in 2010, the world's first passenger car diesel engine that features a variable valve timing system [111].

As it can be seen, VVT has traditionally been used widely in spark ignited (SI) engines rather than in compression ignited (CI) engines. At low loads, the pumping losses in petrol engines are greater than those of diesel engines because of the intake throttling. Without a throttle valve, the control of the air-fuel mixture can be achieved by variation of the intake valve opening period; therefore, VVT has great potential for reducing pumping losses in petrol engines. In diesel engines, whose control of load is performed by regulating the amount of fuel injected, pumping losses at partial loads are lower. The application of VVT in diesel engines is restricted due to the small clearance height between piston and cylinder head at top dead centre (TDC), which allows reaching higher compression ratios than in petrol engines. This restriction means that the valves can have a little or no lift during the valve overlap near TDC, which involves a reduced margin

for advancing the intake opening and retarding the exhaust closing in order to avoid valve to piston contact. Contrarily, there are no restrictions regarding the exhaust opening and intake closing events. As a consequence, ordinary camshaft phasers are used very little in diesel engines, but systems that provide control over the valve open period, and or duration, can be applied [112].

However, in order to optimise the cold start and the heating phase, VVT applications have shown a great potential in diesel engines, making it possible to provide the residual gas required for this situation [113, 114]. This leads to a reduction of CO and HC emissions that are intrinsic to the cold start.

In this chapter, a simulation study is presented and discussed by comparing different exhaust valve actuation strategies so as to increase the exhaust temperature of a light-duty diesel and reduce engine emissions.

The next chapter 5 is focused on developing a variable valve actuation control to reduce tailpipe pollutant emissions based on the results presented in this chapter.

4.1.1 Valve events of a four-stroke engine

Figure 4.1 shows the valve timing diagram of a conventional light-duty diesel engine. In that diagram one can differentiate four valve events: intake opening and closing (IVO and IVC), and exhaust opening and closing (EVO and EVC). The period in which both intake valves and exhaust valves are opened is known as valve overlap and aids in the scavenging of the exhaust gases. It is represented in Figure 4.1 as the striped green area between IVO and EVC.

4.1.2 Variable valve timing strategies

The four different valve events described above are fixed in an ordinary camshaft. Thus, the timing of these valve events is the result of a per-

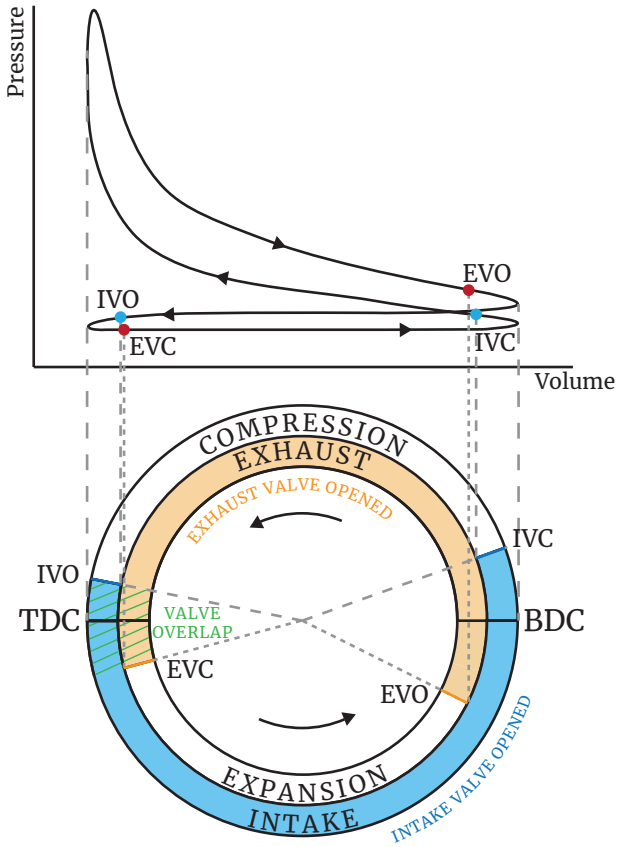

Figure 4.1: Four stroke diesel engine P–V diagram (top) and engine timing diagram (bottom).

formance compromise under different operating conditions. Variable valve timing strategies arise from the need to find the most efficient way to operate the engine depending on its engine speed and load at any point of the engine map. Consequently, different approaches can be described by advancing or delaying the different valve events:

4.1.2.1 Modifying intake valve opening (IVO)

By advancing the IVO event (early IVO or EIVO), intake valve opens before TDC during the exhaust stroke. Thus, increasing the valve overlap and the amount of burnt gases backflow into the intake ports. This part of the ex-

haust gases mixes with fresh air from the intake manifold and serves as an internal gas recirculation (IGR), reducing the combustion temperature and, consequently, reducing the NO_x amount [115] produced during the combustion. Experiments carried on by Tomoda et al. [116], in a 2.2 litres Diesel engine, found that advancing the IVO timing before TDC results in an improvement of the swirl ratio and an increase in the introduced air mass at low and high load. This effect leads to a better trade-off between NO_x and fuel consumption. The fuel economy improvement is produced by and enhanced combustion rate due to the higher swirl ratio and the reduction in pumping losses due to the early IVO [116].

The duration of the valve overlap depends on several factors: the distance between piston and cylinder head at TDC (which usually is lower in a diesel engine due to the high compression ratio), the engine speed and the instantaneous pressures at intake and exhaust ports. In diesel engines, when pressure is higher in the exhaust manifold, valve overlap should be reduced to avoid backflows into the intake manifold [117]. Delaying the IVO (LIVO) event reduces valve overlap, leading to a very low or insignificant backflow into intake manifold. Deppenkemper et al. [118] found, using a one-dimensional engine model, that if the IVO is delayed up to the beginning of the intake stroke, the velocity at which the air enters into the cylinder will be higher due to the lower pressure inside the cylinder. This increase in inlet air velocity enhances in-cylinder turbulence, which improves the mixing process, resulting in lower HC emissions.

4.1.2.2 Modifying intake valve closing (IVC)

Backflow during the compression stroke can be reduced or avoided by advancing IVC. Early IVC (EIVC) strategy reduces the amount of air admitted into the cylinder and thereby reduces slightly the work required for filling the cylinder when compared with a conventional valve timing. Zammit et al. [119] found that EIVC decreases NO_x emissions for advances greater than 30° at low engine speeds and low loads, reduces soot levels and raises exhaust gas temperatures. Nevertheless, CO and HC engine-out emissions increases and fuel economy is deteriorated, since more fuel amount is re-

quired for a lower air charge [119]. Tomoda et al. [116] also claim that when the IVC timing is advanced towards bottom dead centre (BDC), the effective compression ratio increases and this creates an increased compression end temperature, so that HC formation is reduced. The increase in effective compression ratio also allows an increase of EGR rate, resulting in reduced NO_x emissions. At high loads, however, EIVC decreases the amount of charged air mass in the cylinder and results in an increase of HC emissions. According to Tomoda et al. [116], early IVC on one intake valve relative to the other valve allows controlling the swirl strength, resulting in NO_x and soot emissions reduction at high load because it reduces both pumping losses and fuel consumption. Similar conclusions were presented by De Ojeda [120] based on his tests in a 6.4 L V8 engine. He found that the use of EIVC showed significant reductions of soot (above 90 %) and fuel efficiency improvements (of 5 %) with NO_x levels below the US 2010 standard of 0.2g/bhp-hr at loads up to 5 bar BMEP.

On the contrary, performing a late intake valve closing (LIVC) means that intake valves are opened during the first part of the compression stroke. Consequently, some of the air flows back into the intake manifold, leading to a reduction in the effective compression ratio and a lambda reduction (lower combustion chamber charge). These two consequences lead to a higher exhaust gas temperatures and a NO_x engine-out emission reduction [121, 122, 123, 124]. However, Maniatis et al. [125] experiments did not found any benefit in exhaust gas enthalpy nor a reduction of HC and CO emissions. Kim et al. [126] found that the amount of EGR could be reduced to maintain a similar level of NO_x emissions when the IVC timing is retarded. This characteristic also prevents an increase in soot emissions. The combination of EGR and LIVC helped to improve the NO_x-soot trade-off relation [127, 123, 124]. Similarly, Zhou et al. [128] achieved a reduction in particle matter emissions by 32.9 % with a small increase in NO_x by applying LIVC strategy and an optimal control of the VGT and EGR during realistic transient conditions.

4.1.2.3 Modifying exhaust valve opening (EVO)

The early opening of the exhaust valve provides better scavenging of the exhaust gases, but it also causes a reduction in the expansion work, resulting in a reduction of the engine brake power, thus worsening the fuel consumption. Early EVO (EEVO) also produces an increment in exhaust pressure and temperature levels higher than those obtained with the standard valve timing. The greater the advance in EVO, the larger increment in exhaust temperature, but with a larger penalty in terms of BSFC [122, 129]. Regarding pollutant emissions, EEVO results in an increase in engine-out hydrocarbons and CO because their oxidation during the expansion stroke is interrupted with the early EVO [115, 130]. In studies carried on by Gossala et al. [129] at idle conditions, the fuel penalty caused by early EVO produces more NO_x and particle matter emissions due to the higher injected fuel mass. Particle matter emissions can be reduced by increasing the air-fuel ratio, but it also reduces the exhaust temperature increment.

When delaying the exhaust valve opening (LEVO), the exhaust valve is opened later than usual, near BDC or after this point. In this case, a greater expansion work is produced without losses during the power stroke. However, exhaust pumping work increases because of a very late EVO, which results in some restriction to expel the exhaust gases out of the cylinder. According to Piano [122], a fast opening lift of the exhaust valve is usually desirable in order to retard the EVO timing while not penalising BSFC. Moreover, an exhaust valve faster opening may also reduce the blow-down flow losses increasing the energy available at turbine inlet, especially needed at low engine speed where the variable geometry turbine is usually closed.

4.1.2.4 Modifying exhaust valve closing (EVC)

In regular diesel engines, EVC takes place at around 20° after TDC. Advancing this event prevents partially or totally valve overlap, which reduces or avoids the backflow of burnt gases through intake valves. This way, early EVC (EEVC) aids to retain a portion of burnt gases inside the cylinder, which results in a reduction of engine-out NO_x and HC emissions [115]. Nonethe-

less, this strategy has some limitations to be applied on passenger vehicles as some authors reported an audible noise when the compressed exhaust gases eject into the intake manifold [125].

In order to perform a late EVC (LEVC), the exhaust valves are closed well after TDC, increasing the valve overlap period. This long overlap during the intake stroke results in some part of the burnt gases flowing back into the cylinder, creating an internal gas recirculation. Regarding engine-out pollutant emissions, NO_x and HC emissions are reduced when performing LEVC due to this IGR [115].

Because of the small clearance height between piston and cylinder head at TDC in CI engines, LEVC and EIVO are quite limited. This is also the reason why the application of VVT is more restricted in CI engines than in SI engines.

At high engine speed, the time in which both valves are opened is less than at low engine speed. In order to provide higher engine power output, a high valve overlap is beneficial for scavenging of residual gases, since the higher inertia of the gases at high engine speed allows removing residual gases from the cylinder and increases volumetric efficiency. But a large valve overlap is detrimental for low engine speed torque due to the larger amount of residual gases flowing back into the intake manifold.

4.1.2.5 Valve lift actuation

Variable valve timing strategies usually consist of a combination of the different sub-strategies mentioned above, like, for instance, phasing the exhaust; which can be a combination of EEVO and EEVC or, on the other side, a combination of LEVO and LEVC. Moreover, there are other different strategies in order to add flexibility to the engine valvetrain. By modifying valve lift it is also possible to perform different opening-and-closing valve events along the engine cycle. This systems are called as variable valve actuation (VVA).

It is known that IGR can increase the exhaust gas temperature and re-

duce engine-out emissions. This is done with the aid of a charge composition control achieved by an exhaust valve post-lift —also called exhaust valve re-opening (EVrO) or re-breathing— or an intake valve pre-lift during the exhaust stroke [117, 131].

Intake valve pre-lift consists of a previous intake valve opening event during the exhaust stroke. The aim is to create a backflow of exhaust gases into the intake manifold that are re-entrained later during the intake stroke. On the contrary, the exhaust valve re-opening consists of a secondary exhaust valve opening event during the intake stroke. The vacuum created by the downward movement of the piston creates a backflow of exhaust gases from the exhaust manifold into the cylinder. Benajes et al. [117] found that the IGR amount achieved is higher when performing an exhaust valve re-opening than in the case of an intake valve pre-lift, with the advantage of recirculating the same amount of exhaust gases independently of the speed and load.

4.2 Model description

In this numeric study, all the different VVT strategies were simulated trying to keep the same torque of the baseline cam simulations so as to offer a fair comparison. The control sub-model emulates the ECU to control the fuel injection by modifying the injection pressure, the fuel mass split and the start of energisation —of each injection pulse— depending on the engine speed and total fuelling rate at any operating point. This model also takes control over the air flow and intake pressure by means of the turbine rack position, whose control is based on the intake setpoint depending on the engine speed and total fuelling rate as well. It can also modify the position of the EGR and back pressure valves to control the air mass flow.

At any particular engine speed and torque, the required fuel mass is obtained from a calibration map based on experimental data. Once the engine speed and fuel mass are known, the injection pulses timings and masses, intake manifold pressure, injection pressure and air mass flow setpoints are obtained from their respective maps. These maps were created on the ba-

sis of a series of 23 steady-state points spread throughout the entire engine map and using the baseline valvetrain configuration.

The ECU model can increase the injected fuel to meet the torque target. However, there are two fuel limiters: one ensures that the injected fuel does not overpass the one of the full load at that engine speed, the other one limits the fuel rate to avoid an excess of soot. This translates into the possibility that some of the VVT strategies could not meet the torque demand at some specific operating point.

The details and the validation of the virtual engine model used in this study were presented in chapter 3. The simulated engine used for this study is a 1.6L four-stroke four-cylinders diesel engine compliant with Euro 5 emissions regulations, which is the same engine described in section 2.2.

4.3 Variable valve timing methodology

The purpose of considering variable valve timing possibilities is to increase the enthalpy of the burnt gases during the cold start of the engine. In such a way, it is possible to reduce the warm-up period of the after-treatment devices like the DOC, and reduce pollutant emissions during this time. Since modifying the engine valve timing directly affects the conditions in the combustion chamber, the effect on emissions formation of each VVT alternative should be evaluated as well.

Several variable valve timing strategies were studied. The first two strategies consisted on phasing exhaust timings (*Exhaust phasing* and *EEVO + dwell*). Third and fourth strategies consisted on phasing both intake and exhaust timings (*IP + EP*) in all 4 valves and in only one intake valve and one exhaust valve, respectively, remaining unaltered the other two. In contrast, the last two strategies consisted on performing an exhaust valve re-opening modifying the re-opening lift and duration. Intake and exhaust valve lifts according to each strategy are shown in Figure 4.2.

- **Baseline cams**: Corresponds to the original cam valve timing (grey

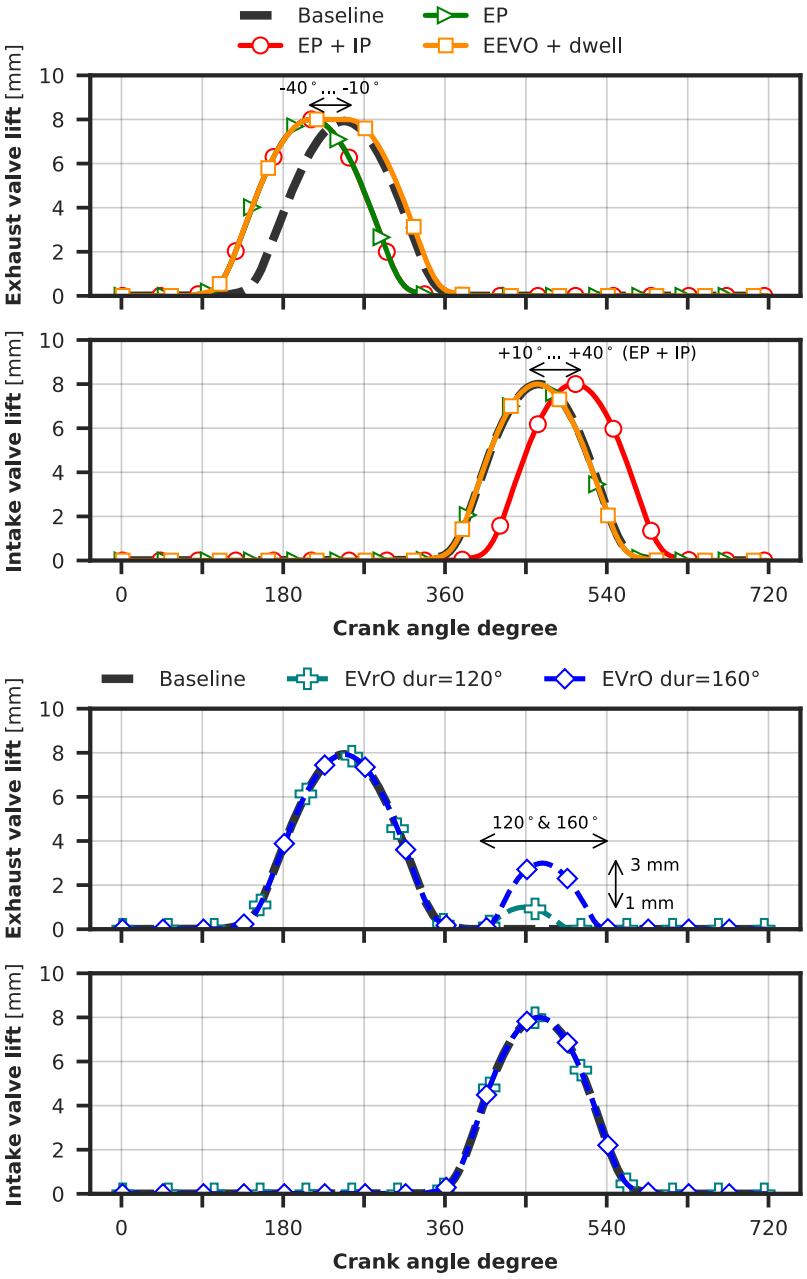

Figure 4.2: Exhaust and intake valve lift profiles for each configuration.

dashed line in Figure 4.2). In this case, EVO and EVC are located at 107° and 392° CA, respectively from the combustion TDC. Regarding intake valve timing, IVO and IVC occur at 326° and 602° CA respectively from

combustion TDC as well.

- **Exhaust phasing (EP)**: This strategy corresponds to an early exhaust valve opening (EEVO) and an early exhaust valve closing (EEVC). The exhaust valves lift profiles are the same as in the original cams, so the event duration is also the same. Intake valve timings remain unaltered in this strategy. Three different configurations were tested by advancing EVO and EVC 20°, 30°, and 40° CA. A fourth configuration advancing the exhaust 60° CA was tested resulting in a dramatic drop of torque. *EP* strategy is represented by a green solid line with triangle markers in Figure 4.2.

- **Exhaust phasing and intake phasing (EP + IP)**: This strategy is similar as the previous one with the difference that intake valve event is symmetrically delayed with respect to the exhaust event. Thus, this results in a combination of both an early exhaust valve opening (EEVO) and a symmetrical late intake valve opening (LIVO). Valve profiles duration for both intake and exhaust valves are not modified (red solid line with circle markers in Figure 4.2), this means that both profiles are phased and EVC and IVC instants are phased as well. As in *EP*, three different configurations were simulated by advancing EVO and EVC, and delaying IVO and IVC simultaneously, 20°, 30°, and 40° CA. Again, a fourth configuration advancing exhaust/delaying intake 60° CA was found to be excessive due to the drop of torque and output power. Another twin alternative is proposed based on this *EP + IP*. Instead of phasing both intake and both exhaust valves, only one of each pair is phased. This second configuration is referred as *EP + IP (2v)* in this chapter.

- **EEVO + dwell**: Represented by an orange solid line with square markers in Figure 4.2, EVO instant was advanced 20°, 30°, and 40° CA, but keeping unchanged the EVC instant. The opening and closing slopes are kept. Thus as a result, there is an angle interval in which the exhaust valves are fully opened. This angle interval will be called *dwell* along this study.

- **EVrO**: Exhaust valve re-opening strategy consists of performing a second exhaust event (also called post-lift or re-breathing in literature) during the intake stroke. For this study two different strategies were

tested. On the one hand, a second exhaust event that lasts for 160° CA (from 392° to 552°) and three different valve lifts (1 mm, 2 mm and 3 mm) were tested. It is represented by a blue dashed line with diamond markers in Figure 4.2. On the other hand, an analogous strategy was tested with the same three different valve lifts but with a shorter re-opening, 120° CA (from 392° to 512°) instead of 160° CA. This re-opening strategy is represented by a light blue solid line with cross markers in Figure 4.2 The exhaust valve re-opening was performed only in one of the two exhaust valves, keeping the original cam profile in the other valve.

Table 4.1 summarises the strategies described above.

	VVT Strategies				
	EP + IP (4v & 2v)	Exhaust phasing	EEVO + dwell	EVrO 160	EVrO 120
IVO (°)	326 + [20, 30, 40]	326	326	326	326
IVC (°)	602 + [20, 30, 40]	602	602	602	602
EVO (°)	107 - [20, 30, 40]	107 - [20, 30, 40]	107 - [20, 30, 40]	107	107
EVC (°)	392 - [20, 30, 40]	392 - [20, 30, 40]	392	392	392
2nd event lift (mm)	-	-	-	1, 2, 3	1, 2, 3
2nd event duration (°)	-	-	-	160	120

Notes: Angles starting from the combustion TDC. EVrO applied only to one of the two exhaust valves.

Table 4.1: Variable valve actuation strategies.

4.4 Results and discussion

In order to perform this study, the resulting torque from the baseline cam simulations was imposed as the torque target for all the different strategies. As explained in section 4.2, the ECU control model basically takes control of the injected fuel mass and the required air mass flow to reach the torque at any operating point, based on the baseline engine calibration that contains several maps for boost pressure, air mass flow and fuel injected. By simulating at the same torque, it is possible to quantify differences on fuel consumption, pumping losses, exhaust temperature and other key outputs when comparing to the baseline configuration.

4.4.1 Steady-state analysis

A total of 23 operating points were tested for each strategy. However, a representative sample is discussed in this study taking a pair of points at 1250 and 1500 rpm and at partial loads. These points, shown in Table 4.2, were measured experimentally without any modification on the engine valvetrain. Moreover, the selected points represent a sample of the low speed stretch of the WLTC, whose transient results are discussed on the next section. It should be noted that any full load point is included in this steady-state analysis. The justification is that the ECU control is not able to reach, in some cases, the torque target without exceeding the full load fuel limit included in the calibration. In most of the configurations it is impossible to do an iso-torque comparison at full load, specially when the exhaust is advanced more than 40° CA at full load and also when performing an exhaust re-opening quite long or with a high lift. At some operating points, when performing a second exhaust valve event *EVrO* 160°, the control is not able to fulfil the torque target. Those points whose torque is 5 % below the baseline one have been removed from the following figures in order to provide an iso-torque comparison.

Figure 4.3 and subsequent figures in this section show the steady-state results for four different operating points (Table 4.2). Several representa-

Engine speed (rpm)	BMEP (bar)	Torque (Nm)
1250	2	25
1250	4	50
1500	2	31
1500	5	65

Table 4.2: Simulated steady-state operating points.

tive variables are presented in different sub-figures comparing the results obtained by each VVT configuration. The values presented have been normalised according to the baseline valvetrain results, so all the figures — except from the DOC inlet temperature, which shows absolute difference in Celsius degrees— represent percentage variations respect to the baseline results. It has to he noted that each variation within the same configuration, e.g. *EVrO* 120° 1, 2 and 3 mm lift, is represented with the same marker in these figures. The marker is larger and darker as greater the lift or the valve event advance/delay.

$$\Delta BSFC_{\text{conf}}\,(\%) = \frac{(BSFC_{\text{conf}} - BSFC_{\text{base}})}{BSFC_{\text{base}}} \cdot 100 \tag{4.1}$$

$$\Delta T_{\text{DOC}_{\text{in, conf}}}\,(^{\circ}C) = T_{\text{DOC}_{\text{in, conf}}} - T_{\text{DOC}_{\text{in, base}}} \tag{4.2}$$

The specific fuel consumption (BSFC) variation in Figure 4.3a, in terms of percentage and calculated according to Equation 4.1, points that all the configurations incur in a penalty in fuel economy. Furthermore, it can be inferred that the increment in exhaust temperature is proportional to the fuel consumption, as it can be observed in all the four operating points, as shown in Figure 4.3a, Figure 4.3b, Figure 4.3c and Figure 4.3d. For the case of *EEVO+dwell* strategy, it can be seen that the temperature increase achieved is about 11 °C in the best case (1250 rpm and 4 bar BMEP in Figure 4.3b), resulting in the worst strategy to increase the exhaust temperature. The temperature variation is calculated comparing it to the baseline one as indicated in Equation 4.2. The justification for the low performance of this strategy is because, since EVC remains unchanged, no additional

amount of exhaust gases is retained in the cylinder for the next cycle. As a result, the entrained gas temperature after the IVC is slightly lower than in the baseline case, leading to an insignificant increment in the exhaust gases temperature for the studied cases. If EVO event is advanced up to 60° CA before TDC within this *EEVO+dwell* strategy, a small higher increment in the exhaust temperature can be achieved. However, the fuel penalty in BSFC goes beyond 20 % is most of the cases. This behaviour is explained by the early exhaust blowdown, since advancing EVO reduces the expansion work by shortening the expansion stroke, which produces an inefficient engine operation due to the higher fuel amount injected to achieve the same brake torque [129]. The case in which *EEVO+dwell* is advanced 60° CA is not shown in the following figures as this advance is not feasible in the other strategies and only comparisons at 20°, 30° and 40° CA are presented.

EVrO 120° strategy offers a good potential when heating the exhaust gases, specially at medium load (4 bar BMEP), where the increase in exhaust temperature is achieved with low penalties in fuel consumption. Furthermore, the greater the maximum lift during the post-lift, the greater the temperature increment in all cases. This configuration presents another advantage: its penalty in fuel economy is not so high compared with other strategies: the increment in BSFC is below 4 % in general, although a maximum of 8 % is reached at 1250 rpm and 4 bar BMEP (Figure 4.3b) with the maximum lift of 3 mm.

On the other side, *EVrO* 160° strategy achieves a higher increase in exhaust temperature compared to *EVrO* 120°, but leading to a slightly higher fuel consumption. The main drawback is that *EVrO* 160° with 3 mm maximum lift (sometimes even with 2 mm) is not able to fulfil the torque demand in most of the cases, since the control tries to provide more fuel before reaching the stoichiometric air-fuel ratio. These points have been removed as explained above, since they do not offer a fair comparison. In Figure 4.3d, *EVrO* 160° is able to meet the torque target only with a 1 mm re-opening lift. In the same way, *EVrO* 120° with 3 mm lift cannot reach the torque target with the full load fuel and soot limiters imposed by the control model. Nonetheless, the 1 mm lift *EVrO* 160° variation is always able to reach the torque target, obtaining an exhaust temperature increment between 25 °C

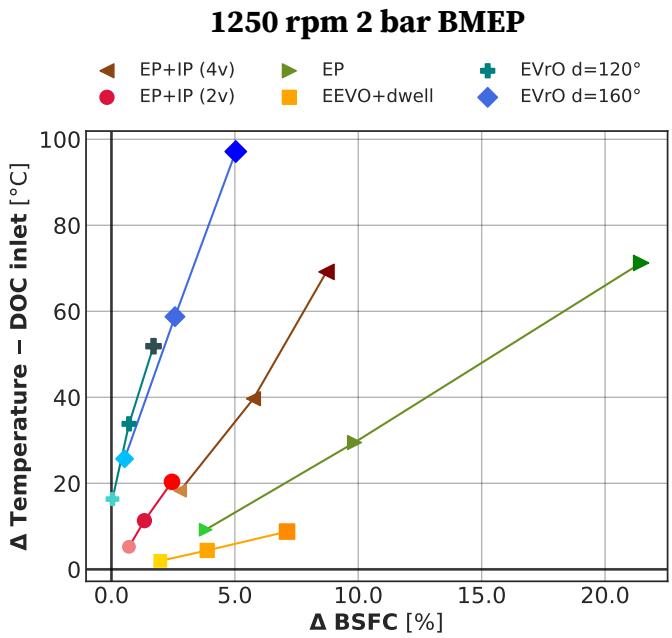

(a) ΔBSFC (%) vs ΔTemperature at DOC inlet (°C), 2 bar BMEP at 1250 rpm.

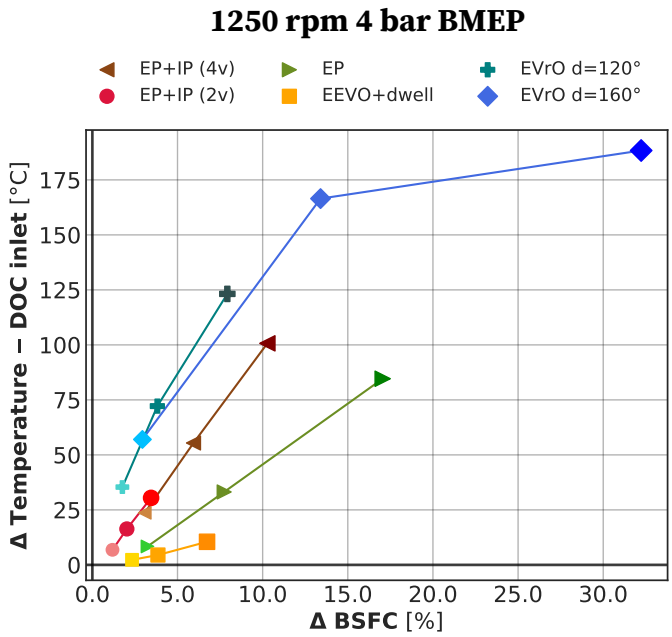

(b) ΔBSFC (%) vs ΔTemperature at DOC inlet (°C), 4 bar BMEP at 1250 rpm.

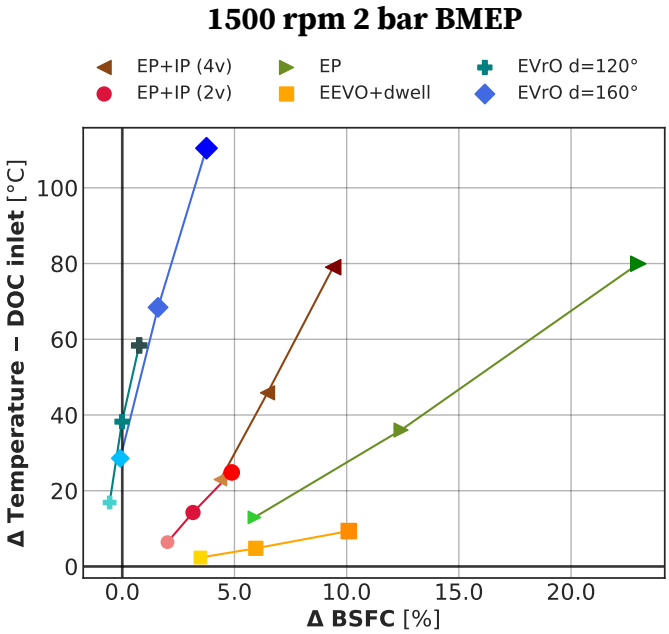

(c) ΔBSFC (%) vs ΔTemperature at DOC inlet (°C), 2 bar BMEP at 1500 rpm.

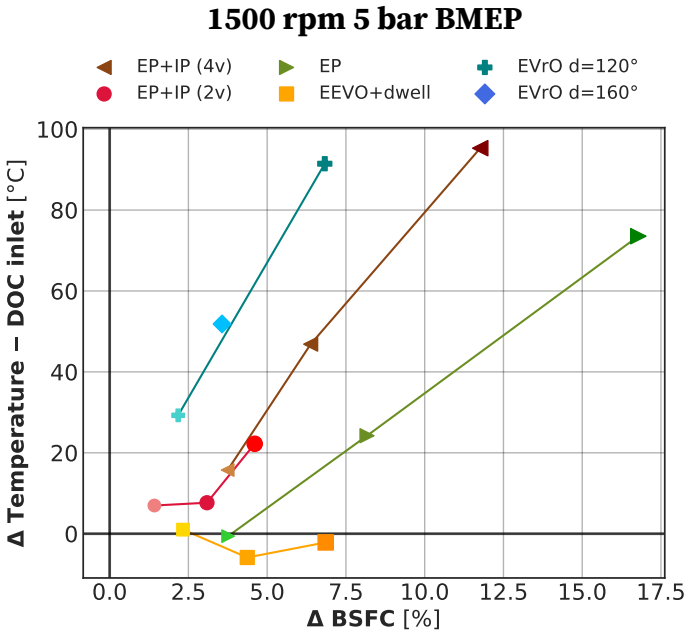

(d) ΔBSFC (%) vs ΔTemperature at DOC inlet (°C), 5 bar BMEP at 1500 rpm.

Figure 4.3: *Steady-state results: BSFC variation vs temperature variation at DOC inlet. The variation is referred to the baseline camshaft.*

and 57 °C at 1250 rpm and 2 bar BMEP and 4 bar BMEP, respectively. In conclusion, a short re-opening (*EVrO* 120°) is more profitable at medium loads than the *EVrO* 160° version in terms of exhaust enthalpy and lift variability.

EP+IP (4v) strategy allows reaching the greatest increase in exhaust temperature when EVrO alternatives are not feasible. In this regard, the greatest phasing of 40° CA offers the greatest exhaust temperature. The fuel penalty is around 5 % to 10 %, but it is higher when increasing the engine load: (12 %) when intake and exhaust are phased 40° CA in Figure 4.3d. The higher fuel consumption compared to the re-opening strategies is due to the compression of the retained burned gases after the EVC, since this compression increases the pumping losses and, thus, the BSFC. The earlier EVO reduces the valve overlap (since EVC is advanced as well), affecting fuel economy as it reduces the power stroke and increases the amount of fuel provided to keep the required torque. This increase in fuel consumption is also observable in *EP* and *EEVO+dwell* strategies. In the case of just phasing a pair of valves (*EP+IP (2v)*), it can be observed the same progression as the 4v alternative in terms of fuel consumption and exhaust temperature gain. However, the maximum temperature raise rarely achieves 25 °C in the four operating points.

In the *EP (exhaust phasing)* strategy the increase in temperature also increases with the greater advance in the exhaust event, in this case with an exhaust temperature increment about 5 °C to 40 °C below the one achieved by the *EP+IP (4v)*. The temperature difference between these two strategies increases when enlarging the exhaust phasing, as can be seen in for example in Figure 4.3c. Contrarily to the exhaust temperature difference, BSFC is higher in *EP* strategy due to the compression of the burned gases after the advanced EVC, which increases pumping losses. In *EP+IP (4v)*, this compression is followed by an expansion of the burned gases due to the later intake which pushes the piston downwards, resulting in a lower penalty in fuel consumption compared to the *EP* strategy. Figure 4.4 shows the in-cylinder pressure-volume diagram at 1500 rpm and 2 bar BMEP. In this figure, the darker the colour and the larger the trace discontinuity within a strategy, the greater the valve advance/delay or re-opening lift. It can be seen that *EP* requires a greater pumping work (green lines) than *EP+IP (4v)*

(brown lines) and, of course, more than *EP+IP (2v)* (red lines) strategies. Valve events are depicted in Figure 4.4, so a triangle is IVO, a diamond indicates IVC, × represents EVO and + indicates EVC. EVrO strategies are not shown in this graph since both of them share the same valve events as the baseline camshaft.

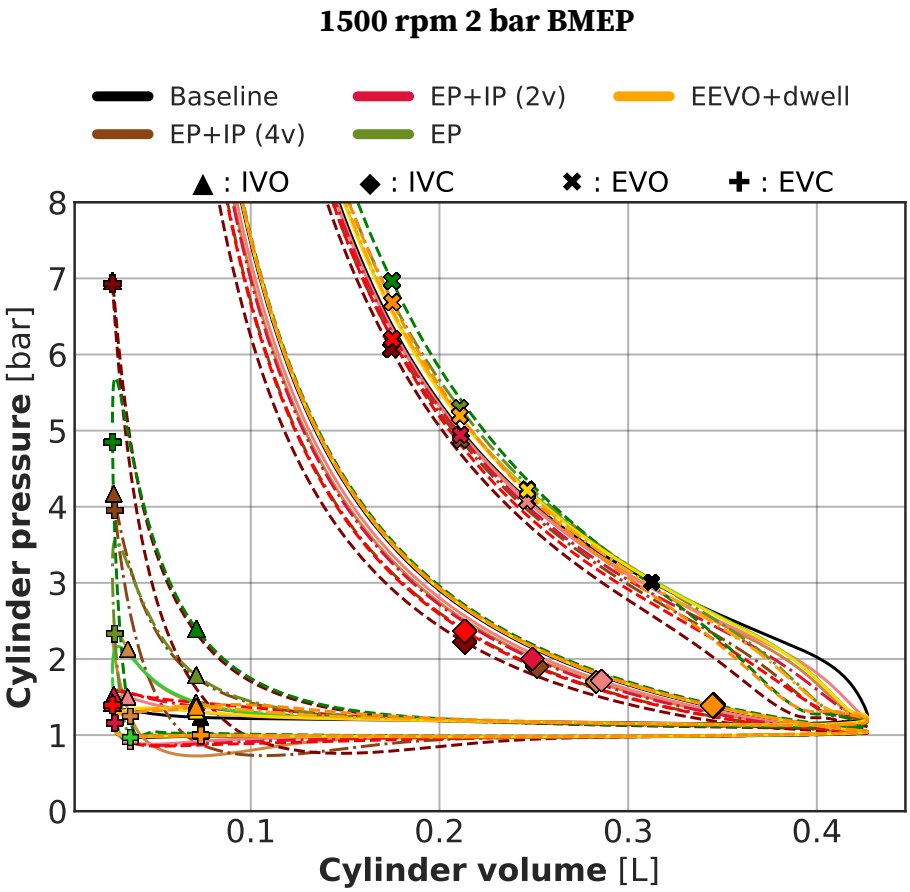

Figure 4.4: *Pressure vs volume diagram, 2 bar BMEP at 1500 rpm.*

As far as pollutant emissions are concerned, even though *EEVO+dwell* strategy does not have a relevant effect on the exhaust temperature, it shows an identifiable trend in NO_x formation reduction as the engine speed increases and engine load decreases (Figure 4.5a and Figure 4.5c). Moreover, the earlier the EVO event, the less nitrogen oxides are formed during the combustion. The explanation to this phenomenon resides in the fast drop of the cylinder temperature towards the middle of the expansion stroke, which results in less residence time of the burnt gases at high tem-

perature. This residence time is lower as the engine speed increases and, besides, it is even lower for greater EEVO.

A similar trend can be observed also for the CO formation, it gets lower as engine load decreases (Figure 4.7a and Figure 4.7b), although there is no much difference between the different EVO advances. In this case the conversion of HC into CO is interrupted as EVO is advanced, resulting in a reduction of CO emissions when compared to the baseline case. It is worth to mention that, due to possible uncertainties in the pollutants formation model, this emissions analysis are focused on trends more than in specific amounts.

Regarding NO_x emissions when performing an exhaust re-opening, it can be observed that emission levels are higher in all the four operating points compared to the baseline case. Indeed, it is the worst strategy in terms of NO_x formation at low load, as it is presented in Figure 4.5a and Figure 4.5c. Exhaust NO_x specific emissions increase with the maximum lift reached during the re-opening and the increment is higher than 50% in most of the cases. The lower CO_2 mass fraction at IVC, which indicates less residual mass in the combustion chamber, leads to greater maximum temperatures during the combustion which increases the NO_x formation. This trend applies to both *EVrO* 160° and EVrO 120° strategies, with slightly less NO_x formation in the short re-opening case. *EVrO* 160° with 3 mm lift in Figure 4.5b deserves a special mention since it achieves a NO_x reduction. Nevertheless, it corresponds to an unusual point with a large fuel penalty, as seen in Figure 4.3b. In general, all the strategies worsen the volumetric efficiency, leading to less trapped mass than in the baseline case. Even though these strategies increase the cylinder temperature at IVC by also increasing the IGR, since the EGR rate is controlled in order to keep the intake air mass flow, at the end, this IGR means lower EGR rate than in the baseline. The lower overall EGR results in more NO_x emissions. Figure 4.6 shows the relative difference (in %) in EGR and IGR featured by the six strategies respect to the baseline case. This results correspond to the 4 bar BMEP at 1250 rpm operating point, but the behaviour is similar in the four operating points presented in previous figures where the trend is to produce more NO_x. In Figure 4.6, it can be seen that, in general, the decrease in EGR (depicted as

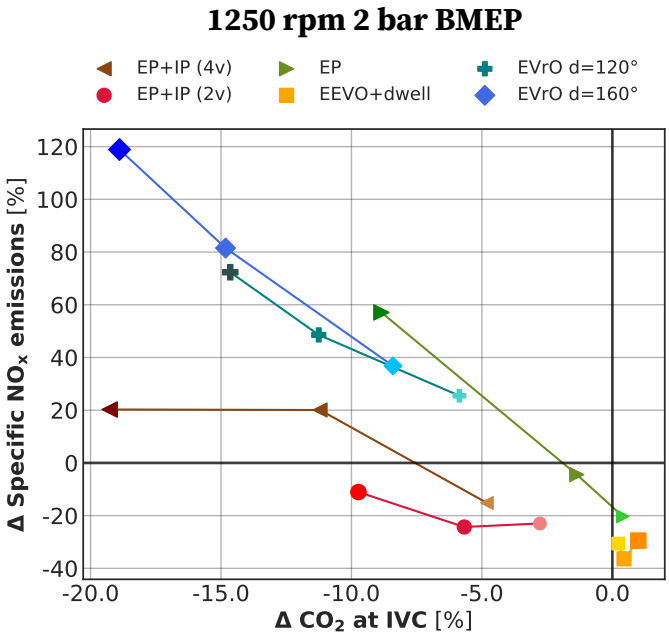

(a) ΔCO_2 *mass fraction at IVC (%) vs* Δ*specific* NO_x *emissions (%), 2 bar BMEP at 1250 rpm.*

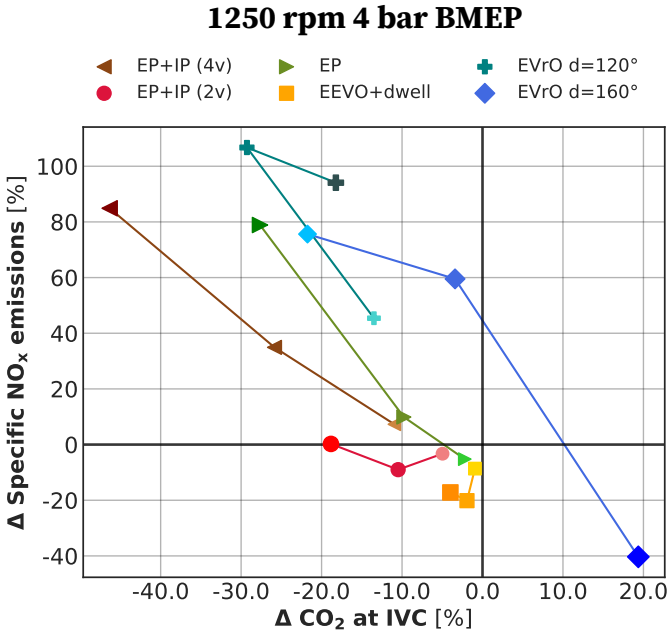

(b) ΔCO_2 *mass fraction at IVC (%) vs* Δ*specific* NO_x *emissions (%), 4 bar BMEP at 1250 rpm.*

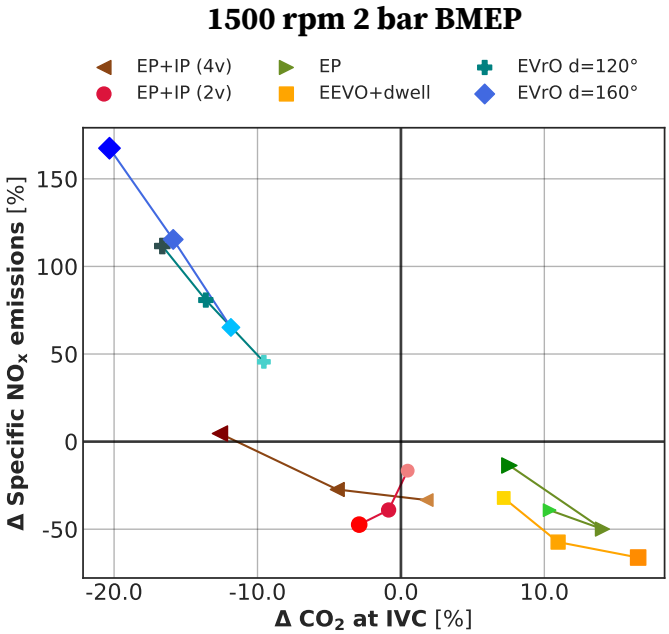

(c) ΔCO_2 *mass fraction at IVC (%) vs* Δ*specific* NO_x *emissions (%), 2 bar BMEP at 1500 rpm.*

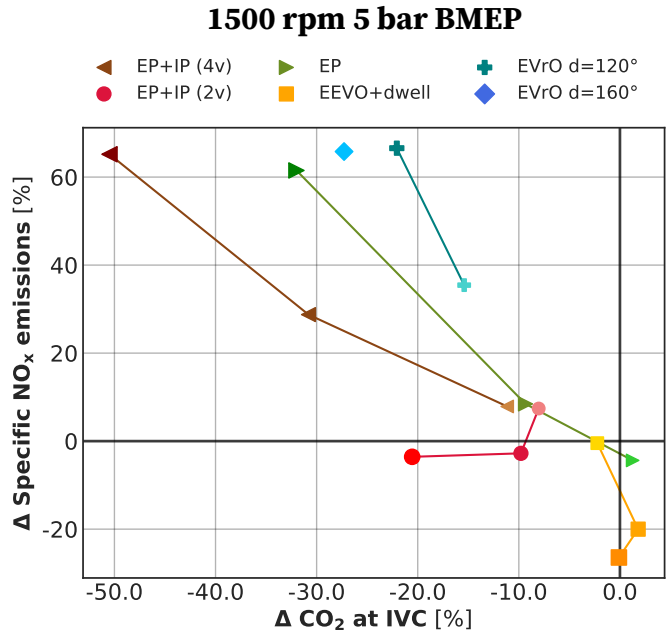

(d) ΔCO_2 *mass fraction at IVC (%) vs* Δ*specific* NO_x *emissions (%), 5 bar BMEP at 1500 rpm.*

Figure 4.5: *Steady-state results:* CO_2 *mass fraction at IVC variation vs specific* NO_x *emissions variation. The variation is referred to the baseline camshaft.*

a diamond) is higher than the increment in IGR (depicted as a circle) for *EP*, *EP+IT (4v)* and *EVrO* strategies, so the total exhaust gas recirculated is lower in this case than the one with the baseline valve timing.

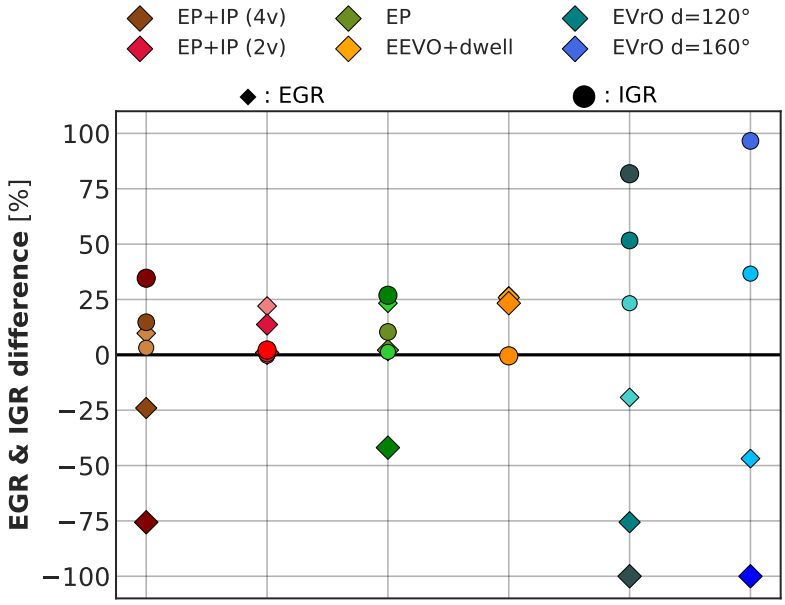

Figure 4.6: EGR and IGR relative difference respect to the baseline, 4 bar BMEP at 1250 rpm.

As far as carbon monoxide emissions are concerned, a potential reduction can be achieved by performing an exhaust valve re-opening. As illustrated in Figure 4.7a, Figure 4.7b, Figure 4.7c and Figure 4.7d it is feasible to reduce combustion CO emissions by 50 % or more, specially at 1250 rpm. The lean mixture —even though λ is slightly lower than in the baseline case because of the higher fuel mass, there is lower EGR flow than in the baseline: Figure 4.5c and Figure 4.6— that can be achieved by applying *EVrO* results in lower CO pollutant emissions. This trend is observed for both *EVrO* strategies being magnified in the 160° CA re-opening duration version. The maximum re-opening valve lift also plays a role in the CO reduction, leading to lower emissions when increasing the lift. When the re-opening lift and duration are higher, there is more fuel to keep the same torque and more residual gases in the combustion chamber. Therefore, all the carbon cannot be converted to CO_2 during the combustion and more CO is formed.

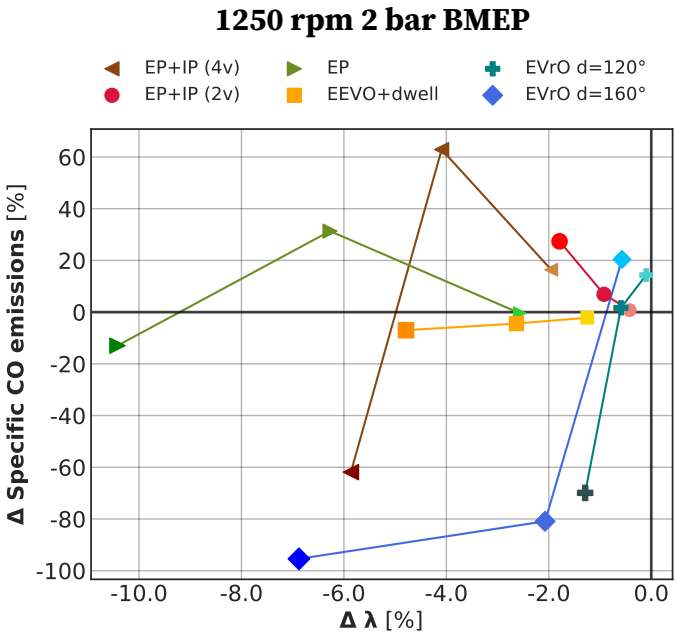

(a) *ΔAir−fuel equivalence ratio (λ) (%) vs Δspecific CO emissions (%), 2 bar BMEP at 1250 rpm.*

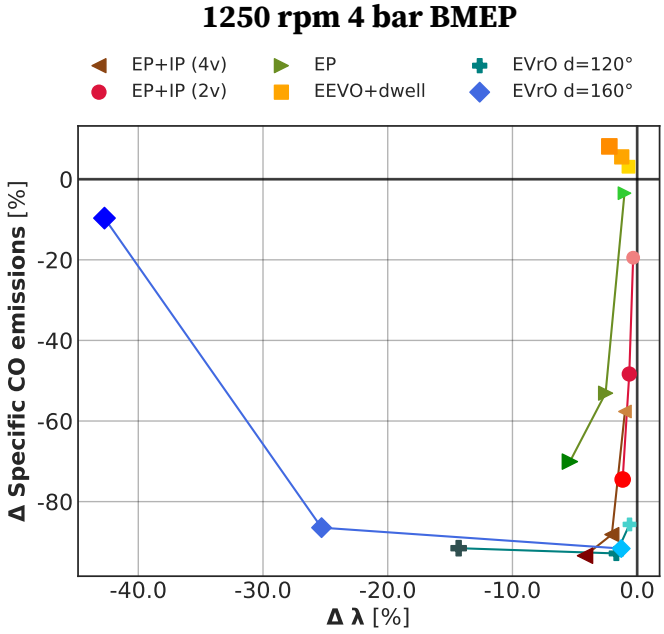

(b) *ΔAir−fuel equivalence ratio (λ) (%) vs Δspecific CO emissions (%), 4 bar BMEP at 1250 rpm.*

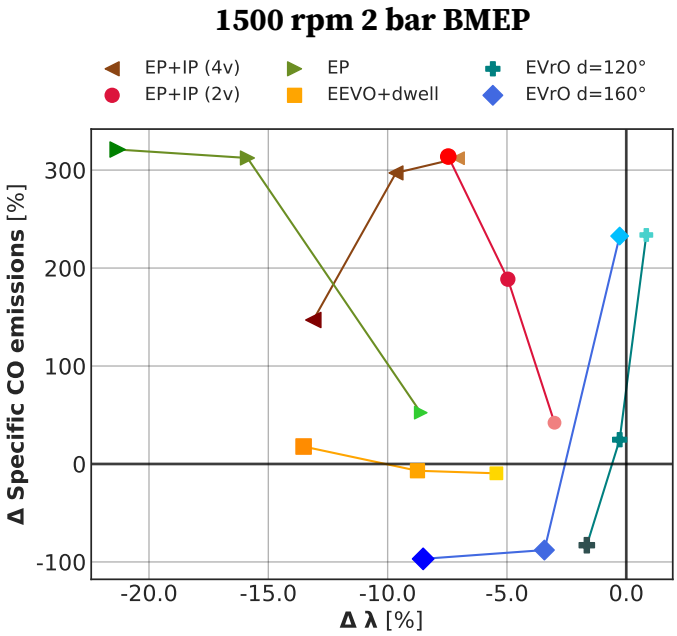

(c) *ΔAir−fuel equivalence ratio (λ) (%) vs Δspecific CO emissions (%), 2 bar BMEP at 1500 rpm.*

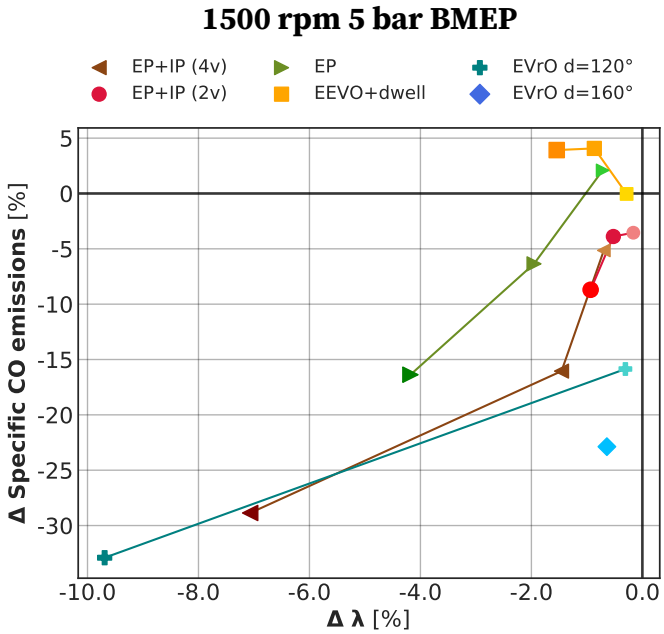

(d) *ΔAir−fuel equivalence ratio (λ) (%) vs Δspecific CO emissions (%), 5 bar BMEP at 1500 rpm.*

Figure 4.7: *Steady−state results: Air−fuel equivalence ratio (λ) variation vs specific CO emissions variation. The variation is referred to the baseline camshaft.*

In case of *EP+IP* strategies, an upward trend is observed in NO_x formation as engine load increases. The increment on NO_x formation compared to the baseline case can be explained because of the lower EGR mass flow when increasing the engine load as indicated by the CO_2 mass fraction at IVC in Figure 4.5b and Figure 4.5d. The lower total EGR (EGR + IGR) shown in Figure 4.6, coupled with an increase in fuel consumption as greater is the valve advance/delay, leads to higher in-cylinder temperatures and, thus, producing more NO_x. Since *EP+IP (2v)* does not incurs in such heavy fuel penalty, it does not produce such increment in NO_x emissions. In fact, it is able to reduce them at low load (2 bar BMEP) both at 1250 and 1500 rpm. The detriment in NO_x formation is worse as greater is the exhaust/intake phasing. An opposite trend can be observed for CO pollutant emissions due the lower residual burned gases retained during the combustion. *EP+IP* strategies are able to reduce CO formation by enlarging the valve phasing in Figure 4.7b and Figure 4.7d.

At low engine load, however, the NO_x formation is reduced for both *EP+IP* and *EP* strategies due to a greater ability to retain some residual burnt gases as indicated in Figure 4.6, where the lighter markers of these two strategies show a small increase in EGR and IGR amounts with respect to the baseline case. This effect is more evident at 1500 rpm rather than at 1250 rpm as can be observed in Figure 4.5c, where a 30 % reduction in NO_x can be achieved with 3 % more CO_2 after IVC by the *EP+IP (4v)* 20° *CA* configuration. On the contrary, higher CO emissions are produced due to the reduction in intake fresh air flow and the increment in fuel consumption (Figure 4.7c). In this regard, the 2 valves variant seems to be more advantageous than the 4 valves since it allows reducing NO_x combustion emissions in the four operating points.

Regarding pollutant emissions formation by applying the *EP (exhaust phasing)* strategy, its behaviour is similar to *EP+IP (4v)* strategy. NO_x formation increases with the engine load and is higher for greater advances in EVO and EVC. Keeping the baseline case intake valve timing leads to NO_x formation values that are slightly lower compared to *EP+IP* strategy. This difference is explained by the higher IGR achieved by *EP*, specially at low load (Figure 4.5c). In terms of CO formation, the trend is similar in both

strategies and opposite to NO_x formation, as explained above.

4.4.2 Transient analysis

As part of the comparison between the presented VVT strategies, a transient analysis has been carried out considering the WLTC type approval test.

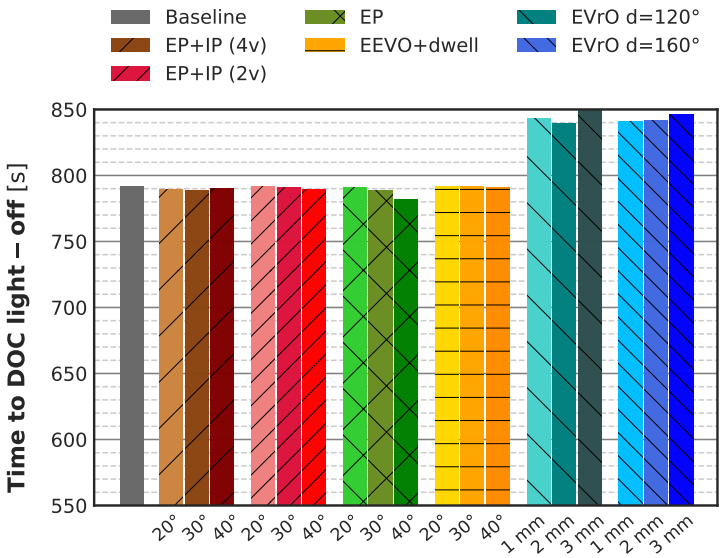

Figure 4.8: Time to reach DOC light-off temperature.

Figure 4.8 represents the time it takes for the DOC monolith to reach the light-off temperature. This temperature —defined as the temperature at which CO conversion efficiency reaches 50 %— is around 200 °C, as it is measured experimentally and according to other authors who studied the DOC efficiency in similar after-treatment systems and in similar diesel engines [118, 132]. In order to evaluate the temperature downstream the DOC, a catalyst model (described in subsection 3.2.5) has been included into the engine model. This model is able to predict the pressure drop and the heat transfer through the monolith, as well as predicting outlet CO and HC emission levels based on the proper oxidation and reduction mechanisms. Thus, it is possible to compare the resulting DOC outlet temperature among the

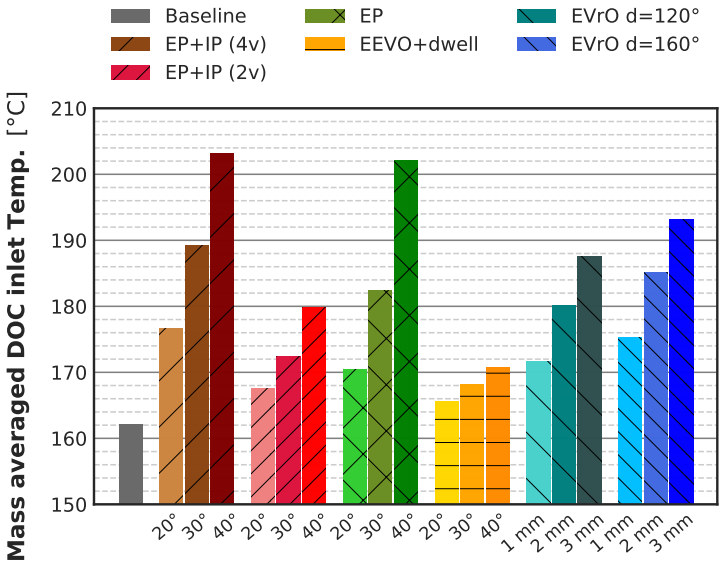

Figure 4.9: Mass averaged temperature at DOC inlet during the low speed stage of the WLTC.

different VVT strategies, since the gas temperature is similar as the one in the channels wall. Looking at Figure 4.8, it can be observed that there is no DOC heat-up improvement in any of the strategies. The reason is more related to the way this temperature is achieved rather than in the strategy used. This light-off temperature occurs at the same time in all the strategies because it coincides with an acceleration in the dynamic transient. However, both *EVrO* configurations delay the time to reach light-off temperature. Although the exhaust valve re-opening can increase the DOC inlet temperature —as it is observed in Figure 4.9 and in the steady-state results— the fact is that in the transient accelerations, where the model is unable to reach the torque target (such as *EVrO* with a valve lift higher than 1 mm) the resulting peaks in the turbine downstream temperature are not reached; thus, DOC is not heated as quickly as in the baseline case. Consequently, the time to reach DOC light-off temperature increases in these cases around 50 seconds.

Figure 4.9 shows the mass averaged temperature downstream the turbine during the low speed phase of the WLTC. This mean temperature is calculated according to Equation 4.3, where the interval 0 to 589 seconds

corresponds to the low speed stage of the WLTC. Relevant information is derived from this comparison. On the one hand, all the strategies show an increase in the exhaust temperature, as it was expected from the steady-state results. However, as indicated above, they do not reduce the time to reach light-off conditions in the catalyst when reproducing the WLTP test cycle. In terms of *EEVO+dwell* performs poorly as it was shown in the steady-state analysis on subsection 4.4.1. On the other hand, both *EP+IP (4v)* and *EP* strategies perform better than *EVrO* ones, showing an average increment from 8 °C to 40 °C when advancing the exhaust (*EP*) and from 15 °C to 41 °C when also delaying the intake *EP+IP*. *EVrO* 160° option shows a greater potential when heating the exhaust than the short re-opening alternative. Their highest average temperature values are 187 °C and 193 °C, respectively and with 3 mm lift. Regarding *EP+IP (2v)* alternative, it performs according to the 4 valves version but in a more restrained way since only two of the four valves are being modified. Nevertheless, this alternative is more useful than *EEVO* in terms of heating the exhaust.

$$T_{\text{avg}} = \frac{\int_0^{589} (\dot{m} \cdot T)\, \mathrm{d}t}{\int_0^{589} \dot{m}\, \mathrm{d}t} \tag{4.3}$$

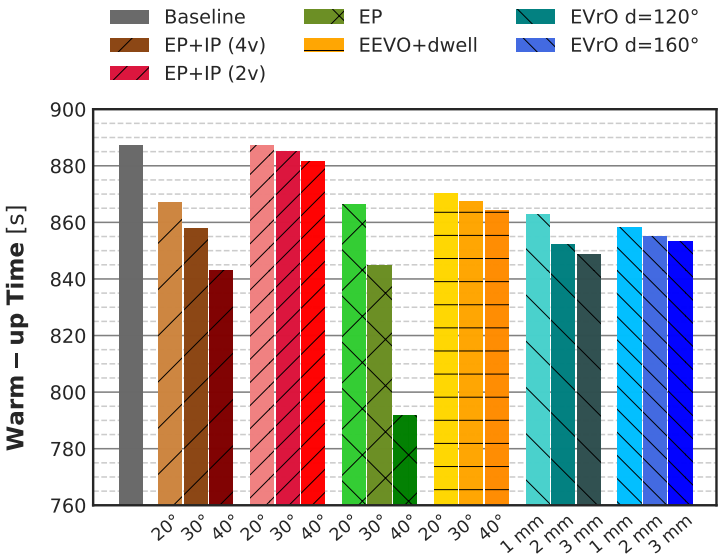

Figure 4.10: Time to reach coolant thermostat threshold (80 °C)

Coolant temperature plays an important role in the engine warm-up as well as in the low pressure EGR activation. Heating up the engine increases its efficiency during the heating phase. During this time the coolant thermostat is closed, so the coolant temperature keeps raising until a determined value is achieved. Figure 4.10 shows the time required to heat the coolant up to 80 °C. It can be observed that all the strategies meet the goal of heating the coolant quicker than the baseline case. This way, a warm-up time reduction between 20 and 45 seconds can be achieved with the *EP+IP (4v)* configuration. The 2 valves versions, contrarily does not results in a faster warm-up. *EEVO+dwell* offers a reduction between 17 and 24 seconds. Both *EVrO* solutions offer a warm-up reduction better than *EEVO+dwell*, going down to 25 seconds with 1 mm lift and 40 seconds with 3 mm lift. In all the cases, a higher lift and a large valve phasing results in higher exhaust temperature and, thus, a shorter time to reach the coolant threshold temperature. However, the fastest warm-up time can only be achieved by the *EP* strategy. The fact that the compression of the trapped exhaust gases after the EVC is not followed by an expansion like in the *EP+IP* cases, leads to a hot backflow of exhaust gases that is released into the intake ports at IVO; thus, resulting in a heating of the coolant that surrounds the intake ports. In this case, it is possible to reduce the warm-up time by 96 seconds.

Regarding fuel consumption, Figure 4.11 shows the accumulated fuel consumption over the first 589 seconds of the WLTC, which corresponds to the low vehicle speed stage. As it was mentioned above in the steady-state analysis, all the strategies incur in a penalty in fuel economy. It can be seen that *EP+IP (2v)* offers the lowest penalty in fuel consumption, which is about 3 g (1.4 %) more than in the baseline cam case. Advancing the exhaust valves opening increases the fuel consumption in order to keep the target torque. This increment stands out in the *EP* cases due to the higher pumping losses which results in a fuel penalty, increasing the fuel consumption around 29 g (14.8 % for the worst case of 40° CA) compared to the baseline case. *EVrO* solutions offer a restrained fuel consumption compared to the potential for increasing the exhaust temperature, since they offer a good trade-off in these terms. The maximum accumulated fuel difference in achieved by *EVrO* 120° and 3 mm lift, whose consumption is 10 g (5.6 %) higher than the baseline solution.

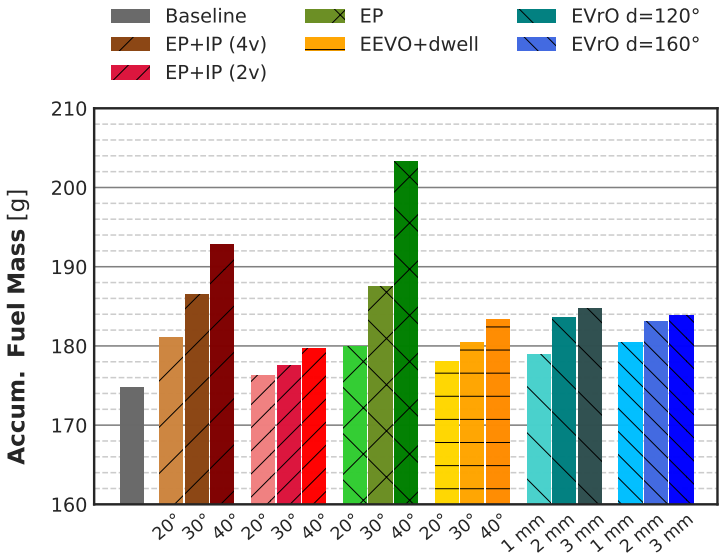

Figure 4.11: Accumulated fuel consumption over the low speed stage of the WLTC.

As far as pollutant emissions are concerned, a reduction in NO_x cylinder-out emissions is only feasible by performing an exhaust valve re-opening. Looking at Figure 4.12, the greater the maximum re-opening lift, the lower the NO_x formation. This trend is higher in the *EVrO* 160° cases whose 3 mm configuration reaches a total abatement of 23 %. The reduction goes down to 11 % in the *EVrO* 160° alternative. Although these values could be contrary to the values shown in Figure 4.5a and Figure 4.5c, the fact is that the exhaust valve re-opening allows retaining part of the exhaust gases within the cylinder and, consequently, reducing NO_x formation, whereas in the baseline case there is no low pressure EGR during the low speed phase of the WLTC in this particular engine. Furthermore, during the accelerations, the ECU closes the HP-EGR valve, but the exhaust re-opening still produces IGR during these transients which results in lower peak exhaust temperatures during the accelerations and a reduction in NO_x emissions. The fact that peak torque values are not reached with the *EVrO* 160° strategy also affects the NO_x comparison with the baseline case, since the fresh air charge gets reduced and the ECU control limits the fuel injected to prevent a high smoke formation. In case of advancing EVO, the increment in NO_x emissions is due to a low IGR during the fast accelerations of the WLTC, which means lower burned residual gas mass than in the baseline case. Consequently, the IGR

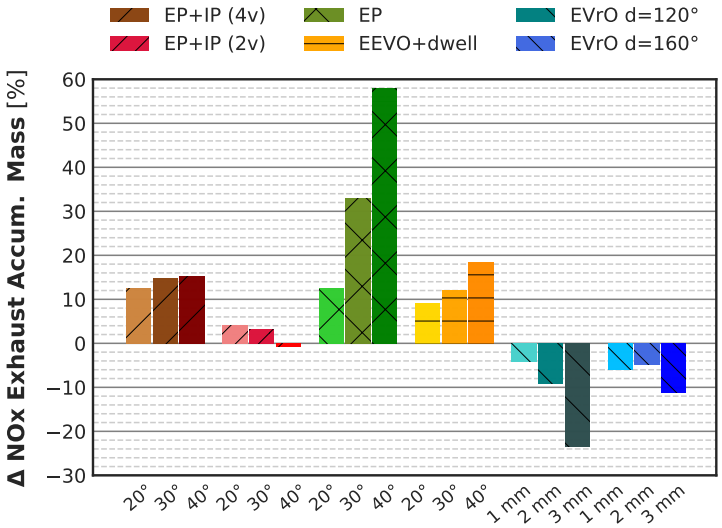

Figure 4.12: *Accumulated combustion NO_x emissions over the low speed stage of the WLTC, difference with respect to the baseline case.*

effect that could reduce NO_x emissions during idle periods and slower accelerations is not remarkable. In this case the transient results are consistent with the steady-state results, leading to higher emissions as greater is the advance in the exhaust. *EP* heightens NO_x formation above 30 % by advancing the exhaust event 30° CA and gets even worse by advancing EVO and EVC 40° CA, leading to an increment of 57 % in NO_x emissions.

Regarding CO (Figure 4.13), hydrocarbons (Figure 4.14) and soot (Figure 4.15) formation, similar trends are observed. A particular difference can be found in case of the "EEVO + dwell" strategy, whose HC and PM (soot) accumulated amounts are high taking into account its low potential in order to heat up the exhaust gases. The greater values are explained due to the fact that performing an EEVO results in an increase in fuel injected mass, which leads to an increment in HC, CO and soot. Moreover, the earlier blowdown interrupts the oxidation of HC and CO during the expansion stroke as stated in subsubsection 4.1.2.3. Different trends can be observed for HC emissions in *EP+IP* and re-opening strategies. On the one hand, *EP+IP (4v)* HC emissions are far higher (above 30 %) than the baseline case due to the EEVO. However, *EP* alternative results in lower HC levels than *EP+IP*. This could be

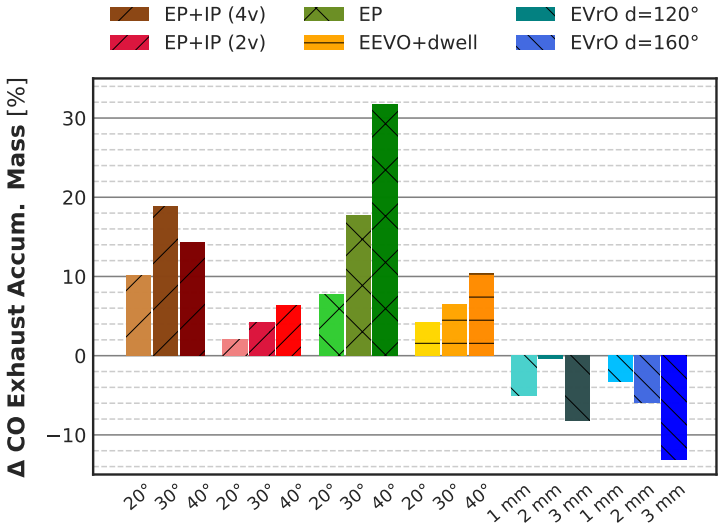

Figure 4.13: Accumulated combustion CO emissions over the low speed stage of the WLTC, difference with respect to the baseline case.

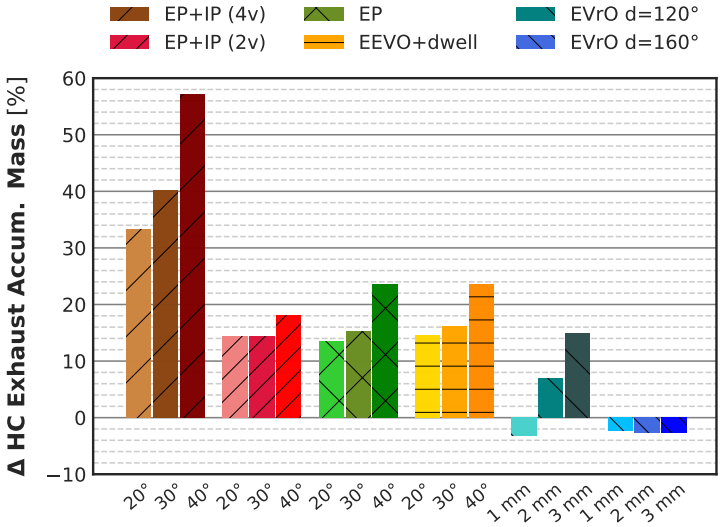

Figure 4.14: Accumulated unburned HC emissions over the low speed stage of the WLTC, difference with respect to the baseline case.

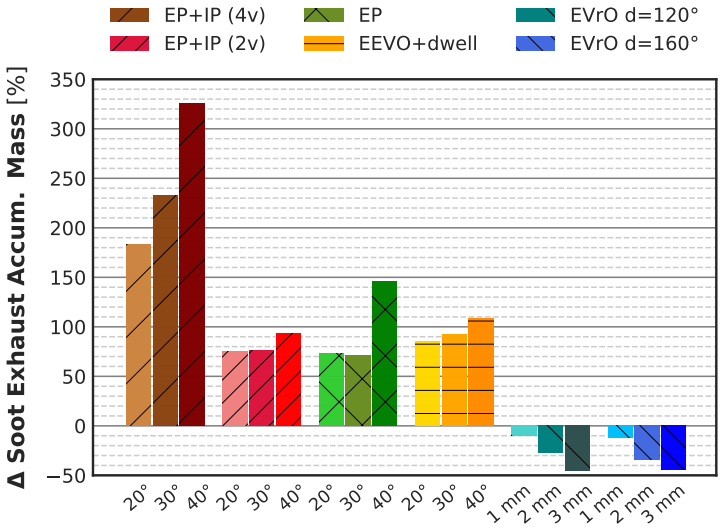

Figure 4.15: Accumulated combustion PM (soot) emissions over the low speed stage of the WLTC, difference with respect to the baseline case.

explained by the slow mixing due to the late IVO and IVC. On the other hand, HC emissions increase as higher is the maximum lift during the re-opening, specially for the short *EVrO* cases, due to the lack of oxygen as engine load increases for low engine speeds, which results in hydrocarbons not burned. *EVrO* 160° does not show a comparable trend in terms of HC and CO formations since it is related with the acceleration power peaks, where the longer re-opening is not able to fully reach the reference power.

In terms of soot formation, the increase in fuel consumption in *EP+IP (4v)*, *EP* and *EEVO+dwell* strategies leads to a higher soot formation. In the case of *EVrO* solutions, the reduced fuel penalty and the reduction in the in-cylinder maximum temperature leads to a slightly decrease in soot emissions. Besides, this two configurations cannot be compared in the same way due to the small output power drop during some of the fast accelerations.

Figure 4.16 shows a performance comparison of all VVT strategies in terms of the average after-treatment temperature versus the corresponding penalty in fuel consumption during the low speed phase of the WLTC, so this figures summarises at a glance the information shown in Figure 4.11 and Figure 4.9, but normalised respect to the baseline values. It can be

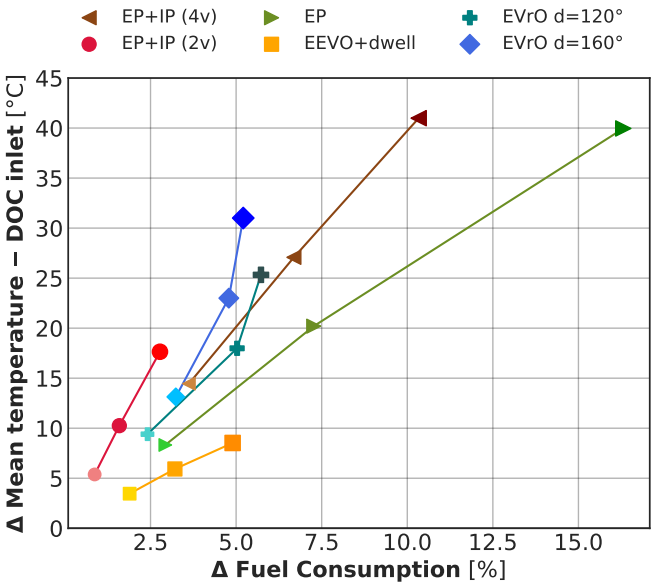

Figure 4.16: Mass averaged temperature at DOC inlet variation (°C) vs fuel consumption variation (%) respect to the baseline during the low speed stage of the WLTC.

noted that *EP* achieves the higher increase in temperature (40 °C with a fuel penalty of 16 %). However, *EP+IP (4v)* strategy performs better than *EP* since it is able to reach around 41 °C while consuming around 11 % more fuel than the baseline valve timing. *EVrO* configurations present a good performance in this sense, since both re-opening configurations are able to surpass an increment of 20 °C with a fuel penalty of 5 %. It results interesting to point out how both *EVrO* curves are not as linear as the rest of alternatives. So higher exhaust temperatures can be achieved by increasing the re-opening lift without compromising the fuel consumption.

On the subject of fuel consumption, temperature gain and NO_x trade-offs during the WLTC low speed phase, Figure 4.17 and Figure 4.18 show the NO_x formation versus fuel consumption and average exhaust temperature, respectively, variation with respect to the baseline valve timings. *EP* strategy shows the worst trade-off since the fuel penalty impacts on higher NO_x emissions. In Figure 4.18 it can be observed that this temperature gain also results in higher NO_x. *EP+IP* alternatives perform quite different. On the one hand, the NO_x emissions remain between 10 % and 20 % in the 3 different possibilities (20°, 30° and 40° CA), so an increment in the exhaust

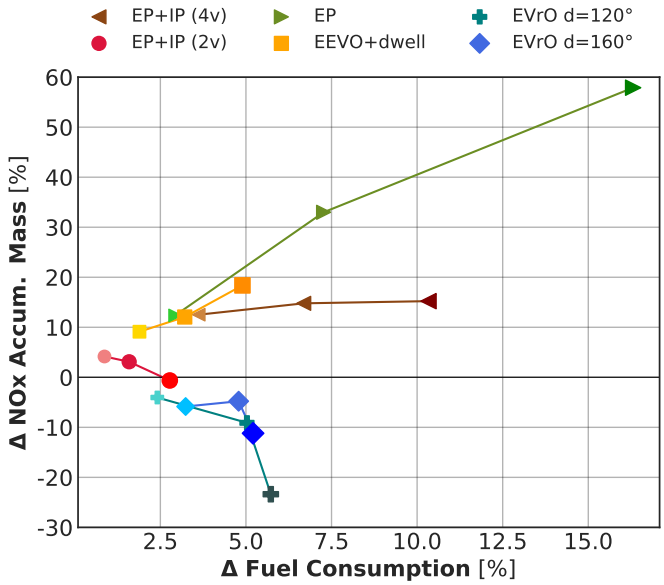

Figure 4.17: NO_x accumulated mass variation (°C) vs fuel consumption variation (%) respect to the baseline during the low speed stage of the WLTC.

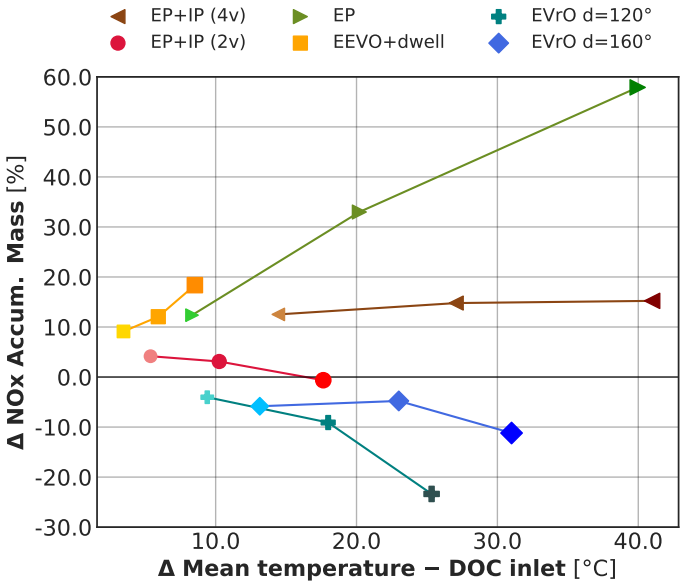

Figure 4.18: NO_x accumulated mass variation (%) vs mass averaged temperature at DOC inlet variation (°C) respect to the baseline during the low speed stage of the WLTC.

mean temperature does not incur in a rise in emissions. On the other hand, the 2 valves alternative is able to match baseline NO_x emissions with an advance/delay of 40° CA and a mean temperature difference of 18 °C. This temperature gain may seem restrained compared to the 4 valves version, but it is better than the performance obtained by the *EEVO+dwell* configuration, which even rises NO_x emissions up to 20 %. Regarding *EVrO* strategies, both offer a good trade-off in terms of NO_x and fuel consumption since it is possible to reduce NO_x to 20 % while increasing the mean temperature around 25 °C with a fuel penalty of 6 %.

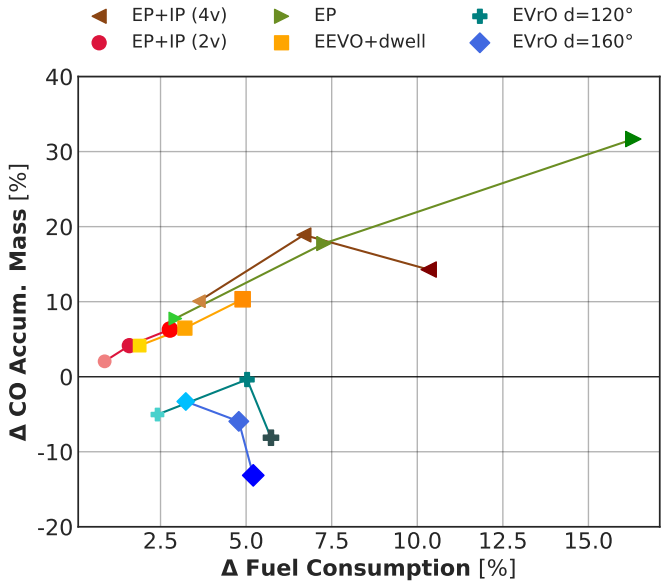

Figure 4.19: CO accumulated mass variation (°C) vs fuel consumption variation (%) respect to the baseline during the low speed stage of the WLTC.

In terms of carbon monoxide formation, the picture does not differ much from NO_x emissions graphs. Figure 4.19 presents the trade-off between CO formation and fuel consumption variation, while Figure 4.20 shows the CO-temperature trade-off (these trade-offs only represent the results during the first stage of the WLTC). CO formation follows a similar pattern in the CO-fuel trade-off (Figure 4.19) for those configuration involving exhaust valve advance. Again, *EP* offers the worst trade-off, since it boosts CO emissions by 30 % while providing a temperature gain of 40 °C (Figure 4.20). In this regard, *EP+IP (4v)* alternative offers a better compromise between temperature increment, fuel consumption and CO formation.

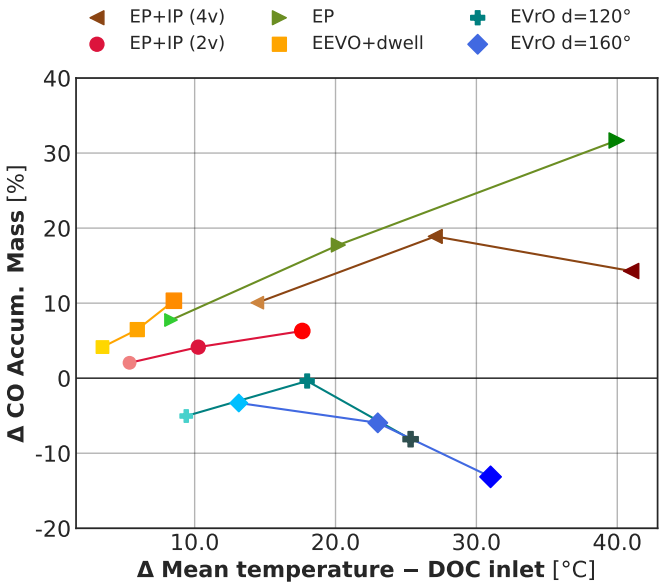

Figure 4.20: CO accumulated mass variation (%) vs mass averaged temperature at DOC inlet variation (°C) respect to the baseline during the low speed stage of the WLTC.

It is possible to also obtain 40 °C more in the exhaust with a fuel penalty of 10 % and 15 % more CO accumulated mass than in the baseline case. *EVrO* alternatives offer again the best trade-off concerning CO emissions, fuel consumption and temperature gain. CO variations are negative for both re-opening durations and for the three different valve lifts. Moreover, they achieve a mean increase in the exhaust temperature up to 30 °C with a fuel penalty below 6 %. The fall in both NO_x and CO emissions when increasing the re-opening lift is due to the lower torque achieved by this strategies during the transient accelerations, since the fresh air charge gets reduced and the ECU control limits the injected fuel to prevent a high smoke formation.

4.5 Conclusions

Several variable valve timing strategies were discussed in this chapter with the aim of achieving an increment in the exhaust temperature while not worsening combustion emissions. Several configurations for each strategy were also compared in terms of exhaust temperature profit, fuel consumption, warm-up time and pollutant emissions. These strategies involve the adjustment of the valve timing and the possibility to perform a second exhaust valve event to re-entrain part of the exhaust gases during the intake stroke. In the spirit to summarise the conclusions obtained along this study, the following points are exposed:

1. Advancing EVO results in an increment in the exhaust temperature due to the early blowdown of hot gases into the exhaust manifold. Advancing also EVC and performing a second exhaust valve event allows a higher exhaust temperature by retaining an amount of the exhaust gases to participate in the next engine cycle (IGR).

2. In the case of *EVrO*, a long re-opening duration performs better than a longer one in order to increase the exhaust temperature and reduce CO emissions since more IGR is able to produce. Regarding NO_x emissions, the shorter re-opening shows a small advantage compared to the longer one (*EVrO* 160°).

3. *EEVO+dwell* strategy does not produce a relevant increase in exhaust temperature, nor a faster DOC light-off, nor an improvement in pollutant emissions.

4. All VVT strategies incur in a penalty in fuel economy, which is lower for *EVrO* cases —below 6 % over the low speed stage of the WLTC.

5. In the same way, all the VVT alternatives enable a faster engine warm-up, which is even faster in the *EP* solution. So around 96 seconds could be saved by advancing the exhaust event 40° CA. This is due to the fact that the compression of the trapped exhaust gases after the EVC is not followed by an expansion like in the *EP+IP* cases, leads to a hot back-

flow of exhaust gases that is released into the intake ports at IVO; thus, resulting in a heating of the coolant that surrounds the intake ports.

6. Both *EVrO* alternatives present the best trade-off between exhaust temperature increment and fuel consumption up to 30 °C. From that temperature onwards, *EP+IP (4v)* configuration offers a better trade-off and is able to reach an increment of 40 °C. *EP* allows higher exhaust temperatures and,but the fuel penalty is far greater than the other solutions (a maximum of 16 %).

7. Exhaust valve re-opening presents the best trade-off between combustion pollutant emissions and fuel efficiency, being able to reduce both NO_x and CO emissions compared to the baseline case. Regarding the other VVT strategies, *EP+IP* presents a better trade-off than *EEVO+dwell* and *EP* solutions in terms of temperature gain and emissions.

8. The partial *EP+IP (2v)* solution, which involves only the modification of the valve timing of one pair of valves, offer results closer to the baseline than to the 4 valves version *EP+IP (4v)*. In all the comparisons *EP+IP (2v)* with and advance/delay of 40° CA is more advantageous than *EP+IP (2v)* with and advance/delay of 20° CA —specially in terms of emissions formation.

An exhaust advance and an intake delay has been found to be a good technique to increase exhaust temperature and reduce warm-up time. The presented results at dynamic operating conditions show that exhaust valve re-opening is an interesting technique in terms of IGR production, exhaust temperature increment, fuel consumption compromise and pollutant emissions reduction. However, in this study only the re-opening lift has been modified, neither the duration not the re-opening starting angle. Besides, at some acceleration peaks, *EVrO* alternatives are not able to reach the required power output. For these reasons, an active control to modify the re-opening start, lift and duration according to the operating point is presented in the next chapter.

The exhaust temperature increase obtained by VVT applications is of special interest to evaluate the performance of LNT and SCR, and even ac-

celerate the activation of these devices in order to reduce NO_x emissions. A SCR model is currently under development by our research group and it will be included in the virtual engine model presented in this work.

In chapter 5, an active control is developed and presented to adapt both *EP+IP* and re-opening parameters to any operating point without compromising fuel efficiency. In this regard, *EEVO+dwell* and *EP* solutions are dismissed: the former due to its low capability rising the exhaust enthalpy and the latter because of its high fuel consumption.

Chapter 4 References

[107] G. Torazza and D. Giacosa. "Valve-actuating mechanism for an internal combustion engine". Pat. 3641988. 1972. url: https://www.freepatentsonline.com/3641988.html (cit. on p. 141).

[108] G. Garcea. "Timing variator for the timing system of a reciprocating internal combustion engine". Pat. 4231330. 1980. url: https://www.freepatentsonline.com/4231330.html (cit. on p. 141).

[109] Honda Motor Co., Ltd. *The VTEC Engine / 1989*. Accessed 2020-09-28 at https://global.honda/heritage/episodes/1989vtecengine.html. 2020 (cit. on p. 142).

[110] S. Benett. *Medium/Heavy Duty Truck Engines, Fuel & Computerized Management Systems*. 5th ed. Cengage Learning, 2016, p. 1008. isbn: 9781305578555 (cit. on p. 142).

[111] Mitsubishi Motors. *Mitsubishi Motors Launches RVR New Compact Crossover*. Accessed 2020-09-28 at https://www.mitsubishi-motors.com/publish/pressrelease_en/products/2010/news/detail0729.html. 2010 (cit. on p. 142).

[112] T. Lancefield, I. Methley, U. Räse, and T. Kuhn. "The application of variable event valve timing to a modern diesel engine". *SAE 2000 World Congress*. SAE International, 2000. doi: 10.4271/2000-01-1229 (cit. on p. 143).

[113] M. A. Gonzalez and D. Di Nunno. "Internal Exhaust Gas Recirculation for Efficiency and Emissions in a 4-Cylinder Diesel Engine". *SAE 2016 International Powertrains, Fuels and Lubricants Meeting*. SAE International, 2016. doi: 10.4271/2016-01-2184 (cit. on p. 143).

[114] J. R. Serrano, P. Piqueras, R. Navarro, J. Gómez, M. Michel, and B. Thomas. "Modelling Analysis of Aftertreatment Inlet Temperature Dependence on Exhaust Valve and Ports Design Parameters". *SAE 2016 World Congress and Exhibition*. SAE International, 2016. doi: 10.4271/2016-01-0670 (cit. on p. 143).

[115] R. M. Siewert. "How individual valve timing events affect exhaust emissions". *International Mid-Year Meeting*. SAE International, 1971. doi: 10.4271/710609 (cit. on pp. 145, 147, 148).

[116] T. Tomoda, T. Ogawa, H. Ohki, T. Kogo, K. Nakatani, and E. Hashimoto. "Improvement of diesel engine performance by variable valve train system". *International Journal of Engine Research*, 11 (5), (2010), pp. 331–344. issn: 14680874. doi: 10.1243/14680874JER586 (cit. on pp. 145, 146).

[117] J. Benajes, E. Reyes, and J. M. Luján. "Modelling study of the scavenging process in a turbocharged diesel engine with modified valve operation". *Proceedings of the Institution of Mechanical Engineers, Part C: Journal of Mechanical Engineering Science*, 210 (4), (1996), pp. 383–393. issn: 09544062. doi: 10.1243/PIME_PROC_1996_210_210_02 (cit. on pp. 145, 149).

[118] K. Deppenkemper, C. Zyalcin, M. Ehrly, M. Schoenen, D. Bergmann, and S. Pischinger. "1D Engine Simulation Approach for Optimizing Engine and Exhaust Aftertreatment Thermal Management for Passenger Car Diesel Engines by Means of Variable Valve Train (VVT) Applications". *WCX World Congress Experience*. SAE International, 2018. doi: 10.4271/2018-01-0163 (cit. on pp. 145, 168).

[119] J. P. Zammit, M. J. McGhee, P. J. Shayler, T. Law, and I. Pegg. "The effects of early inlet valve closing and cylinder disablement onfuel economy and emissions of a direct injection diesel engine". *Energy*, 79, (2015), pp. 100–110. issn: 03605442. doi: 10.1016/j.energy.2014.10.065 (cit. on pp. 145, 146).

[120] W. De Ojeda. "Effect of variable valve timing on Diesel combustion characteristics". *SAE 2010 World Congress and Exhibition*. SAE International, 2010. doi: 10.4271/2010-01-1124 (cit. on p. 146).

[121] A. Piano, F. Millo, D. Di Nunno, and A. Gallone. "Numerical Assessment of the CO2 Reduction Potential of Variable Valve Actuation on a Light Duty Diesel Engine". *CO2 Reduction for Transportation Systems Conference*. SAE International, 2018. doi: 10.4271/2018-37-0006 (cit. on p. 146).

[122] A. Piano. "Analysis of Advanced Air and Fuel Management Systems for Future Automotive Diesel Engine Generation". PhD thesis. Politecnico di Torino, 2018 (cit. on pp. 146, 147).

[123] W. Guan, V. B. Pedrozo, H. Zhao, Z. Ban, and T. Lin. "Variable valve actuation–based combustion control strategies for efficiency improvement and emissions control in a heavy-duty diesel engine". *International Journal of Engine Research*, 21 (4), (2020), pp. 578–591. issn: 20413149. doi: 10.1177/1468087419846031 (cit. on p. 146).

[124] W. Guan, H. Zhao, Z. Ban, and T. Lin. "Exploring alternative combustion control strategies for low-load exhaust gas temperature management of a heavy-duty diesel engine". *International Journal of Engine Research*, 20 (4), (2019), pp. 381–392. issn: 20413149. doi: 10.1177/1468087418755586 (cit. on p. 146).

[125] P. Maniatis, U. Wagner, and T. Koch. "A model-based and experimental approach for the determination of suitable variable valve timings for cold start in partial load operation of a passenger car single-cylinder diesel engine". *International Journal of Engine Research*, 20 (1), (2019), pp. 141–154. issn: 20413149. doi: 10.1177/1468087418817119 (cit. on pp. 146, 148).

[126] J. Kim and C. Bae. "An investigation on the effects of late intake valve closing and exhaust gas recirculation in a single-cylinder research diesel engine in the low-load condition". *Proceedings of the Institution of Mechanical Engineers, Part D: Journal of Automobile Engineering*, 230 (6), (2016), pp. 771–787. issn: 09544070. doi: 10.1177/0954407015595149 (cit. on p. 146).

[127] J. Benajes, S. Molina, R. Novella, and M. Riesco. "Improving pollutant emissions in diesel engines for heavy-duty transportation using retarded intake valve closing strategies". *International Journal of Automotive Technology*, 9 (3), (2008), pp. 257–265. issn: 12299138. doi: 10.1007/s12239-008-0032-7 (cit. on p. 146).

[128] X. Zhou, E. Liu, D. Sun, and W. Su. "Study on transient emission spikes reduction of a heavy-duty diesel engine equipped with a variable intake valve closing timing mechanism and a two-stage turbocharger". *International Journal of Engine Research*, 20 (3), (2019), pp. 277–291. issn: 20413149. doi: 10.1177/1468087417748837 (cit. on p. 146).

[129] D. B. Gosala et al. "Diesel engine aftertreatment warm-up through early exhaust valve opening and internal exhaust gas recirculation during idle operation". *International Journal of Engine Research*, 19 (7), (2018), pp. 758–773. issn: 20413149. doi: 10.1177/1468087417730240 (cit. on pp. 147, 156).

[130] G. B. Parvate-Patil, H. Hong, and B. Gordon. "Analysis of variable valve timing events and their effects on single cylinder diesel engine". *2004 Powertrain & Fluid Systems Conference & Exhibition*. SAE International, 2004. doi: 10.4271/2004-01-2965 (cit. on p. 147).

[131] A. Piano, F. Millo, D. Di Nunno, and A. Gallone. "Numerical Analysis on the Potential of Different Variable Valve Actuation Strategies on a Light Duty Diesel Engine for Improving Exhaust System Warm Up". *13th International Conference on Engines & Vehicles*. SAE International, 2017. doi: 10.4271/2017-24-0024 (cit. on p. 149).

[132] C. Guardiola, B. Pla, P. Bares, and J. Mora. "An on-board method to estimate the light-off temperature of diesel oxidation catalysts". *International Journal of Engine Research*, 21 (8), (2020), pp. 1480–1492. issn: 20413149. doi: 10.1177/1468087418817965 (cit. on p. 168).

“True optimisation is the revolutionary contribution of modern research to decision processes.”

— George Bernhard Dantzig

Chapter 5

Development of a VVT control to improve DOC efficiency and emissions

Contents

5.1 Introduction 190
5.2 Model preparation 192
5.3 Control system methodology 194
5.4 Results and discussion 206
5.4.1 Adding DOC light-off temperature in the VVT control. 222
5.5 Conclusions 227
Chapter 5 References 231

5.1 Introduction

Variable valve timing began to be adopted in the automotive industry since the 1960 decade as a way to reduce hydrocarbon and carbon monoxide emissions, since air pollution became a major issue —specially in populated areas like Los Angeles [133]. This concern raised the need to know how to reduce emissions. In this way, researchers like Hagen et al. [134] in 1962, studied the composition of the exhaust gases by investigating the air-fuel ratio, engine speed, spark timing, exhaust back pressure, intake manifold pressure and also the valve overlap.

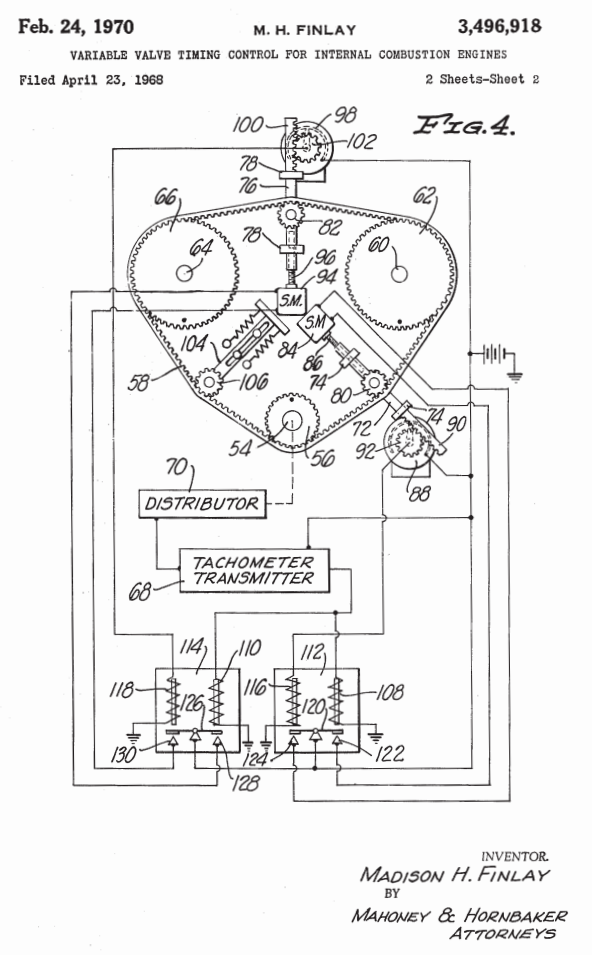

Figure 5.1: VVT control patented by Madison Finlay, 1968.

Since then, some systems were developed to automatically modify the valves timing in different operating conditions. The first control systems were based on the engine speed, as the electro-mechanic one proposed by Finlay in 1968 [135], whose sketch in shown in Figure 5.1. Later, with the development of electronics, these control systems were based not only on the engine speed but on the throttle position, the coolant temperature or the intake pressure. Currently, camless engine valvetrains are the greatest innovations [136], which provides greater freedom for controlling the different valve events and even independence between cylinders.

Variable valve timing technology offers multiple possibilities for controlling the combustion process. Murata et al. [137] studied late intake valve closing to achieve premixed diesel combustion. LIVC combined with EGR and injection timing control allowed to reduce NO_x and smoke emissions. VVT also has been applied to advanced combustion modes like in the work carried out by Hunicz et al. [138], who experimentally studied the combustion rate by applying variable intake and exhaust valve in a homogeneous charge compression ignition (HCCI) engine. In the same way, Xu et al. [139] studied VVT to adjust the effective compression ratio in a reactivity controlled compression ignition (RCCI) engine. They found than at low and mid loads, high effective compression ratio, large premix ratio, and early fuel injection can be utilised to realise Euro 6 nitrogen oxides limit with ultra-low soot emissions and low fuel consumption by using variable compression ratio and VVT strategies.

Regarding VVT theory, in chapter 4, different variable valve timing possibilities were presented. section 4.1 discusses the effects on engine efficiency and pollutant emissions formation while tweaking the different intake and exhaust valve events, as well as the objective pursued when performing an exhaust valve re-opening during the intake stroke. Besides, a brief history of variable valve timing application in the automotive industry was pointed out. In this chapter, *EEVO+dwell* technique is dismissed due to its limited scope for heating the after-treatment system and reduce pollutant emissions. In a far different way, *EP* technique has been excluded from this study due to its poor fuel economy and the greater NO_x and CO formation, which are two major caveats of this strategy.

Different VVT control strategies are presented in this chapter involving exhaust valve re-opening (*EVrO*) and exhaust negative phasing and intake positive phasing (*EP+IP*) solutions presented in section 4.3. The control strategies are focused on increasing the exhaust gas temperature with a minimum impact on fuel economy.

5.2 Model preparation

For this study, the thermo-and fluid dynamic model (VEMOD) presented and described in chapter 3 has been used. The engine model is the same already tested in chapter 4, which corresponds to a HSDI 1.6 L diesel engine. While in chapter 4, a wide study exploring different variable valve timing possibilities were explored, the results presented in this chapter concern the development of a variable valve timing control. In this regard, it is essential that intake and exhaust valve events can be modified in runtime, so it could be possible to adapt them to the current operating point.

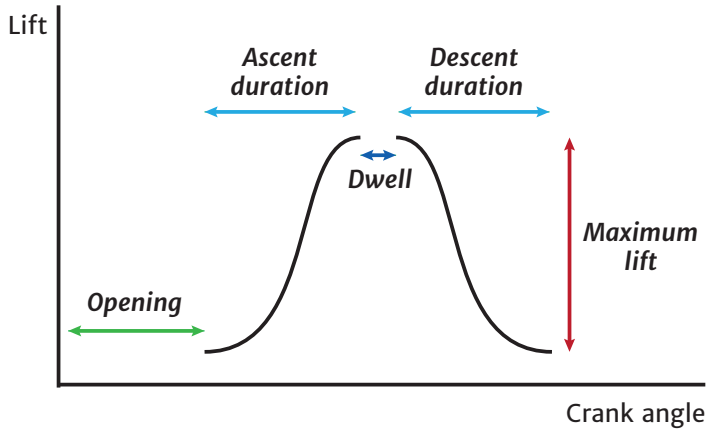

Figure 5.2: Valve profile parameters that can be modified in runtime.

To this end, several actuators have been included in the model. As indicated in Figure 5.2, this actuators allow controlling the starting of a valve event, the duration of the ascent and descent ramps, the dwell period (which is the angle a certain valve lift can be held) and the maximum

lift. The valve lift profile has to be redefined in order to use this actuators. Instead of a bi-dimensional array of crank angle and the corresponding valve lift to each angle step, a non-dimensional valve lift array is used. This means that at the event starting angle (X=0), the non-dimensional lift is 0 (Y=0), but at the end of the ascent ramp (X=1) the non-dimensional valve lift is 1 (Y=1). The opposite occurs in the descent ramp, where Y is equal to 1 at X=0 and Y is equal to 0 when X=1.

Recalling the control system in section 4.2, the simulations in this study were performed setting the torque of the baseline engine. At any particular engine speed and torque, the required fuel mass is obtained from a calibration map based on experimental data. Once the engine speed and fuel mass are known, the injection pulses timings and masses, intake manifold pressure, injection pressure and air mass flow setpoints are obtained from their respective maps.

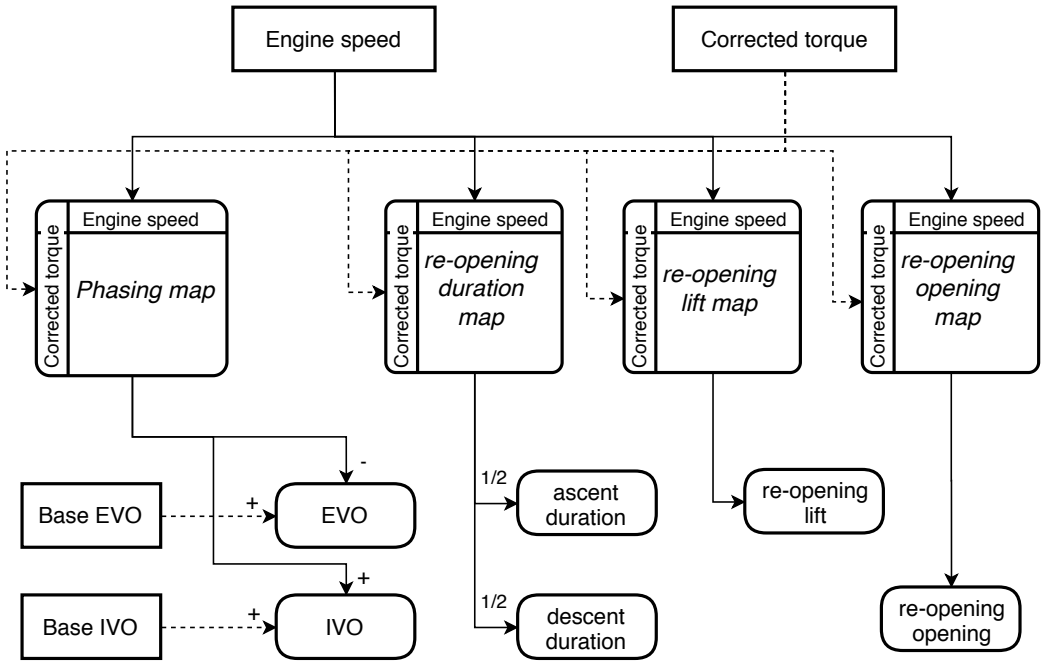

Figure 5.3: EP+IP and EVrO control blocks.

As explained in section 4.2, the ECU model can increase the injected fuel to meet the torque target. However, there are two fuel limiters: one ensures that the injected fuel does not overpass the one of the full load at that engine

speed, the other one limits the fuel rate to avoid an excess of soot. After this corrected torque is defined, along with the current engine speed, it is possible to obtain the corresponding valve advance/delay (since in *EP+IP* both valve events are symmetrically shifted), the re-opening lift, duration and moment of opening. These values are sent via an actuator signal to the virtual engine model, as indicated by the rounded boxes in Figure 5.3. This figure represents the control diagram and summarises the process explained above.

Although it is possible to define different ascent and descent ramps durations, they are considered to have the same duration in this study, so the re-opening duration is divided by two (ascent ramp and descent ramp) as shown in Figure 5.3. The maps are obtained by simulating a wide matrix of steady-state operating points and provide the optimum value satisfying a specific condition, for instance, to maximise the exhaust temperature with a maximum fuel penalty of 10 %. The details concerning the elaboration of this maps are presented in the following section 5.3.

5.3 Control system methodology

This work is centred on how the exhaust temperature can be increased by means of variable valve timing systems. Along this work, three systems have been studied based on a the solutions proposed in chapter 4. The first two systems consists in advancing the exhaust event (both EVO and EVC) and, in the same proportion, delaying the intake event (both IVO and IVC). The last systems consists in a second exhaust opening event (also called re-opening, post-lift or re-breathing in the literature) during the intake stroke. The aim of these techniques is to raise the exhaust temperature by two different methods described below:

- **Exhaust phasing and Intake phasing (EP + IP)**: The exhaust event and the intake event are shifted the same angle, respect to the baseline valve timings. The intake and exhaust valve lifts are represented by a red line with diamond markers in Figure 5.4. Two versions of this system have been modelled and simulated: one actuating over the 4

cylinder valves and other actuating only over one intake valve and one exhaust valve. The increase in the exhaust temperature is created, partially, due to the EEVO, since the exhaust blowdown of hot gases from the combustion into the exhaust ports increases the temperature downstream this point. Moreover, due to the early EVC, some amount of burnt gases are retained later during the intake stroke, increasing the air-charge temperature at IVC. The late IVO avoids a hot backflow of these burnt gases into the intake manifold, and compensates the pumping losses due to the compression of these gases with the following brief expansion between TDC and IVO. A parametric study has been done in steady-state conditions by modifying the advance/delay from 10° CA to 80° CA in 10° steps, as seen in Figure 5.4.

- **Exhaust valve re-opening (EVrO)**: It consists in a second exhaust event during the intake stroke. The intake and exhaust valve lifts are represented by a blue line with triangle markers in Figure 5.4. The light blue dashed lines represent the minimum and maximum re-opening possibilities. In this case, the re-opening is only applied over one of the exhaust valves and the way it increases the exhaust temperature is by aspiring part of the expelled gases from the exhaust ports back to the cylinder during the intake stroke. In this way, the air-charge temperature at IVC is higher than in the baseline case. A parametric study has been carried out by modifying the re-opening lift from 1 to 5 mm, in steps of 1 mm; re-opening start from 370° CA (just after EVC) to 430° CA, in 10° CA steps; and re-opening duration from 60° CA to 160° CA, in 20° CA steps, resulting in a 3D matrix of 210 combinations.

The methodology procedure is represented by the flow-chart in Figure 5.5. First, the parametric study has been carried out by simulating each combination of the *EP+IP* and re-opening matrices in steady-state operating conditions. The selected steady-state operating points consists of 23 points trying to cover the full speed-load engine map. These 23 points (defined in Table 2.3) were tested in the engine test bench and used in the calibration and validation of some of the VEMOD sub-models, as indicated in chapter 3. The 23 points can be identified as well in the specific consumption (BSFC) map at the top of Figure 5.5.

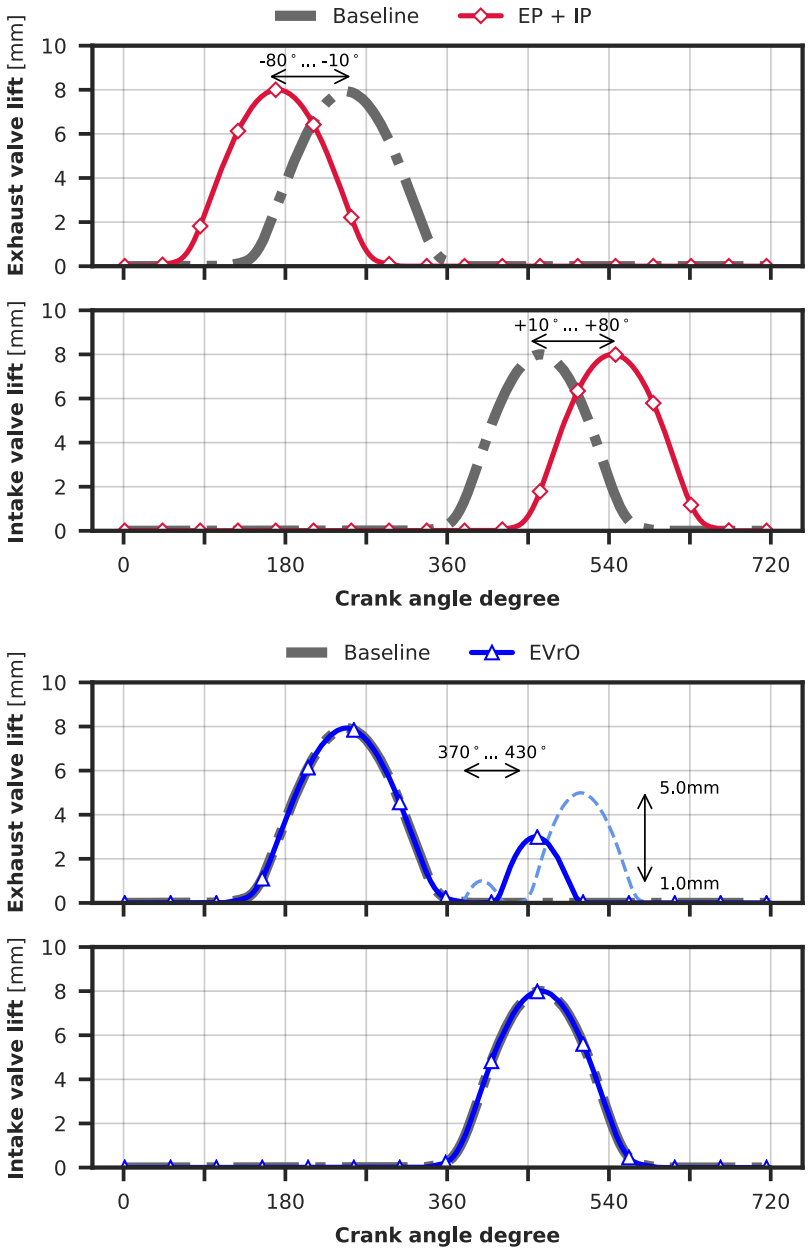

Figure 5.4: Exhaust and intake valve lift profiles for each case.

The simulation of the steady-state operating points was performed by setting the torque and engine speed of the homologous points corresponding to the original valvetrain configuration. As mentioned in the previous

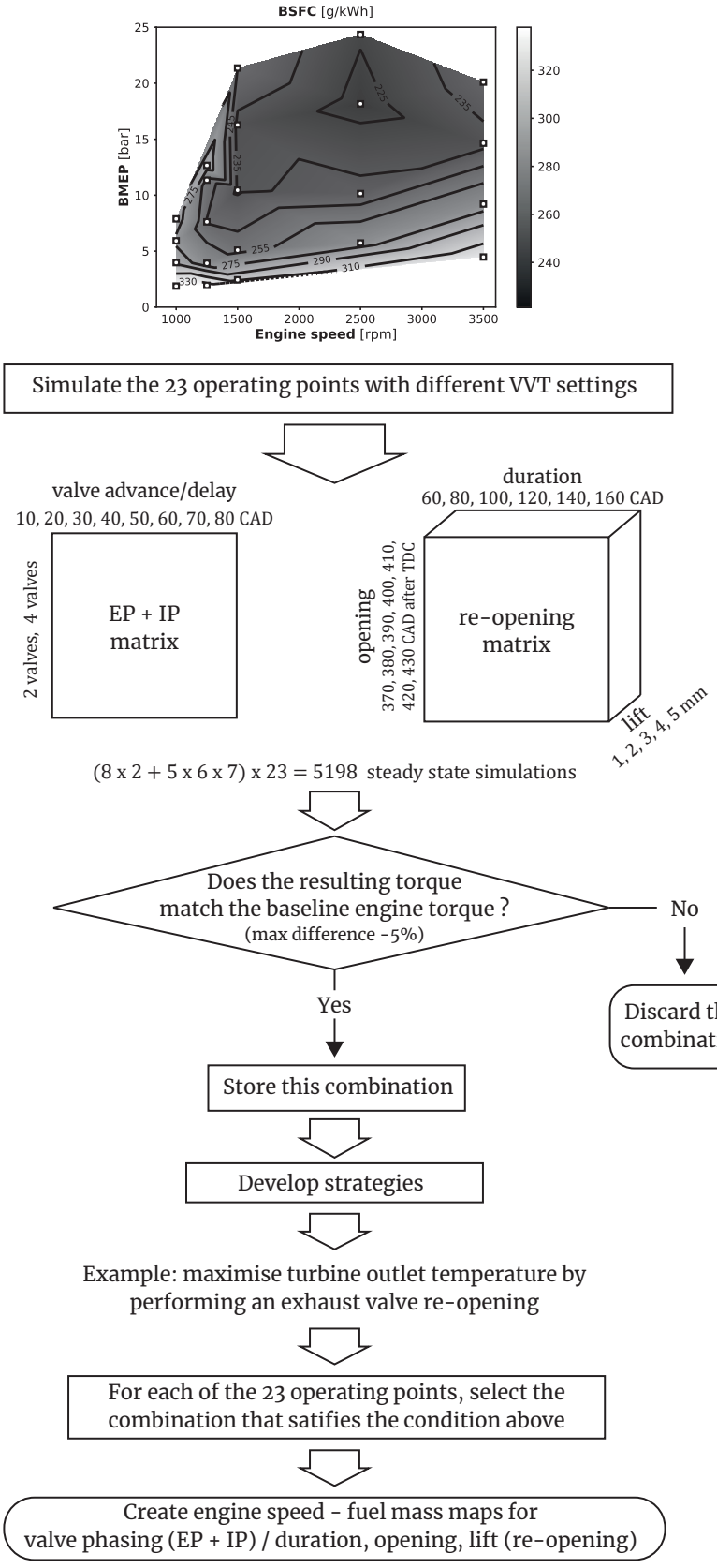

Figure 5.5: *Methodology flow-chart.*

section 5.2, the ECU sub-model can increase the injected fuel to meet the torque target; however, there are two fuel limiters. This translates into the possibility that some of the combinations cannot meet the torque demand at some specific operating point. For these reason, all the combinations have been checked for each of the 23 points, excluding them if the resulting torque is more than a 5 % lower with respect to the baseline in that specific operating point.

Figure 5.6 shows the maps of the discarded and accepted simulations for four *EP+IP* combinations. Those points were the baseline engine torque is met are within the white area, while the discarded points fall into the grey area. If the intake delay and exhaust advance is applied only in one pair of valves and the angular shift is 20 CAD (Figure 5.6a), the control sub-model is able to fulfil the torque requirements at any of the 23 operating points with the original calibration. When the same angular shift is applied to the four cylinder valves (Figure 5.6b), the full-load operating points from 1500 rpm onwards are discarded, since the engine is not able to reach their respective torque setpoints in this *EP+IP* combination with the current fuel limiters. As the angular shift is increased up to 60 CAD, more difficult is to apply this strategy for all the engine map, being discarded all full-load operating points and high load points at low engine speed in Figure 5.6c). As it is expected, this high angular shift results excessive when it is applied in the four valves. Therefore, only those low load and low engine speed operating points meet the torque requirements, as seen in Figure 5.6d).

In the same way, Figure 5.7 shows the discarded and accepted simulations for four re-opening combinations. In this case, a shorter exhaust re-opening near the first EVC (Figure 5.7a) presents less restrictions to achieve the torque setpoint around the engine map —offering also a lower increment in the gas temperature at turbine outlet— than a long re-opening far from the first EVC (Figure 5.7c), since it diminishes the volumetric efficiency and thus the trapped mass and the engine torque. However, the most restrictive parameter is the re-opening maximum lift —which is 5 mm. A high valve lift not only prevents the re-opening to be applied at full-load, but also at middle and low loads at 1500-2500 rpm. Thus, as observed by the maps in Figure 5.7, *EVrO* solutions are restrained to low loads and low

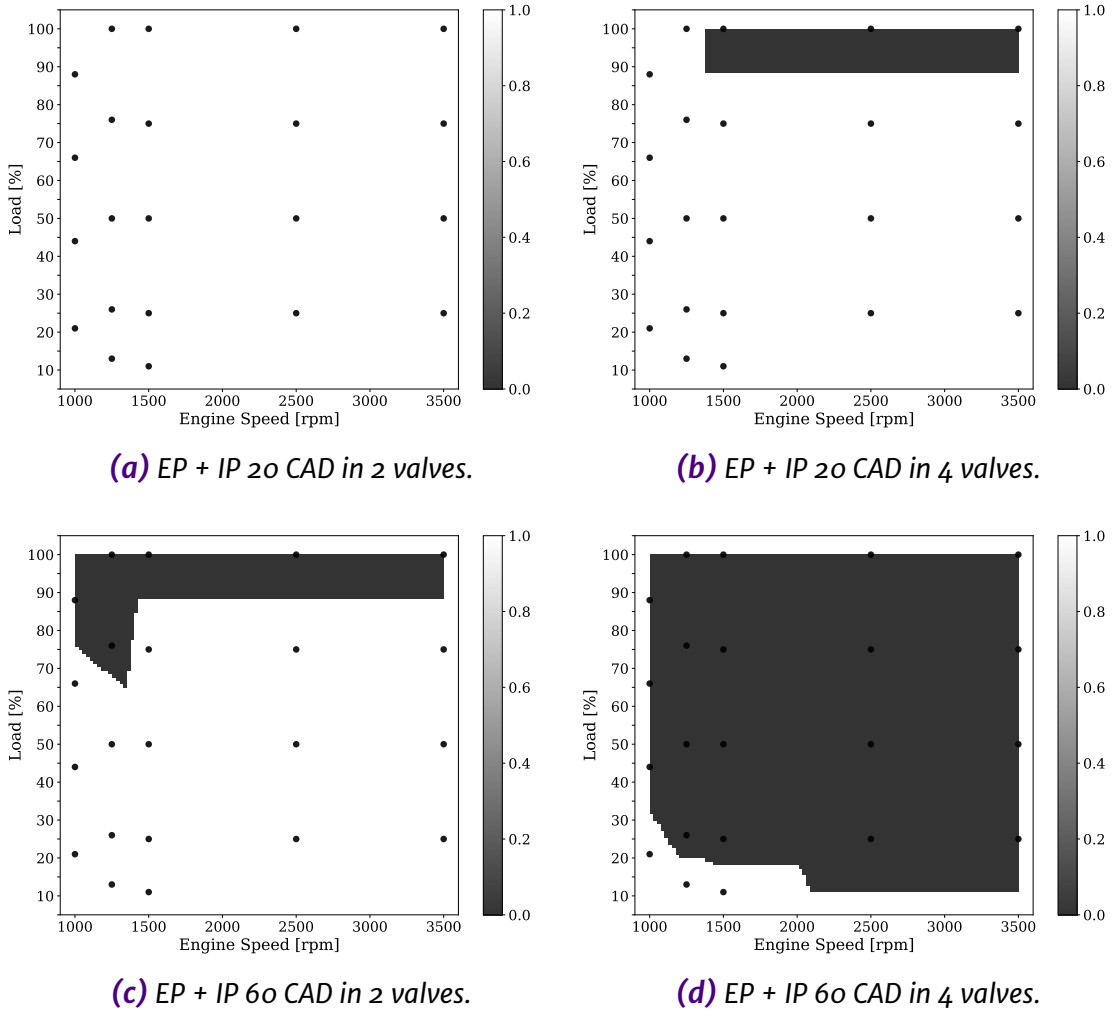

(a) EP + IP 20 CAD in 2 valves.

(b) EP + IP 20 CAD in 4 valves.

(c) EP + IP 60 CAD in 2 valves.

(d) EP + IP 60 CAD in 4 valves.

Figure 5.6: *Discarded and stored steady-state simulations applying EP + IP with an intake delay/exhaust advance of 20 and 60 CAD in 2 and 4 valves.*

engine speed operating points.

With all the information gathered from the parametric study, it is possible to state objectives and select those combinations that meet the objective for each steady-state operating point. For this study, five different cases have been defined with the aim of achieving the higher exhaust temperature. This five cases, plus the baseline, are summarised in Table 5.1. One case corresponds to the *EP+IP* alternative applied on the four cylinder

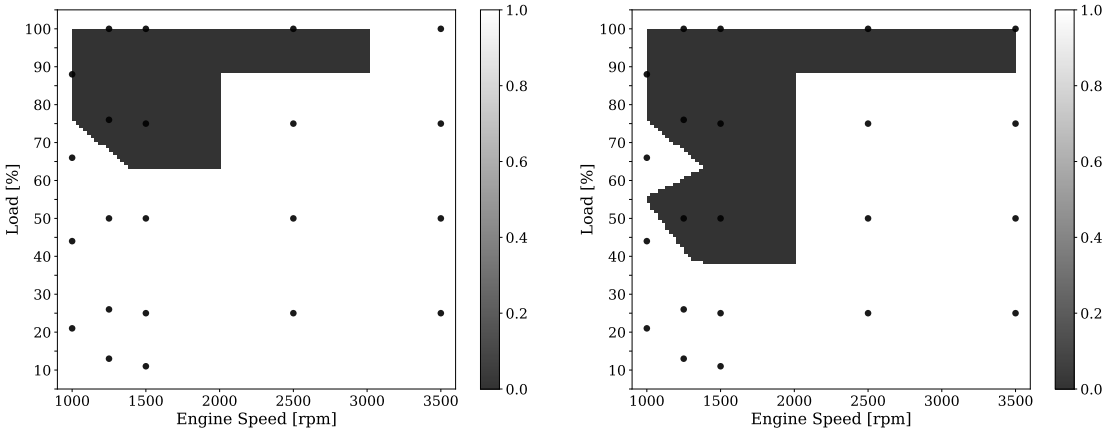

(a) EVrO opening at 370 CAD, duration 60 CAD, lift 1 mm.

(b) EVrO opening at 370 CAD, duration 60 CAD, lift 5 mm.

(c) EVrO opening at 420 CAD, duration 160 CAD, lift 1 mm.

(d) EVrO opening at 420 CAD, duration 160 CAD, lift 5 mm.

Figure 5.7: *Discarded and stored steady-state simulations applying EVrO with different exhaust opening, duration and lift.*

valves. Two cases (Case 2 and 3) considers the *EP+IP* alternative, but applied on one intake valve and one exhaust valve. The two cases left correspond to the goal of maximise DOC inlet gas temperature by performing an exhaust re-opening. Case 3 and Case 5 represents Case 2 and 4, respectively, but imposing a maximum fuel penalty of 10 % respect to the baseline.

In this way it is possible to sort the valid *EP+IP* and *EVrO* combinations

Case	Technology	Objective
Baseline	Original valve timing	-
Case 1	EP+IP in the 4 valves	Maximise DOC inlet temperature
Case 2	EP+IP in only 2 valves	Maximise DOC inlet temperature
Case 3	EP+IP in only 2 valves	Maximise DOC inlet temperature, limiting the fuel penalty up to 10%
Case 4	EVrO in only 2 valves	Maximise DOC inlet temperature
Case 5	EVrO in only 2 valves	Maximise DOC inlet temperature, limiting the fuel penalty up to 10%

EP+IP: Exhaust negative phasing and intake positive phasing,
EVrO: Exhaust valve re-opening

Table 5.1: *Transient cases.*

by the maximum exhaust temperature gain and apply other criteria like the minimum fuel penalty. By selecting the best combination at each operating point, it is possible to create an angular shift map for each *EP+IP* strategy and the corresponding opening, duration and lift maps for each *EVrO* strategy.

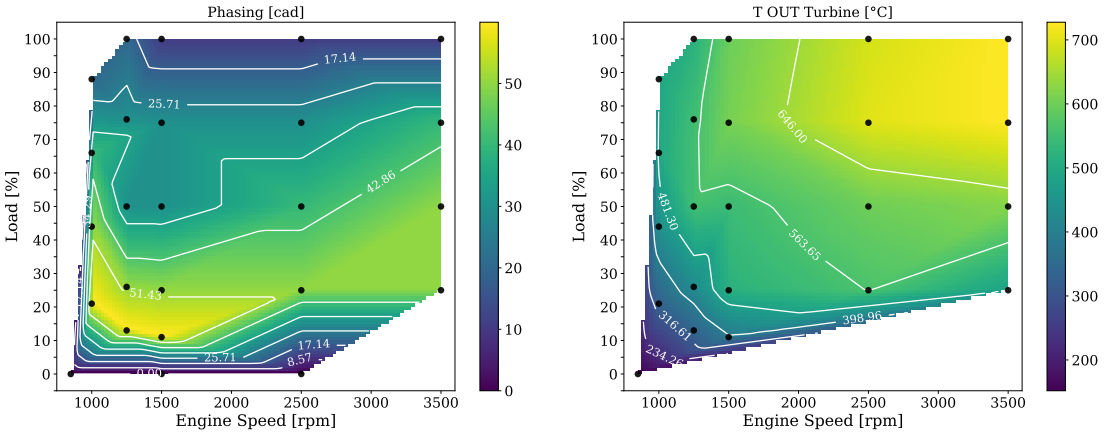

Figure 5.8: *EP+IP angular shift and turbine outlet temperature for Case 1.*

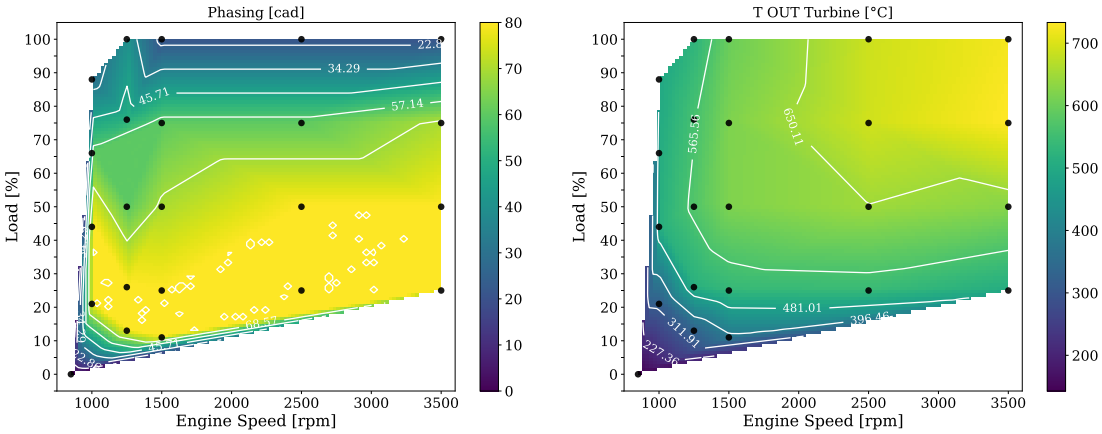

Figure 5.9: EP+IP angular shift and turbine outlet temperature for Case 2.

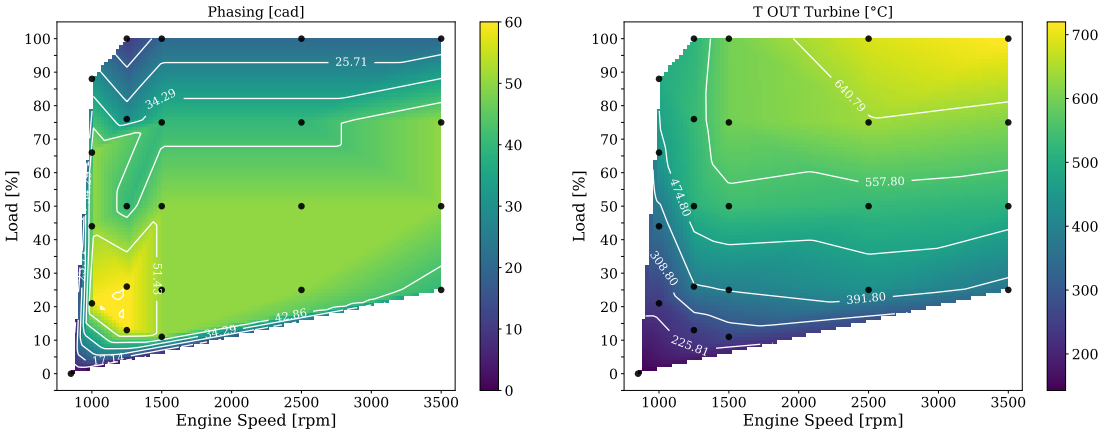

Figure 5.10: EP+IP angular shift and turbine outlet temperature for Case 3.

Figure 5.8 presents the intake and exhaust angle shift map (left) to obtain the turbine outlet temperature (right) according to the objective defined in Case 1: maximise the turbine outlet temperature by using *EP+IP* in the four cylinder valves. As indicated above, the angular shift is near zero at full-load to accomplish with the torque demand. The maximum angular shift of 60 CAD is only feasible at low load in the range of 1000 to 1500 rpm. Note that also there is no intake delay and exhaust advance at very low load (near zero) not at idle since these points are outside the engine map considered before. Since an angular shift value as to be defined in these region

to use this map later in the simulations at transient speed and load conditions, it has been considered not to perform *EP+IP* at very low load to keep the power output during fast accelerations starting from idle.

In Figure 5.9 the same maps according to Case 2 are presented. In this case, due to the fact that shifting only the intake and exhaust events in one pair of valves is less restrictive than in the four valves, a larger angular shift of 80 CAD is feasible in a wide range of the engine map, comprising from 15 to 50 % load from 1000 to 3500 rpm. It is even possible to apply an angular shift of about 20 CAD in the full-load line. The higher intake delay and exhaust advance results in a small increment in the temperature at turbine outlet all over the engine map.

Case 3 is represented in Figure 5.10. The angular shift in the left subfigure is similar to the one of Case 2. However and in order to limit the fuel penalty up to a 10 % respect to the baseline valvetrain, the maximum angular shift is reduced compared to case 2 and it is located in the sweet spot at low load (10-20 %) between 1000 and 1500 rpm. Consequently, the exhaust temperature is lower than in the non-limited fuel strategy.

Figure 5.11 presents the three maps that define the re-opening parameters of Case 4 plus the turbine outlet temperature map. These parameters are the opening of the second exhaust event (Figure 5.11a), the duration of the re-opening (Figure 5.11b) and the maximum lift (Figure 5.11c). It can be observed how, in the points where *EVrO* is not feasible (full load at 1250 and 1500 rpm), the re-opening lift is 0 mm, so no re-opening is performed. The same happens at idle and very low load in order to adapt the re-opening maps for transient operating conditions.

Case 5 maps are illustrated in Figure 5.12. It can be observed that the distribution of each map is quite similar as in Case 5. However, since now there is a limit on the maximum fuel penalty of 10 % with respect to baseline case, *EVrO* opening, duration and lift maximum values have been limited. It can be observed that the 1000 rpm and 88 % load point is not feasible now due to its excessive fuel consumption, which is near 20 % and it was not a limitation in Case 4. As a result of the fuel limitation, the temperature map at the turbine outlet side shown in Figure 5.12d presents a smaller temperature

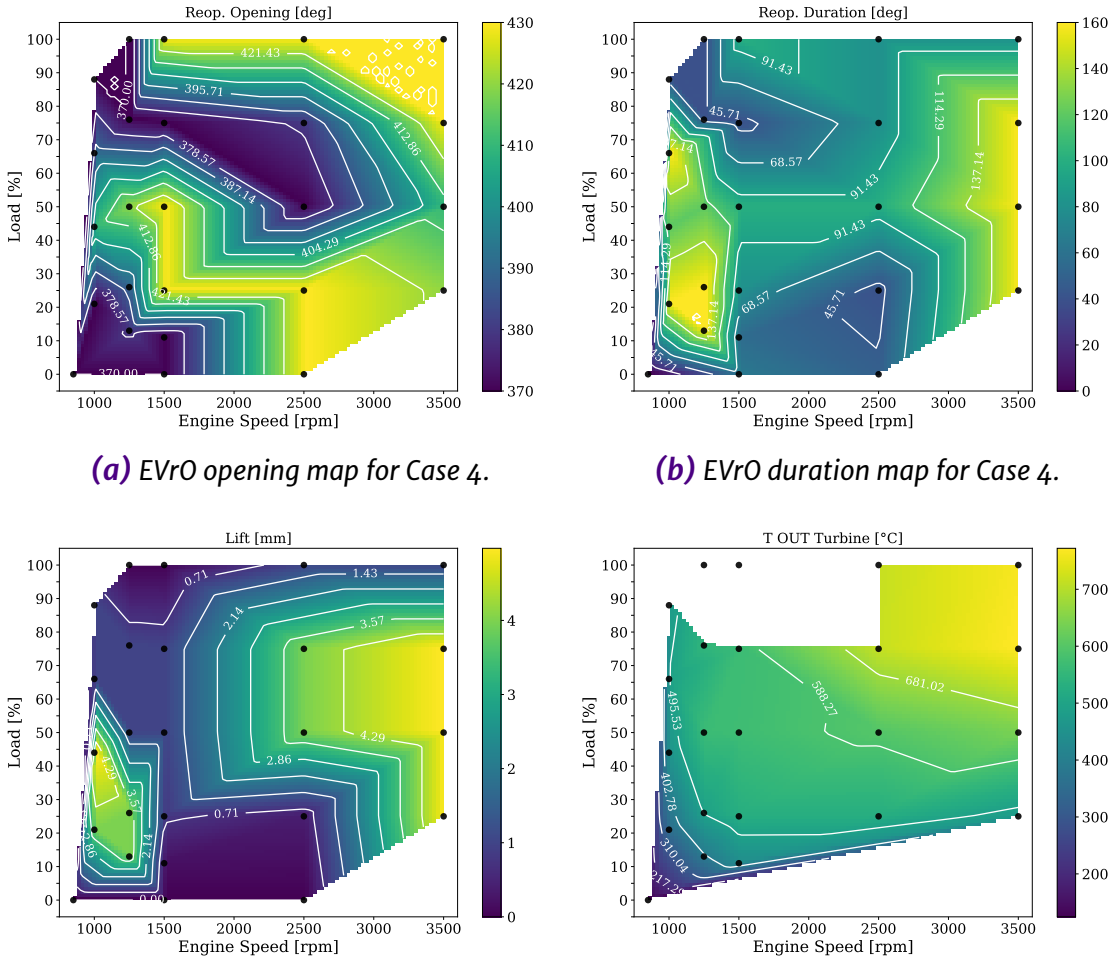

(a) EVrO opening map for Case 4.

(b) EVrO duration map for Case 4.

(c) EVrO lift map for Case 4.

(d) Turbine outlet temp. map for Case 4.

Figure 5.11: EVrO parameters maps and turbine outlet temperature for Case 4.

gain than in Case 4. The fact that Case 4 and Case 5 maps are quite similar indicated that only few operating points exceed the fuel penalty limit. Thus, it is expected that both cases perform similar in transient conditions.

In order to carry out the transient simulations an *EP+IP* control (intake delay and exhaust advance) and an *EVrO* control (start, duration and lift) were included in the ECU sub-model. This controllers read the current value of re-opening opening, duration, lift and angular shift from the maps shown above based on the current engine speed and total fuel injected.

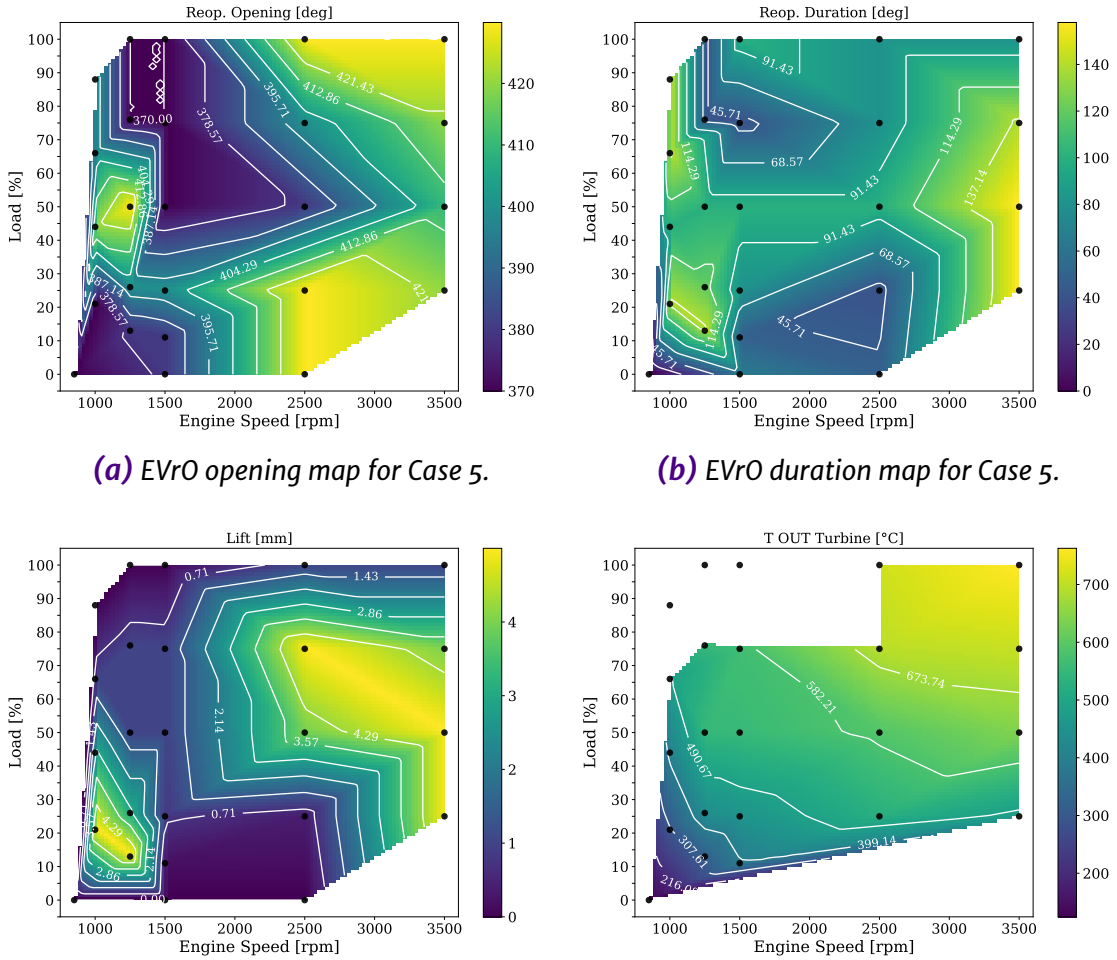

(a) EVrO opening map for Case 5.

(b) EVrO duration map for Case 5.

(c) EVrO lift map for Case 5.

(d) Turbine outlet temp.map for Case 5.

Figure 5.12: *EVrO parameters maps and turbine outlet temperature for Case 5.*

Finally, the WLTC cycle starting from cold engine start, at a room temperature of 20 °C, is simulated keeping the settings of each case and using their respective maps for *EP+IP* phasing or *EVrO* start, duration and lift.

5.4 Results and discussion

The main goal of this study is to achieve greater exhaust temperatures in order to increase the efficiency of the after-treatment devices during their heating phase. In Figure 5.13 the temperature at the turbine outlet section, intermediately preceding the catalyst, achieved by each case is presented. It can be observed that this temperature is higher than the baseline in the five cases throughout the whole WLTC. This temperature difference can be better observed in the lower subplot. At the low speed stage, both *EVrO* cases do not offer a remarkable difference in the temperature increment. Comparing the three *EP+IP* cases, Case 2 performs better during this low speed stage than Case 1, achieving instantaneous peak differences higher than 100 °C and an average difference at this stage of 67 °C. From the medium speed stage onwards, both *EVrO* cases perform better than Case 3. This means that, with the same limitation in fuel consumption, Case 5 is able to obtain more exhaust temperature than Case 3. Case 1, in which the intake and exhaust phasing is applied on the four valves, generally performs worse than the two valves case. The average temperature difference in Case 1 is 98 °C throughout the whole WLTC, in contrast to the 121 °C achieved by Case 2.

Figure 5.14 shows how much time the temperature at the turbine outlet section is above a certain value. The minimum temperature values (the initial ones) are shown at the top of the graph, since for the total test time (1800 seconds) the temperature is above this minimum values. The maximum values are shown in the bottom of the graph because they are only achieved at one instant. Maximum values are also indicated in the legend. It can be observed that all the Cases allow reaching higher temperatures than the baseline valvetrain. Both *EVrO* cases present a similar behaviour all over the cycle duration. Case 3 performs, in general, better than Cases 4 and 5 in terms of exhaust gases heating. Case 2 depicts the higher temperature of all cases and Case 1 performs in between of Case 2 and 3. If a vertical line is drawn between 200 °C and 250 °C, where the DOC conversion efficiency surpasses 50 %, the temperature of the baseline case will be above this value for 800 seconds, which represents a 44 % of the cycle duration. In Cases 3, 4 and 5, this time is extended up to 900 - 950 seconds, which is around 50

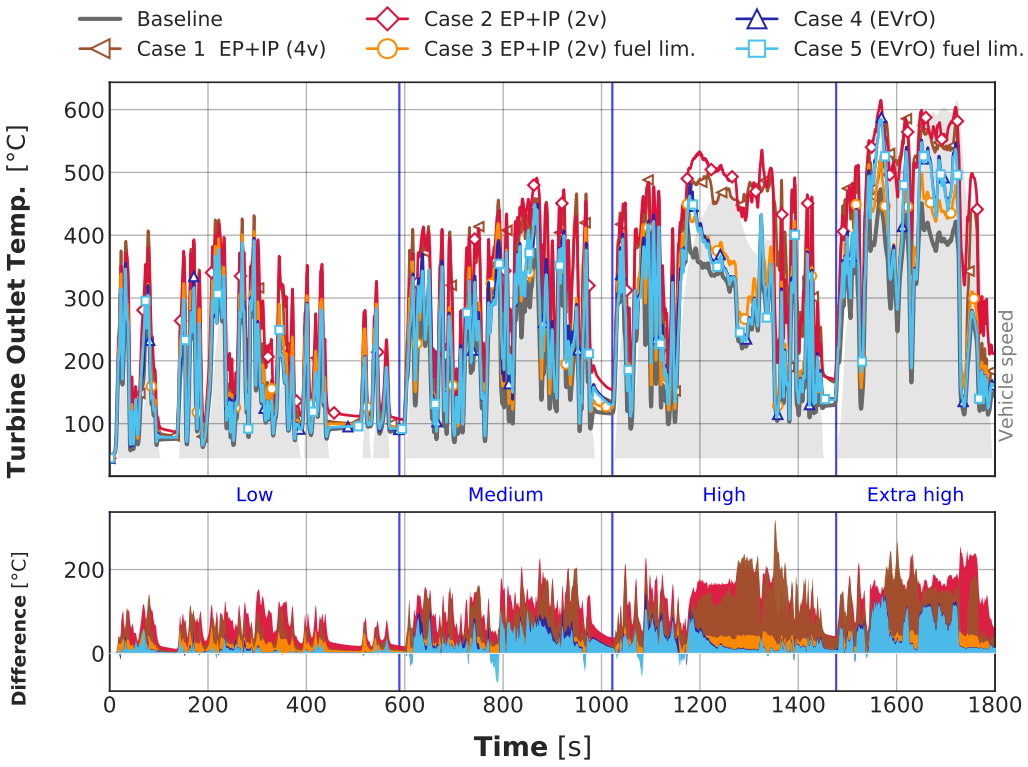

Figure 5.13: WLTC temperature at turbine outlet.

to 53 % of the time. By applying *EP+IP* in the four cylinder valves, according to Case 1, it is possible to stay over the light-off temperature around 1050 seconds (58 % of the time). And at best, Case 2 is able to keep a temperature above this level for 1150 seconds, representing the 64 % of the WLTC cycle.

In addition to the DOC inlet temperature, it is also interesting to analyse how the different cases affect the gases temperature at DOC outlet section. A temperature increment at this point could be beneficial for increasing the efficiency of a NO_x adsorber, or to regenerate the diesel particle filter. Figure 5.15 shows the gas temperature downstream the DOC, before entering the DPF. Similarly to Figure 5.13, *EP+IP* cases perform better than *EVrO* ones and Case 2 achieves the greatest increment in temperature. Its average increment throughout the test cycle is 80 °C, followed by case 1 with an average of 53 °C. It is also noticeable how Case 4 and Case 5 obtain less temperature than the baseline case at some moments, like the one near 800 seconds. At this time, the engine is accelerating from 1000 rpm to 1250 rpm at a

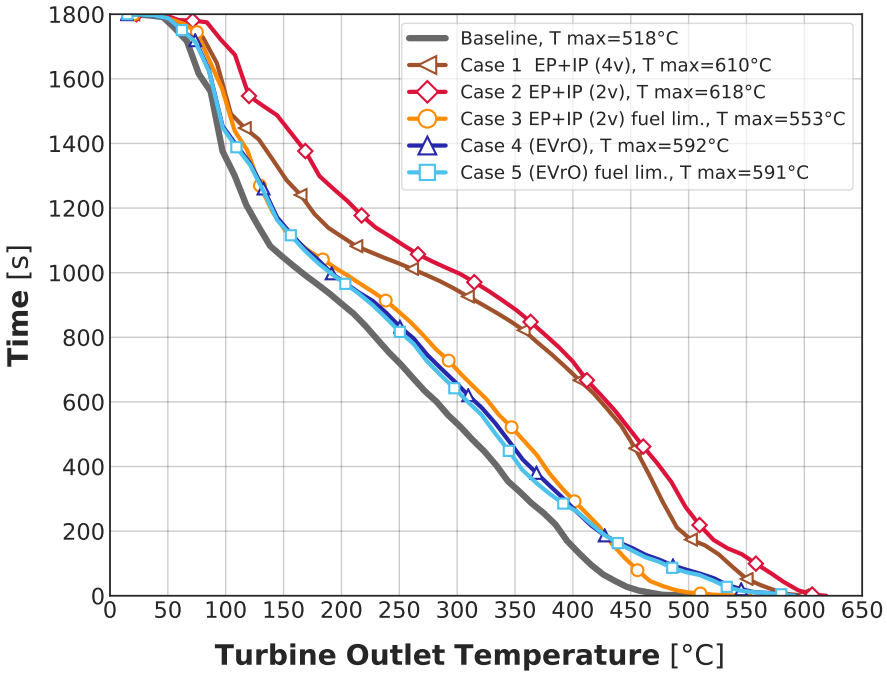

Figure 5.14: *Time above a certain temperature at turbine outlet.*

low torque. According to the re-opening lift and duration maps obtained by the steady-state optimisation in Figure 5.11c and Figure 5.11b, the relatively high lift and re-opening values in this region of the map causes a torque fall down during this fast accelerations.

Figure 5.16 shows the exhaust (top) and the intake (bottom) valve phasing for each case. It can be observed that Case 2 is able to extend the valve phasing range between 60° and 80° CA without resulting in a torque loss, since two valves remain unaltered. Case 1, on the contrary, is not able to apply a valve advance/delay beyond 60° CA without compromising the imposed torque. Case 3 mainly operates with a valve phasing between 40° and 60° CA, avoiding low advances (below 30° CA) at low and mid loads in order to reduce the fuel penalty.

Figure 5.17 presents the re-opening start (top), duration (middle) and lift (bottom) actuators signals for both *EVrO* cases. It is observed how the control delays the re-opening start at the acceleration peaks, since the exhaust temperature increases during these transients and it is more prof-

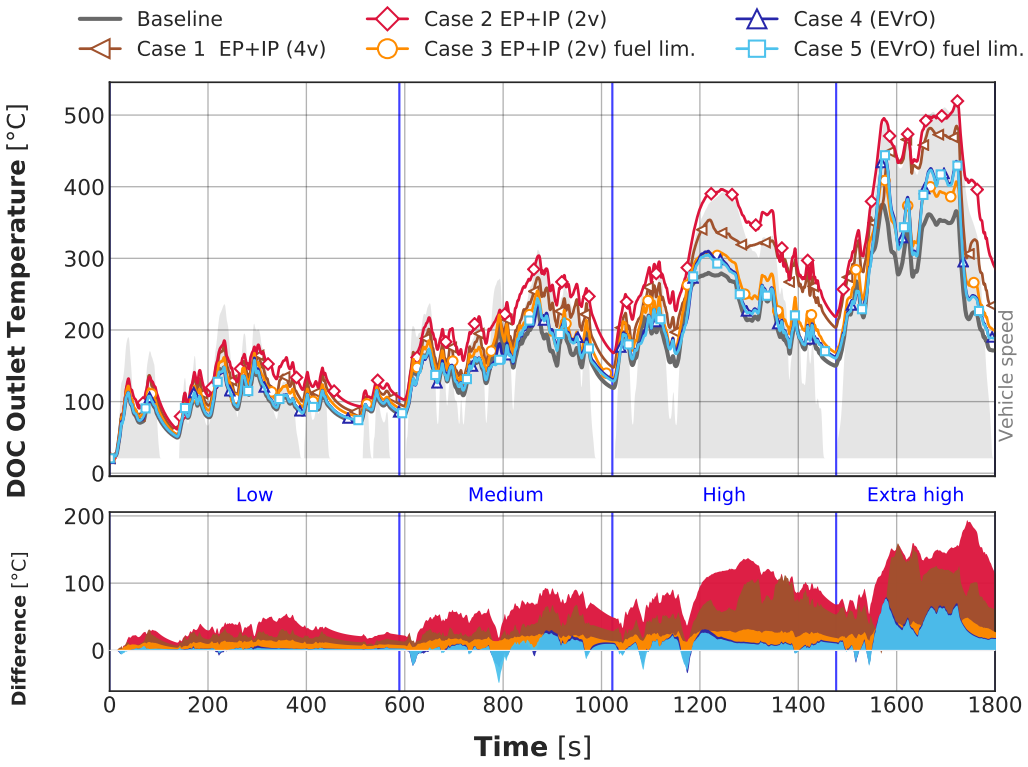

Figure 5.15: WLTC DOC outlet temperature.

itable to perform an exhaust valve re-opening. The same happens in the case of the re-opening duration and lift trying to raise even more the exhaust enthalpy. It should be noted that the control shortens the re-opening duration and the lift during periods at sustained medium loads, as it can be observed in the high speed stage of the WLTC. This control action ensures no torque losses; however, it blurs the re-opening effect and almost no advantage is achieved in terms of exhaust temperature gain as it is observed in Figure 5.13, where *EP+IP* cases are able to produce a greater temperature increment. The same happens at idle periods, where no re-opening is performed. Regarding the differences between Case 4 and 5, they mainly concern the re-opening start and duration. The control system reduces the re-opening start in order to reduce the fuel penalty in Case 4, where it rarely goes beyond 415° CA. In terms of re-opening duration, the control also cuts the duration to not undermine fuel economy during the fast accelerations. On the contrary, the valve lift in both cases is almost the same along the

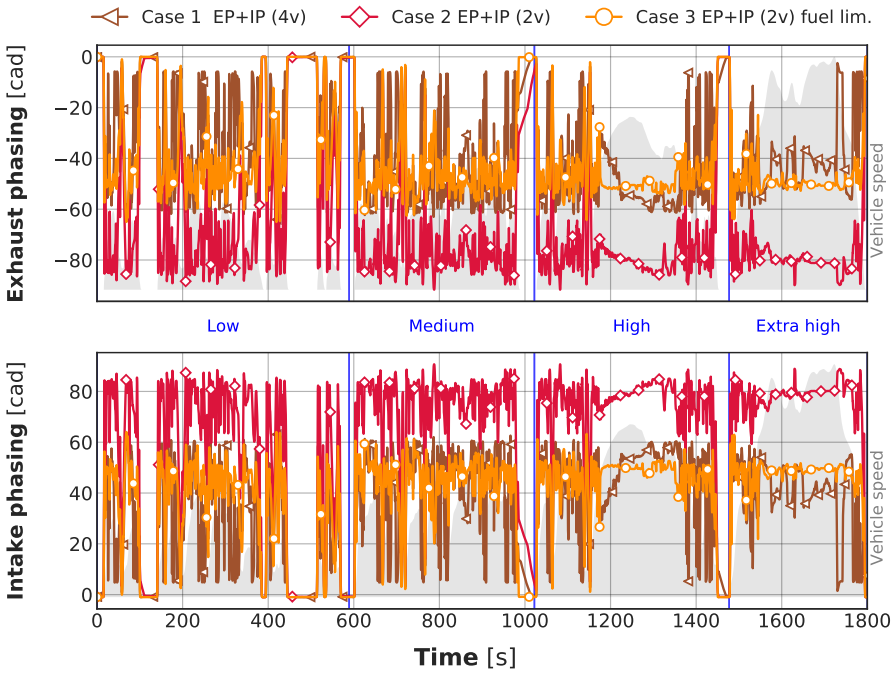

Figure 5.16: WLTC exhaust advance and intake delay.

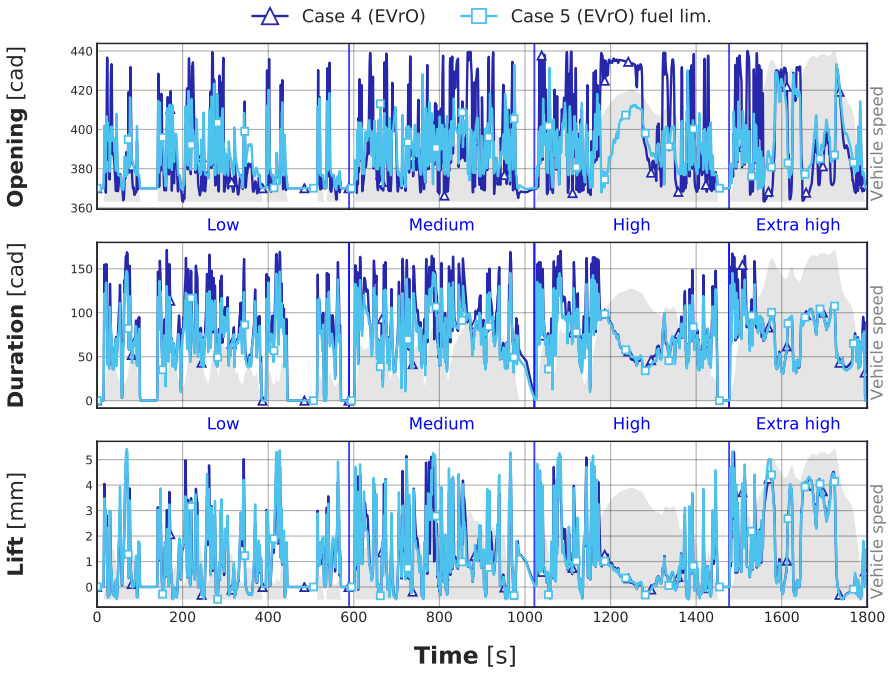

Figure 5.17: WLTC EVrO opening, duration and lift.

entire cycle.

Figure 5.18 and Figure 5.19 represent the HC and CO accumulated conversion efficiencies in the DOC, respectively, and calculated according to Equation 5.1 (where *n* refers to the either HC or CO, and *i* refers to the current time). As commented above, a higher gas temperature across the DOC increases HC and CO conversion efficiencies. Regarding HC conversion, Case 2 is able to increase the conversion efficiency an 8.5 % during the low speed stage, respect to the baseline case, being able to reach an efficiency of 0.97. In other words, Case 2 is able to remove the 98 % of the inbound HC. Case 1 increases the HC conversion a 4 % during the first stage, far enough of *EVrO* cases which improves slightly the conversion of the baseline. At the end of the cycle, the accumulated HC conversion efficiency of Case 2 drops down, since the HC formation increases during the extra high speed stage due to its fuel penalty, compared to the baseline case. The same effect is observable for Case 3. Contrarily, the accumulated conversion in Case 1 (*EP+IP* applied on both pair of valves) continuously increases to reach a final value of 0.98.

$$\textit{Accum. conversion } \eta_{n,\,i} = \sum_{t=1}^{i} \left(\frac{\int_{i-1}^{i} (Y_{n,\,in} \cdot \dot{m}_{in})\,dt - \int_{i-1}^{i} (Y_{n,\,out} \cdot \dot{m}_{out})\,dt}{\int_{i-1}^{i} (Y_{n,\,in} \cdot \dot{m}_{in})\,dt} \right) \tag{5.1}$$

With respect to CO accumulated conversion efficiency in Figure 5.19, a similar trend is observable. It is noticeable how the CO conversion of Case 4 and 5 is lower than in the baseline, this is not due to an increment in CO formation but with the inability to reduce DOC outbound CO emissions due to a lower exhaust enthalpy compared to the baseline case. From the second idle period of the cycle onwards, *EVrO* cases reflect a minor improvement in CO conversion. Case 1 reaches the higher CO conversion efficiency due to its highest temperature increment, with an average increment of 18 %. However, as it happened with the HC conversion, it falls down by the end of the WLTC due to the fuel penalty of *EP+IP* at high load. This effect is less evident in Case 3, where the maximum fuel penalty is limited to 10 %.

In terms of NO_x formation, Figure 5.20 shows how there are no impor-

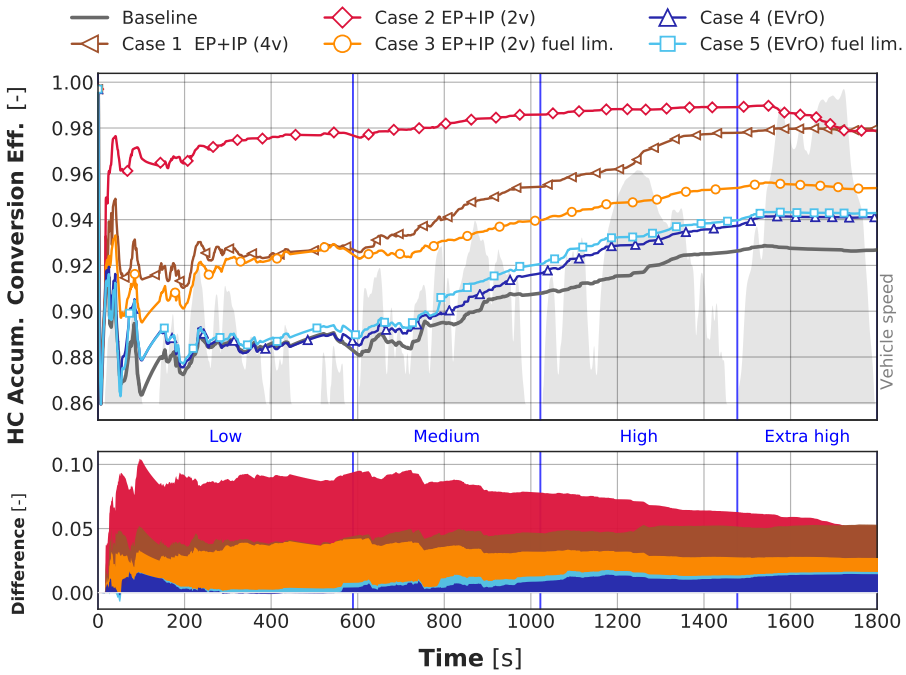

Figure 5.18: WLTC HC accumulated conversion efficiency.

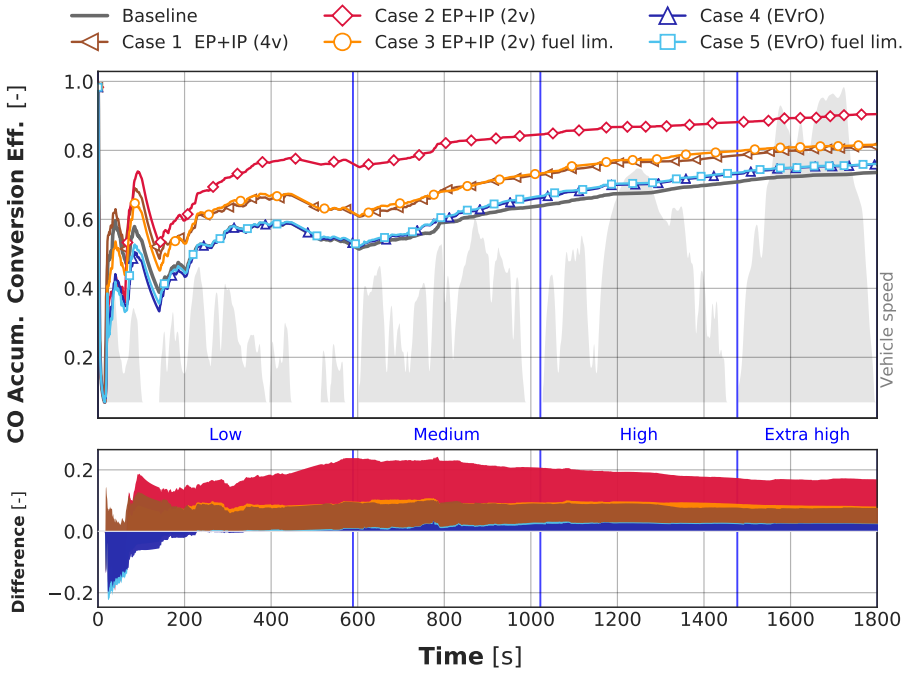

Figure 5.19: WLTC CO accumulated conversion efficiency.

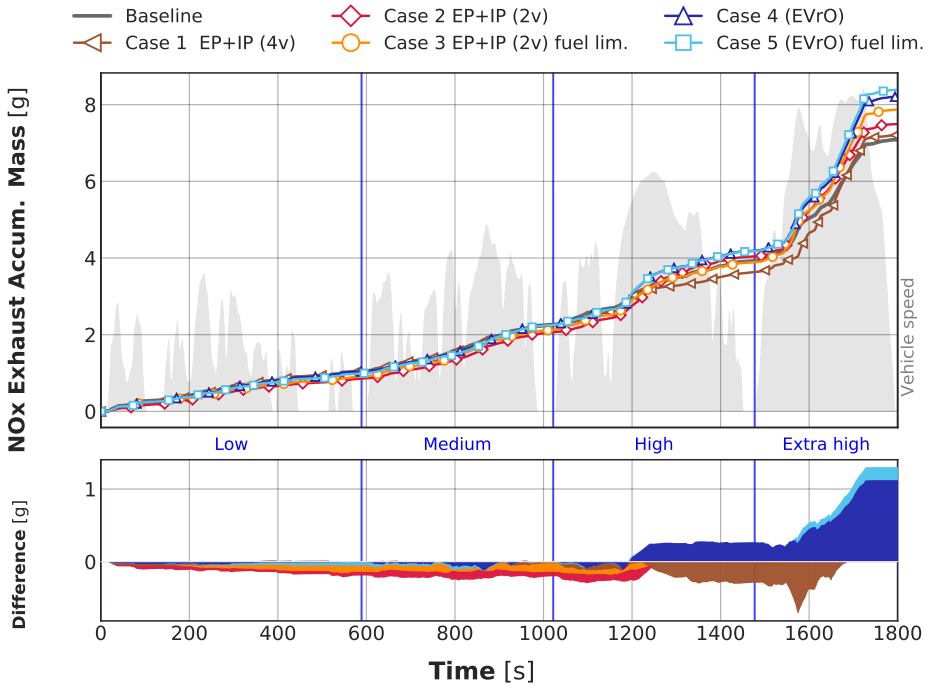

Figure 5.20: WLTC NO_x accumulated mass.

tant differences until the high speed stage of the WLTC. During the fast accelerations at high engine speed, Cases 1 and 3 produce a higher amount of IGR than *EVrO* cases. Thus, reducing NO_x formation at high engine speed. Cases 4 and 5, on the contrary, do not perform so well in terms of exhaust gases retention. This, plus the fact that the air loop controller closes the LP-EGR valve more than in the baseline case due to the lower volumetric efficiency at high engine speed, leads to a greater NO_x formation, which can be observed better in the bottom subplot of Figure 5.20. Accumulated differences of NO_x emissions are later described in relative terms in Figure 5.24, which they are separated into emissions at the end of the low speed stage and emissions at the end of the full WLTC.

Figure 5.21 and subsequent display some interesting values regarding the performance and emissions of each case in transient operating conditions. Except for the light-off time and warm-up time, each case is represented by two bars. The first bar indicates the accumulated value variation, with respect to the baseline case, at the end of the low speed stage (L) of the

WLTC (at 589 seconds); whilst the second bar indicates the final accumulated value variation (F). In terms of DOC activation (Figure 5.21), as it was shown before, Case 2 allows to obtain the greatest temperature in the DOC temperature, so the DOC light-off is achieved a 18.7 % sooner (around 150 seconds before the baseline). Case 1 and 3 cannot reduce the light-off time since they do not reach at least 200 °C in the previous accelerations. Regarding Case 4 and 5, their delay in the light-off time (a 6.6 % later) is due to the slight lack of power in the preceding acceleration near 800 seconds; otherwise, there would be no difference between Cases 1, 3, 4 and 5.

Warm-up time is defined as the time it takes for the coolant to reach a certain temperature, which is around 80 °C in this particular engine, and the thermostat valve starts to funnel the coolant flow through the radiator cooler to stabilise its temperature. Moreover, the coolant temperature plays an important role in this engine since it controls the switch between HP-EGR to LP-EGR. As it can be observed in Figure 5.22, the warm-up stage can be shortened in all cases, being Case 1 and 2 the ones that present a higher reduction of 4.7 and 4.3 %, respectively. The higher temperature in the exhausts ports results in a heating of the coolant that surrounds these ports, and hence reducing the warm-up time.

In terms of fuel consumption in Figure 5.23, it can be observed how the three *EP+IP* cases incur in a fuel penalty higher than the one of both *EVrO* cases. The higher fuel consumption compared to the re-opening cases is due to the compression of the retained burned gases after the EVC, since this compression increases the pumping losses and thus the BSFC. The earlier EVO also affects fuel economy as it reduces the power stroke and increases the amount of fuel injected to keep the required torque. This fuel penalty increases with the engine load, as it can be seen by the accumulated values at the end of the WLTC. Case 2, while offering the highest exhaust temperature increment, incurs in the highest fuel penalty with a total difference of 32.2 % (340 g more than the baseline). Case 3 offers a better solution in fuel economy as it is a version of Case 2 in which fuel injected has been limited. On the other side, both Case 4 and 5 do not affect fuel economy in the same way. Their total accumulated fuel burned variations are 4.4 % (+46 g) and 3.8 % (+39 g), respectively.

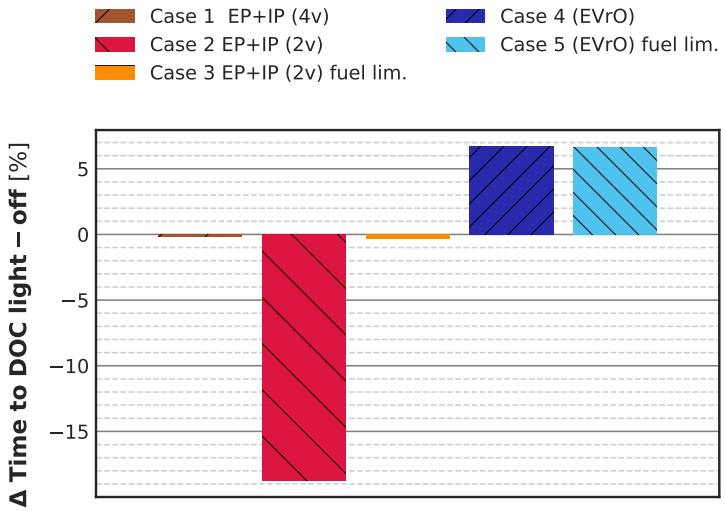

Figure 5.21: Time to reach DOC light-off temperature, engine start at 20 °C ambient temperature. Percentage variation compared to the baseline case.

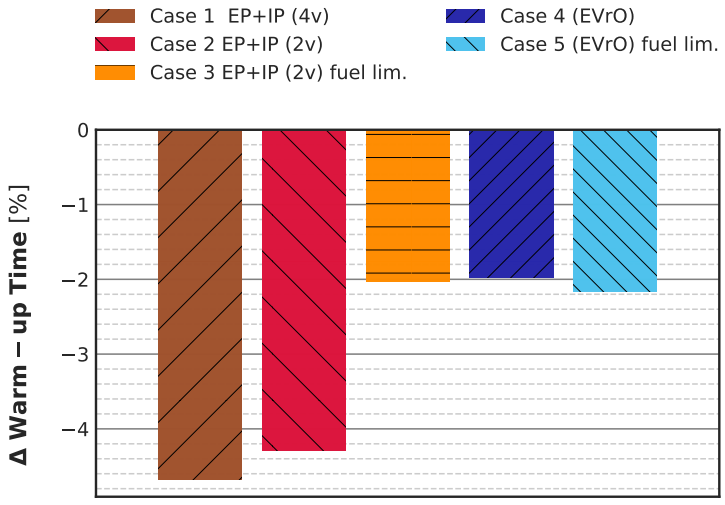

Figure 5.22: Time to reach coolant thermostat threshold, engine start at 20 °C ambient temperature. Percentage variation compared to the baseline case.

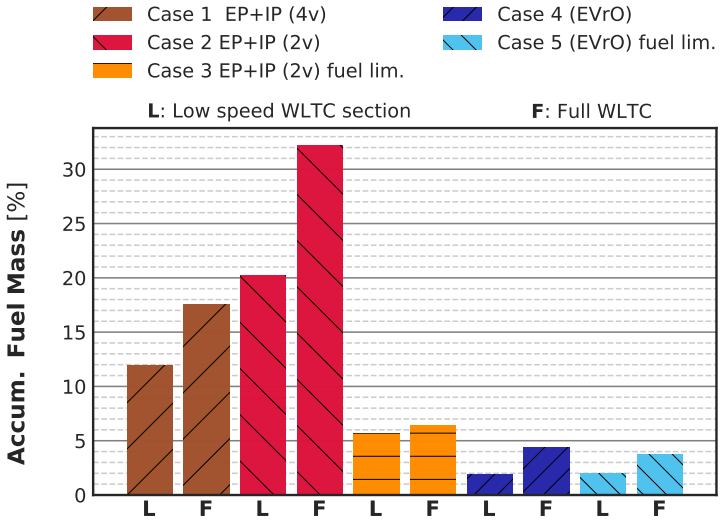

Figure 5.23: Accumulated fuel consumption, engine start at 20 °C ambient temperature. Percentage variation compared to the baseline case.

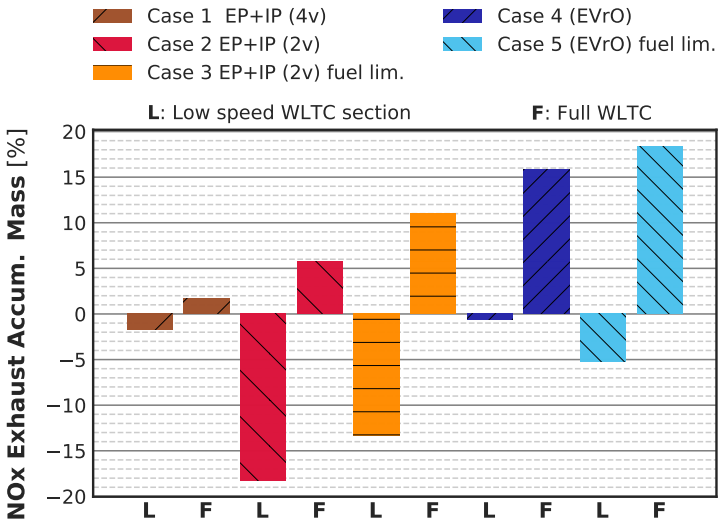

Figure 5.24: Accumulated tailpipe NO_x emissions, engine start at 20 °C ambient temperature. Percentage variation compared to the baseline case.

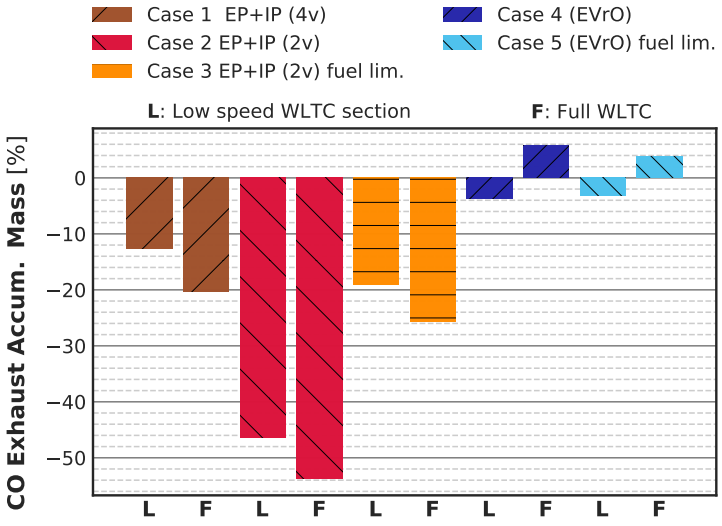

Figure 5.25: Accumulated CO emissions at DOC outlet, engine start at 20 °C ambient temperature. Percentage variation compared to the baseline case.

Regarding NO_x emissions, it is observed an increase in all cases at the end of the cycle. When it comes to *EP+IP* cases, an upward trend is observed in NO_x formation as engine speed increases; since the accumulated values during the low speed stage are lower than in the baseline but higher at the end of the cycle. The increase in NO_x formation compared to the baseline case can be explained because of the lower EGR mass flow when increasing the engine speed. In the extra high speed stage of the WLTC, the air loop controller closes the LP-EGR valve in all cases more than in the baseline one. However, considering the CO_2 mass fraction at IVC, both *EVrO* cases show a lower exhaust gas retention power at high speed. Thereby, the NO_x formation is higher in Cases 4 and 5 during this last stage. 18.2 % reduction in NO_x formation can be obtained in Case 2 over the low speed stage of the WLTC. Analysing NO_x emissions when performing an exhaust re-opening it can be observed that emission levels are higher in both cases. Exhaust NO_x emissions increase with the engine speed as the amount of IGR created by the re-opening is lower at high engine speed, leading to a final increase of 18.4 % in Case 5, respect to the baseline in case.

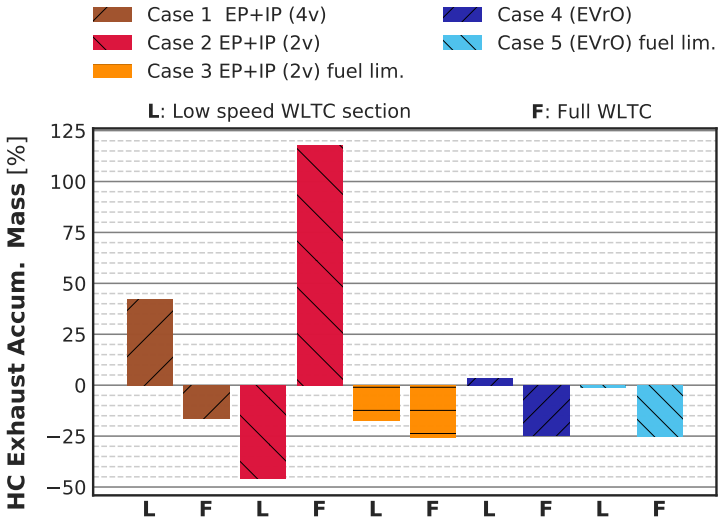

Figure 5.26: Accumulated HC emissions at DOC outlet, engine start at 20 °C ambient temperature. Percentage variation compared to the baseline case.

Figure 5.25 shows the CO accumulated mass downstream the diesel catalyst. Even though performing an exhaust re-opening does not affect the CO formation (specially at low engine speed), the poor potential in order to heat the catalyst leads to CO emission levels higher than those achieved by the *EP+IP* cases. Case 2 is the most effective in this respect with a reduction 46.4 % at the end of the low speed stage and a 53.7 % reduction over the full cycle, compared to the baseline case.

As regards HC emissions downstream the DOC, Figure 5.26 depicts that Case 2 and Case 3 improve HC emissions during the low speed stage of the cycle. However, in Case 2, due to the high fuel penalty during the extra high speed stage, the final HC emissions double the baseline ones (an increase of 117 %). This is also observable in Figure 5.18 where there is a decrease in the accumulated HC conversion efficiency. Case 4 and 5 are able to reduce HC emissions down to a 25 % at the end of the cycle due to their contribution in the DOC gas enthalpy while not incurring in an excessive fuel penalty at the high speed stage.

Figure 5.27 and Figure 5.28 represent some trade-offs between engine consumption and CO and HC emissions only during the low speed stage of

the WLTC. Emissions inbound the DOC are shown on the left side, while emissions outbound the DOC are placed on the right side. It can be seen that Cases 1, 2 and 3 increase the CO formation (Figure 5.27a). The greater values are explained due to the fact that performing an EEVO results in an increase in fuel injected mass, which leads to an increment in HC and CO. Moreover, the earlier blowdown interrupts the oxidation of HC and CO during the expansion stroke. The fuel consumption difference between Case 1 and Case 2 (*EP+IP* in 4v vs in 2v) is because, when phasing both pair of valves, it is difficult to keep the target torque with high EEVO and LIVO angles. In case of phasing just one intake valve and one exhaust valve, the phasing range is wider. However, extending this range leads to a higher fuel consumption in Case 2, which is a 20 % more than the baseline. In Figure 5.27b it can be seen how the excess in CO formation of *EP+IP* cases is later compensated by the increase in CO conversion. Accordingly, Case 3 offers a good trade-off between fuel penalty and CO emissions, being able to reduce them by a 20 % with a fuel penalty of 6 %.

Figure 5.28a and Figure 5.28b presents similar trends to CO pollutant emissions. The fuel penalty caused by advancing EVO moment increases HC emissions. This consumption increase is almost directly proportional to the exhaust temperature increase. Figure 5.28b shows how the HC formation in Case 2 and 3 are later compensated by the increment in the HC conversion efficiency. Nonetheless, Case 1 is unable to reduce total HC emissions at the end of the low speed stage. Even though the reduction between inlet and outlet emissions is near 71 %, higher than the reduction in Case 3 (51 %), the hydrocarbons formed over the combustion are higher compared to Case 3, Case 4 and Case 5.

It is interesting to note that the fuel consumed by Case 4 and Case 5 is pretty much the same. In fact, the difference in fuel consumption, compared to the baseline case, across the engine map is below 10 % for a wide region of that. Case 5 just ensures it does not exceed a fuel penalty of 10 % in any region of the fuel map.

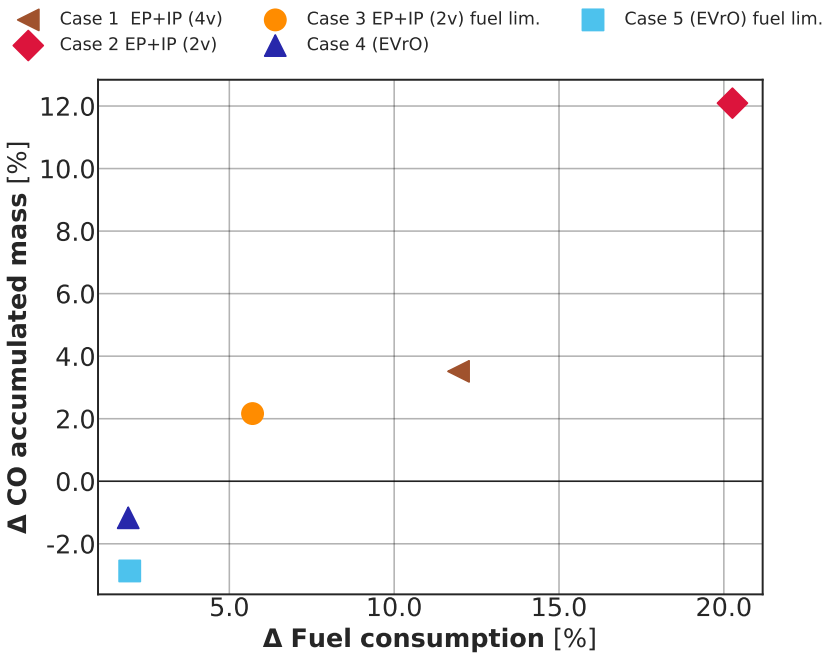

(a) Fuel consumption (%) versus CO accumulated mass (%) ***upstream*** *the DOC.*

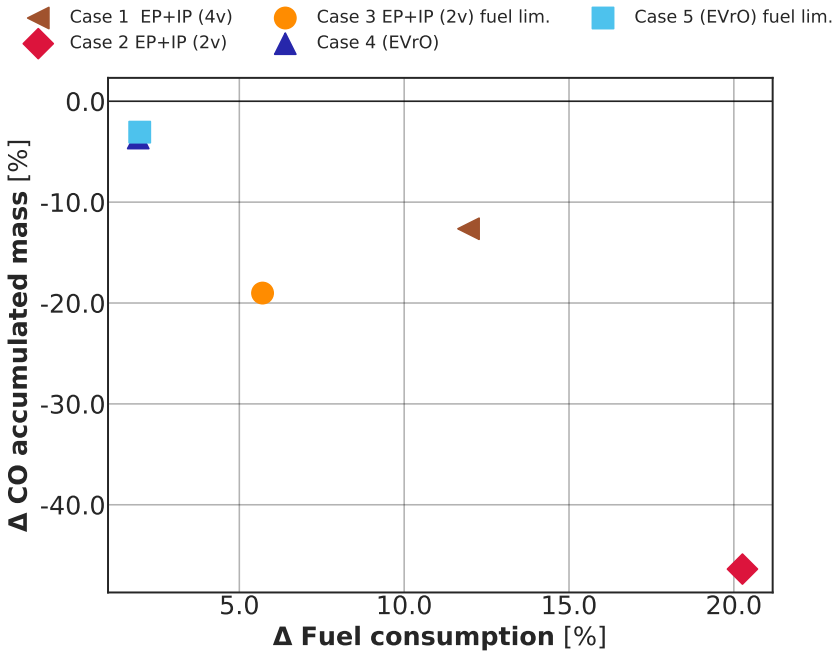

(b) Fuel consumption (%) versus CO accumulated mass (%) ***downstream*** *the DOC.*

Figure 5.27: *Fuel consumption variation (%) versus CO accumulated mass variation (%) trade-offs during the low speed stage of the WLTC, variations with respect to the baseline.*

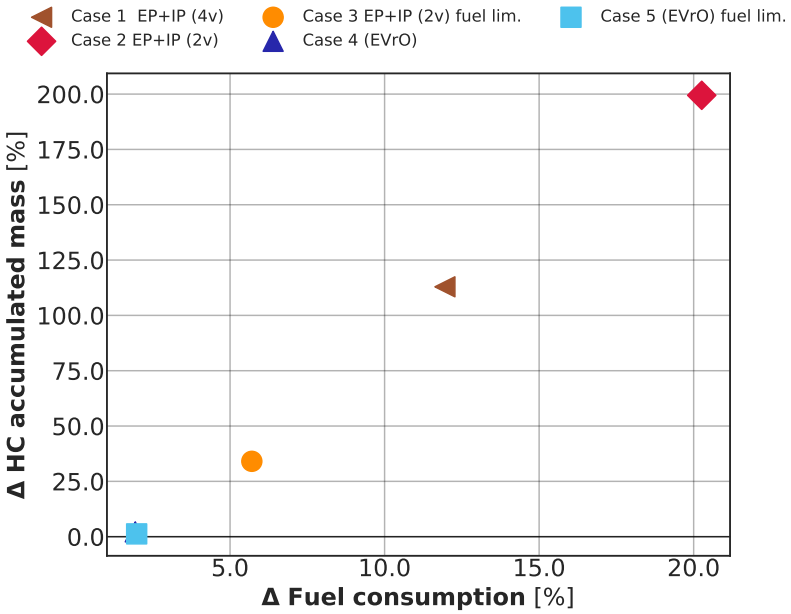

(a) Fuel consumption (%) versus HC accumulated mass (%) ***upstream*** *the DOC.*

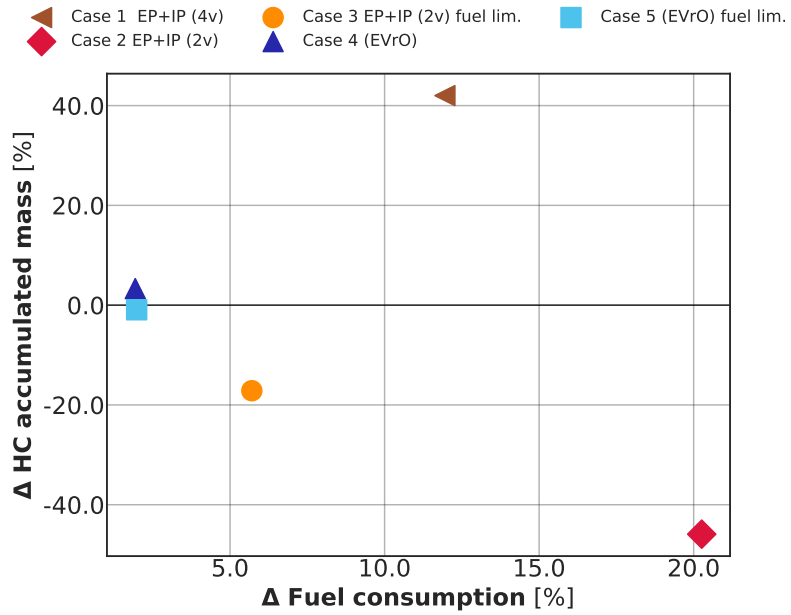

(b) Fuel consumption (%) versus HC accumulated mass (%) ***downstream*** *the DOC.*

Figure 5.28: *Fuel consumption variation (%) versus HC accumulated mass variation (%) trade-offs during the low speed stage of the WLTC, variations with respect to the baseline.*

5.4.1 Adding DOC light-off temperature in the VVT control.

In the results presented before, it is observed that cases 4 and 5 —performing a second exhaust re-opening— do not improve the catalyst warm-up during the first stage of the cycle compared to the cases 1, 2 and 3. Moreover, intake delay and exhaust advance cases get into an excessive fuel consumption —specially Case 1 and 2— when these strategies are applied over the full cycle (see Figure 5.23). Case 3, even though its fuel penalty its limited up to a 10 %, presents an accumulated increase in NO_x emissions of 11 % at the end of the WLTC (see Figure 5.24). Case 2 is considered the best solution to reduce HC and CO emissions during the catalyst warm-up; however, it increases HC emissions to a large extent due to the excessive fuel penalty over the extra high speed stage of the transient cycle (see Figure 5.26). Thus, trying to take the most of *EP+IP* strategies while reducing their drawbacks at high engine speed and load, a new variable was introduced into the VVT control system. A temperature sensor placed between DOC outlet and DPF inlet sends the temperature value to the ECU submodel. On the one hand, if this temperature is below a threshold of 210 °C, the control system actuates over the variable valve system. On the other hand, if the temperature is above this threshold, the control system applies the same valve timings as in the baseline valvetrain.

Figure 5.29 shows the temperature at DOC outlet in the previous cases 1, 2 and 3, plus their new variations where *EP+IP* is not being performed when the DOC temperature is above 210 °C. This three new cases are named Case 1b, Case 2b and Case 3b, respectively and are traced with a solid line in Figure 5.29, in contrasts to Case 1, Case 2 and Case 3 which are drawn with a dashed line. It can be seen that new 'b' variations overlaps their respective cases 1, 2 and 3 until the DOC outlet temperature threshold is reached, which happens near 800 seconds. From this instant, temperature in cases 1b, 2b and 3b are quite similar as the baseline one, but a bit higher than this one since the control system is still performing an *EP+IP* when the temperature falls below the threshold value.

Figure 5.30 shows the exhaust advance (top) and the intake delay (bot-

tom) applied by the VVT control over the full WLTC cycle. Again, it can be observed that the control system disables *EP+IP* strategies once the DOC outlet temperature is above the light-off threshold. There are two long periods where the control is imposing the baseline valve timings (Case 1b, Case 2b and Case 3b). These periods correspond to the extra-urban stretches during the high (from 1160 to 1360 seconds) and extra high (from 1500 to 1770 seconds) vehicle speed stages. This *EP+IP* deactivation is reflected in Figure 5.29 (bottom), where only a small increment in the exhaust temperature is observed at these periods due to the thermal inertia of the exhaust gases generated by the previous *EP+IP* activation.

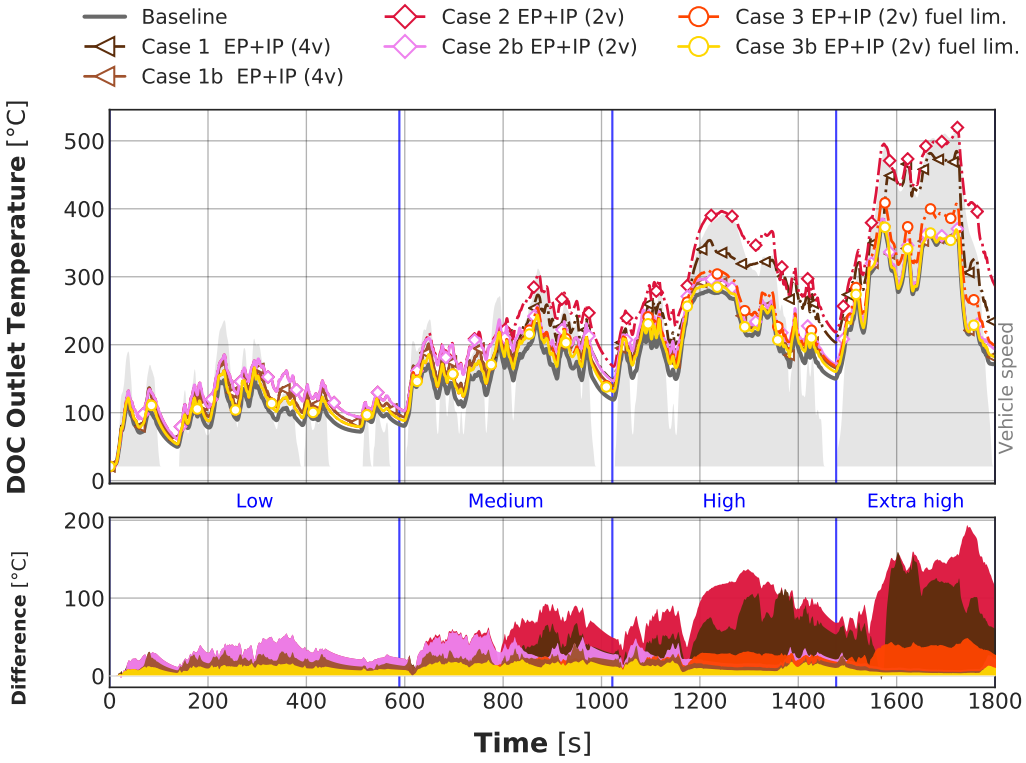

Figure 5.29: *WLTC DOC outlet temperature.*

Since Case 1, Case 2 and Case 3 present the same performance as their 'b' versions until the DOC temperature threshold is achieved, which happens near 800 seconds after the start of the cycle, the accumulated fuel consumed and pollutant emissions are the same in these cases and their 'b' variations over the low speed stage. Figure 5.31 shows the accumulated fuel

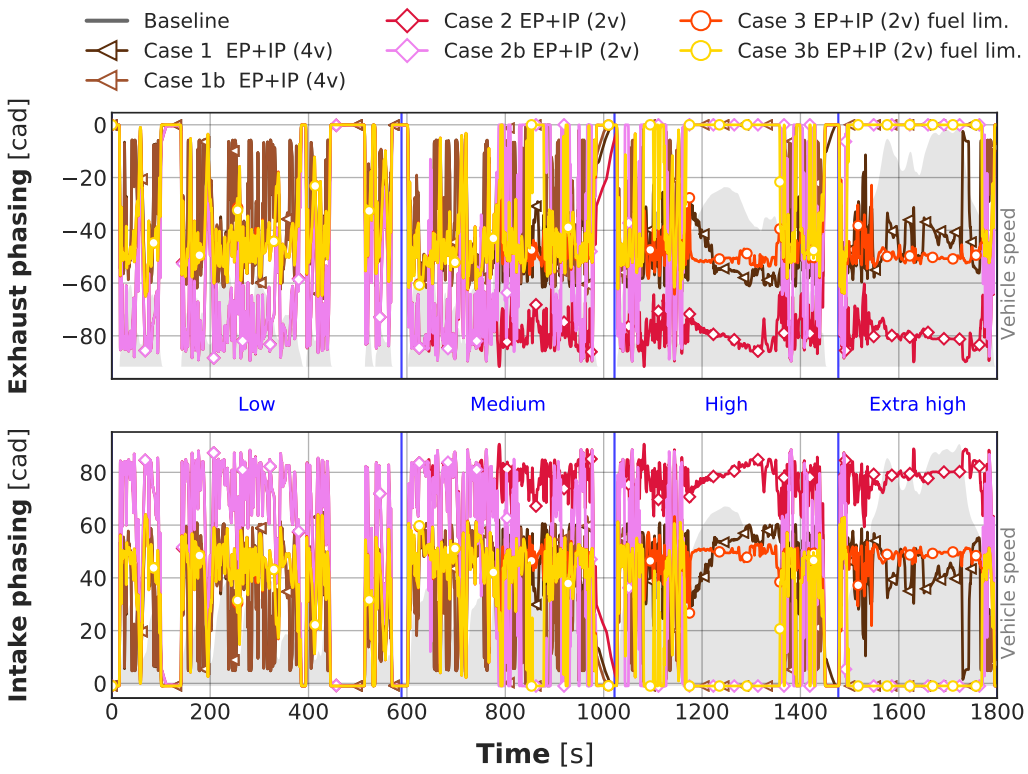

Figure 5.30: WLTC exhaust advance and intake delay.

mass at the end of the low speed stage and at the end of the complete cycle. With the new objective of enabling only *EP+IP* when the DOC temperature is below the light-off threshold it is possible to reduce fuel consumption along the complete cycle. Now, the total fuel penalty in Case 2b —which is the one that achieves a higher exhaust temperature gain— is around 6 % compared to the excessive 32 % fuel penalty in Case 2. Case 1b also improves its fuel economy presenting a fuel increment of 4 %, which is lower than the 17 % of Case 1. Case 3b does not show an excessive improvement since Case 3 already consider a fuel penalty restriction. In this case, the difference with respect to the baseline valvetrain is about 2 % at the end of the cycle.

In terms of NO_x formation, there is an improvement when *EP+IP* is disabled at high vehicle speed. As explained in previous Figure 5.20, *EP+IP* increases the internal exhaust gases recirculation; however, it worsens volumetric efficiency specially at high engine speed and, thus, reduces the trapped mass. As a consequence and to control the intake air, the control

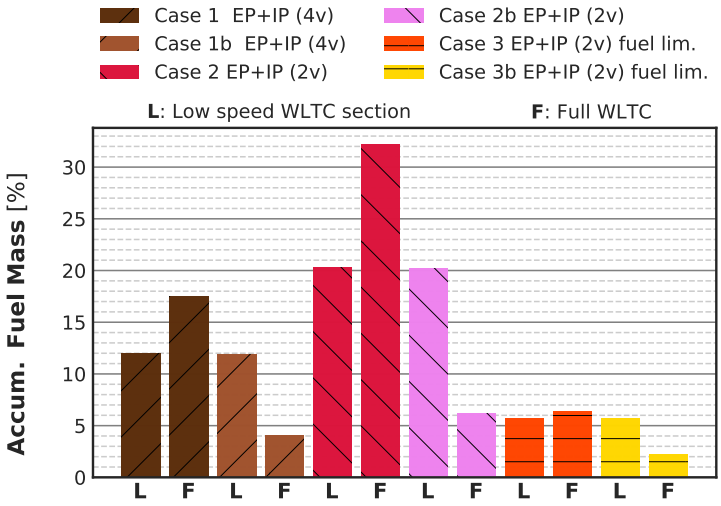

Figure 5.31: Accumulated fuel consumption, engine start at 20 °C ambient temperature. Percentage variation compared to the baseline case.

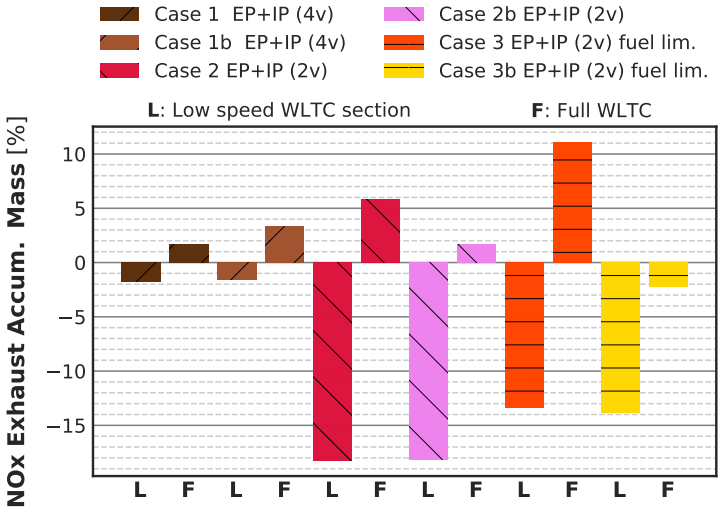

Figure 5.32: Accumulated tailpipe NO_x emissions, engine start at 20 °C ambient temperature. Percentage variation compared to the baseline case.

sub-model closes the LP-EGR valve more than in the baseline case. The lower total amount of EGR leads to higher NO_x emissions. With the new strategy, since at high engine speed no *EP+IP* is enabled, there is more EGR

and a slight improvement is observed. Case 2b reduces NO_x emissions from about 6 % in Case to 2 % in Case 2b. Case 3b allows producing 2 % less NO_x emissions than in the baseline case, considering that in Case 3 they are 11 % higher.

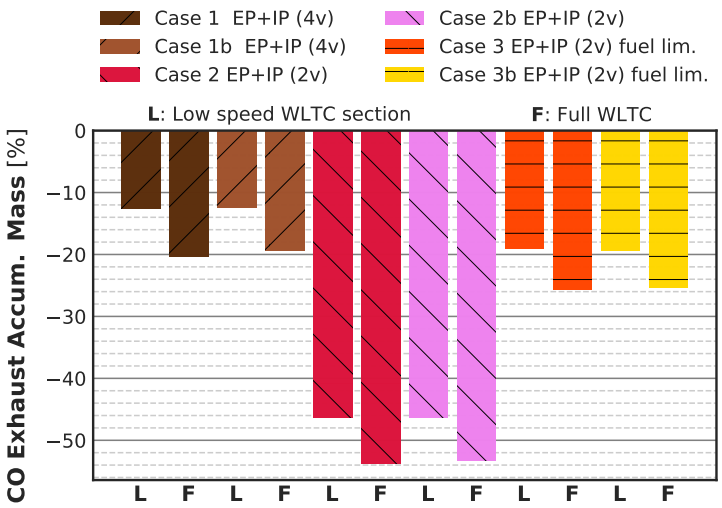

Figure 5.33: *Accumulated CO emissions at DOC outlet, engine start at* 20 °C *ambient temperature. Percentage variation compared to the baseline case.*

Figure 5.33 presents the tailpipe accumulated CO mass difference at the end of the low speed stage and the complete cycle. It may result interesting that there is no differences between Case 1, Case 2, Case 3 and their respective 'b' versions. The reasons is that, as observed in the previous Figure 5.19, almost all the CO is converted as the light-off temperature is achieved. Since this event happens about 800 seconds after the start of the cycle (a little bit in Case 2 and Case 2b), the later *EP+IP* activation when the temperature falls down the threshold value, keeps the CO conversion at the same level as the previous Cases 1, 2 and 3.

Regarding HC emissions, Figure 5.34 shows slightly higher HC emissions at the end of the cycle and in the previous situation. This is because the DOC temperature at high and extra high vehicle speed is lower than in Case 1b is lower than in Case 1, as well as in Case 2b and Case 3b, thus resulting in a slightly lower HC conversion efficiency. In the most advantageous Case

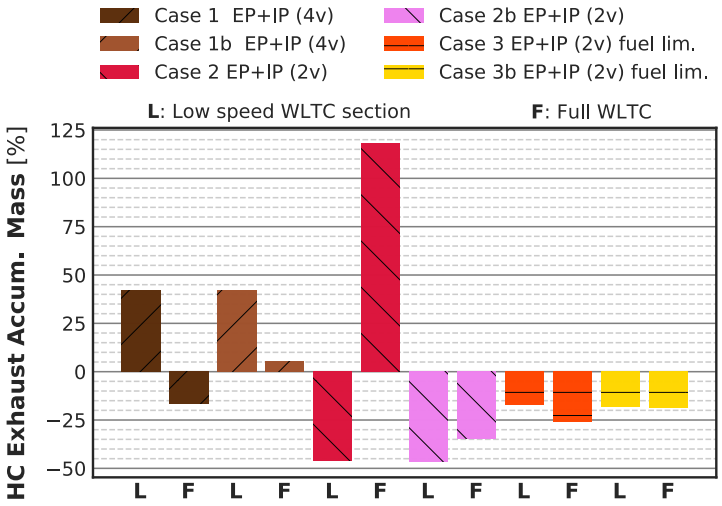

Figure 5.34: Accumulated HC emissions at DOC outlet, engine start at 20 °C ambient temperature. Percentage variation compared to the baseline case.

2b, there is a large reduction in HC emissions compared to Case 2. *EP+IP* deactivation during the extra high vehicle speed stage removes the excessive HC formation produced by the excessive fuel penalty. The increase in HC emissions in Case 2 at this stage is commented above and it can be observed in the HC accumulated conversion efficiency drop in Figure 5.18. With the deactivation of *EP+IP*, Case 2b is able to reduce HC emissions about 35 % at the end of the cycle with respect to the baseline case.

5.5 Conclusions

Several variable valve timing alternatives have been discussed in this chapter with the aim of improving the temperature upstream the diesel catalyst. Three types of variable valve solutions have been studied based on previous studies shown in chapter 4: advancing EVO and EVC, with a symmetrical delay in IVO and IVC —on one and on both pairs of cylinder valves— and an exhaust valve re-opening during the intake stroke. In order to operate with optimum values of intake/exhaust phasing, and re-opening lift and duration, a control system has been integrated to the ECU sub-model. These

values were obtained by means of a parametric study in steady-state operating conditions. With the proper *EP+IP* and re-opening maps for each case, a simulation of the WLTC cycle starting at cold start at 20 °C was carried out for each case. These five cases have been compared in terms of exhaust temperature profit, fuel consumption, warm-up and light-off time and pollutant emissions. For the sake of summarising the conclusions obtained, the following points are exposed:

1. The exhaust temperature is increased and warm-up time reduced in all the five cases. The increase in the exhaust gas temperature allows higher CO and HC conversion efficiencies in the catalyst. *EP+IP* cases are the most effective in this way. Case 2 achieves an average increment in exhaust temperature of 67 °C, followed by Case 1 with an average increase of 42 °C over the low speed stage. Case 2 allows the greatest increment in HC and CO accumulated conversion efficiency: 8.5 % more than the baseline, for HC conversion, and 18 % for the CO over the low speed stage of the WLTC.

2. *EVrO* alternatives (Cases 4 and 5) do not offer a noticeable increase in the exhaust temperature over the low speed stage of the test cycle, compared to the other cases. Their average increase over this stage of the WLTC is around 8 °C.

3. Case 4 and 5 can reduce slightly CO and HC formation. However, they cannot reduce tailpipe emissions as much as Case 1, 2 and 3 (specially over the low speed stage) due to their low contribution towards increasing the exhaust gases enthalpy. At the end of the low speed stage of the WLTC, HC and CO accumulated conversion efficiencies of both *EVrO* cases are fairly similar as the baseline ones.

4. Despite the high temperature increase offered by Case 2, its accumulated fuel penalty reaches a 20 % at the end of the low speed stage; and it is even higher during the extra high speed. In terms of fuel consumption and emission trade-off, Case 3 arises as a good alternative to reduce HC and CO emissions and provide an increase in the tailpipe temperature, which is beneficial for NO_x adsorbers placed downstream the DOC.

5. Regarding NO_x formation, Cases 2 and 3 allow to obtain a slight reduction in absolute values during the low speed stage of the WLTC, reducing NO_x emissions by 18 % and 13 %, respectively. On the contrary, the maximum excess in NO_x is near 16 %, which is reached by Case 5 over the last high speed transients of the WLTC. *EVrO* strategies (Cases 4 and 5) do not achieve the same exhaust gas retention power as the other cases for the fast accelerations during the extra high speed stage.

6. Regarding *EP+IP* cases, when the phasing is applied on the four valves, rather than on two valves, the phasing range gets reduced in order to keep the torque target. Nonetheless, a high advance of the EVO, like in Cases 1 and 2, increases drastically the fuel consumption. The fuel penalty in Case 1 is about 12 %, while the one of Case 2 is about 20 % at the end of the low speed stage.

7. In order to reduce the fuel penalty of *EP+IP* cases, a study in which *EP+IP* is only performed when the catalyst temperature is below the light-off threshold has been performed. With this approach, it is possible to reduce the fuel penalty, NO_x and HC emissions of Cases 1, 2 and 3 over the full WLTC cycle.

As a concluding remark, both *EVrO* cases do not offer a remarkable advantage during the warm-up stage of the diesel catalyst. On the contrary, Case 2 presents the greater exhaust temperature increment and the lower NO_x, CO and HC emissions during the first low speed stage of the cycle. Besides, it presents the faster catalyst heat-up, which is about 19 % faster than in the baseline case. However, its main caveat is the high fuel penalty around 20 % with respect to the baseline valvetrain. Case 3 presents the best CO-fuel and HC-fuel trade-offs. Moreover, it is possible to achieve an 18 % reduction in NO_x emissions following this strategy during the low speed stage of the WLTC. Its accumulated fuel consumption is about 5 % more than the baseline case, which is the lowest of all three *EP+IP* strategies.

The solution proposed in Case 2b is the best alternative, since it offers the advantages of Case 2 until the DOC light-off is achieved, while avoid-

ing the excessive fuel consumption during the high and extra high vehicle speed stages. Case 2b presents a 53 % reduction in CO emissions, and a 34 % reduction in HC emissions with a fuel penalty of 6 % at the end of the WLTC cycle with respect to the baseline valvetrain. A better alternative to reduce the fuel consumption during the low speed stage would be a mix of Case 2b and Case 3b: trying to heat-up quickly the after-treatment system while constraining the fuel penalty, and then switching off the strategy once the DOC is already active.

Chapter 5 References

[133] A. J. Haagen-Smit. "Chemistry and Physiology of Los Angeles Smog". *Industrial & Engineering Chemistry*, 44 (6), (1952), pp. 1342–1346. issn: 0019-7866. doi: 10.1021/ie50510a045 (cit. on p. 190).

[134] D. F. Hagen and G. W. Holiday. "The effects of engine operating and design variables on exhaust emissions". *Pre-1964 SAE International*. SAE International, 1962. doi: 10.4271/620404 (cit. on p. 190).

[135] M. Finlay. "Variable valve timing control for internal combustion engines". Pat. US3496918A. 1968. url: https://patents.google.com/patent/US3496918A/en (cit. on p. 191).

[136] Z. Dimitrova, M. Tari, P. Lanusse, F. Aioun, and X. Moreau. "Development and Control of a Camless Engine Valvetrain". *IFAC-PapersOnLine*, 52 (5), (2019). 9th IFAC Symposium on Advances in Automotive Control AA 2019. issn: 24058963. doi: 10.1016/j.ifacol.2019.09.064 (cit. on p. 191).

[137] Y. Murata, J. Kusaka, M. Odaka, Y. Daisho, D. Kawano, H. Suzuki, H. Ishii, and Y. Goto. "Achievement of medium engine speed and load premixed diesel combustion with variable valve timing". *SAE 2006 World Congress & Exhibition*. SAE International, 2006. doi: 10.4271/2006-01-0203 (cit. on p. 191).

[138] J. Hunicz and M. Mikulski. "Application of Variable Valve Actuation Strategies and Direct Gasoline Injection Schemes to Reduce Combustion Harshness and Emissions of Boosted HCCI Engine". *Journal of Engineering for Gas Turbines and Power*, 141 (7), (2019). issn: 0742-4795. doi: 10.1115/1.4043418 (cit. on p. 191).

[139] G. Xu, M. Jia, Y. Li, Y. Chang, H. Liu, and T. Wang. "Evaluation of variable compression ratio (VCR)and variable valve timing (VVT)strategies in a heavy-duty diesel engine with reactivity controlled compression ignition (RCCI)combustion under a wide load range". *Fuel*, 253, (2019), pp. 114–128. issn: 00162361. doi: 10.1016/j.fuel.2019.05.020 (cit. on p. 191).

“Heat, like gravity, penetrates every substance of the universe, its rays occupy all parts of space.”

— Jean-Baptiste-Joseph Fourier

Chapter 6

Exhaust thermal insulation under transient conditions

Contents

6.1 Introduction 236
6.2 Model preparation 238
6.3 Exhaust insulation methodology 240
6.4 Results and discussion 245
6.5 Conclusions 260
Chapter 6 References 264

6.1 Introduction

During the last years, the emissions legislation in the major automotive regions have established more restrictive limits of the air pollutants released into the atmosphere in order to reduce the environmental impact of the transportation activities [140]. For this purpose, new developments in after-treatment systems have been adopted during the last decade, such as DOC + DPF systems in combination with LNT or SCR [141].

Specially in diesel engines, cold start and heating phase imply a considerable challenge, since heating techniques are a compromise between a fast heat-up of the after-treatment system —burning some extra fuel— and a low penalty in fuel consumption. To address this issue, some authors have proposed solutions from the side of the engine calibration so as to increase the exhaust temperature. These solutions include shifting the combustion towards the exhaust phase, avoiding the turbine distributor to be fully closed in certain conditions, or implementing an intake throttling to slightly reduce the trapped mass and increase the injected fuel [142, 143, 144].

As it was manifested in chapter 3, VVT is a technical solution to raise the exhaust temperature by increasing the retention of burnt gases in the combustion chamber. However, other alternatives have been explored by directly modifying the exhaust line layout. In this way, Luján et al. proposed a pre-turbo after-treatment placement to achieve a faster after-treatment warm-up and improve the DPF passive regeneration [145, 146].

Regarding thermal barrier coatings (TBC) solutions, a major breakthrough in diesel engine technology has been achieved by the pioneering work done by Kamo and Bryzik, since the end of the 1970s, as the first persons in introducing TBC system for internal combustion engines [147, 148]. Kamo and Bryzik used thermally insulating materials such as silicon nitride to insulate different surfaces of the combustion chamber. The application of thermal barrier coatings in thermal engines has been widely explored as a way to reduce the heat rejected in the combustion chamber [149, 150,

151, 152, 153, 154, 155] in order to improve engine efficiency and reduce NO_x emissions.

While insulating the combustion chamber also increases the exhaust gas temperature, some authors have studied the application of TBC in the insulation of exhaust manifolds to keep the burnt gases enthalpy. EkstrÖm et al. [156] analysed several types of barrier coatings to insulate the internal walls of a diesel engine exhaust manifold for improving its fatigue life. Their results showed that it is possible to reduce the temperature in the metal up to 50°C by applying a 3 mm thick layer of a TBC with a thermal conductivity of 1.5 W/m K, like, for instance, yttria-stabilised zirconia (YSZ). Working towards this direction, Thibblin et al. [157] experimentally studied the thermal cyclic life of different TBC materials in a heavy-duty diesel engine exhaust manifold.

These kind of researches have been carried out in petrol engines as well. Kishi et al. [158] studied the thermal insulation of a petrol exhaust manifold and its impact on the exhaust gas temperature and hydrocarbon emissions. Their results, in combination with an engine equipped with a variable valve timing system, shown an increment in the exhaust gas temperature as well as an 8 % increment in HC conversion efficiency.

Concerning the internal and external heat transfer in exhaust manifolds, Zidat and Parmentier [159] studied it to minimise the catalyst light-off time. They concluded that the internal heat transfer is the most dominant mode of heat loss from the exhaust manifold. Reducing the internal heat transfer will significantly increase the catalyst temperature. Moreover, external heat insulation becomes more and more important as the exhaust manifold gets warmer.

In a more recent study carried out by Serrano et al. [160], the thermal insulation of the combustion chamber and the exhaust manifold in a six cylinder heavy-duty engine was experimentally tested. According to their results, a 1 % specific fuel consumption reduction was obtained by insulating the exhaust manifold. Furthermore, a slight improvement in both NO_x-Soot and NO_x-BSFC trade-offs was achieved, compared to other solutions concerning the insulation of the pistons and the cylinder head.

Considering how the insulation of the exhaust ports and the turbine affects the temperature upstream the after-treatment systems, Luján et al. [161] performed a numerical study of the potential of thermal insulation of these elements in steady-state operating conditions.

As an example of application of the engine model described in chapter 3, this chapter presents a study of the exhaust line heat transfer effect in the engine and after-treatment performances. To this extent, a simulation study has been carried out comparing different exhaust thermal insulation solutions in dynamic conditions of speed and load. As proceeded in the same way as in the VVT study in chapter 5, the european WLTC class 3 test cycle has been considered as the standard dynamic test for this study. These solutions consider the division of the exhaust system in 3 parts upstream the DOC + DPF brick: ports, manifold and turbine. The different solutions represent the insulation of these elements and some combinations of them. With the aim of understanding the influence of each element in the catalyst inlet temperature, each solution assumes an adiabatic insulation of the elements involved in it. It means, for instance, that the insulation of the exhausts ports assumes no heat transfer between the hot gases and the surface of these ports. The results obtained are discussed in terms of fuel economy, exhaust gas temperature increment, HC and CO conversion efficiencies and HC and CO pollutant emissions reduction.

6.2 Model preparation

Recalling the heat transfer model in pipes (subsubsection 3.2.1.2) indicated in Equation 3.6, the convective heat transfer from gas to the pipe walls is multiplied by a coefficient. This coefficient is usually 1 to account for the heat transfer. To block this heat flux, the coefficient has been turned to 0 in the exhaust ports (*EP* cases). The intake and exhaust ports are connected to the lumped conductance model of the engine block —through the cylinder head node— and the coolant circuit model. Thus, the thermal insulation of the exhaust ports should reduce coolant temperature as less heat is transferred to the cylinder head.

In the same way, the heat transferred from the exhaust gases to the exhaust manifold (*EM* cases) is blocked by cancelling the convective heat transfer coefficient (h) in Equation 6.1. Currently, a direct way to do this in the model is by turning to 0 the Nusselt constant in Equation 6.2 (where Re and Pr are the Reynolds and Prandt numbers, respectively), since the Nusselt number (Nu) is later used to calculate the heat transfer coefficient in Equation 6.3 (where k is the thermal conductivity of the gas and L is the characteristic length of the exhaust manifold).

$$q = A_{\text{manifold}} \cdot h \cdot (T_{\text{g}} - T_{\text{w, int}}) \cdot \Delta t \tag{6.1}$$

$$Nu = 0 \cdot Re^{0.7} \cdot Pr^{0.33} \tag{6.2}$$

$$h = \frac{Nu \cdot k}{L} \tag{6.3}$$

Finally, to block the heat transfer from the gas to the turbine metal node in the turbocharger heat transfer model (*TI* cases), the multiplier coefficient of the convective heat transfer correlation is turned to zero. The heat transferred from the turbine metal to the ambient (*TE* cases) is cancelled in an analogous fashion.

As in the previous chapter, all the simulations were performed keeping the torque of the baseline case, which is the one with the non-insulated exhaust system of the reference engine described in section 2.2. To attain this objective, the control system included in VEMOD emulates the ECU to control the injection by modifying the injection pressure, the fuel mass split and the start of energisation depending on the engine speed and total fuelling rate. The model also controls the air loop by means of the VGT rack position (whose control is based on the intake pressure setpoint, depending on the engine speed and total fuelling rate), and LP-EGR, HP-EGR and back pressure valves, whose control is based on the air mass flow setpoint.

For any specific engine speed and torque, the required fuel mass is obtained from a calibration map. Once the engine speed and fuel mass are

known, the injection pulses timings and masses, intake manifold pressure, injection pressure and air mass flow setpoints are obtained from their respective maps.

6.3 Exhaust insulation methodology

This work is centred on how the exhaust temperature can be increased by insulating different parts of the engine exhaust line. These elements, or parts of the exhaust line, are the engine exhaust ports, exhaust manifold and the turbine volute. In this study, all these elements have been fully insulated (making them adiabatic) from the inner side of the element, in order to have an idea of the maximum increment in the exhaust temperature since no heat is transferred to the metal. According to this, nine different configurations have been simulated: a baseline case without any thermal insulation in the exhaust line, three cases insulating only one of these elements and five cases representing different thermal insulation combinations of these elements. Table 6.1 summarises the adiabatic elements for each configuration. Thus, the baseline configuration does not consider any additional insulation, it represents the original engine model presented in chapter 2. *EP* configuration considers no heat transfer from the hot gases to the eight exhaust ports walls. In *EM* case, there is no heat transfer between the exhaust gases and the exhaust manifold walls (including the volume between the exhaust ports and the turbine inlet section). *TI* configuration considers no heat transfer between the exhaust gases and the turbine volute. The rest of configurations are combinations of these three adiabatic cases. A special mention must be made for *Full Exhaust* case, which is the sum of the previous cases plus a completely insulated turbine housing (internal and external); hence there is no convection between the turbine metal and the ambient.

Figure 6.1 tries to clarify which parts of the exhaust system are involved in this study. It represents the engine layout and the different exhaust components referred in Table 6.1.

The main reason why there is not any configuration just insulating the

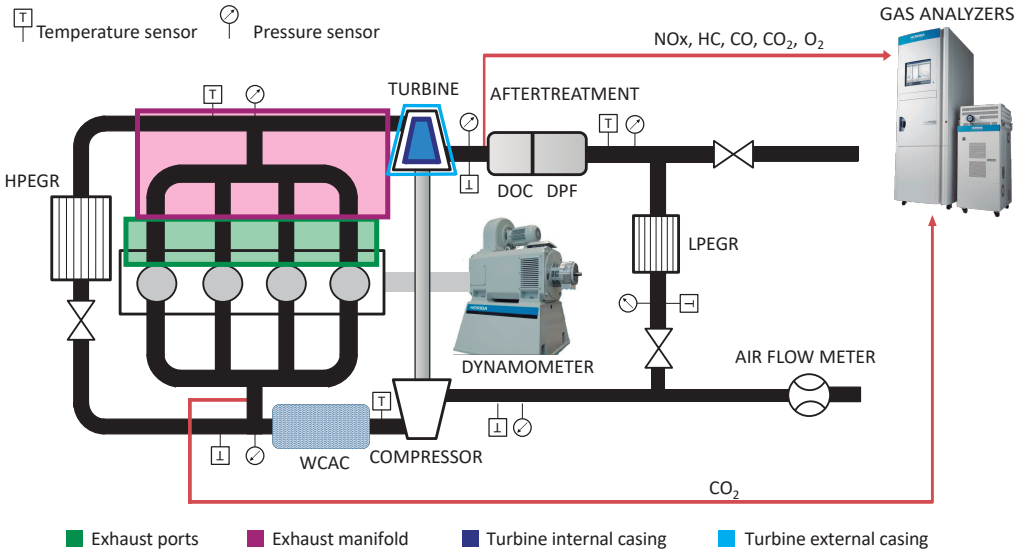

Figure 6.1: Engine layout with the exhaust components which have been thermally insulated.

external layer of the turbine housing, nor a combination with other configuration, is because it has no significant impact in the temperature at turbine outlet. The explanation for these poor performance of the external turbine insulation is due to the alternative path for the heat to be transferred along the turbocharger. Although there is no convection between the metal and the environment, the heat is driven axially through the metal and removed partially by the lubrication oil. This can be observed in Figure 6.2, where there is a great difference in the accumulated heat from the turbocharger to the ambient between cases baseline and *TE* (turbine external insulation); whilst there is no such difference when it comes to the accumulated heat to oil. The same occurs if another configuration is considered and the same one plus the turbine external insulation (*EM* and *EM + TE*). Regarding the decline that can be seen in the accumulated heat to oil graph in Figure 6.2 (bottom), it happens because, at the end of the cycle, the temperature of the turbocharger housing metal node in contact with oil is greater than the oil temperature. This means that the heat flux goes from the metal to the oil, considered as negative; contrarily to what happens for more than half of the cycle, where the oil is hotter than the metal. Oil, turbine node, compressor

Cases	Heat transfer: *Exhaust ports*	*Exhaust manifold*	*Turbine internal casing*	*Turbine external casing*
Baseline	✓	✓	✓	✓
EP	O	✓	✓	✓
EM	✓	O	✓	✓
EP + EM	O	O	✓	✓
TI	✓	✓	O	✓
EP + TI	✓	✓	O	✓
EM + TI	✓	O	O	✓
EP + EM + TI	O	O	O	✓
Full Exhaust	O	O	O	O

✓: heat transfer unchanged, O: adiabatic

Table 6.1: *Thermal insulation cases.*

node and housing 2 temperatures are traced in Figure 6.3. These nodes of the turbocharger lumped heat transfer model are defined in Figure 3.6 in subsubsection 3.2.1.3. The top subplot in Figure 6.3 represents these node temperatures in the reference engine exhaust line, while the middle subplot represents the node temperatures in case *EM + TE*. Green areas represent the temperature difference when oil, which enters into the turbocharger at the same temperature as into the engine block, is hotter than the turbocharger metal node in contact with it. Contrarily, read areas represent when the oil temperature is below the housing 2 node temperature, so the heat flux goes from the metal to the oil, explaining the heat to oil drop at the end of the cycle in Figure 6.2. These temperature difference between oil and housing 2 is transferred to Figure 6.3 (bottom), where the grey area

indicates when that difference is greater in the baseline case than in *EM + TE*. The orange area represents the opposite situation. It is observed that this temperature difference is bigger in the baseline case than in *EM + TE*, since the thermal insulation of the exhaust manifold and the turbine casing external surface slightly increases the housing 2 node temperature. Contrarily, the oil temperature is almost constant in both cases since it depends mainly on the engine block temperature and the oil cooler efficiency. Since this temperature difference (oil - housing 2 node) is responsible of the heat transferred to the oil in the turbocharger, consequently, the accumulated heat to oil traces in Figure 6.2 are below the baseline one.

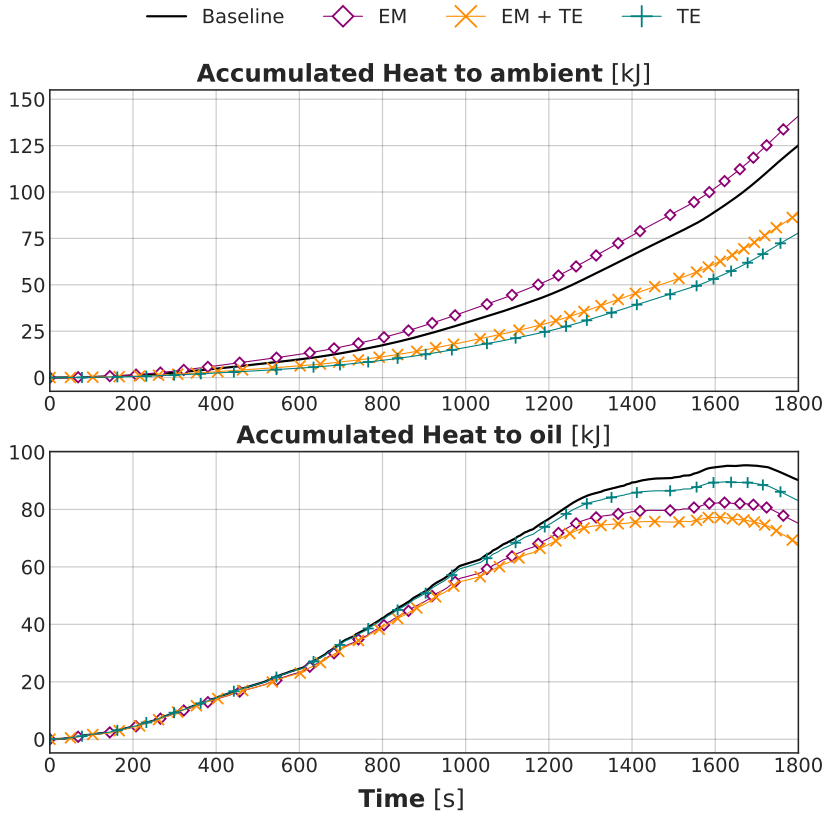

Figure 6.2: *Accumulated turbocharger heat to ambient and heat to oil over the WLTC at 20°C room temperature.*

In order to perform this study, the resulting torque from the baseline simulation was imposed as the torque target for all the different insula-

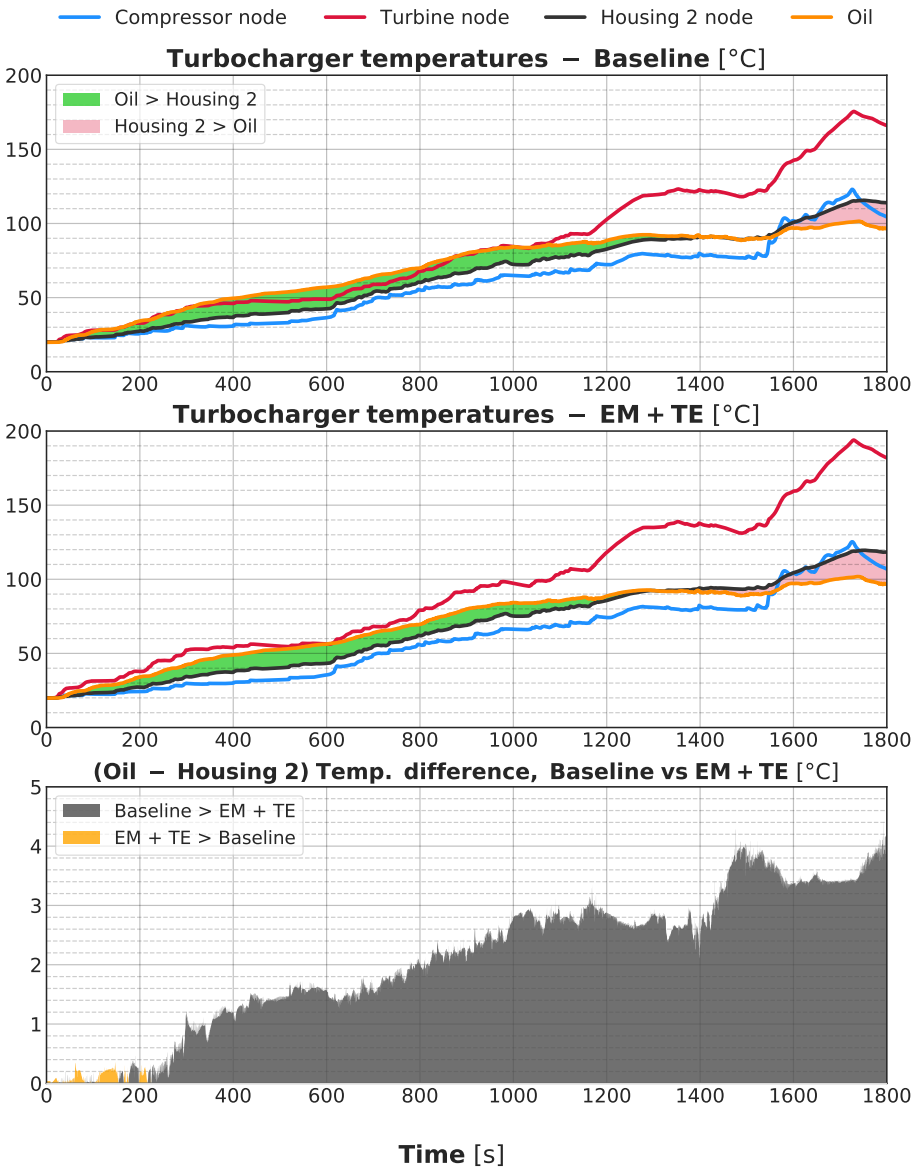

Figure 6.3: Turbocharger temperatures of the baseline engine exhaust and the EM + TE case over the WLTC at 20°C room temperature.

tion combinations. The ECU control model basically takes control on the fuel mass injected and the required air mass flow to reach the torque ant any operating point —based on the engine calibration that contains several maps for boost pressure, air mass flow and fuel injected. In this way,

it is possible to quantify differences on fuel consumption, pumping losses, exhaust temperature and other key outputs when compared to the baseline configuration.

An analysis in transient conditions of engine speed and load has been carried out considering the worldwide harmonized light vehicles test cycle (WLTC) in three different temperature conditions. Table 6.2 lists these different conditions. Thus *warm* refers to the WLTC at the room temperature of 20°C and an engine temperature near 80°C. The *ambient* conditions refer to the WLTC at the room temperature of 20°C, but with the engine starting from cold. Finally, the *cold* conditions refer to an engine cold start while keeping the room temperature at −7°C.

Name	Cycle	Engine temp.	Test cell temp.
Warm	WLTC	already warm (≈ 80°C)	20°C
Ambient	WLTC	cold start (≈ 20°C)	20°C
Cold	WLTC	cold start (≈ −7°C)	−7°C

Table 6.2: Simulation transient conditions.

6.4 Results and discussion

The main goal to insulate the exhaust gases path is to achieve greater temperatures in order to increase the efficiency of the after-treatment devices and/or recover part of the available energy of the hot gases. The accumulated gas enthalpy downstream the turbine is presented in Figure 6.4 as the absolute difference with respect to baseline case. It can be observed that all the configurations achieve some increment in the exhaust enthalpy compared to the baseline case in the three temperature conditions. As it was expected, the lowest increment is obtained by the *TI* configuration because it has less scope than any other to keep the exhaust enthalpy, since there are heat losses in the elements upstream the turbine and the volute contact surface is smaller than the ones of the exhaust manifold and exhaust ports. On the contrary, the *Full Exhaust* configuration performs best, achieving an increment of 3350 kJ (12.1 %), 2920 kJ (12.0 %) and 3365 kJ (14.5 %) respect to

the baseline case at *warm*, *ambient* and *cold*, respectively. In terms of temperature, it implies an increment between 50°C, at partial loads, to 100°C at full load. The results obtained by *EM* are better than *EP* configuration during the low speed stage of the WLTC, since the exhaust manifold volume is higher than the one of the exhaust ports and heat losses are greater during the heating process of the manifold. However, by the high speed part of the WLTC when the exhaust ports are insulted, the advantage in heat retention are greater. This is due to the fact that heat transfer in the exhaust manifold is lower than during the heating phase and the high load transients of this zone of the cycle contribute significantly to increase the exhaust enthalpy.

The rest of configurations achieve exhaust temperatures in between of these two alternatives. The configurations that are a combination of two others perform right below the *Full Exhaust*. Comparing just the *EM* and *EP* alternatives, show that insulating the exhaust ports makes more sense in terms of heat recovery because the temperature of the gases is higher at this point. Consequently, *EP* achieves an increment in enthalpy around 1 % higher than *EM*, going up to 2 % in *cold* conditions; since more energy is lost in these conditions where the thermal gradient between hot gases and the ambient is higher and the metal parts are getting warmer throughout the transient. *EP + EM + TI* and *Full Exhaust* configurations perform quite similar as observed in Figure 6.4. When the volute internal surface has been completely thermally insulated, the major part of the heat transferred to the turbine casing has been blocked, so insulating also the turbine casing external layer has no effect on the heat transferred to the ambient.

Figure 6.5 shows the coolant temperature at engine outlet for each temperature condition (*warm*, *ambient* and *cold*). In all the three conditions, the configurations in which the exhaust ports are insulated (*EP*, *EP + EM*, *EP + TI*, *EP + EM + TI*, and *Full Exhaust*) lead to a lower coolant temperature. This phenomenon is more evident during the warm-up period (*ambient* and *cold*), concluding with differences between 3 to 10 Celsius degrees respect to the baseline case. When the exhaust ports are not completely insulated, a considerable amount of the heat is collected by the coolant circulating inside the cylinder head; thus explaining the temperature difference in these configurations.

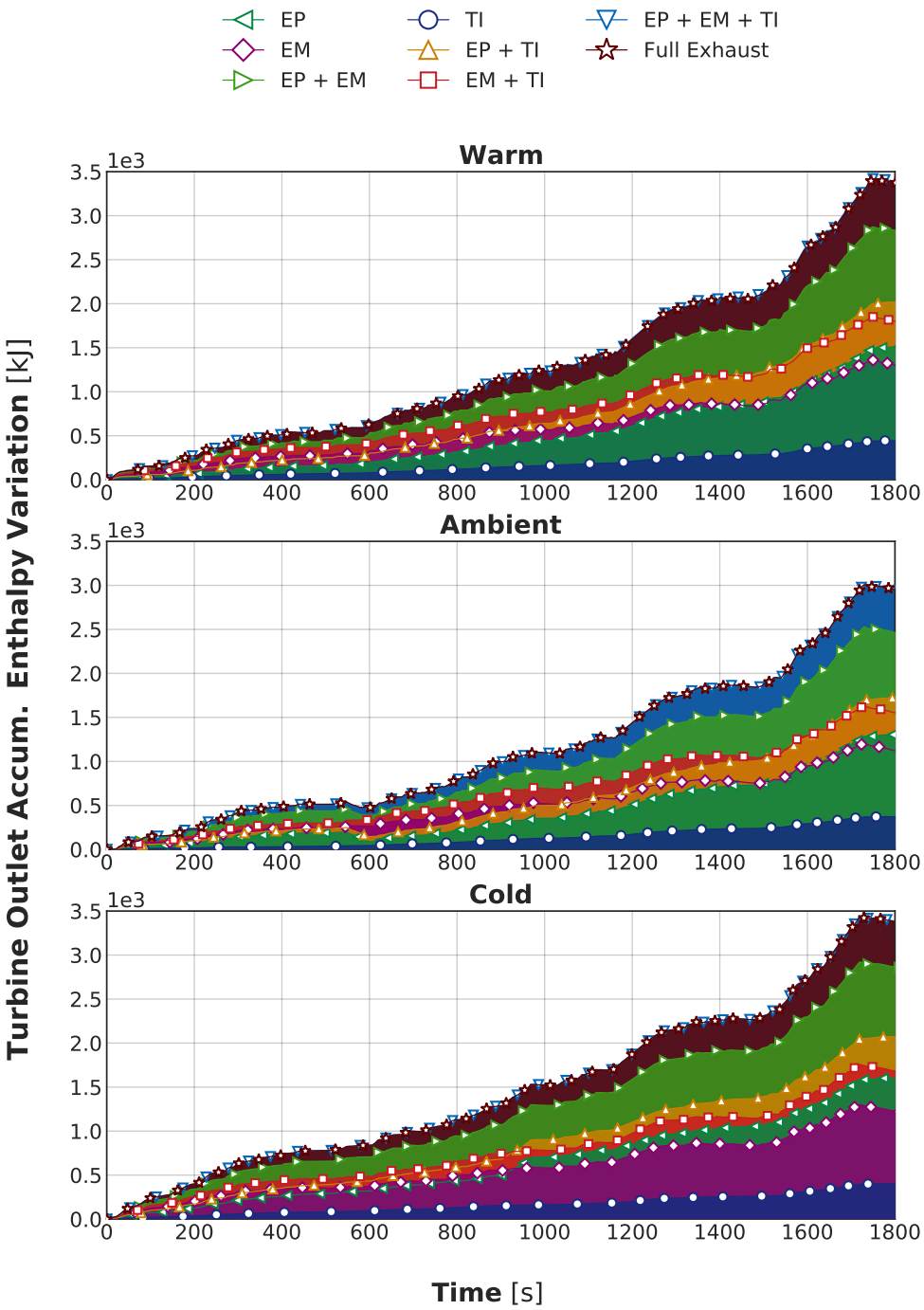

Figure 6.4: WLTC accumulated gas enthalpy at turbine outlet, difference respect to the baseline case.

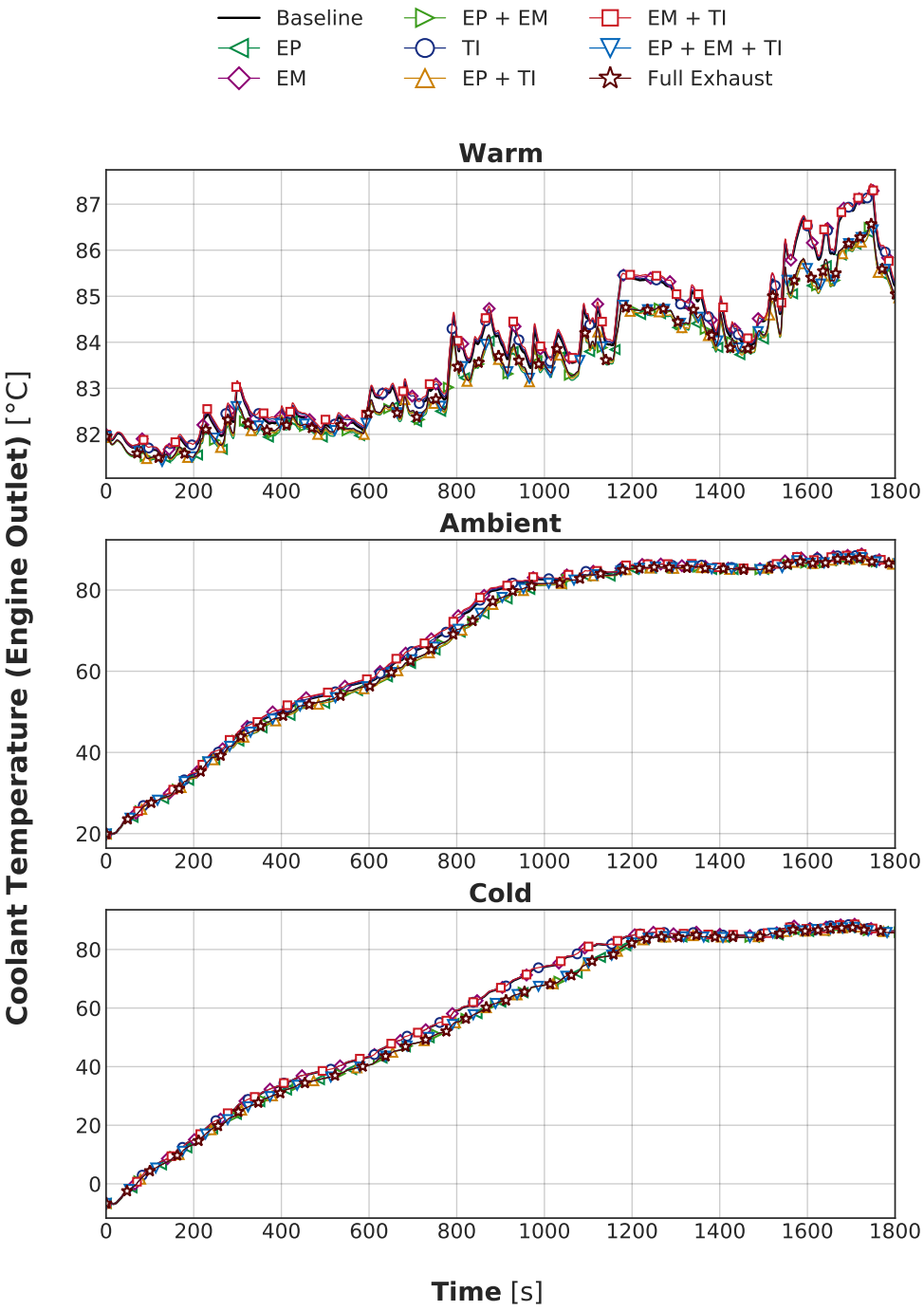

Figure 6.5: Coolant temperature at engine outlet over the WLTC transient cycle.

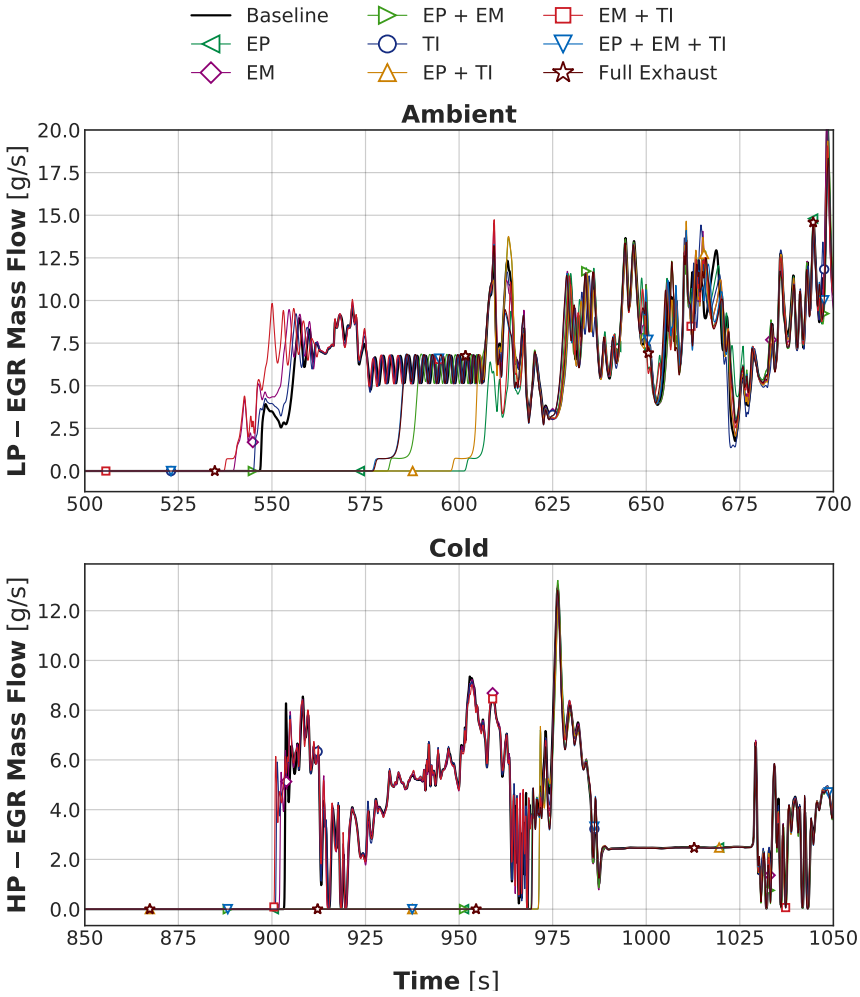

Figure 6.6: LP-EGR and HP-EGR activation at ambient and cold conditions, respectively.

The coolant temperature plays an important role in this engine when enabling the EGR system. In this particular EURO 5 engine, the activation of the two EGR routes depends on the intake temperature and the coolant temperature. According to this behaviour, variations of the coolant temperature affects the activation of the EGR, leading to a direct effect on exhaust pollutant emissions. In the cases where the exhaust ports are insulated, the LP-EGR/HP-EGR activation is delayed, as it can be seen in Figure 6.6. At *ambient* conditions, the delay in the LP-EGR activation is about 51 seconds for the *EP* case and 54 seconds for the *EP + TI* one. At *cold* conditions there is no difference among these alternatives and the delay in the HP-EGR activation is about 67 seconds. These delay in the LP-EGR activation may in-

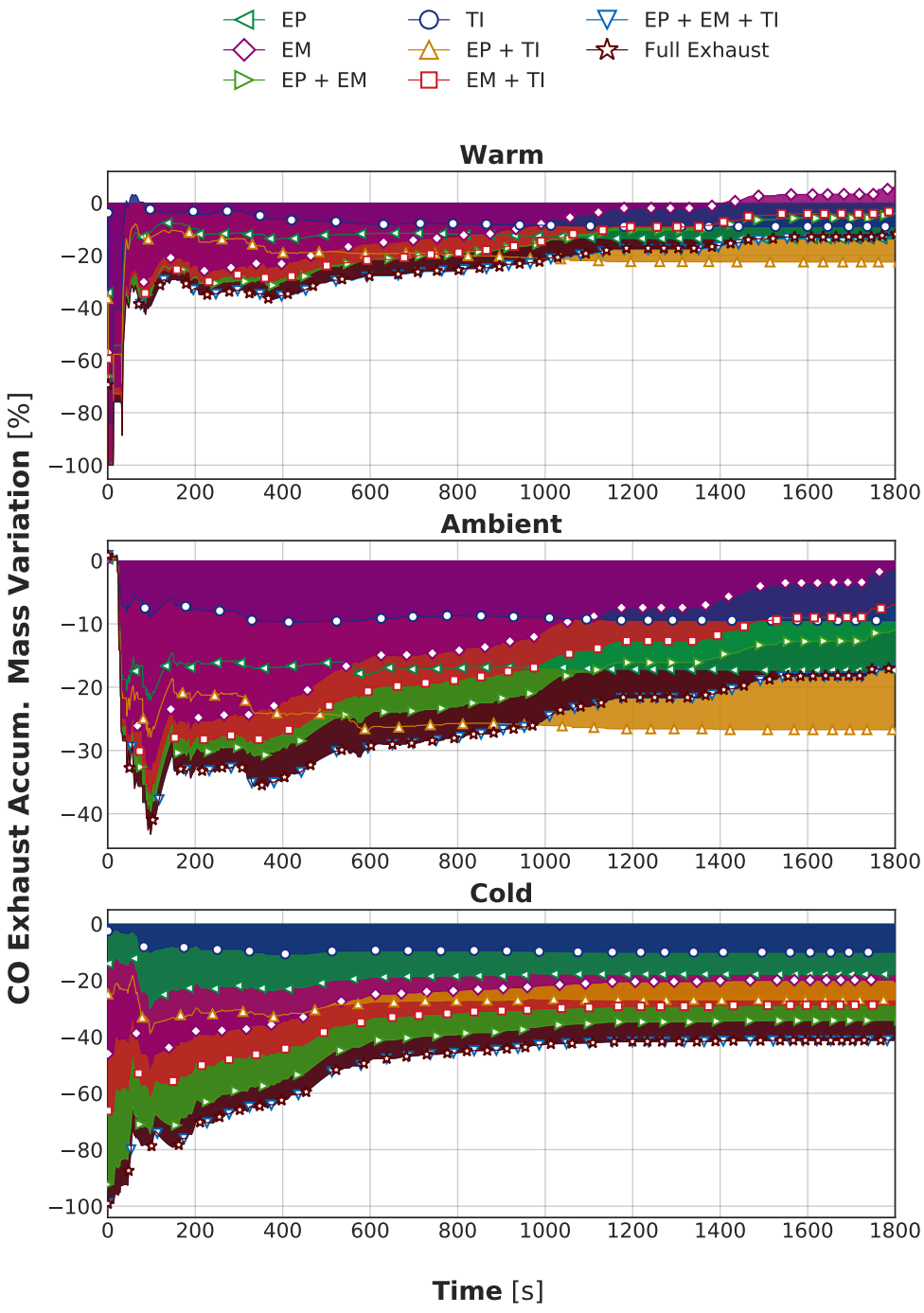

Figure 6.7: WLTC CO accumulated emissions variation downstream the after-treatment system.

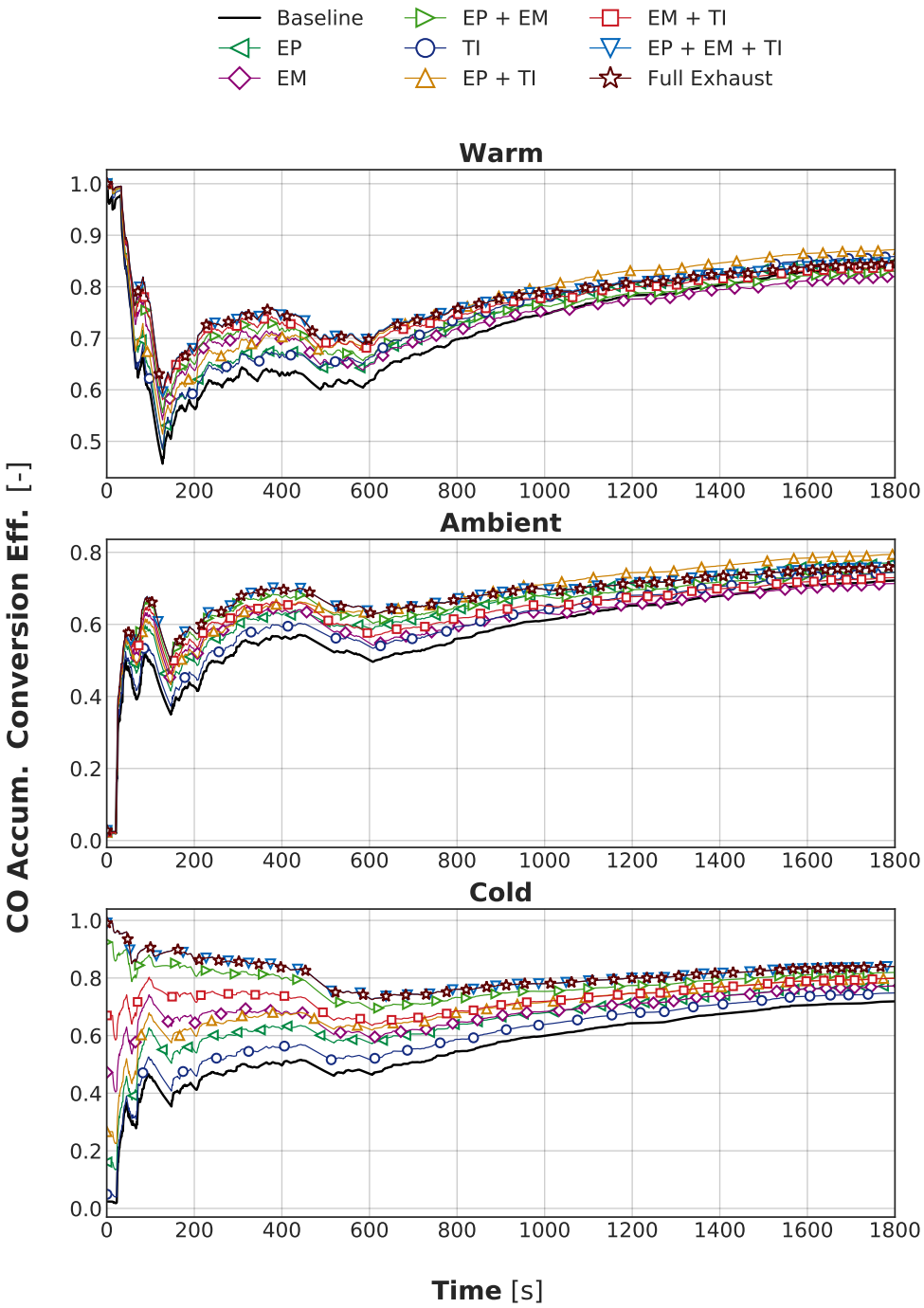

Figure 6.8: WLTC CO accumulated conversion efficiency.

crease NO_x emissions, specially at *cold* temperature conditions when there is no HP-EGR. However, according to the results, the maximum accumulated increase in NO_x emissions at the end of the transient cycle is around 0.5 g more than in the baseline exhaust, which is practically negligible.

Regarding pollutant emissions downstream the after-treatment, Figure 6.7 shows the accumulated CO emitted mass variation (respect to the baseline case) throughout the entire WLTC. As it was expected, the increment in the exhaust temperature accelerates the light-off in the diesel catalyst, meaning that optimum values for the HC and CO conversion efficiencies are reached faster. This effect is observed in Figure 6.8 where the CO accumulated conversion efficiency is 12 %, 14 % and 45 % higher in the *Full Exhaust* case at *warm*, *ambient* and *cold* conditions, respectively, at its maximum difference respect to the baseline case. The maximum CO accumulated conversion efficiency increases along the cycle, hence the shape of the CO mass graphs, from the middle of the cycle onwards, the major part of the CO is oxidised.

The same trend is observed for the after-treatment outlet HC emissions in Figure 6.9. The *Full Exhaust* configuration is presented as the cleanest option due to the increase in the HC conversion efficiency (Figure 6.10). In this case, a reduction of 44 % in HC emissions can be achieved at *cold* conditions, where the exhaust insulation shows its great potential for two reasons. On one hand, due to the greater pollutants formation at low temperatures; on the other hand, because of the greater time to heat up the DOC at low temperatures.

The lower emissions are targeted by the configurations that achieve a greater increment in the exhaust gases enthalpy. In this case, a complete insulation in the exhaust line outlines the cleanest alternative, presenting a 16 % and a 41 % reduction of CO at room temperatures of 20°C and −7°C, respectively. In terms of HC emissions, it presents a reduction of 19 % at 20°C and 45 % at −7°C. As stated above, there is no difference between this case and keeping the turbine housing unaltered (*EP + EM + TI*).

The emissions results presented in Figure 6.7 and Figure 6.9 are the result of an increment in the DOC temperature. The different insulation con-

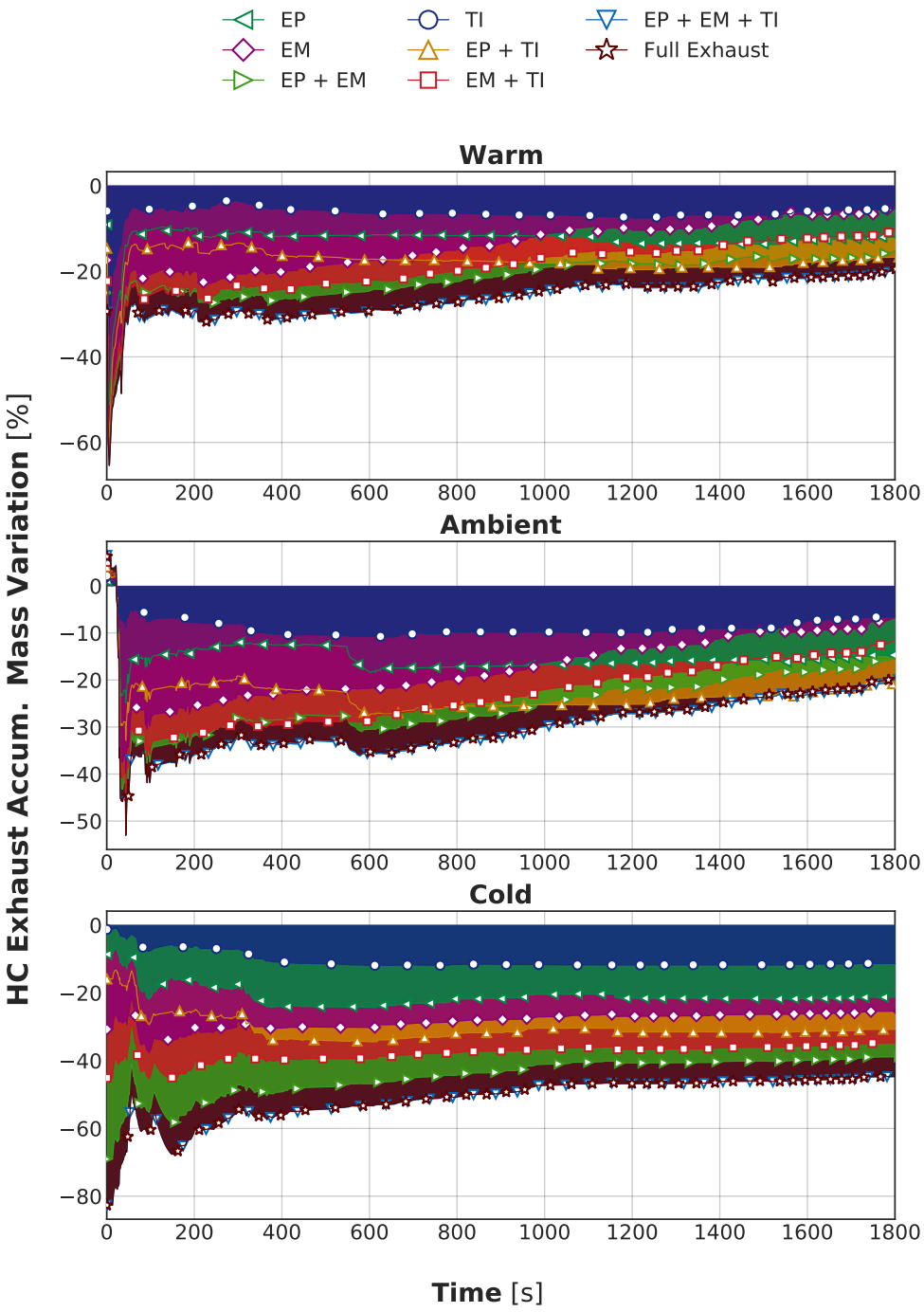

Figure 6.9: WLTC HC accumulated emissions variation downstream the after-treatment system.

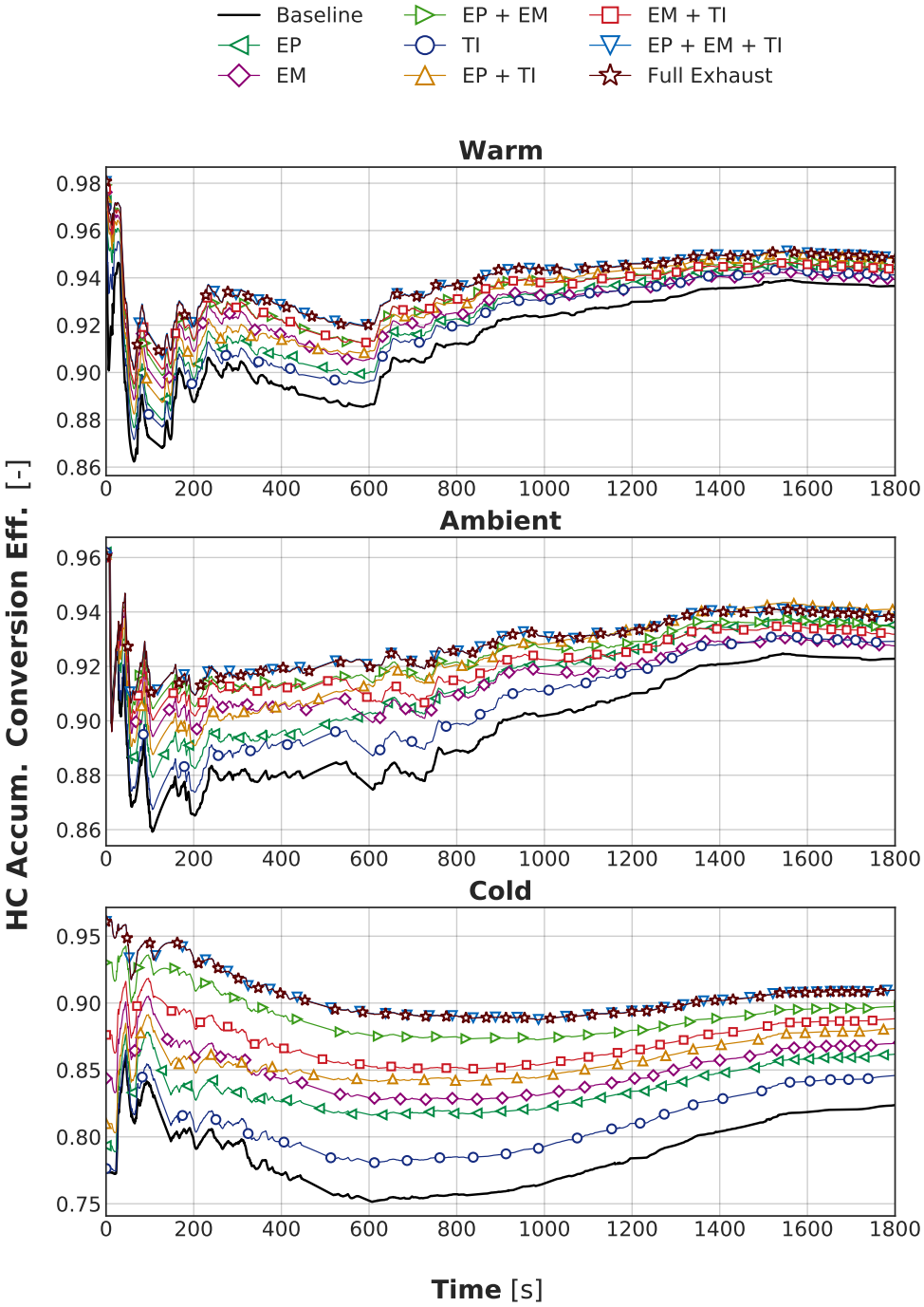

Figure 6.10: WLTC HC accumulated conversion efficiency.

figurations have a considerable impact in the light-off time as shown in Figure 6.11a. The results shown a mean time reduction from the 800 seconds of the baseline case to 650-610 seconds for the combined insulation alternatives, which represents a 24 per cent reduction in time for the *EP + EM*, *EM + TI*, *EP + EM + TI* and *Full Exhaust* cases. The turbine internal insulation *TI* has very little impact on the light-off time improvement.

Figure 6.11b shows the time required for each configuration to reach around 80°C in the coolant temperature at the engine outlet. At this temperature, the coolant starts to be funnelled through the radiator branch of the coolant circuit to stabilise its temperature around this value. As inferred from Figure 6.5, insulating the exhaust ports results in a decrement in the coolant temperature; thus, increasing the warm-up time by 65 seconds at *ambient* and 87 seconds at *cold* conditions with the *EP* alternative (an increase of 7.3 % and 8.0 %, respectively). Only a slight improvement in the engine warm-up time of 20 seconds (-2.3 % variation) is achieved by insulating the exhaust manifold and the turbine internal layer at *ambient* conditions. The rest of alternatives get a small increment of this time, though this increment is about a minute and does not make a substantive difference.

Figure 6.12 presents the accumulated CO, HC and fuel consumed as a function of the accumulated gas enthalpy gain. The values are the final cumulative values for each case relative to the baseline case and presented as a percentage. In all three sub-figures a trend can be observed: the greater the enthalpy gain, the lower the CO and HC emissions and the lower the fuel consumed. Regarding fuel consumption, there is not much improvement in fuel economy, specially at *cold* and *ambient* conditions. The *TI* alternative show some minor fuel penalty lower than 1 %. This penalty is due to the increase in pumping losses, as reflected in Figure 6.13, where the internal turbine insulation shows an increase up to 13 % in pumping losses at low speed and load (Figure 6.13a) and almost 4 % at high speed and load (Figure 6.13b). Insulating the internal surface of the turbine volute makes the VGT close, thus increasing the turbine inlet pressure and increasing pumping losses. In the same way, pumping losses are higher in the *EM + TI* and *EP + TI* cases than in the *EM* and *EP* cases. In fact, the fuel variations in Fig-

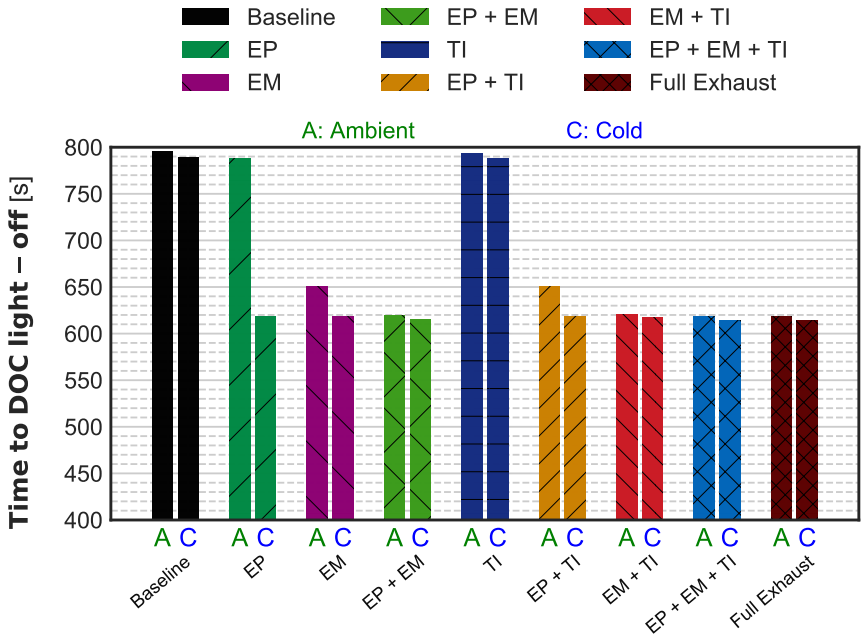

(a) Time to reach the DOC light-off temperature.

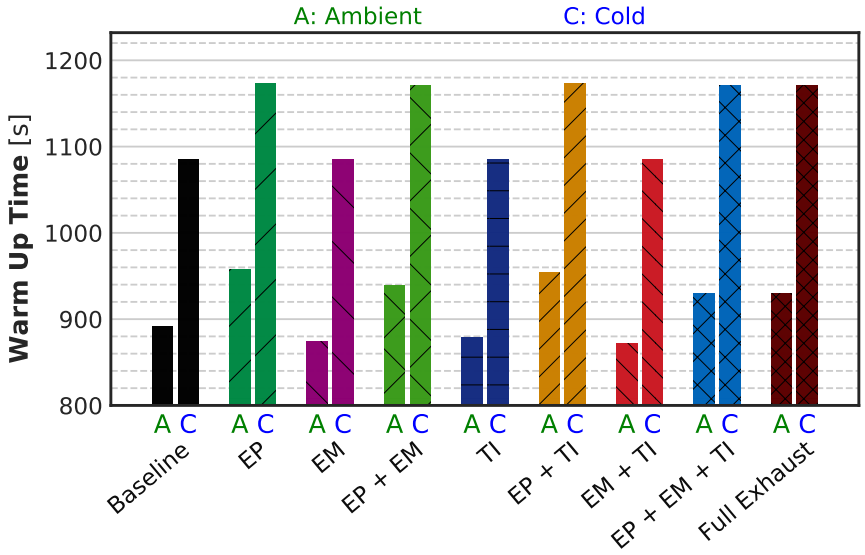

(b) Time to reach coolant thermostat threshold (80°C).

Figure 6.11: *Time to reach light-off temperature and warm-up time when simulating the WLTC transient cycle.*

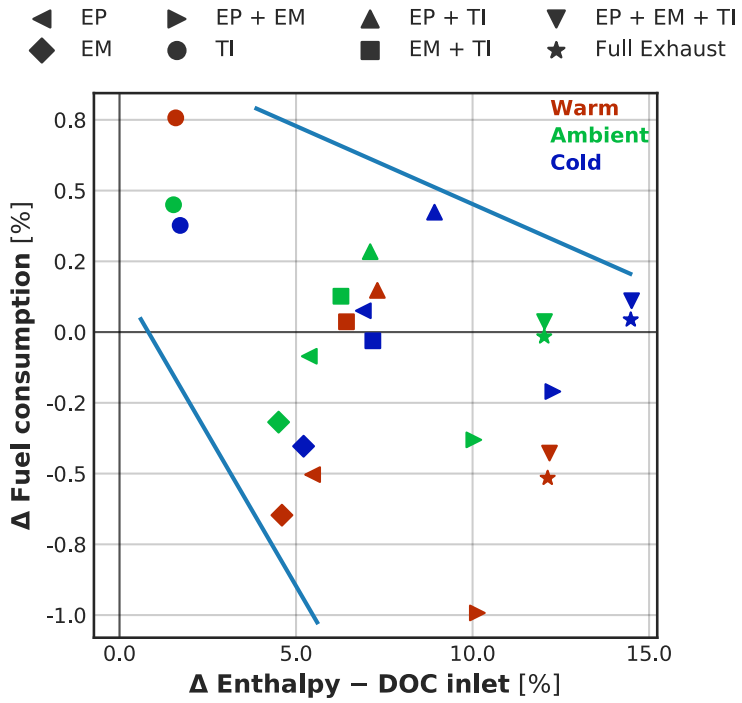

(a) Fuel consumption variation versus exhaust enthalpy variation.

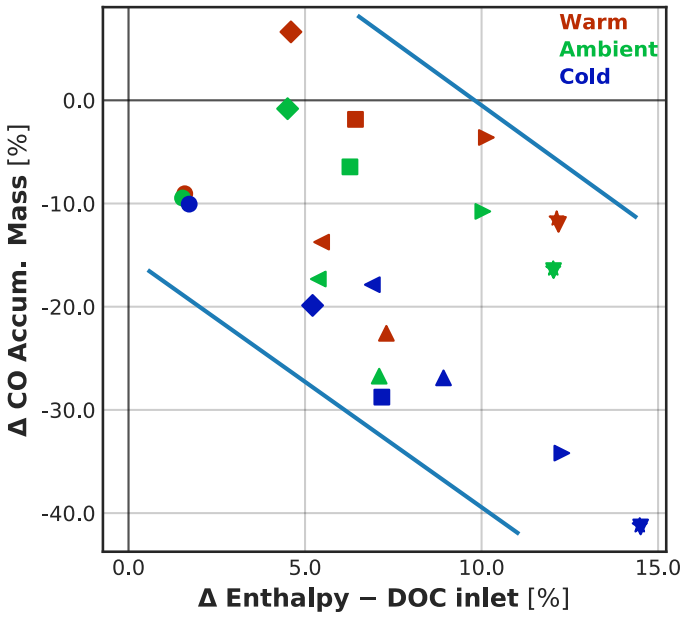

(b) CO emissions variation versus exhaust enthalpy variation.

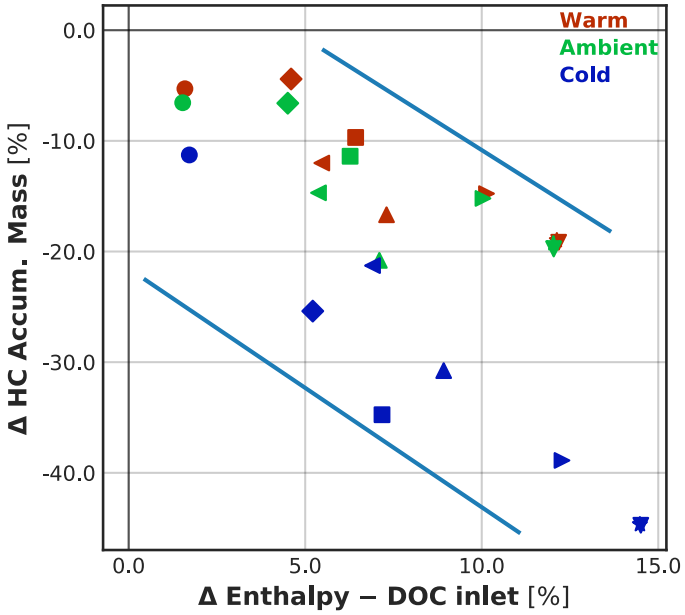

(c) HC emissions variation versus exhaust enthalpy variation.

Figure 6.12: *Accumulated fuel consumption, CO and HC emissions versus accumulated exhaust enthalpy. Variations compared to the baseline case.*

ure 6.12a are the result of the pumping losses variation in Figure 6.13. Consequently, in those cases where pumping losses are lower than the baseline, there is a small decrease in fuel consumption.

In spite of the little contribution of *TI* in the exhaust gas enthalpy, in combination with the insulation of the exhaust manifold or the exhaust ports, it allows obtaining intermediate results between both *EM* and *EP*, and *Full Exhaust* configurations. As it can be observed in Figure 6.12a, is it slightly profitable the *EP + TI* configuration rather than *EM + TI*. *EP + TI* obtains a higher increase in the exhaust gas enthalpy, specially when the room temperature is –7°C. When combining both solutions in case *EP + TI* the VGT is more opened, so the pumping losses result even more reduced, as shown in Figure 6.13b and the expansion ratio in the turbine is also lower, causing a smaller drop in temperature from inlet to outlet. If only the low speed stage of the WLTC is considered, probably, *EM + TI* case would be more profitable, since the enthalpy gain during this stage is greater in Figure 6.4 and the pumping losses are lower than *EP + TI* case, as can be seen in Figure 6.13a.

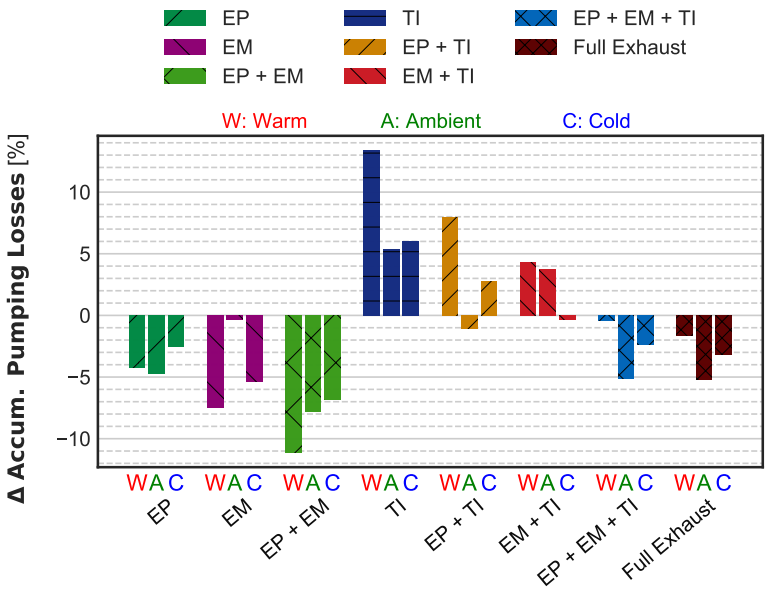

(a) Accumulated pumping losses variation over the low speed stage of the WLTC.

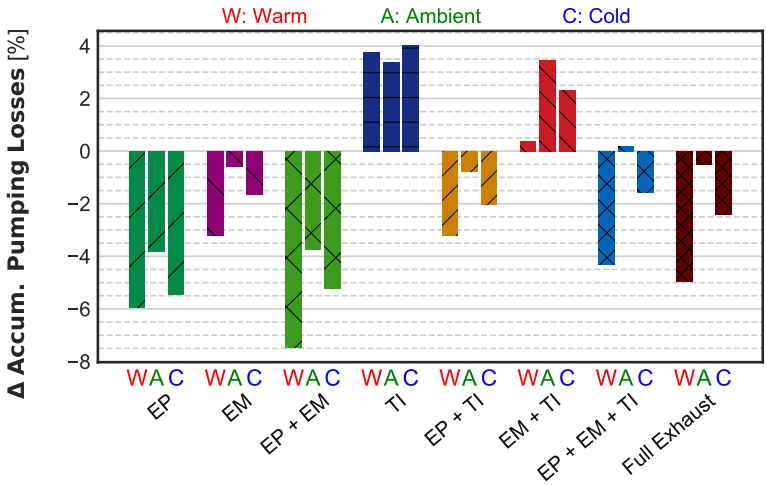

(b) Accumulated pumping losses variation over the extra high speed stage of the WLTC.

Figure 6.13: Accumulated pumping losses variation compared to the baseline case.

In terms of pollutant emissions reduction, positive results are observable. Greater emissions reductions can be obtained at *cold* conditions by insulating the exhaust manifold as well as the exhaust ports, reducing up to 40 % these emissions. At *warm* and *ambient* conditions, since the use of the EGR is more extensive and the DOC is hot for a longer period of time, the total reduction potential is lower, achieving a reduction between 5 and 15 % for CO emissions and 5 to 20 % for HC emissions.

6.5 Conclusions

Several exhaust thermal insulation alternatives have been discussed in this chapter with the aim of achieving an increment in the exhaust temperature. In order to have an idea of the maximum exhaust enthalpy gain, the different parts along the exhaust line between the engine and the diesel catalyst have been considered as adiabatic. These alternatives have been compared in terms of exhaust temperature profit, fuel consumption, warm-up and light-off time and pollutant emissions at three different temperature conditions. To carry out this study a one-dimensional engine model has been developed and exploited to simulate the different exhaust insulation configurations at transient (WLTC) conditions of speed and load. For the sake of summarising the conclusions obtained, the following points are exposed:

1. All the exhaust insulation configurations achieve an increment in the exhaust gas temperature. Hence, the DOC efficiency is increased and lower pollutant emission levels are expelled to the environment.
2. A 20 % reduction in CO emissions can be obtained by insulating just the exhaust ports or the exhaust manifold at cold conditions. Regarding HC emissions, this reduction can increase up to 25%. The CO and HC emissions reduction can surpass the 40 % by insulating both elements.
3. The insulation of the exhaust manifold leads to a reduction in the time to reach DOC light-off. The combined insulation of the exhausts ports and the exhaust manifold may reach the light-off time up to 180 seconds earlier than in the baseline case.

4. On the contrary, insulating the exhaust ports increases the warm-up time since part of the heat cannot be recovered by the coolant circuit. This increase goes up to 65 seconds at *ambient* conditions and 87 seconds at *cold* conditions, which represents an increase of 7.3 % and 8.0 %, respectively.

5. In terms of fuel consumption there is no evident improvement. Only around 1 % gain in fuel economy can be achieved by insulating the exhaust ports and the exhaust manifold at warm conditions.

6. The turbine insulation alternatives do not present remarkable benefits, since it is more profitable to insulate the elements close to the engine. However, by also insulating the inner part of the turbine housing, the effectiveness of the exhaust ports insulation is increased. The same happens when combining the exhaust manifold insulation and the turbine internal insulation, specially the low speed stage of the WLTC.

Regarding the potential of TBC in increasing the exhaust gas temperature, realistic TBC should be considered for the thermal insulation of exhausts ports, exhaust manifold and the turbine internal casing layer. The adiabatic assumption has been considered as an approach to determine which parts of the exhaust line could take advantage of the insulation process. There is growing interest in reducing pollutant emissions during the warm-up of the engine and the after-treatment systems, so thermal barrier coatings should be considered —along with other alternatives such as exhaust heaters, delayed fuel post-injections or early exhaust valves opening— in this regard.

With respect to pollutant emissions prediction of the engine model, specially CO and unburned hydrocarbons, an improvement of the neural network results may be considered by training the network with experimental data in dynamic conditions of speed and load, and at different test bench temperatures.

Chapter 6 References

[140] N. Hooftman, M. Messagie, J. Van Mierlo, and T. Coosemans. "A review of the European passenger car regulations – Real driving emissions vs local air quality". *Renewable and Sustainable Energy Reviews*, 86, (2018), pp. 1–21. issn: 1364-0321. doi: 10.1016/j.rser.2018.01.012 (cit. on p. 236).

[141] M. Williams and R. Minjares. "A technical summary of Euro 6/VI vehicle emission standards". *The International Council on Clean Transportation*, (2016). url: https://theicct.org/sites/default/files/publications/ICCT_Euro6-VI_briefing_jun2016.pdf (cit. on p. 236).

[142] G. D. Neely, J. V. Sarlashkar, and D. Mehta. "Diesel cold-start emission control research for 2015-2025 LEV III emissions". *SAE International Journal of Engines*, (2013). issn: 19463944. doi: 10.4271/2013-01-1301 (cit. on p. 236).

[143] G. D. Neely, D. Mehta, and J. Sarlashkar. "Diesel Cold-Start Emission Control Research for 2015-2025 LEV III Emissions - Part 2". *SAE International Journal of Engines*, (2014). issn: 19463944. doi: 10.4271/2014-01-1552 (cit. on p. 236).

[144] N. Cavina, G. Mancini, E. Corti, D. Moro, M. De Cesare, and F. Stola. "Thermal management strategies for SCR after treatment systems". *11th International Strategies Conference on Engines & Vehicles*. SAE International, 2013. doi: 10.4271/2013-24-0153 (cit. on p. 236).

[145] J. M. Luján, V. Bermúdez, P. Piqueras, and O. García-Afonso. "Experimental assessment of pre-turbo aftertreatment configurations in a single stage turbocharged diesel engine. Part 1: Steady-state operation". *Energy*, 80, (2015), pp. 599–613. issn: 03605442. doi: 10.1016/j.energy.2014.05.048 (cit. on p. 236).

[146] J. M. Luján, J. R. Serrano, P. Piqueras, and O. García-Afonso. "Experimental assessment of a pre-turbo aftertreatment configuration in a single stage turbocharged diesel engine. Part 2: Transient operation". *Energy*, 80, (2015), pp. 614–627. issn: 03605442. doi: 10.1016/j.energy.2014.12.017 (cit. on p. 236).

[147] R. Kamo and W. Bryzik. "Adiabatic turbocompound engine performance prediction". *1978 Automotive Engineering Congress and Exhibition*. SAE International, 1978. doi: 10.4271/780068 (cit. on p. 236).

[148] R. R. Sekar, R. Kamo, and J. C. Wood. "Advanced adiabatic diesel engine for passenger cars". *SAE International Congress and Exhibition*. SAE International, 1984. doi: 10.4271/840434 (cit. on p. 236).

[149] P. Olmeda, J. Martín, R. Novella, and D. Blanco-Cavero. "Assessing the optimum combustion under constrained conditions". *International Journal of Engine Research*, 21 (5), (2020), pp. 811–823. issn: 20413149. doi: 10.1177/1468087418814086 (cit. on p. 236).

[150] A. Kawaguchi, Y. Wakisaka, N. Nishikawa, H. Kosaka, H. Yamashita, C. Yamashita, H. Iguma, K. Fukui, N. Takada, and T. Tomoda. "Thermo-swing insulation to reduce heat loss from the combustion chamber wall of a diesel engine". *International Journal of Engine Research*, 20 (7), (2019), pp. 805–816. issn: 20413149. doi: 10.1177/1468087419852013 (cit. on p. 236).

[151] E. Gingrich, M. Tess, V. Korivi, P. Schihl, J. Saputo, G. M. Smith, S. Sampath, and J. Ghandhi. "The impact of piston thermal barrier coating roughness on high-load diesel operation". *International Journal of Engine Research*, Advance online publication, (2019). issn: 20413149. doi: 10.1177/1468087419893487 (cit. on p. 237).

[152] T. Powell, R. O'Donnell, M. Hoffman, Z. Filipi, E. H. Jordan, R. Kumar, and N. J. Killingsworth. "Experimental investigation of the relationship between thermal barrier coating structured porosity and homogeneous charge compression ignition engine combustion". *International Journal of Engine Research*, Advance online publication, (2019). issn: 20413149. doi: 10.1177/1468087419843752 (cit. on p. 237).

[153] J. Somhorst, M. Oevermann, M. Bovo, and I. Denbratt. "Evaluation of thermal barrier coatings and surface roughness in a single-cylinder light-duty diesel engine". *International Journal of Engine Research*, Advance online publication, (2019). issn: 20413149. doi: 10.1177/1468087419875837 (cit. on p. 237).

[154] A. Poubeau, A. Vauvy, F. Duffour, J. M. Zaccardi, G. de Paola, and M. Abramczuk. "Modeling investigation of thermal insulation approaches for low heat rejection Diesel engines using a conjugate heat transfer model". *International Journal of Engine Research*, 20 (1), (2019), pp. 92–104. issn: 20413149. doi: 10.1177/1468087418818264 (cit. on p. 237).

[155] S. Caputo, F. Millo, G. Boccardo, A. Piano, G. Cifali, and F. C. Pesce. "Numerical and experimental investigation of a piston thermal barrier coating for an automotive diesel engine application". *Applied Thermal Engineering*, 162, (2019), p. 114233. issn: 13594311. doi: 10.1016/j.applthermaleng.2019.114233 (cit. on p. 237).

[156] M. Ekström, A. Thibblin, A. Tjernberg, C. Blomqvist, and S. Jonsson. "Evaluation of internal thermal barrier coatings for exhaust manifolds". *Surface and Coatings Technology*, 272, (2015), pp. 198–212. issn: 02578972. doi: 10.1016/j.surfcoat.2015.04.005 (cit. on p. 237).

[157] A. Thibblin and U. Olofsson. "A test rig for evaluating thermal cyclic life and effectiveness of thermal barrier coatings inside exhaust manifolds". *WCX SAE World Congress Experience*. SAE International, 2019. doi: 10.4271/2019-01-0929 (cit. on p. 237).

[158] N. Kishi, H. Hashimoto, K. Fujimori, K. Ishii, and T. Komatsuda. "Development of the ultra low heat capacity and highly insulating (ULOC) exhaust manifold for ULEV". *International Congress & Exposition*. SAE International, 1998. doi: 10.4271/980937 (cit. on p. 237).

[159] S. Zidat and M. Parmentier. "Exhaust manifold design to minimize catalyst light-off time". *SAE 2003 World Congress & Exhibition*. SAE International, 2003. doi: 10.4271/2003-01-0940 (cit. on p. 237).

[160] J. R. Serrano, F. J. Arnau, J. Martin, M. Hernandez, and B. Lombard. "Analysis of Engine Walls Thermal Insulation: Performance and Emissions". *SAE 2015 World Congress & Exhibition*. SAE International, 2015. doi: 10.4271/2015-01-1660 (cit. on p. 237).

[161] J. M. Luján, J. R. Serrano, P. Piqueras, and B. Diesel. "Turbine and exhaust ports thermal insulation impact on the engine efficiency and aftertreatment inlet temperature". *Applied Energy*, 240, (2019), pp. 409–423. issn: 03062619. doi: 10.1016/j.apenergy.2019.02.043 (cit. on p. 238).

“A conclusion is the place where you got tired thinking.”

— Martin H. Fischer

Chapter 7

Concluding remarks

Contents

7.1 Introduction 268
7.2 VVT and thermal insulation comparison 268
7.3 Future works 275

7.1 Introduction

In previous chapter 4, chapter 5 and chapter 6 two different approaches to improve DOC efficiency by increasing the enthalpy of the exhaust gases have been explored. On the one hand, an active solution implementing a variable valve system. This solution allows a control of the exhaust temperature as seen in chapter 5 but incurring in a fuel penalty since the internal gases recirculation reduces the volumetric efficiency and thereby the engine performance. On the other hand, the thermal insulation of the exhaust line offers a passive solution to reduce heat losses between the cylinders exhaust ports and the after-treatment device, a DOC + DPF brick in the reference engine.

In this chapter, two combined solutions of the best thermal insulation case in chapter 6 and the two best VVT cases in chapter 5 are presented and discussed in terms of fuel efficiency and pollutant emissions reduction.

Finally, some remarks are made regarding future works and improvements of the work carried out in this thesis.

7.2 VVT and thermal insulation comparison

As a conclusion of the studies carried out in the previous chapters, two new cases have been simulated. Case 2b + insulation, depicted by an indigo colour trace and cross markers in Figure 7.1, is the combination of Case 2b in chapter 5 and *Full Exhaust* in chapter 6. Therefore, the exhaust and intake valves closing and opening events are controlled trying to maximise the exhaust temperature. Besides, the exhaust line is completely thermally insulated, so there is neither convective heat transfer from the exhaust gas to the exhaust ports, nor to the exhaust manifold, nor from the gas to the turbine volute. Case 3b + insulation, represented by a turquoise colour trace and up-triangles markers in Figure 7.1, is the combination of Case 3b in chapter 5 and *Full Exhaust* in chapter 6. This means that, the exhaust line

is fully insulated as in the previous case and both intake and exhaust valve events are controlled to maximise the exhaust temperature while restraining the injected fuel excess up a to maximum of 10 % with regard to the baseline calibration.

Figure 7.1 shows the turbine outlet temperature over the WLTC cycle with an engine start at a room temperature of 20 °C. For a better comparison, Case 2b, Case 3b from chapter 5 and *Full Exhaust* case chapter 6 are included in this and the following charts. It is observed how the exhaust insulation rapidly boosts the benefits of Case 2b and Case 3b solutions, so it is possible to reach peak temperatures over 600 °C. This high increase, specially in Case 2b + insulation is not so noticeable during the medium vehicle speed stage than at during the low speed stage. The explanation is that, recalling the exhaust temperature and closing/opening shift maps in section 5.3, the maximum intake delay/exhaust advance are feasible between 20 to 40 % load; thereby obtaining the maximum temperature difference with respect to the baseline valve timing at this zone of the engine operating map.

Once the DOC is active and warm, the control system only actuates over the valve timings when the temperature at DOC outlet falls down the light-off threshold. From this point until the end of the cycle, and excepting these few situations, the valve timings is the same as in the baseline valvetrain. Consequently, the temperature difference observed in Case 2b + insulation and Case 3b + insulation is due to the thermal insulation of the exhaust line. This can be observed in Figure 7.1 (bottom) where the blue area representing *Full Exhaust* case overlaps and matches the area of the two new cases.

As proceeded in chapter 5, it is possible to translate the turbine outlet temperature into Figure 7.2. In this chart, only the low vehicle speed stage of the WLTC is considered and it shows how much time the turbine outlet temperature is above a certain value for each case. It can be observed that *Full Exhaust* case allows higher temperatures than Case 2b and Case 3b. With respect to Case 2b, *Full Exhaust* reaches temperatures higher than Case 2b over 100 seconds, which represents almost a 20 % of the low speed stage. Case 2b + insulation and Case 3b + insulation take advantage of the exhaust thermal insulation and both allow obtaining higher temperatures. Case 2b

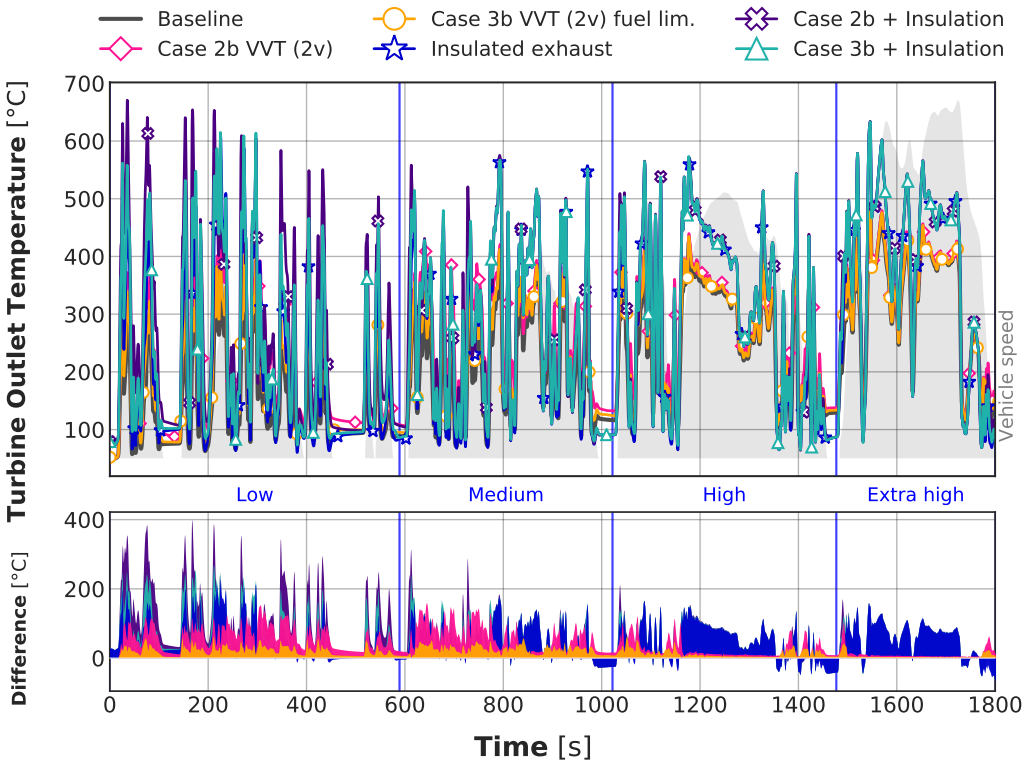

Figure 7.1: *Turbine outlet temperature, WLTC at a room temperature of* 20 °C.

+ insulation is over Case 2b for about 350 seconds (60 % of the low speed stage duration); while Case 3b + insulation is over Case 3b for about 400 seconds, which is around 70 % of the duration of this low speed stage. It must be mentioned that Case 3b + insulation, that supposes a fuel penalty improvement compared to Case 2b, performs better than Case 2b for about 170 seconds.

Figure 7.3 shows the time reduction to reach the DOC light-off temperature for each case. The values are relative to the time it takes for the baseline case in percent. Even though the light-off temperature, which is above 200 °C in this diesel catalyst, has been reached during the low speed stage at some points as shown in Figure 7.1, it is not since the medium vehicle speed stage when this temperature is maintained for a longer period. In Figure 7.3, both Case 2b + insulation and Case 3b + insulation reduce the time to reach light-off in the same way as *Full Exhaust*, about a 23 % quicker than in the baseline case. This similarity between both cases is due to the

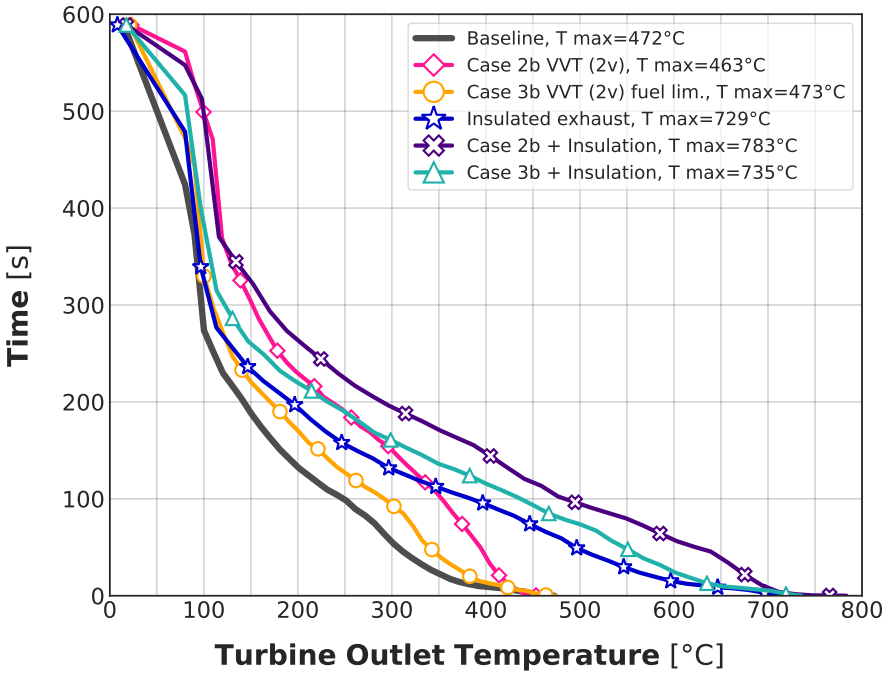

Figure 7.2: Time above a certain temperature at turbine outlet considering the low speed stage of the WLTC, room temperature of 20 °C.

thermal insulation, that prevent heat losses during the first driving period in this medium speed stage and heats the DOC quickly.

Regarding fuel economy, the thermal insulation of the exhaust system reduces the fuel penalty of both VVT cases. Since the insulation achieves exhaust temperatures greater than 210 °C for a longer time, then the control system reduces the time in which the exhaust and intake events are advanced and delayed. Consequently, the fuel penalty gets reduced by 8 % from Case 2b to Case 2b + insulation over the low speed stage and by 3 % over the entire WLTC. The fuel consumption difference between Case 2b and Case 2b + insulation is negligible since Case 2b is already limiting the maximum fuel penalty.

In terms of NO_x formation, a increase in Case 2b + insulation and Case 3b + insulation is observed during the low speed stage. In Case 2b and Case 3b, the application of an intake delay with a symmetrical exhaust advance leads to a NO_x reduction by increasing the IGR. With the exhaust system

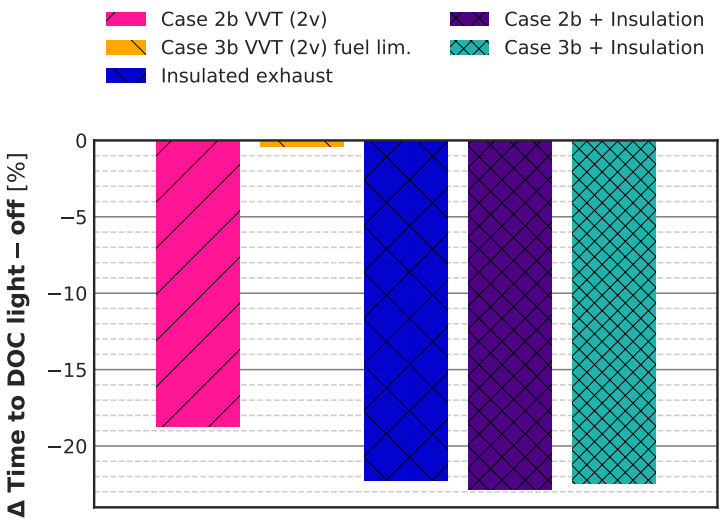

Figure 7.3: Time to reach DOC light-off temperature, engine start at 20 °C ambient temperature. Percentage variation compared to the baseline case.

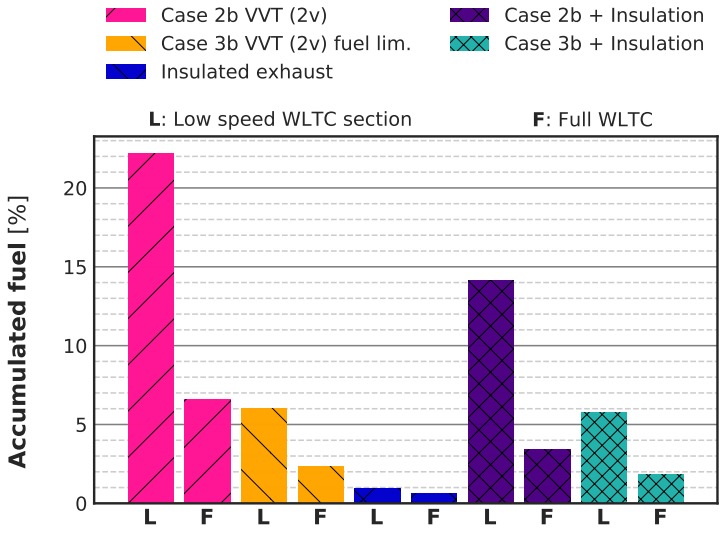

Figure 7.4: Accumulated fuel consumption, engine start at 20 °C ambient temperature. Percentage variation compared to the baseline case.

completely insulated, the VVT control system is applying the baseline valve timings for a longer time, presenting a disadvantage in terms of NO_x formation at low engine speed. In this way, Case 3b goes from a 17.5 % reduction

over the first stage of the WLTC to no reduction with the thermal insulation. In a similar way, Case 3b passes from a 14 % reduction to a 6.5 % reduction during this first stage. In this case, the more limited application of the VVT strategy due to the fuel restriction and the lower exhaust temperature gain compared to Case 3b + insulation, results in a smaller increase in NO_x emissions compared to the latter case.

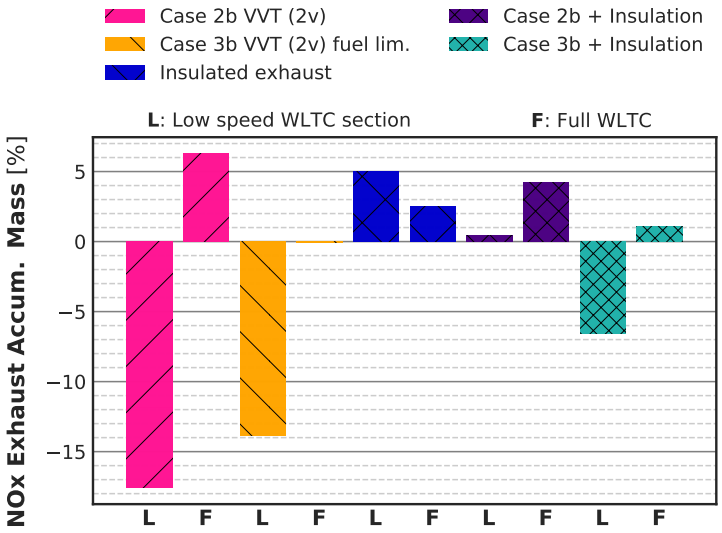

Figure 7.5: Accumulated tailpipe NO_x emissions, engine start at 20 °C ambient temperature. Percentage variation compared to the baseline case.

In terms of CO and HC tailpipe emissions, the addition of the exhaust thermal insulation to the previously discussed VVT strategies offers a greater reduction of these pollutant emissions. Figure 7.6 illustrates the percent variation with respect to the baseline CO tailpipe emissions. The longer DOC activation period leads to a CO reduction from 46 % in Case 2b to 62 % in Case 2b + insulation. Considering the entire WLTC cycle, the reduction is about 61 %; since, once the DOC is warm, the valve timings of the baseline case are applied and the major part. Consequently, even though there is a DOC temperature increment due to the thermal insulation, there is less temperature increment due to the VVT settings than in Case 2b. The same situation is observed with regard to Case 3b + insulation. In this case the 18 % CO emissions reduction in Case 2b turns into a 44 % reduction with the addition of the exhaust insulation during the low speed stage. Consid-

ering the complete cycle, an increment in this reduction is also observed from 23 % to almost 34 %.

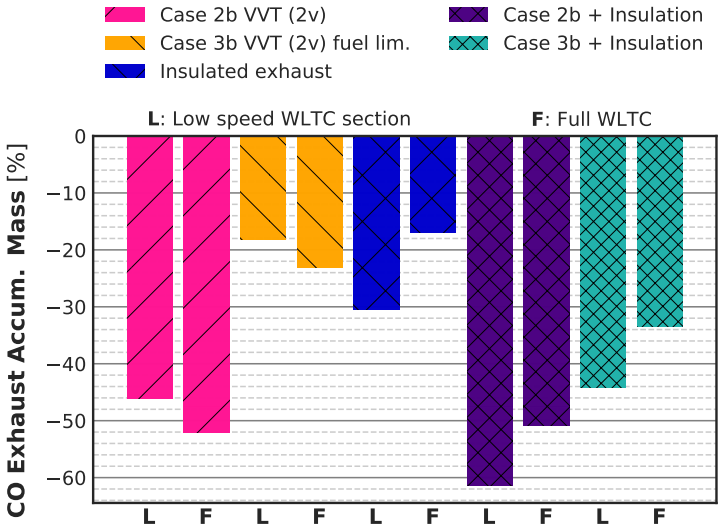

Figure 7.6: Accumulated CO emissions at DOC outlet, engine start at 20 °C ambient temperature. Percentage variation compared to the baseline case.

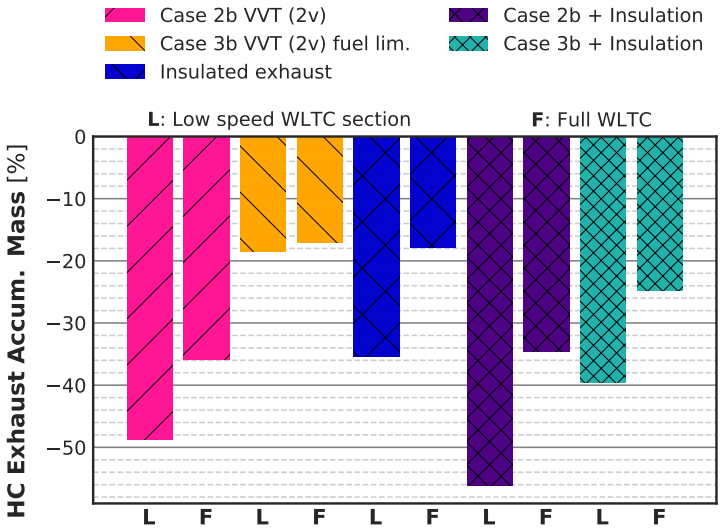

Figure 7.7: Accumulated HC emissions at DOC outlet, engine start at 20 °C ambient temperature. Percentage variation compared to the baseline case.

The reduction in terms of HC tailpipe emissions is shown in Figure 7.7.

Similarly to CO emissions, the greater exhaust temperature achieved by the addition of the thermal insulation to the VVT strategies leads to a 56 % reduction in Case 2b + insulation over the first stage of the WLTC. Analogously, Case 3b + insulation achieves a reduction in HC emissions by 40 % at the end of the low speed stage of the type approval cycle. Considering the complete cycle, the reduction is about 25 %, representing 8 % less emissions than in Case 3b.

7.3 Future works

From the study carried on in this chapter, it is possible to reduce CO and HC emissions down to 40 % and slightly reduce NO_x emissions a 6 % with a minimum fuel penalty of 6 % by combining an intake delay and exhaust advance control with a thermal insulation of the exhausts ports, exhaust manifold and turbine volute (Case 3b + insulation).

Even though the adiabatic assumption of the exhaust line is not realistic it allows analysing the maximum benefit of the exhaust thermal insulation. A study including real thermal barrier coatings (TBC) like YSZ and a multilayer design of the exhausts ports and the exhaust manifold considering aluminium, air and TBC should be developed in order to account for an approximation of the results presented in this chapter.

Regarding the engine model, new features and improvements have to be implemented in future projects. Some of the improvements that can be implemented to enrich the results presented in this thesis are:

- A better prediction of pollutant emissions, specially CO and HC whose predictions are based on a neural network. This network can be improved by including new inputs and training data in order to asses a better prediction in transient conditions.
- Including both LNT and SCR models into the engine model means having a significant feature for engine modelling according to the new EURO 6d emissions regulation. Furthermore, it will give an extra di-

mension to the VVT study carried on in this work, since the exhaust enthalpy increase could be evaluated according to the performance of this two deNO_x devices.

- The addition of elements derived from the electrification of new thermal engines like electric heaters, battery cells and the modelling of the energy management of these hybrid or mild hybrid vehicles.
- This is not a requirement for the studies carried out in this thesis. However, future works should be centred on assessing the real time simulation of the complete engine by developing a mean-value model of this.

Bibliography

[1] J. Martin, F. Arnau, P. Piqueras, and Á. Auñón. "Development of an Integrated Virtual Engine Model to Simulate New Standard Testing Cycles". *WCX World Congress Experience*. SAE International, 2018. doi: 10.4271/2018-01-1413 (cit. on p. xi).

[2] F. J. Arnau, J. Martín, B. Pla, and Á. Auñón. "Diesel engine optimization and exhaust thermal management by means of variable valve train strategies". *International Journal of Engine Research*, Advance online publication, (2020). issn: 20413149. doi: 10.1177/1468087419894804 (cit. on p. xi).

[3] F. J. Arnau, J. Martín, P. Piqueras, and Á. Auñón. "Effect of the exhaust thermal insulation on the engine efficiency and the exhaust temperature under transient conditions". *International Journal of Engine Research*, Advance online publication, (2020). doi: 10.1177/1468087420961206 (cit. on p. xi).

[4] J. R. Serrano, F. J. Arnau, J. Martín, and Á. Auñón. "Development of a Variable Valve Actuation Control to Improve Diesel Oxidation Catalyst Efficiency and Emissions in a Light Duty Diesel Engine". *Energies*, 13 (17), (2020), p. 4561. doi: 10.3390/en13174561 (cit. on p. xi).

[5] International Energy Agency (IEA). *Global car sales by key markets, 2005-2020*. Accessed 2020-12-10 at https://www.iea.org/data-and-statistics/charts/global-car-sales-by-key-markets-2005-2020. 2020 (cit. on p. 2).

[6] J. S. Gaffney and N. A. Marley. "The impacts of combustion emissions on air quality and climate – From coal to biofuels and beyond". *Atmospheric Environment*, 43 (1), (2009), pp. 23 –36. issn: 1352-2310. doi: https://doi.org/10.1016/j.atmosenv.2008.09.016 (cit. on p. 2).

[7] J. Cook et al. "Consensus on consensus: a synthesis of consensus estimates on human-caused global warming". *Environmental Research*

Letters, 11 (4), (2016), p. 048002. doi: 10.1088/1748-9326/11/4/048002 (cit. on p. 2).

[8] CAIT data: Climate Watch. *GHG Emissions*. Accessed 2020-12-05 at https://www.climatewatchdata.org/ghg-emissions. World Resources Institute. 2020 (cit. on p. 2).

[9] H. Ritchie and M. Roser. *Emissions by sector*. Accessed 2020-12-04 at https://ourworldindata.org/emissions-by-sector. Our World in Data. September, 2020 (cit. on p. 2).

[10] N. Lenssen, G. Schmidt, J. Hansen, M. Menne, A. Persin, R. Ruedy, and D. Zyss. "Improvements in the GISTEMP uncertainty model". *J. Geophys. Res. Atmos.*, 124 (12), (2019), pp. 6307–6326. doi: 10.1029/2018JD029522 (cit. on p. 3).

[11] GISTEMP Team. NASA Goddard Institute for Space Studies. *GISS Surface Temperature Analysis (GISTEMP), version 4*. Dataset accessed 2020-12-5 at https://data.giss.nasa.gov/gistemp/. 2020 (cit. on p. 3).

[12] Council of European Union. "Regulation (EU) 2019/631 of the European Parliament and of the Council of 17 April 2019 setting CO2 emission performance standards for new passenger cars and for new light commercial vehicles, and repealing Regulations (EC) No 443/2009 and (EU) No 510/2011". *Official Journal of the European Union*, L 111, (2019), pp. 13–53. url: http://data.europa.eu/eli/reg/2019/631/oj (cit. on p. 4).

[13] European Comission. *Standard Eurobarometer 92. Public opinion in the European Union*. Accessed 2020-12-7 at https://ec.europa.eu/commfrontoffice/publicopinion/index.cfm/ResultDoc/download/DocumentKy/88848. November, 2019 (cit. on p. 4).

[14] European Comission. *Standard Eurobarometer 92. Europeans' opinions about the European Union's priorities*. Accessed 2020-12-7 at https://ec.europa.eu/commfrontoffice/publicopinion/index.cfm/ResultDoc/download/DocumentKy/90252. November, 2019 (cit. on p. 4).

[15] M. Krzyzanowski, B. Kuna-Dibbert, and J. Schneider. *Engine Emissions Measurement Handbook*. WHO Regional Office for Europe, 2005. isbn: 92-890-1373-7 (cit. on p. 4).

[16] Council of European Union. "Directive 2008/50/EC of the European Parliament and of the Council of 21 May 2008 on ambient air quality and cleaner air for Europe". *Official Journal of the European Union*, L 152, (2008). url: https://eur-lex.europa.eu/eli/dir/2008/50/2015-09-18 (cit. on p. 4).

[17] Ministère de l'Environnement, de l'Énergie et de la Mer. "Décret nº 2016-847 du 28 juin 2016 relatif aux zones à circulation restreinte." *Journal Officiel de la République Française*, 150 (3), (2016). url: https://www.legifrance.gouv.fr/jorf/id/JORFTEXT000032790919 (cit. on p. 4).

[18] The CLARS Platform. *Urban Access Regulations in Europe*. Accessed 2020-12-8 at https://urbanaccessregulations.eu/countries-mainmenu-147/france/paris. Sadler Consultants Ltd. 2017 (cit. on p. 4).

[19] X. Mosquet, A. Arora, A. Xie, and M. Renner. *Who Will Drive Electric Cars to the Tipping Point?* Accessed 2020-12-05 at https://www.bcg.com/publications/2020/drive-electric-cars-to-the-tipping-point. Boston Consulting Group. 2020 (cit. on pp. 4, 5).

[20] G. Crabtree. "The coming electric vehicle transformation". *Science*, 366 (6464), (2019), pp. 422–424. issn: 0036-8075. doi: 10.1126/science.aax0704 (cit. on p. 5).

[21] International Energy Agency (IEA). *Global EV Outlook 2020*. Accessed 2020-12-10 at https://www.iea.org/reports/global-ev-outlook-2020. 2020 (cit. on p. 5).

[22] M. Adachi and H. Nakamura. *Engine Emissions Measurement Handbook*. Horiba Ltd., 2013. doi: 10.4271/jpf-hor-002 (cit. on p. 18).

[23] A. Maiboom, X. Tauzia, and J. F. Hétet. "Infuence of high rates of supplemental cooled EGR on NOx and PM emissions of an automotive HSDI diesel engine using an LP EGR loop". *International Journal of Energy Research*, 32 (15), (2008), pp. 1383–1398. issn: 0363907X. doi: 10.1002/er.1455. url: https://onlinelibrary.wiley.com/doi/abs/10.1002/er.1455 (cit. on p. 18).

[24] F. Vera. "Efecto de la recirculación del gas de escape en el proceso de la renovación de la carga en motores turbo-sobrealimentados". PhD thesis. Universitat Politècnica de València, 2004 (cit. on p. 18).

[25] J. Pavlovic, B. Ciuffo, G. Fontaras, V. Valverde, and A. Marotta. "How much difference in type-approval CO2 emissions from passenger cars in Europe can be expected from changing to the new test procedure (NEDC vs. WLTP)?" *Transportation Research Part A: Policy and Practice*, 111, (2018), pp. 136–147. issn: 09658564. doi: 10.1016/j.tra.2018.02.002 (cit. on p. 23).

[26] J. T. Messer, N. N. Clark, and D. W. Lyons. "Measurement delays and modal analysis for a heavy duty transportable emissions testing laboratory". *International Congress and Exposition*. SAE International, 1995. doi: 10.4271/950218 (cit. on p. 25).

[27] G. Konstantas and A. Stamatelos. "Quality assurance of exhaust emissions test data". *Proceedings of the Institution of Mechanical Engineers, Part D: Journal of Automobile Engineering*, 218 (8), (2004), pp. 901–914. issn: 09544070. doi: 10.1243/0954407041581075 (cit. on p. 25).

[28] J. D. Pakko. "Reconstruction of time-resolved vehicle emissions measurements by deconvolution". *SAE International Journal of Fuels and Lubricants*, 2 (1), (2009), pp. 697–707. issn: 19463952. doi: 10.4271/2009-01-1513 (cit. on p. 25).

[29] Council of European Union. "Directive 2005/55/EC of the European Parliament and of the Council of 28 September 2005 on the approximation of the laws of the Member States relating to the measures to be taken against the emission of gaseous and particulate pollutants from compression-ignition engines for use in vehicles, and the emission of gaseous pollutants from positive-ignition engines fuelled with natural gas or liquefied petroleum gas for use in vehicles". *Official Journal of the European Union*, L 275, (2005). url: http://data.europa.eu/eli/dir/2005/55/oj (cit. on p. 26).

[30] A. Moratal. "Experimental Analysis of Thermal Management Influence on Performance and Emissions in Diesel Engines at low ambient Temperature". PhD thesis. Universitat Politècnica de València, 2018 (cit. on p. 27).

[31] K. Robinson, S. Ye, Y. Yap, and S. T. Kolaczkowski. "Application of a methodology to assess the performance of a full-scale diesel oxidation catalyst during cold and hot start NEDC drive cycles". *Chemical Engineering Research and Design*, 91 (7), (2013), pp. 1292–1306. issn: 02638762. doi: 10.1016/j.cherd.2013.02.022 (cit. on p. 28).

[32] CMT – Motores Térmicos, Universitat Politècnica de València. *OpenWAM*. Accessed 2020-10-26 at http://openwam.webs.upv.es/docs/. 2016 (cit. on p. 39).

[33] J. M. Corberán. "Contribución al modelado del proceso de renovación de la carga en motores de combustión interna alternativos." PhD thesis. Universitat Politècnica de València, 1984 (cit. on p. 39).

[34] R. S. Benson and N. D. Whitehouse. *Internal Combustion Engines: A Detailed Introduction to the Thermodynamics of Spark and Compression Ignition Engines, Their Design and Development, Volume 1*. 1979. isbn: 1483140024 (cit. on p. 39).

[35] J. M. Desantes, M. D. Chust, and J. Llorens. "Análisis comparativo de métodos numéricos para la resolución del flujo no estacionario en colectores de motores de combustión interna alternativos". *II Congreso de Métodos Numéricos en Ingeniería*. 1993 (cit. on p. 39).

[36] F. Payri, J. Galindo, J. R. Serrano, and F. J. Arnau. "Analysis of numerical methods to solve one-dimensional fluid-dynamic governing equations under impulsive flow in tapered ducts". *International Journal of Mechanical Sciences*, 46 (7), (2004), pp. 981 –1004. issn: 0020-7403. doi: https://doi.org/10.1016/j.ijmecsci.2004.07.014 (cit. on p. 39).

[37] F. Payri, J. M. Desantes, and J. M. Corberán. "A quasi-steady model on gas exchange process, some results". *Motor Sympo'88*. 1988 (cit. on p. 39).

[38] F. Payri, J. Benajes, and M. Reyes. "Modelling of supercharger turbines in internal-combustion engines". *International Journal of Mechanical Sciences*, 38 (8-9), (1996), pp. 853–869. issn: 00207403. doi: 10.1016/0020-7403(95)00105-0 (cit. on p. 39).

[39] F. Payri, J. Galindo, and J. R. Serrano. "Variable geometry turbine modelling and control for turbocharged diesel engines transient operation". *THIESEL 2000*. Thermo- and Fluid-dynamic Processes in Diesel Engines, 2000. doi: 10.1243/09544070260137507 (cit. on p. 39).

[40] M. Á. Reyes. "Contribución al modelado del proceso de transferencia de calor en colectores de escape de motores alternativos". PhD thesis. Universitat Politècnica de València, 1994 (cit. on pp. 39, 49).

[41] J. R. Serrano. "Análisis y modelado del transitorio de carga en motores turboalimentados de encendido por compresión". PhD thesis. Universitat Politècnica de València, 1999 (cit. on p. 39).

[42] J Galindo, J. R. Serrano, H Climent, and F. J. Arnau. "New one-dimensional fluid-dynamic model for automotive intercoolers". *Conference A proceeding of 8th European Automotive Congress (EAEC)*. 2001 (cit. on p. 39).

[43] J. Galindo. "Diseño de uniones de colectores de escape de motores alternativos". PhD thesis. Universitat Politècnica de València, 1998 (cit. on p. 39).

[44] F. Payri, E. Reyes, and J. R. Serrano. "A model for load transients of turbocharged diesel engines". *International Congress & Exhibition*. SAE International, 1999. doi: 10.4271/1999-01-0225 (cit. on p. 39).

[45] J. Benajes, J. M. Luján, V. Bermúdez, and J. R. Serrano. "Modelling of turbocharged diesel engines in transient operation. Part 1: Insight into the relevant physical phenomena". *Proceedings of the Institution of Mechanical Engineers, Part D: Journal of Automobile Engineering*, 216 (5), (2002), pp. 431–441. issn: 09544070. doi: 10.1243/0954407021529237 (cit. on p. 39).

[46] F. Payri, J. Benajes, J. Galindo, and J. R. Serrano. "Modelling of turbocharged diesel engines in transient operation. Part 2: Wave action models for calculating the transient operation in a high speed direct injection engine". *Proceedings of the Institution of Mechanical Engineers, Part D: Journal of Automobile Engineering*, 216 (6), (2002), pp. 479–493. doi: 10.1243/09544070260137507 (cit. on p. 39).

[47] J. Galindo, J. R. Serrano, F. J. Arnau, and P. Piqueras. "Description of a semi-independent time discretization methodology for a one-dimensional gas dynamics model". *Journal of Engineering for Gas Turbines and Power*, 131 (3), (2009). 034504. issn: 07424795. doi: 10.1115/1.2983015 (cit. on p. 43).

[48] R. J. LeVeque. *Finite Volume Methods for Hyperbolic Problems*. Cambridge University Press, 2002. doi: 10.1017/cbo9780511791253 (cit. on p. 43).

[49] S. K. Godunov. "A difference method for numerical calculation of discontinuous solutions of the equations of hydrodynamics [English title page]". *Matematicheskii Sbornik*, (1959) (cit. on p. 43).

[50] B. van Leer. "Towards the ultimate conservative difference scheme. V. A second-order sequel to Godunov's method". *Journal of Computational Physics*, 32 (1), (1979), pp. 101–136. issn: 10902716. doi: 10.1016/0021-9991(79)90145-1 (cit. on p. 43).

[51] E. F. Toro, M. Spruce, and W. Speares. "Restoration of the contact surface in the HLL-Riemann solver". *Shock Waves*, 4 (1), (1994), pp. 25–34. issn: 1432-2153. doi: 10.1007/BF01414629 (cit. on p. 43).

[52] R. Courant, K. Friedrichs, and H. Lewy. "Über die partiellen Differenzengleichungen der mathematischen Physik". *Mathematische Annalen*, 100 (1), (1928), pp. 32–74. issn: 1432-1807. doi: 10.1007/BF01448839 (cit. on p. 45).

[53] C. Depcik and D. Assanis. "A universal heat transfer correlation for intake and exhaust flows in an spark-ignition internal combustion engine". *SAE 2002 World Congress & Exhibition*. SAE International, 2002. doi: 10.4271/2002-01-0372 (cit. on p. 49).

[54] R. Santos. "Estudio del aprovechamiento de la energía de los gases de escape en motores diésel". PhD thesis. Universitat Politècnica de València, 1999 (cit. on p. 49).

[55] S. W. Churchill and M. Bernstein. "A correlating equation for forced convection from gases and liquids to a circular cylinder in cross-flow". *Journal of Heat Transfer*, 99 (2), (1977), pp. 300–306. issn: 15288943. doi: 10.1115/1.3450685 (cit. on p. 49).

[56] V. Dolz. "Contribución al Modelado de la transmisión de calor en los MCIA y su aplicación en el aprovechamiento energético de los gases de escape durante los transitorios de carga". PhD thesis. Universitat Politècnica de València, 2006 (cit. on p. 49).

[57] J. R. Serrano, F. J. Arnau, L. M. García-Cuevas, A. Dombrovsky, and H. Tartoussi. "Development and validation of a radial turbine efficiency and mass flow model at design and off-design conditions". *Energy Conversion and Management*, (2016). issn: 01968904. doi: 10.1016/j.enconman.2016.09.032 (cit. on p. 49).

[58] J. Galindo, R. Navarro, L. M. García-Cuevas, D. Tarí, H. Tartoussi, and S. Guilain. "A zonal approach for estimating pressure ratio at compressor extreme off-design conditions". *International Journal of Engine Research*, 20 (4), (2019), pp. 393–404. doi: 10.1177/1468087418754899 (cit. on p. 49).

[59] J. Galindo, A. Tiseira, R. Navarro, D. Tarí, H. Tartoussi, and S. Guilain. "Compressor Efficiency Extrapolation for 0D-1D Engine Simulations". SAE International, 2016. doi: 10.4271/2016-01-0554 (cit. on p. 49).

[60] J. R. Serrano, P. Olmeda, F. J. Arnau, and V. Samala. "A holistic methodology to correct heat transfer and bearing friction losses from hot turbocharger maps in order to obtain adiabatic efficiency of the turbomachinery". *International Journal of Engine Research*, 21 (8), (2020), pp. 1314–1335. issn: 20413149. doi: 10.1177/1468087419834194 (cit. on p. 49).

[61] O. Leufvén. "Modeling for control of centrifugal compressors". PhD thesis. Linköpings universitet, 2013. url: https://citeseerx.ist.psu.edu/viewdoc/download?doi=10.1.1.393.817&rep=rep1&type=pdf (cit. on p. 49).

[62] G. Martin, V. Talon, P. Higelin, A. Charlet, and C. Caillol. "Implementing turbomachinery physics into data map-based turbocharger models". *SAE World Congress & Exhibition*. SAE International, 2009. doi: 10.4271/2009-01-0310 (cit. on p. 49).

[63] J. P. Jensen, A. F. Kristensen, S. C. Sorenson, N. Houbak, and E. Hendricks. "Mean value modeling of a small turbocharged diesel engine". SAE International, 1991. doi: 10.4271/910070 (cit. on p. 49).

[64] P. Olmeda, V. Dolz, F. J. Arnau, and M. A. Reyes-Belmonte. "Determination of heat flows inside turbochargers by means of a one dimensional lumped model". *Mathematical and Computer Modelling*, 57 (7-8), (2013), pp. 1847–1852. issn: 08957177. doi: 10.1016/j.mcm.2011.11.078 (cit. on p. 50).

[65] F. Payri, P. Olmeda, F. J. Arnau, A. Dombrovsky, and L. Smith. "External heat losses in small turbochargers: Model and experiments". *Energy*, 71, (2014), pp. 534–546. issn: 03605442. doi: 10.1016/j.energy.2014.04.096 (cit. on p. 50).

[66] J. R. Serrano, P. Olmeda, A. Tiseira, L. M. García-Cuevas, and A. Lefebvre. "Theoretical and experimental study of mechanical losses inautomotive turbochargers". *Energy*, 55, (2013), pp. 888–898. issn: 03605442. doi: 10.1016/j.energy.2013.04.042 (cit. on p. 51).

[67] F. A. Williams. *Combustion Theory (2nd Ed.)* Benjamin-Cummings Publishing Co., 1985. isbn: 0805398015 (cit. on p. 51).

[68] M. Lapuerta, R. Ballesteros, and J. R. Agudelo. "Effect of the gas state equation on the thermodynamic diagnostic of diesel combustion". *Applied Thermal Engineering*, 26 (14-15), (2006), pp. 1492–1499. issn: 13594311. doi: 10.1016/j.applthermaleng.2006.01.001 (cit. on p. 52).

[69] C. D. Rakopoulos, G. M. Kosmadakis, and E. G. Pariotis. "Critical evaluation of current heat transfer models used in CFD in-cylinder engine simulations and establishment of a comprehensive wall-function formulation". *Applied Energy*, 85 (5), (2010), pp. 1612–1630. issn: 03062619. doi: 10.1016/j.apenergy.2009.09.029 (cit. on p. 52).

[70] F. Payri, A. Broatch, J. R. Serrano, L. F. Rodríguez, and A. Esmorís. "Study of the potential of intake air heating in automotive DI Diesel engines". *SAE 2006 World Congress & Exhibition*. SAE International, 2006. doi: 10.4271/2006-01-1233 (cit. on p. 52).

[71] C. D. Rakopoulos, G. M. Kosmadakis, A. M. Dimaratos, and E. G. Pariotis. "Investigating the effect of crevice flow on internal combustion engines using a new simple crevice model implemented in a CFD code". *Applied Energy*, 88 (1), (2011), pp. 111–126. issn: 03062619. doi: 10.1016/j.apenergy.2010.07.012 (cit. on p. 52).

[72] F. Payri, P. Olmeda, J. Martín, and A. García. "A complete 0D thermodynamic predictive model for direct injection diesel engines". *Applied Energy*, 88 (12), (2011), pp. 4632–4641. issn: 03062619. doi: 10.1016/j.apenergy.2011.06.005 (cit. on p. 53).

[73] B. Tormos, J. Martín, R. Carreño, and L. Ramírez. "A general model to evaluate mechanical losses and auxiliary energy consumption in reciprocating internal combustion engines". *Tribology International*, 123, (2018), pp. 161–179. issn: 0301679X. doi: 10.1016/j.triboint.2018.03.007 (cit. on pp. 53, 104, 105).

[74] S. Furuhama and T. Tada. "On the Flow of Gas Through the Piston-Rings : 1st Report, The Discharge Coefficient and Temperature of Leakage Gas". *Bulletin of JSME*, 4 (16), (1961), pp. 684–690. doi: 10.1299/jsme1958.4.684 (cit. on p. 54).

[75] R. Payri, F. J. Salvador, J. Gimeno, and G. Bracho. "A new methodology for correcting the signal cumulative phenomenon on injection rate measurements". *Experimental Techniques*, 32, (2008), pp. 46–49. issn: 07328818. doi: 10.1111/j.1747-1567.2007.00188.x (cit. on p. 60).

[76] I. I. Vibe. "Brennverlauf und Kreisprozess von Verbrennungsmotoren". *VEB Verlag Technik*, (1970) (cit. on p. 65).

[77] F. G. Chmela and G. C. Orthaber. "Rate of heat release prediction for direct injection diesel engines based on purely mixing controlled combustion". *International Congress & Exposition*. SAE International, 1999. doi: 10.4271/1999-01-0186 (cit. on p. 65).

[78] J. Arrègle, J. J. López, J. M. García, and C. Fenollosa. "Development of a zero-dimensional Diesel combustion model. Part 1: Analysis of the quasi-steady diffusion combustion phase". *Applied Thermal Engineering*, 23 (11), (2003), pp. 1301–1317. issn: 13594311. doi: 10.1016/S1359-4311(03)00079-6 (cit. on p. 65).

[79] J. Arrègle, J. J. López, J. M. García, and C. Fenollosa. "Development of a zero-dimensional Diesel combustion model: Part 2: Analysis of the transient initial and final diffusion combustion phases". *Applied Thermal Engineering*, 23 (11), (2003), pp. 1319–1331. issn: 13594311. doi: 10.1016/S1359-4311(03)00080-2 (cit. on p. 65).

[80] A. A. Amsden, T. D. Butler, P. J. O'Rourke, and J. D. Ramshaw. "KIVA-A comprehensive model for 2-D and 3-D engine simulations". *SAE International Congress and Exposition*. SAE International, 1985. doi: 10.4271/850554 (cit. on p. 65).

[81] A. A. Amsden. "KIVA-3V: A Block-Structured KIVA Program for Engines with Vertical or Canted Valves". *LA Report*. Los Alamos National Laboratory, 1997 (cit. on p. 65).

[82] M. A. Gonzalez D., Z. W. Lian, and R. D. Reitz. "Modeling diesel engine spray vaporization and combustion". *International Congress and Exposition*. SAE International, 1992. doi: 10.4271/920579 (cit. on p. 65).

[83] S. C. Kong, Z. Han, and R. D. Reitz. "The development and application of a diesel ignition and combustion model for multidimensional engine simulation". *International Congress and Exposition*. SAE International, 1995. doi: 10.4271/950278 (cit. on p. 65).

[84] Y. Yi and R. D. Reitz. "Modeling the effect of primary atomization on diesel engine emissions". *SAE 2003 World Congress & Exhibition*. SAE International, 2003. doi: 10.4271/2003-01-1041 (cit. on p. 65).

[85] J. Arrègle, J. J. López, J. Martín, and E. M. Mocholí. "Development of a mixing and combustion zero-dimensional model for diesel engines". *SAE 2006 World Congress & Exhibition*. SAE International, 2006. doi: 10.4271/2006-01-1382 (cit. on p. 66).

[86] J. M. Desantes, J. Arrègle, J. J. López, and A. Cronhjort. "Scaling laws for free turbulent gas jets and diesel-like sprays". *Atomization and Sprays*, 16 (4), (2006), pp. 443–474. issn: 10445110. doi: 10.1615/AtomizSpr.v16.i4.60 (cit. on pp. 66, 69).

[87] V. Hamosfakidis and R. D. Reitz. "Optimization of a hydrocarbon fuel ignition model for two single component surrogates of diesel fuel". *Combustion and Flame*, 132 (3), (2003), pp. 433–450. issn: 00102180. doi: 10.1016/S0010-2180(02)00489-3 (cit. on p. 67).

[88] J. C. Livengood and P. C. Wu. "Correlation of autoignition phenomena in internal combustion engines and rapid compression machines". *Symposium (International) on Combustion*, 5 (1), (1955), pp. 347–356. issn: 00820784. doi: 10.1016/S0082-0784(55)80047-1 (cit. on p. 67).

[89] F. Payri, P. Olmeda, J. Martin, and R. Carreño. "A New Tool to Perform Global Energy Balances in DI Diesel Engines". *SAE International Journal of Engines*, 7 (1), (2014), pp. 43–59. issn: 19463944. doi: 10.4271/2014-01-0665 (cit. on p. 72).

[90] F. Payri, J. Arrègle, J. Javier López, and E. Mocholí. "Diesel NOx modeling with a reduction mechanism for the initial NOx coming from EGR or re-entrained burned gases". *SAE World Congress & Exhibition*. SAE International, 2008. doi: 10.4271/2008-01-1188 (cit. on p. 76).

[91] Y. B. Zeldovich. "25. The Oxidation of Nitrogen in Combustion and Explosions". *Selected Works of Yakov Borisovich Zeldovich, Volume I*. Princeton University Press, 2015. doi: 10.1515/9781400862979.364 (cit. on p. 76).

[92] F. Posada, A. Isenstadt, and H. Badshah. *Estimated cost of diesel emissions-control technology to meet future california low NOx standards in 2024 and 2027*. Tech. rep. International Council on Clean Transportation, 2020. url: https://theicct.org/sites/default/files/publications/HDV-emissions-compliance-cost-may2020.pdf (cit. on p. 82).

[93] *Future Light and Heavy Duty ICE Powertrain Technologies*. Tech. rep. ERTRAC Working Group, 2016. url: https://www.ertrac.org/uploads/documentsearch/id11/Future%20Light-duty%20Powertrain%20Technologies%20and%20Fuels.pdf (cit. on p. 82).

[94] F. Payri, F. J. Arnau, P. Piqueras, and M. J. Ruiz. "Lumped Approach for Flow-Through and Wall-Flow Monolithic Reactors Modelling for Real-Time Automotive Applications". *WCX World Congress Experience*. SAE International, 2018. doi: 10.4271/2018-01-0954 (cit. on pp. 82, 86–89).

[95] J. Galindo, J. R. Serrano, P. Piqueras, and Ó. García-Afonso. "Heat transfer modelling in honeycomb wall-flow diesel particulate filters". *Energy*, 43 (1), (2012), pp. 201–213. issn: 03605442. doi: 10.1016/j.energy.2012.04.044 (cit. on pp. 83, 86).

[96] J. R. Serrano, H. Climent, P. Piqueras, and E. Angiolini. "Filtration modelling in wall-flow particulate filters of low soot penetration thickness". *Energy*, 112, (2016), pp. 883–898. issn: 03605442. doi: 10.1016/j.energy.2016.06.121 (cit. on p. 83).

[97] J. R. Serrano, F. J. Arnau, P. Piqueras, and Ó. García-Afonso. "Packed bed of spherical particles approach for pressure drop prediction in wall-flow DPFs (diesel particulate filters) under soot loading conditions". *Energy*, 58, (2013), pp. 644–654. issn: 03605442. doi: 10.1016/j.energy.2013.05.051 (cit. on p. 83).

[98] D. Kryl, P. Kočí, M. Kubíček, M. Marek, T. Maunula, and M. Härkönen. "Catalytic converters for automobile diesel engines with adsorption of hydrocarbons on zeolites". *Industrial and Engineering Chemistry Research*, 44 (25), (2005), pp. 9524–9534. issn: 08885885. doi: 10.1021/ie050249v (cit. on p. 87).

[99] F. Payri, X. Margot, A. Gil, and J. Martin. "Computational study of heat transfer to the walls of a di diesel engine". *SAE 2005 World Congress & Exhibition*. SAE International, 2005. doi: 10.4271/2005-01-0210 (cit. on p. 96).

[100] J. Benajes, P. Olmeda, J. Martín, and R. Carreño. "A new methodology for uncertainties characterization in combustion diagnosis and thermodynamic modelling". *Applied Thermal Engineering*, 71 (1), (2014), pp. 389–399. issn: 13594311. doi: 10.1016/j.applthermaleng.2014.07.010 (cit. on pp. 96, 99).

[101] L. Jarrier, J. C. Champoussin, R. Yu, and D. Gentile. "Warm-up of a D.I. diesel engine: Experiment and modeling". *SAE 2000 World Congress*. SAE International, 2000. doi: 10.4271/2000-01-0299 (cit. on p. 96).

[102] C. Samhaber, A. Wimmer, and E. Loibner. "Modeling of engine warm-up with integration of vehicle and engine cycle simulation". *Vehicle Thermal Management Systems Conference & Exposition*. SAE International, 2001. doi: 10.4271/2001-01-1697 (cit. on p. 96).

[103] A. Roberts, R. Brooks, and P. Shipway. "Internal combustion engine cold-start efficiency: A review of the problem, causes and potential solutions". *Energy Conversion and Management*, 82, (2014), pp. 327–350. issn: 01968904. doi: 10.1016/j.enconman.2014.03.002 (cit. on pp. 96, 97).

[104] S. Uppuluri, H. R Khalane, Y. Umbarkar, and A. Naiknaware. "Cold-Ambient Warm-Up Predictions: A Novel Approach Using 1D Computational Models". *SAE 2016 World Congress & Exhibition*. SAE International, 2016. doi: 10.4271/2016-01-0198 (cit. on pp. 96, 97).

[105] A. Broatch, P. Olmeda, J. Martin, and J. Salvador-Iborra. "Development and Validation of a Submodel for Thermal Exchanges in the Hydraulic Circuits of a Global Engine Model". *WCX World Congress Experience*. SAE International, 2018. doi: 10.4271/2018-01-0160 (cit. on p. 104).

[106] B. E. Flores. "A pragmatic view of accuracy measurement in forecasting". *Omega*, 14 (2), (1986), pp. 93–98. issn: 03050483. doi: 10.1016/0305-0483(86)90013-7 (cit. on p. 117).

[107] G. Torazza and D. Giacosa. "Valve-actuating mechanism for an internal combustion engine". Pat. 3641988. 1972. url: https://www.freepatentsonline.com/3641988.html (cit. on p. 141).

[108] G. Garcea. "Timing variator for the timing system of a reciprocating internal combustion engine". Pat. 4231330. 1980. url: https://www.freepatentsonline.com/4231330.html (cit. on p. 141).

[109] Honda Motor Co., Ltd. *The VTEC Engine / 1989*. Accessed 2020-09-28 at https://global.honda/heritage/episodes/1989vtecengine.html. 2020 (cit. on p. 142).

[110] S. Benett. *Medium/Heavy Duty Truck Engines, Fuel & Computerized Management Systems*. 5th ed. Cengage Learning, 2016, p. 1008. isbn: 9781305578555 (cit. on p. 142).

[111] Mitsubishi Motors. *Mitsubishi Motors Launches RVR New Compact Crossover*. Accessed 2020-09-28 at https://www.mitsubishi-motors.com/publish/pressrelease_en/products/2010/news/detail0729.html. 2010 (cit. on p. 142).

[112] T. Lancefield, I. Methley, U. Räse, and T. Kuhn. "The application of variable event valve timing to a modern diesel engine". *SAE 2000 World Congress*. SAE International, 2000. doi: 10.4271/2000-01-1229 (cit. on p. 143).

[113] M. A. Gonzalez and D. Di Nunno. "Internal Exhaust Gas Recirculation for Efficiency and Emissions in a 4-Cylinder Diesel Engine". *SAE 2016 International Powertrains, Fuels and Lubricants Meeting*. SAE International, 2016. doi: 10.4271/2016-01-2184 (cit. on p. 143).

[114] J. R. Serrano, P. Piqueras, R. Navarro, J. Gómez, M. Michel, and B. Thomas. "Modelling Analysis of Aftertreatment Inlet Temperature Dependence on Exhaust Valve and Ports Design Parameters". *SAE 2016 World Congress and Exhibition*. SAE International, 2016. doi: 10.4271/2016-01-0670 (cit. on p. 143).

[115] R. M. Siewert. "How individual valve timing events affect exhaust emissions". *International Mid-Year Meeting*. SAE International, 1971. doi: 10.4271/710609 (cit. on pp. 145, 147, 148).

[116] T. Tomoda, T. Ogawa, H. Ohki, T. Kogo, K. Nakatani, and E. Hashimoto. "Improvement of diesel engine performance by variable valve train system". *International Journal of Engine Research*, 11 (5), (2010), pp. 331–344. issn: 14680874. doi: 10.1243/14680874JER586 (cit. on pp. 145, 146).

[117] J. Benajes, E. Reyes, and J. M. Luján. "Modelling study of the scavenging process in a turbocharged diesel engine with modified valve operation". *Proceedings of the Institution of Mechanical Engineers, Part C: Journal of Mechanical Engineering Science*, 210 (4), (1996), pp. 383–393. issn: 09544062. doi: 10.1243/PIME_PROC_1996_210_210_02 (cit. on pp. 145, 149).

[118] K. Deppenkemper, C. Zyalcin, M. Ehrly, M. Schoenen, D. Bergmann, and S. Pischinger. "1D Engine Simulation Approach for Optimizing Engine and Exhaust Aftertreatment Thermal Management for Passenger Car Diesel Engines by Means of Variable Valve Train (VVT) Applications". *WCX World Congress Experience*. SAE International, 2018. doi: 10.4271/2018-01-0163 (cit. on pp. 145, 168).

[119] J. P. Zammit, M. J. McGhee, P. J. Shayler, T. Law, and I. Pegg. "The effects of early inlet valve closing and cylinder disablement onfuel economy and emissions of a direct injection diesel engine". *Energy*, 79, (2015), pp. 100–110. issn: 03605442. doi: 10.1016/j.energy.2014.10.065 (cit. on pp. 145, 146).

[120] W. De Ojeda. "Effect of variable valve timing on Diesel combustion characteristics". *SAE 2010 World Congress and Exhibition*. SAE International, 2010. doi: 10.4271/2010-01-1124 (cit. on p. 146).

[121] A. Piano, F. Millo, D. Di Nunno, and A. Gallone. "Numerical Assessment of the CO2 Reduction Potential of Variable Valve Actuation on a Light Duty Diesel Engine". *CO2 Reduction for Transportation Systems*

Conference. SAE International, 2018. doi: 10.4271/2018-37-0006 (cit. on p. 146).

[122] A. Piano. "Analysis of Advanced Air and Fuel Management Systems for Future Automotive Diesel Engine Generation". PhD thesis. Politecnico di Torino, 2018 (cit. on pp. 146, 147).

[123] W. Guan, V. B. Pedrozo, H. Zhao, Z. Ban, and T. Lin. "Variable valve actuation–based combustion control strategies for efficiency improvement and emissions control in a heavy-duty diesel engine". *International Journal of Engine Research*, 21 (4), (2020), pp. 578–591. issn: 20413149. doi: 10.1177/1468087419846031 (cit. on p. 146).

[124] W. Guan, H. Zhao, Z. Ban, and T. Lin. "Exploring alternative combustion control strategies for low-load exhaust gas temperature management of a heavy-duty diesel engine". *International Journal of Engine Research*, 20 (4), (2019), pp. 381–392. issn: 20413149. doi: 10.1177/1468087418755586 (cit. on p. 146).

[125] P. Maniatis, U. Wagner, and T. Koch. "A model-based and experimental approach for the determination of suitable variable valve timings for cold start in partial load operation of a passenger car single-cylinder diesel engine". *International Journal of Engine Research*, 20 (1), (2019), pp. 141–154. issn: 20413149. doi: 10.1177/1468087418817119 (cit. on pp. 146, 148).

[126] J. Kim and C. Bae. "An investigation on the effects of late intake valve closing and exhaust gas recirculation in a single-cylinder research diesel engine in the low-load condition". *Proceedings of the Institution of Mechanical Engineers, Part D: Journal of Automobile Engineering*, 230 (6), (2016), pp. 771–787. issn: 09544070. doi: 10.1177/0954407015595149 (cit. on p. 146).

[127] J. Benajes, S. Molina, R. Novella, and M. Riesco. "Improving pollutant emissions in diesel engines for heavy-duty transportation using retarded intake valve closing strategies". *International Journal of Automotive Technology*, 9 (3), (2008), pp. 257–265. issn: 12299138. doi: 10.1007/s12239-008-0032-7 (cit. on p. 146).

[128] X. Zhou, E. Liu, D. Sun, and W. Su. "Study on transient emission spikes reduction of a heavy-duty diesel engine equipped with a variable intake valve closing timing mechanism and a two-stage turbocharger". *International Journal of Engine Research*, 20 (3), (2019), pp. 277–291. issn: 20413149. doi: 10.1177/1468087417748837 (cit. on p. 146).

[129] D. B. Gosala et al. "Diesel engine aftertreatment warm-up through early exhaust valve opening and internal exhaust gas recirculation during idle operation". *International Journal of Engine Research*, 19 (7), (2018), pp. 758–773. issn: 20413149. doi: 10.1177/1468087417730240 (cit. on pp. 147, 156).

[130] G. B. Parvate-Patil, H. Hong, and B. Gordon. "Analysis of variable valve timing events and their effects on single cylinder diesel engine". *2004 Powertrain & Fluid Systems Conference & Exhibition*. SAE International, 2004. doi: 10.4271/2004-01-2965 (cit. on p. 147).

[131] A. Piano, F. Millo, D. Di Nunno, and A. Gallone. "Numerical Analysis on the Potential of Different Variable Valve Actuation Strategies on a Light Duty Diesel Engine for Improving Exhaust System Warm Up". *13th International Conference on Engines & Vehicles*. SAE International, 2017. doi: 10.4271/2017-24-0024 (cit. on p. 149).

[132] C. Guardiola, B. Pla, P. Bares, and J. Mora. "An on-board method to estimate the light-off temperature of diesel oxidation catalysts". *International Journal of Engine Research*, 21 (8), (2020), pp. 1480–1492. issn: 20413149. doi: 10.1177/1468087418817965 (cit. on p. 168).

[133] A. J. Haagen-Smit. "Chemistry and Physiology of Los Angeles Smog". *Industrial & Engineering Chemistry*, 44 (6), (1952), pp. 1342–1346. issn: 0019-7866. doi: 10.1021/ie50510a045 (cit. on p. 190).

[134] D. F. Hagen and G. W. Holiday. "The effects of engine operating and design variables on exhaust emissions". *Pre-1964 SAE International*. SAE International, 1962. doi: 10.4271/620404 (cit. on p. 190).

[135] M. Finlay. "Variable valve timing control for internal combustion engines". Pat. US3496918A. 1968. url: https://patents.google.com/patent/US3496918A/en (cit. on p. 191).

[136] Z. Dimitrova, M. Tari, P. Lanusse, F. Aioun, and X. Moreau. "Development and Control of a Camless Engine Valvetrain". *IFAC-PapersOnLine*, 52 (5), (2019). 9th IFAC Symposium on Advances in Automotive Control AA 2019. issn: 24058963. doi: 10.1016/j.ifacol.2019.09.064 (cit. on p. 191).

[137] Y. Murata, J. Kusaka, M. Odaka, Y. Daisho, D. Kawano, H. Suzuki, H. Ishii, and Y. Goto. "Achievement of medium engine speed and load premixed diesel combustion with variable valve timing". *SAE 2006 World Congress & Exhibition*. SAE International, 2006. doi: 10.4271/2006-01-0203 (cit. on p. 191).

[138] J. Hunicz and M. Mikulski. "Application of Variable Valve Actuation Strategies and Direct Gasoline Injection Schemes to Reduce Combustion Harshness and Emissions of Boosted HCCI Engine". *Journal of Engineering for Gas Turbines and Power*, 141 (7), (2019). issn: 0742-4795. doi: 10.1115/1.4043418 (cit. on p. 191).

[139] G. Xu, M. Jia, Y. Li, Y. Chang, H. Liu, and T. Wang. "Evaluation of variable compression ratio (VCR)and variable valve timing (VVT)strategies in a heavy-duty diesel engine with reactivity controlled compression ignition (RCCI)combustion under a wide load range". *Fuel*, 253, (2019), pp. 114–128. issn: 00162361. doi: 10.1016/j.fuel.2019.05.020 (cit. on p. 191).

[140] N. Hooftman, M. Messagie, J. Van Mierlo, and T. Coosemans. "A review of the European passenger car regulations – Real driving emissions vs local air quality". *Renewable and Sustainable Energy Reviews*, 86, (2018), pp. 1–21. issn: 1364-0321. doi: 10.1016/j.rser.2018.01.012 (cit. on p. 236).

[141] M. Williams and R. Minjares. "A technical summary of Euro 6/VI vehicle emission standards". *The International Council on Clean Transportation*, (2016). url: https://theicct.org/sites/default/files/publications/ICCT_Euro6-VI_briefing_jun2016.pdf (cit. on p. 236).

[142] G. D. Neely, J. V. Sarlashkar, and D. Mehta. "Diesel cold-start emission control research for 2015-2025 LEV III emissions". *SAE International Journal of Engines*, (2013). issn: 19463944. doi: 10.4271/2013-01-1301 (cit. on p. 236).

[143] G. D. Neely, D. Mehta, and J. Sarlashkar. "Diesel Cold-Start Emission Control Research for 2015-2025 LEV III Emissions - Part 2". *SAE International Journal of Engines*, (2014). issn: 19463944. doi: 10.4271/2014-01-1552 (cit. on p. 236).

[144] N. Cavina, G. Mancini, E. Corti, D. Moro, M. De Cesare, and F. Stola. "Thermal management strategies for SCR after treatment systems". *11th International Strategies Conference on Engines & Vehicles*. SAE International, 2013. doi: 10.4271/2013-24-0153 (cit. on p. 236).

[145] J. M. Luján, V. Bermúdez, P. Piqueras, and O. García-Afonso. "Experimental assessment of pre-turbo aftertreatment configurations in a single stage turbocharged diesel engine. Part 1: Steady-state operation". *Energy*, 80, (2015), pp. 599–613. issn: 03605442. doi: 10.1016/j.energy.2014.05.048 (cit. on p. 236).

[146] J. M. Luján, J. R. Serrano, P. Piqueras, and O. García-Afonso. "Experimental assessment of a pre-turbo aftertreatment configuration in a single stage turbocharged diesel engine. Part 2: Transient opera-

tion". *Energy*, 80, (2015), pp. 614–627. issn: 03605442. doi: 10.1016/j.energy.2014.12.017 (cit. on p. 236).

[147] R. Kamo and W. Bryzik. "Adiabatic turbocompound engine performance prediction". *1978 Automotive Engineering Congress and Exhibition*. SAE International, 1978. doi: 10.4271/780068 (cit. on p. 236).

[148] R. R. Sekar, R. Kamo, and J. C. Wood. "Advanced adiabatic diesel engine for passenger cars". *SAE International Congress and Exhibition*. SAE International, 1984. doi: 10.4271/840434 (cit. on p. 236).

[149] P. Olmeda, J. Martín, R. Novella, and D. Blanco-Cavero. "Assessing the optimum combustion under constrained conditions". *International Journal of Engine Research*, 21 (5), (2020), pp. 811–823. issn: 20413149. doi: 10.1177/1468087418814086 (cit. on p. 236).

[150] A. Kawaguchi, Y. Wakisaka, N. Nishikawa, H. Kosaka, H. Yamashita, C. Yamashita, H. Iguma, K. Fukui, N. Takada, and T. Tomoda. "Thermo-swing insulation to reduce heat loss from the combustion chamber wall of a diesel engine". *International Journal of Engine Research*, 20 (7), (2019), pp. 805–816. issn: 20413149. doi: 10.1177/1468087419852013 (cit. on p. 236).

[151] E. Gingrich, M. Tess, V. Korivi, P. Schihl, J. Saputo, G. M. Smith, S. Sampath, and J. Ghandhi. "The impact of piston thermal barrier coating roughness on high-load diesel operation". *International Journal of Engine Research*, Advance online publication, (2019). issn: 20413149. doi: 10.1177/1468087419893487 (cit. on p. 237).

[152] T. Powell, R. O'Donnell, M. Hoffman, Z. Filipi, E. H. Jordan, R. Kumar, and N. J. Killingsworth. "Experimental investigation of the relationship between thermal barrier coating structured porosity and homogeneous charge compression ignition engine combustion". *International Journal of Engine Research*, Advance online publication, (2019). issn: 20413149. doi: 10.1177/1468087419843752 (cit. on p. 237).

[153] J. Somhorst, M. Oevermann, M. Bovo, and I. Denbratt. "Evaluation of thermal barrier coatings and surface roughness in a single-cylinder light-duty diesel engine". *International Journal of Engine Research*, Advance online publication, (2019). issn: 20413149. doi: 10.1177/1468087419875837 (cit. on p. 237).

[154] A. Poubeau, A. Vauvy, F. Duffour, J. M. Zaccardi, G. de Paola, and M. Abramczuk. "Modeling investigation of thermal insulation approaches for low heat rejection Diesel engines using a conjugate heat transfer model". *International Journal of Engine Research*, 20 (1), (2019), pp. 92–104. issn: 20413149. doi: 10.1177/1468087418818264 (cit. on p. 237).

[155] S. Caputo, F. Millo, G. Boccardo, A. Piano, G. Cifali, and F. C. Pesce. "Numerical and experimental investigation of a piston thermal barrier coating for an automotive diesel engine application". *Applied Thermal Engineering*, 162, (2019), p. 114233. issn: 13594311. doi: 10.1016/j.applthermaleng.2019.114233 (cit. on p. 237).

[156] M. Ekström, A. Thibblin, A. Tjernberg, C. Blomqvist, and S. Jonsson. "Evaluation of internal thermal barrier coatings for exhaust manifolds". *Surface and Coatings Technology*, 272, (2015), pp. 198–212. issn: 02578972. doi: 10.1016/j.surfcoat.2015.04.005 (cit. on p. 237).

[157] A. Thibblin and U. Olofsson. "A test rig for evaluating thermal cyclic life and effectiveness of thermal barrier coatings inside exhaust manifolds". *WCX SAE World Congress Experience*. SAE International, 2019. doi: 10.4271/2019-01-0929 (cit. on p. 237).

[158] N. Kishi, H. Hashimoto, K. Fujimori, K. Ishii, and T. Komatsuda. "Development of the ultra low heat capacity and highly insulating (ULOC) exhaust manifold for ULEV". *International Congress & Exposition*. SAE International, 1998. doi: 10.4271/980937 (cit. on p. 237).

[159] S. Zidat and M. Parmentier. "Exhaust manifold design to minimize catalyst light-off time". *SAE 2003 World Congress & Exhibition*. SAE International, 2003. doi: 10.4271/2003-01-0940 (cit. on p. 237).

[160] J. R. Serrano, F. J. Arnau, J. Martin, M. Hernandez, and B. Lombard. "Analysis of Engine Walls Thermal Insulation: Performance and Emissions". *SAE 2015 World Congress & Exhibition*. SAE International, 2015. doi: 10.4271/2015-01-1660 (cit. on p. 237).

[161] J. M. Luján, J. R. Serrano, P. Piqueras, and B. Diesel. "Turbine and exhaust ports thermal insulation impact on the engine efficiency and aftertreatment inlet temperature". *Applied Energy*, 240, (2019), pp. 409–423. issn: 03062619. doi: 10.1016/j.apenergy.2019.02.043 (cit. on p. 238).

“Never confuse education with intelligence, you can have a PhD and still be an idiot.”

—quote attributed to Richard P. Feynman